TRINITY
COLLEGE
DUBLIN

CHARACTERISATION OF AN INTEGRATED TELEMETRIC TEMPERATURE SENSOR FOR CFRP MILLING APPLICATIONS

By

KEVIN KERRIGAN

A thesis submitted to the University of Dublin in partial fulfillment of the requirements for the degree of

DOCTOR IN PHILOSOPHY

Department of Mechanical and Manufacturing Engineering
University of Dublin, Trinity College

May 2013

"All our knowledge is the offspring of our perceptions"

Leonardo Da Vinci

DECLARATION

I declare that the works submitted in this thesis have not been submitted as an exercise for a degree at this or any other university. Further, I declare that the works herein are entirely my own unless acknowledged otherwise in the text wherever included. Finally, I agree that the Library may lend or copy this thesis upon request. This permission covers only single copies made for study purposes, subject to normal conditions of acknowledgement.

SUMMARY

The concept of a sensor designed to measure the behaviour of a machining process is a fundamental part of process monitoring and control. The perception of such a sensor is often underestimated when novel applications are investigated and as a result the value of the overall monitoring process is lost. One such novel application is the milling of carbon fibre reinforced polymer (CFRP) composites. There has been a rapid rise to the forefront in CFRP particularly in the aerospace industry due to rapid transition to such materials that feature numerous advantages over traditional materials. An exhaustive literature review has indicated that various sensors have been developed to monitor the machining process temperature. However, interrupted high speed composite machining processes that involve complex geometries in rotation, remain without a robust production-friendly and accurate temperature process monitoring tool. This lack of sensor suitability is also due to the requirement that such a sensor must not significantly change the process conditions and must satisfy conditions of robustness and reliability in industrial processes.

The primary goal of this investigation is to characterise a novel integrated telemetric thermocouple (ITT), sensor for the application of tool temperature measurement in CFRP peripheral milling.

In order to achieve this goal, a structured methodology was followed. The sequence is outlined through the following activities:

1) Characterise the steady-state behaviour of the ITT sensor using a highly accurate controlled temperature calibration unit.
2) Characterise the dynamic behaviour of the ITT sensor. Thermal resistance effects associated with the embedded tool setup were investigated by developing a finite element model (FEM). The model was validated using a cutting-analogous heat delivery experimental setup. The setup employed a known heat flux value, supplied to the outer surface of the tool to simulate the heat generated in the cutting process. A second sensor, an infrared thermal imaging camera, was used to determine the surface temperature during the process.
3) Using the validated model, surface tool temperatures for CFRP edge trimming experiments were investigated. An iterative process was used to obtain comparable profiles results to the experimental temperature profiles of both ITT sensor and IR camera. Tool surface temperatures were then compared with 3D surface roughness data, obtained via white light interferometry, in order to investigate the effect of specific cutting parameters on both the surface tool temperature and the workpiece

quality prior to any tool wear. The reason for such an investigation was to determine whether a relationship could be seen between the parameters.

Initial FEM approximations indicated non-conformance between modelled and experimental temperature profiles in a cutting scenario. The non-conformance was found to be due to the restriction of the model to using a constant heat flux shape function as a boundary condition. In order to accelerate heat flux shape function optimization, the heat flux boundary for the model replaced the experimentally obtained ITT sensor temperature profiles. This allowed for the average heat flux at the cutting surface to be determined for different machining parameters.

In this research, an FEM of the ITT sensor was developed and validated through both analogous heat flux experiments and cutting experiments. This model validated model allowed for heat flux shape functions associated with the cutting process to be characterized. The refinement of the shape function allowed for an enhanced FEM to represent the behavior of the tool as a thermal system during cutting. Parametric analyses using the FEM indicated that axial heat source variation along the tool length causes heat choking at the tool tip. This results in a substantially greater tool surface temperature. Through CFRP edge trimming investigations, it was observed that such trends were also found when CFRP cutting experiments were performed using specific machining parameters. Due to the sensitivity of the epoxy matrix, the heat-choking hypothesis proved to cause significant damage to the surface quality of the workpiece.

Investigations into the heat flux associated with the CFRP edge trimming process indicated a general trend throughout all combinations of investigated cutting parameters in which an initial spike in thermal energy occurs. This is followed by an exponential decay until an approximately constant heat flux value for the remainder of cutting. Analysis of the heat flux and force values indicates that the axial location of the cutting interface on the tool has a minor effect on the process. This is in contrast to the effect of feed rate, which causes significant changes in the process responses. Such in-process effects are linked to the workpiece surface quality via the use of surface roughness quantification.

ACKNOWLEDGEMENTS

I am deeply indebted to my supervisor and mentor, Dr. Garret O'Donnell, who provided me with the opportunity to do postgraduate research in Trinity. Without his vast knowledge, support, guidance and patience I would not be in a position to submit this thesis. Apart from the technical skills I have learned from him, Dr. O'Donnell has taught me many important life skills which I have no doubt will prove invaluable in the future.

Special thanks must also go to Dr. Tony Robinson for his perpetual positive attitude, immense knowledge and for always having his door open when I had a problem. Special thanks also to Prof. Andrew Torrance, Prof. Pedro Arrazola, Mr. Kevin Kelly, Mr. Theo Revil, Mr. Neal Leddy and Mr. Rob Hewison for their insight and valuable advice at different times during the project and to all the staff of the Mechanical and Manufacturing Engineering Department at Trinity College.

The technical support that enabled this research was provided by Sean Doonan, Mick Reilly, Alex, Gabriel and JJ in the workshop, who must be given huge thanks for their skillful efforts, patience and desire for excellence. I would like to thank Gerry Byrne for all his help and support at every point in my research.

I would also like to say a very big thank you to all the people in the Department of Mechanical Engineering in UCD for allowing me to use the equipment in their excellent facility, in particular Dr. Eamonn Ahearne and Richard Byrne.

Thanks also to Livy, Mom, Dad, Paula and Nan, each of whom provided me with motivation, inspiration, support, courage and the drive to see this project through. Without all of them, this thesis would not have happened.

I would also like to thank all of my postgraduate friends who helped me to realise this thesis. Through many humorous, technical, motivational and heartfelt coffee breaks, they kept me sane throughout my time in Trinity. In particular, I would like to thank my flat mate, Paul Ervine, along with the rest of the manufacturing researchers, Paul H, Stuart, Peadar, Oana, Eoin, Aoife, Emma, Jeff, Darren, Rory, Sean, and Barry, as well as the thermo lads and lasses Seamus, Rayhaan, Al, Gerard, Tom, Brian, Oisin, Maurice, Aimee, Kate, Karl and all the French students. I would also like to offer my best wishes to Eoin and Robin who have been my office mates for the last few months.

TABLE OF CONTENTS

NOMENCLATURE

Notation		Description
a_e	:	Radial depth of cut (mm)
c	:	299 792 458 (m/s) (speed of light in a vacuum)
c	:	Speed of propagation (m/s)
C_F	:	Number of flutes
C_P	:	Specific heat (J/kgK)
d	:	Fibre diameter (mm)
dA	:	Surface area (m^2)
D_{tool}	:	Tool diameter (m)
f	:	Feed per revolution (mm/rev)
f_z	:	Feed per tooth (mm/tooth)
F_R	:	Resultant cutting horizontal force (N)
F_X	:	Horizontal cutting force in the x-direction (N)
F_Y	:	Horizontal cutting force in the y-direction (N)
F_Z	:	Vertical cutting force (N)
Fo	:	Dimensionless fourier number
h_i	:	*i*th of N small contiguous areas (μm^2)
h	:	6.626 176 x 10^{-34} ($W s^2$) (Planck constant)
k	:	Thermal conductivity (W/m K)
k	:	1.380662 x 10^{23} (W s/K) (Boltzmann constant)
L_c	:	Length of cut (m)
L_c	:	Length from the tool tip to the centre of the heat ring (m)
M	:	Emittance (W/m^2)
$M_b(T)$	:	Radiant exitance of a black body at same temperature (W/m^2)
M(T)	:	Radiant exitance (W/m^2)
N	:	Spindle speed (rpm)
q	:	Heat flux (W/m^2)
R_a	:	Arithmetic mean roughness (µm)
R	:	Characteristic length through which conduction occurs (m)
R_q	:	Quadratic roughness (µm)
R_y or R_{max}	:	Maximum peak-to-valley roughness (µm)
r_1	:	Thermal resistance related to diffusivity of a material (m^2K/W)
t	:	Characteristic thickness (mm)

T_B	:	Temperature of a heated body (K)
T_S	:	Temperature of the sensor (K)
T	:	Temperature (K)
t	:	Time (s)
T_t	:	Temperature of the contact point on the target (K)
T_c	:	Temperature of the contact point on the contact (K)
T'	:	Temperature derivative (K)
TCC	:	Thermal contact conductance (W/m^2K)
ν	:	Frequency of a wavelength (hz)
v_c	:	Cutting speed (m/s)
v_f	:	Feed rate (mm/min)

Greek letters

Notation		**Description**
α	:	Thermal diffusivity (m^2/s)
Φ	:	Energy flux (W)
λ	:	Wavelength (μm)
ρ	:	Density (kg/m^3)
σ_{AB}	:	Seebeck coefficient (V/°C)

ABBREVIATIONS

Notation		Description
ANOVA	:	Analysis of variance
AWJ	:	Abrasive water jet
CBN	:	Cubic boron nitride
CFRP	:	Carbon fibre reinforced polymer
CMA	:	Centre for microscopy and analysis
CTE	:	Coefficient of thermal expansion
DAQ	:	Data acquisition
DEA	:	Dielectric analysis
DMA	:	Dynamic mechanical analysis
EDM	:	Electro discharge machining
EM	:	Electromagnetic
EMF	:	Electromotive force
FEA	:	Finite element analysis
FRP	:	Fibre reinforced polymer
FRPs	:	Fibre reinforced plastics
FTIR	:	Fourier transform infrared
GFRP	:	Glass fibre reinforced polymer
IHCT	:	Inverse heat conduction technique
ITT	:	Integrated telemetric thermocouple
KFRP	:	Kevlar FRP
PCD	:	Polycrystalline diamond
PCR	:	Percentage contribution ratio
PMC	:	Polymer matrix composite
RMS	:	Root mean square
RTD	:	Resistive thermal device
RTDs	:	Resistance thermometer detectors
SEM	:	Scanning electron microscope
SIM	:	Simulation
SFSM	:	Sequential function specification method
SR	:	Surface roughness
SS	:	Sums of squares
TCC	:	Thermal contact conductance
TCR	:	Thermal contact resistance
TFTs	:	Thin film thermocouples
TGA	:	Thermogravimetric analysis

UMT	:	Ultimate maximum temperature
USV	:	Ultrasonic-vibration
WP	:	Workpiece

1 INTRODUCTION

The utilisation of new materials such as composites and plastics rather than more traditional materials such as metals has had a tremendous impact on the manner in which components are machined [1]. However, due to rapid transitions to such materials, driven by numerous factors including the demands of a globally reaching market, environmental awareness and the quest for energy efficiency, today's manufacturing sector is expected to adapt and respond with the same rapidity as the materials being processed. It is this rapid need to understand new manufacturing processes and adapt appropriately that has made process monitoring and control so important in today's manufacturing industries.

The monitoring process is highly reliant on accurate information supplied by sensors, which are either directly or indirectly associated with the process. A sensor is defined as a device that receives and responds to a signal or stimulus [2]. The concept of a sensor designed to measure some response or behaviour of a machining process is a fundamental part of process monitoring and control. However, machining processes seldom facilitate direct sensing due to the impact on the process and hence many sensor systems are based on aspects of the machine tool or the cutting tool becoming sensorised. This newly sensorised tool combined with the associated measurement chain can often reduce the fundamental sensitivity to the measureable phenomena occurring during materials processing. This is more clearly understood by way of the sequence of events in a process monitoring and control system as outlined by Teti *et al.* [3]: Process variables → sensorial perception → data processing and feature extraction → cognitive decision making → action.

Focusing on sensorial perception defined by Teti *et al.* [3] as the process of attaining awareness or understanding of sensory information, the level of understanding associated with the sensory information should not be underestimated. The theory of active processing of kinetic intelligence, as described by Gregory [4], is a popular theory in which stored-from-the-past potential intelligence of knowledge is selected and applied to solve current perceptual problems by active processing of kinetic intelligence. Relating this form of active perception to a machining process, one must consider the influence of senses/sensors, surroundings and the value of the information received into the brain or computer from the sensor. It is this active perception that will be investigated in the current measurement application.

Traditional categories of direct and indirect measurement approaches are typically used to quantify process responses. A key process response of carbon fibre reinforced polymer (CFRP) machining, which utilises an indirect process measurement sensor, is temperature. Temperature has long been correlated to deleterious and costly production facets of

traditional metal machining, such as tool wear, and has formed the basis of extensive research efforts which have been well summarised by Davies *et al.* [5]. While tool wear has been thoroughly explored and related to increases in the process temperature [6], polymer-based materials such as fibre reinforced plastics (FRPs) have introduced a new challenge in the form of workpiece thermal damage. Such damage can initiate at modest temperatures beyond the glass transition temperature of the matrix material, which can be as high as 200°C. As plastic and composite machining have become ubiquitous in areas such as the aerospace, automotive, marine and numerous sporting equipment industries [7], the need for awareness and monitoring of the process temperature has become critical due to the sensitivity of such workpiece materials to either visual or incipient thermal damage.

Various sensors have been developed to monitor the machining process temperature [8]. However, interrupted high speed composite machining processes involving complex geometries in rotation remain without a robust production-friendly and accurate temperature process monitoring tool. This lack of sensor suitability is also due to the requirement that such a sensor must not significantly change the process conditions and must satisfy conditions of robustness and reliability in industrial processes which has been highlighted as a limitation in many keynote papers on monitoring [3, 9].

This research introduces a novel temperature sensor that has been designed specifically for the purpose of monitoring temperature in milling and drilling processes. The work examines in detail the sensor characteristics for temperature monitoring of machining processes such as milling of composite materials.

1.1 Existing and emerging issues in CFRP composite machining

Current global demand for carbon fibre, of which CFRP composites form a large proportion, is approximately 46,000 tonnes and rising [10]. By application such materials are found in aerospace – 17%, industrial, including wind energy and automotive – 67% and sporting goods – 16% sectors [10]. The rapid growth rate has seen the global CFRP composite annual spend increase to €11.4 billion in 2012, with an anticipated compound annual growth rate of 13%, resulting in a rise in annual spend to €28 billion by 2020 [11]. It is well known that the abundant use of CFRP is due to its superior combination of strength-weight and modulus-weight ratios in comparison to metals, allowing light weight, robust construction [12]. However, additional advantages also include longer life, i.e. no corrosion, tailorable strength and stiffness to load directions, inherent damping and improved thermal conductivity [13]. The strength-weight advantage has been recognised and capitalised upon to good effect by the aerospace industry, where composites are becoming more prevalent in aircraft designs, as illustrated in Figure 1.1.

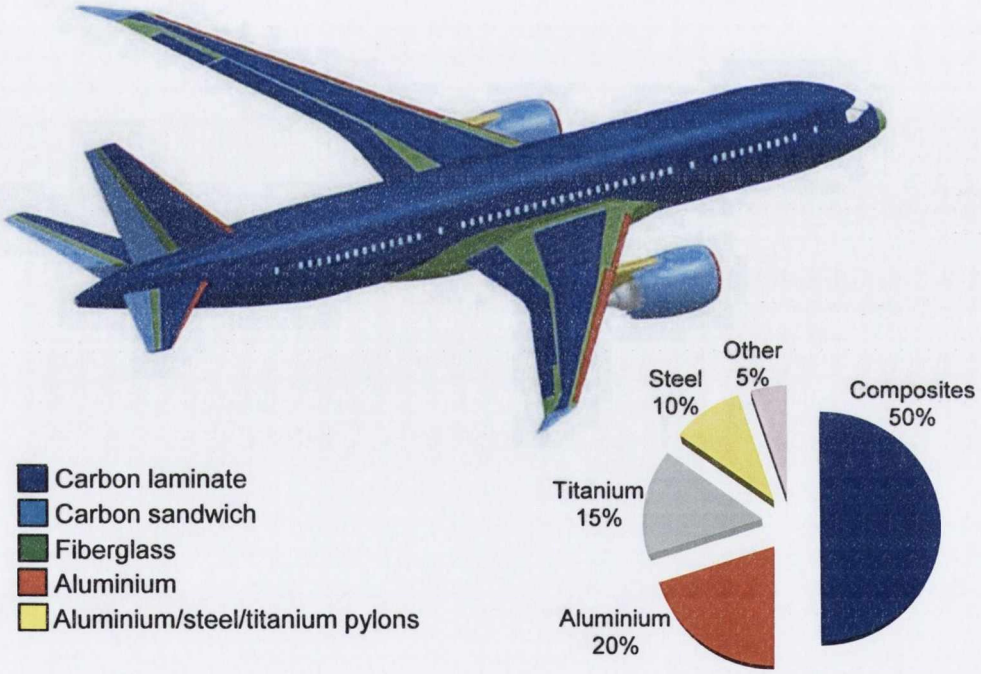

Figure 1.1: The material break-down of the Boeing 787 Dreamliner.

(Adapted from Nelson *et al.* [14])

During the formation of a CFRP composite, a number of processes take place to move from basic fibre and resin matrix components, through to prepregs and then on to the final high modulus or high stiffness component. The application for which a CFRP component is ultimately to be used places a high degree of importance upon the process employed to form

such components. It would be realistic to observe processes such as hot melting of the prepreg, hand layup of plies, bag-moulding, vacuum consolidation, oven curing, and post-processing, for example drilling, milling and turning, if the early life-cycle of the composite were to be tracked. A closer look at some of these processes indicates that there are at least two stages during which the incomplete composite requires a material removal process; 1) during the layup of plies, as the individual laminae need to be shaped to the part requirements and 2) post-curing, in order to trim excess material generated during consolidation, create features and revise surfaces. In early research, Konig [15] stipulated a number of cutting processes and their suitability for prepreg and fully-cured component cutting as reproduced in Figure 1.2. While this model has become outdated due to advancements in material removal processes, in particular water jet cutting, over the last 27 years, it stood as a basis for a large amount of work, in both industry and academia, performed previously.

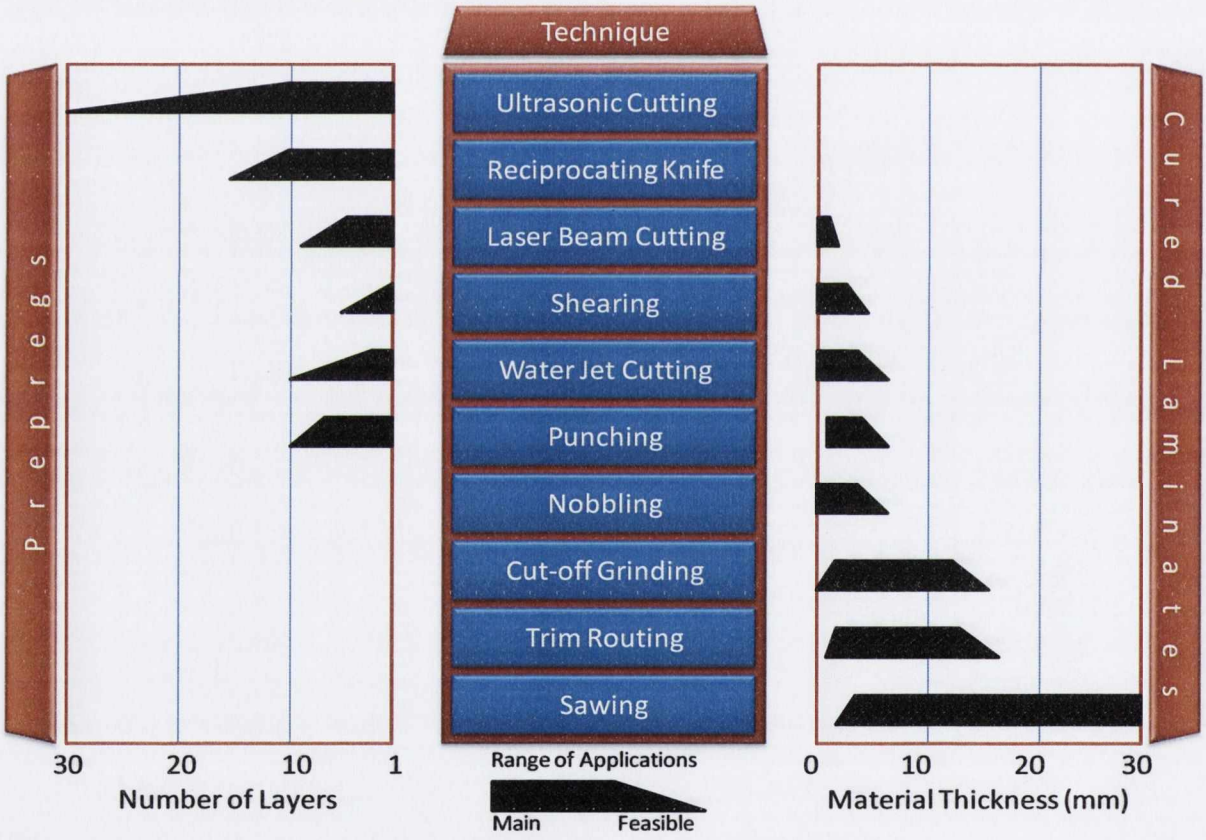

Figure 1.2: Techniques used in cutting of prepregs and cured laminates.

(Adapted from Konig *et al.* [15])

It is expressed by Schulze *et al.* [7] and reiterated here that the ultimate goal in CFRP component manufacture should be to manufacture parts without any mechanical machining. However, due to the complexity of processing techniques currently employed during

component manufacture, there is still a need for many subsequent machining operations. This is particularly important for near-net shape, high value added parts.

Another application of composite machining that has seen rapid growth in recent times is that of composite mould tools. The use of composites for tooling is due to the fact that they are light-weight, relatively cheap to manufacture and have the same coefficient of thermal expansion (CTE) as the component being manufactured. However, their widespread use has been limited due to the difficulty in achieving the geometric tolerance and surface finish required of the part. This has led to the use of sacrificial CFRP materials which are created oversized and machined back down to size, a high accuracy process that requires large amounts of material removal..

In general machining terms, Walker *et al.* [17] outlines the cutting process as a controlled interaction among the workpiece, tool and the machine. These are not the only influences in the cutting process as illustrated in Figure 1.3. This figure indicates that tool and workpiece clamping, cutting fluid, machine rigidity and power capabilities, and cutting conditions are also critical in determining the level of control associated with the process.

A number of damage types unique to composite machining have been identified including thermal, mechanical and chemical damage. These damage types are described in more detail in the literature review. Due to the nature of the application of many CFRP components in the aerospace industry in particular, the potential for component failure as a result of such damage is unacceptable.

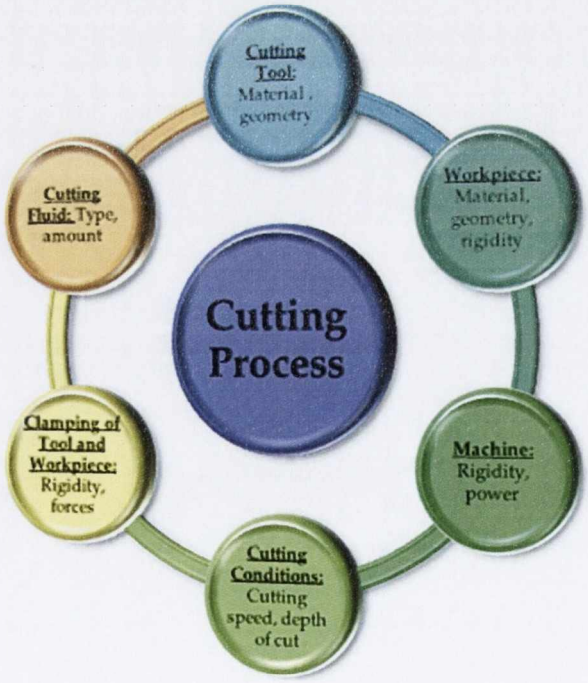

Figure 1.3: Interaction between the workpiece, tool and machine in cutting processes. (Adapted from Walker et al.[17])

1.2 Research goals and objectives

The goal of this research is to characterise a novel temperature-sensorised cutting tool system for use in CFRP edge trimming process monitoring. The novel sensor incorporates wireless telemetry to overcome transmission limitations associated and rotation, using the embedded-tool thermocouple sensor technique previously developed by Barlier [18-20]. This unique technology combination is coined the integrated telemetric thermocouple (ITT) sensor.

In order to achieve this goal, a number of research objectives were set out:

1. Characterise the steady state behaviour of the ITT sensor using highly calibrated calibration equipment.
2. Characterise the dynamic behaviour of the ITT sensor using:
    - A numerical parametric analysis tool using a finite element model specifically tailored to the cutting tool associated with this process.
    - A customised dynamic calibration of the ITT sensor using an experimental setup in which an analogous heat flux is generated to represent the thermal system associated with an actual cutting process.
3. Apply the characterised ITT sensor in monitoring the temperature during the machining of CFRP composites.

2 LITERATURE REVIEW

2.1 Composite material decomposition

Mallick [21] states that fiber-reinforced composite materials consist of fibers of high strength and modulus embedded in or bonded to a matrix with distinct interfaces between the materials. In this form both fibers and matrix retains their physical and chemical identities, yet produce a combination of properties that cannot be achieved with either of the constituents acting alone.

This research is focused within the engineered section of composites, with a specific focus on PMC and FRP engineered composites. Honing in to a much more specific level, this research centres on CFRP prepreg laminate composite structures such as those used in aerospace, wind turbine and automotive industries [22]. It should be noted that CFRP composites appear as a subset of both PMC and FRP due to the various methods by which composites are classified, i.e. by reinforcement or matrix material. This is detailed in greater detail in Appendix 1. Therefore, in order to fully understand the overall CFRP composite, a deeper look into both reinforcement and matrix subsections of the material must be undertaken.

2.1.1 Reinforcement materials

According to Åström, [23] the reinforcement is the constituent that primarily carries the structural loads to which a composite is subjected. As a result of this role, the reinforcement typically defines the core mechanical properties of the composite, such as stiffness, UTS and yield strength. Reinforcements may be in the form of fibres, particles or whiskers with fibres being the predominant choice in most applications [23]. All common fibres are manufactured using several processes including the use of a drawing process in which liquid raw material is drawn from an orifice. This drawing process ensures that the molecules of fibres are aligned and parallel to the direction of drawing. The result of such alignment is to significantly increase the strength and stiffness of the composite in the axial direction as opposed to the transverse direction. However, the fibre itself is not the only mechanical property-defining parameter. The orientation and form, as indicated in Figure 2.1, also contributes significantly to such properties.

The main types of fibre-reinforcements are carbon, glass and amorphous. This research will focus specifically on carbon fibre-reinforcement material.

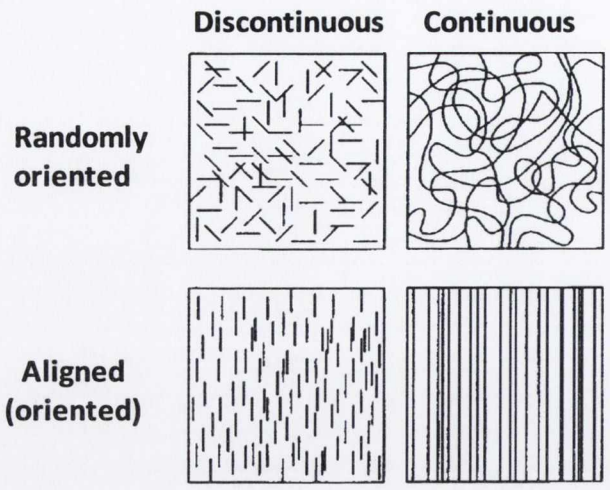

Figure 2.1: Illustration of the various possible reinforcement arrangements [23].

Carbon Fibres

In 1878, Thomas Alva Edison, in his efforts to find a suitable material for lamp filaments, used cotton fibres, and later bamboo, to produce carbon fibres [23]. Carbon fibre is defined as a fibre containing at least 92 wt% carbon, while the fibre containing at least 99 wt% carbon is usually called a graphite [24]. The most impressive feature of this material is that it has the highest strength and stiffness of any composite-reinforcement candidate. Other properties of carbon which make it attractive to a wide range of applications are low densities, high thermal and chemical stabilities in the absence of oxidizing agents, good thermal and electrical conductivities and high creep resistance [25].

Carbon fibres can be described quantitatively as ultra-high modulus (>500 GPa), high modulus (>300 GPa), intermediate modulus (>200 GPa), low modulus (100 GPa) and high strength (>4 GPa) [23, 26].

While unidirectional fibre systems in composites are still in use, it is common for carbon to be woven into a more practical fabric structure. Fibres running along the length of a roll of fabric are referred to as the warp fibres, while those across the width are called the weft. There are several fabric styles that are commonly employed in the composite industry, such as a plain weave, twill weaves and satin weaves as illustrated in Figure 2.2.

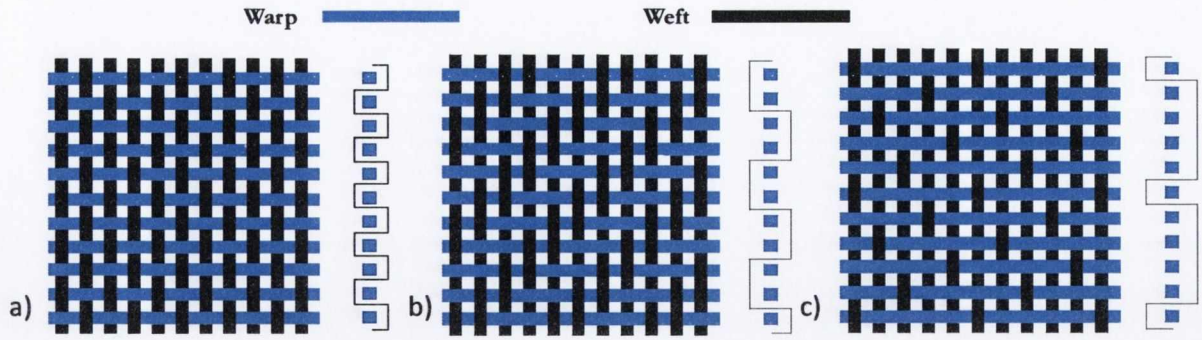

Figure 2.2: (a) Plain weave provides near unidirectional format - low drapability, (b) 2 X 2 Twill weave create a 'herringbone' pattern and are commonly used for complex profiles – medium to high drapability and (c) Satin weave styles tend to be unbalanced and this must therefore be designed into the component – high drapability. (Adapted from [27])

2.1.2 Matrix materials

The matrix material in a composite has several functions:

- **Binder:** Holds the reinforcement in place.
- **Load transfer:** Transfers external loads to the reinforcements.
- **Protection:** Provides reinforcement from adverse environmental effects.
- **Load redistribution:** Crucial when individual fibres fracture.
- **Lateral support:** Prevents buckling in compression.

There are a number of materials, such as metals, ceramics, polymers and carbon, which have become highly popular matrix materials depending on their intended application. The aim in this chapter is to focus more specifically on epoxy matrix materials and identify the basic polymer science associated with this matrix material.

Epoxy

A polymer is a high molecular-weight compound that is composed of a multitude of repeated small segments. Polymers are organic compounds primarily based on carbon and hydrogen atoms bound to each other by primary, or covalent, bonds [23].

The type of polymer focused upon in this research was the thermosetting resin, Epoxy. Common chemical practice dictates that molecules can be classified by the functional groups contained within [28]. In the case of epoxide molecules, these can be identified by the presence of the epoxide group shown in Figure 2.3.

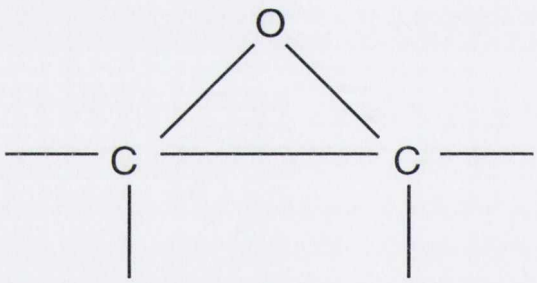

Figure 2.3: The basic epoxide group containing 3-member rings of 1 oxygen and 2 carbon atoms.

Within thermosets, epoxy resins are described as a group of cross-linking polymers and are sometimes known as the oxirane group, which is reactive towards a broad range of curing agents [29]. In such reactions, the low-weight resins are converted into 3D thermoset structures exhibiting valuable properties. In simple terms, the epoxy matrix is made up of a combination of low-molecular-weight organic liquid resins containing a number of epoxide groups, and a curing agent which initiates the polymerisation reaction, i.e. curing, to transform the liquid resin to the solid state [12].

The reaction can be sped up or slowed down with the application or removal of heat from the system respectively, resulting in a B-stage resin form. B-stage occurs before all of the molecules are cross-linked, i.e. formed at widely spaced intervals [25]. This process is used to develop prepreg composites in which an ungelled liquid of very high viscosity, but with the necessary tack, flexibility and shelf life to facilitate part production is prepared [30].

According to Mallick, [25] the volume and type of curing agent dictates the curing time and temperature to complete polymerisation. Some agents operate at room temperature while others require elevated temperatures to extend the B-stage life of the epoxy.

2.2 Carbon fibre reinforced polymer (CFRP) composites

There are numerous methods employed in industry to obtain various CFRP composite shapes and mechanical properties given specific time/throughput constraints. These include hand layup or bag-moulding, compression moulding, pultrusion, filament winding, liquid moulding techniques such as resin transfer moulding (RTM) and structural reaction injection moulding [25, 31]. The method used is also highly dependent on the form of the reinforcement, i.e. continuous fibres, particulates or whiskers.

2.2.1 Fundamentals of FRP composites manufacture

Samples of woven CFRP laminate are made using stacks of continuous fibre laminae prepregs formed via vacuum bag-moulding. Important composite manufacturing fundamentals, as stated by Mallick [25], are:

- **Degree of Cure:** This is typically described as a percentage between 0% and 100% of a chemical or mechanical property which is achieved by the exposure time to a specified temperature and pressure during the curing process.
- **Viscosity:** Viscosity is the measure of a fluid's resistance to flow under shear stresses. During the early stages of the curing process, viscosity of the resin is seen to increase slowly with increasing time and temperature. However, after a threshold degree of cure is achieved, which occurs at the gel-time, the viscosity of the resin is seen to increase rapidly [25].
- **Resin Flow:** Resin flow is important in order to prevent voids occurring in the part and ensuring good fibre wet-out. In thermoset resins, such as some epoxies, curing may take place simultaneously with resin flow, and if the resin viscosity rises too rapidly due to curing, voids may form and the product will experience poor interlaminar adhesion.
- **Consolidation:** According to Chung [32], consolidation involves the use of pressure to bring the fibre layers closer to together and the use of heat to melt the resin in the prepreg, so that the resin flow will allow the layers to come even closer together. During this phase of the manufacturing process, just prior to curing, a portion of resin may be squeezed out. During this consolidation process, the thickness of the prepreg laminate stack reduces. It is this phase of the manufacturing process, in conjunction with shrinkage, which causes the component to require additional or secondary processing, i.e. machining, due to the inexact nature of the consolidation phase.
- **Gel-Time Test (Pot Life):** Knowing the length of time that an epoxy resin formulation will remain fluid is important for manufacturers of composite components as it allows for the relevant lay-up method to be selected. The gel-time

test is designed to determine the curing characteristics of a resin-catalyst combination. Once the gelation stage is reached in the curing cycle, liquid-like flow becomes unattainable as the viscosity rises rapidly [28].

- **Shrinkage:** This is the reduction in volume or linear dimensions caused by curing and thermal contraction of the component. Thermal shrinkage is found to occur during the cooling phase following curing while the component is within or outside of the mould, or both [25]. Interestingly, it is possible to control the degree of shrinkage to an extent via the use of a tixotropic additive [30].
- **Voids:** A type of defect produced during the curing stage of a composite laminate. Voids are a critical factor controlling the mechanical properties of the final composite component, as stress concentrations can occur around such voids resulting in premature failure of the laminate [28].

2.2.2 Composite manufacturing – fibre matrix systems

Peters [13] describes the possible steps of processing and fabrication which go into the end product composite structure seen by the customer in Figure 2.4. The method employed for the CFRP composites used in this research are outlined in Figure 2.4 via red arrows.

Prepregs

Prepreg sheets are defined as thin sheets of fibres impregnated with predetermined amounts of uniformly distributed polymer matrix [25]. According to Mallick, [25] epoxy is the most common matrix material used in prepreg sheets and typical sheet thickness is between 0.13 and 0.25 mm.

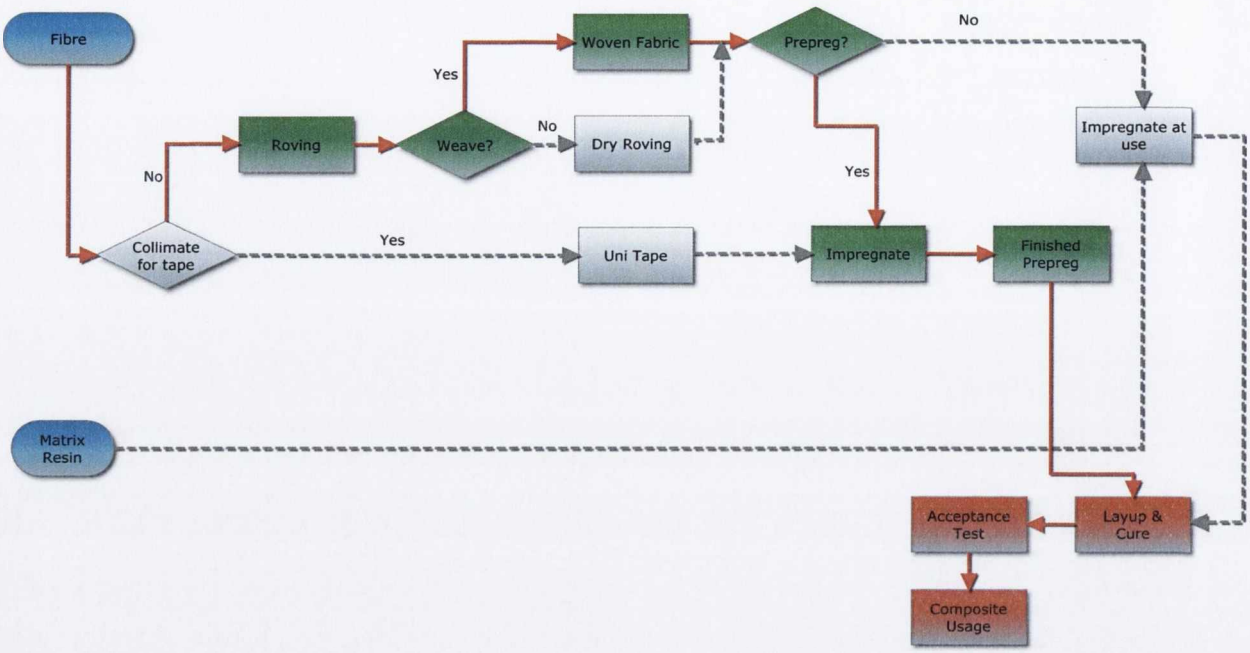

Figure 2.4: Various manufacturing steps associated with composite structures.

2.2.3 Vacuum bag moulding process and nomenclature

The bag moulding process is typically used in the aerospace industry due to the lowered importance placed on high production rates [25]. Such techniques are used to fabricate complex shapes, double contours and relatively large components. In this process, several consumable layers are utilised in order to ensure the removal of air and volatiles and consolidate the lay-up during cure. These are described below and illustrated in Figure 2.5.

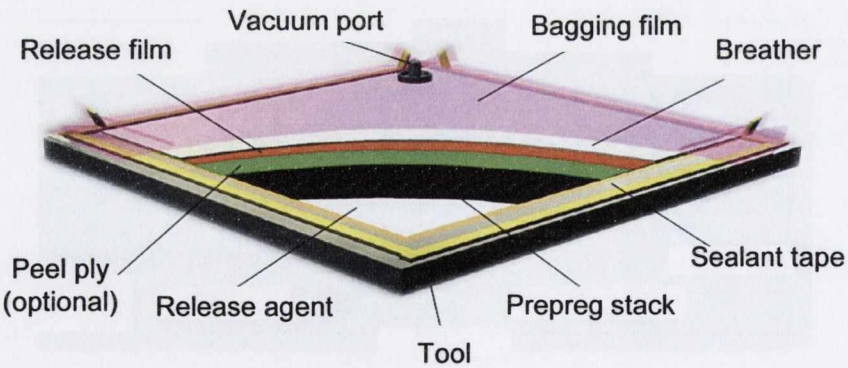

Figure 2.5: Schematic of a typical vacuum bag.

Release Agent: Allows release of the cured component from the tool.

Peel Ply: This is an optional light weight fabric applied and moulded onto the component surface. It protects the surface and can provide a surface for secondary bonding after removal.

Release Film: This allows the removal of vacuum consumables from the laminate. It can be a solid or perforated with various hole patterns to control resin bleed during cure. Solid release films do not allow any resins or gases to escape.

Breather: Allows the free passage of air under the vacuum bag over the laminate to ensure the level of vacuum is equalised over the whole surface.

Bagging Film: Normally nylon film, this forms the bag which is used to remove air and volatiles.

Sealant Tape: A mastic tape used to seal the vacuum bag to itself or to the surface of the mould tool.

2.3 Machining of CFRP composites

2.3.1 Overview of the milling process

The milling process is the focal machining process of this research. This is an interrupted cutting process in which cutting edges periodically enter and exit the workpiece [17]. As a result of this periodicity, cyclic thermal and mechanical loads occur on the tool and workpiece, which lead to fatigue failure mechanisms not encountered in continuous cutting [8]. However, when machining composites the magnitude of this cyclic effect is reduced to near-steady state. This is due to uncontrolled intermittent fracture during FRP cutting, resulting in tool designs which incorporate an increased number of teeth on the cutting tool to distribute the chip load [31]. There are a number of types of milling, as described in Figure 2.6 [33]. Of these types of milling, the sensor associated with this research will focus on peripheral milling, also known as edge trimming. Two different types of edge trimming employed during the machining of CFRP are down or climb milling and up milling. Each of these alternatives is associated with a different material removal mechanism, with the former generating a larger initial chip size and the latter generating largest chip size at the end of the cut [34].

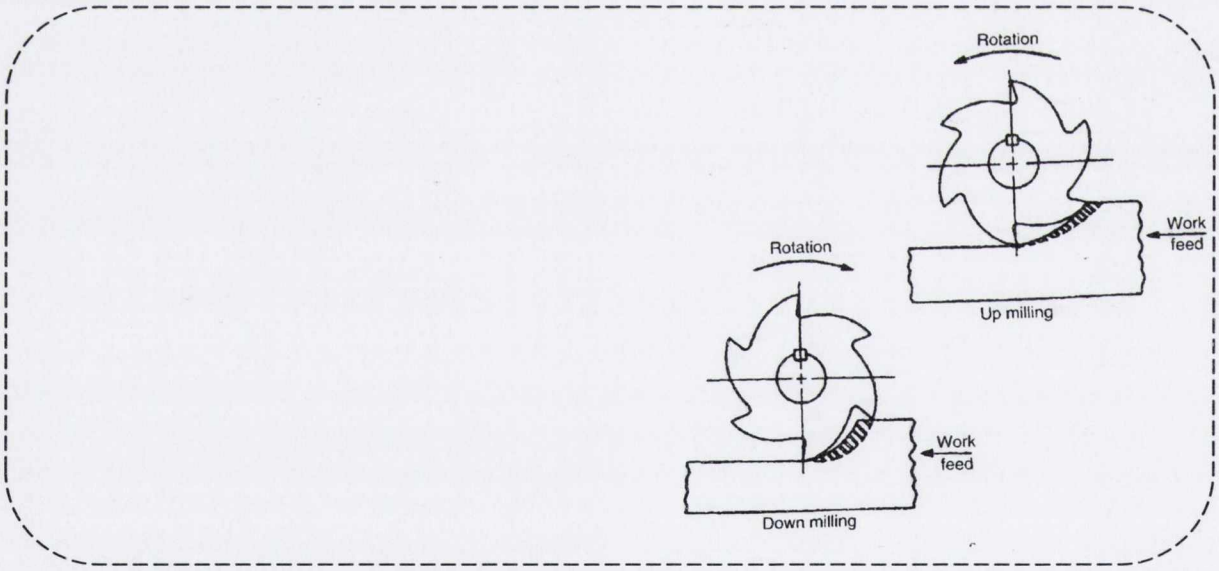

Figure 2.6: Types of milling [33].

The main machining parameter relationships are shown in Figure 2.7 and represented mathematically using Equations 2.1 - 2.9.

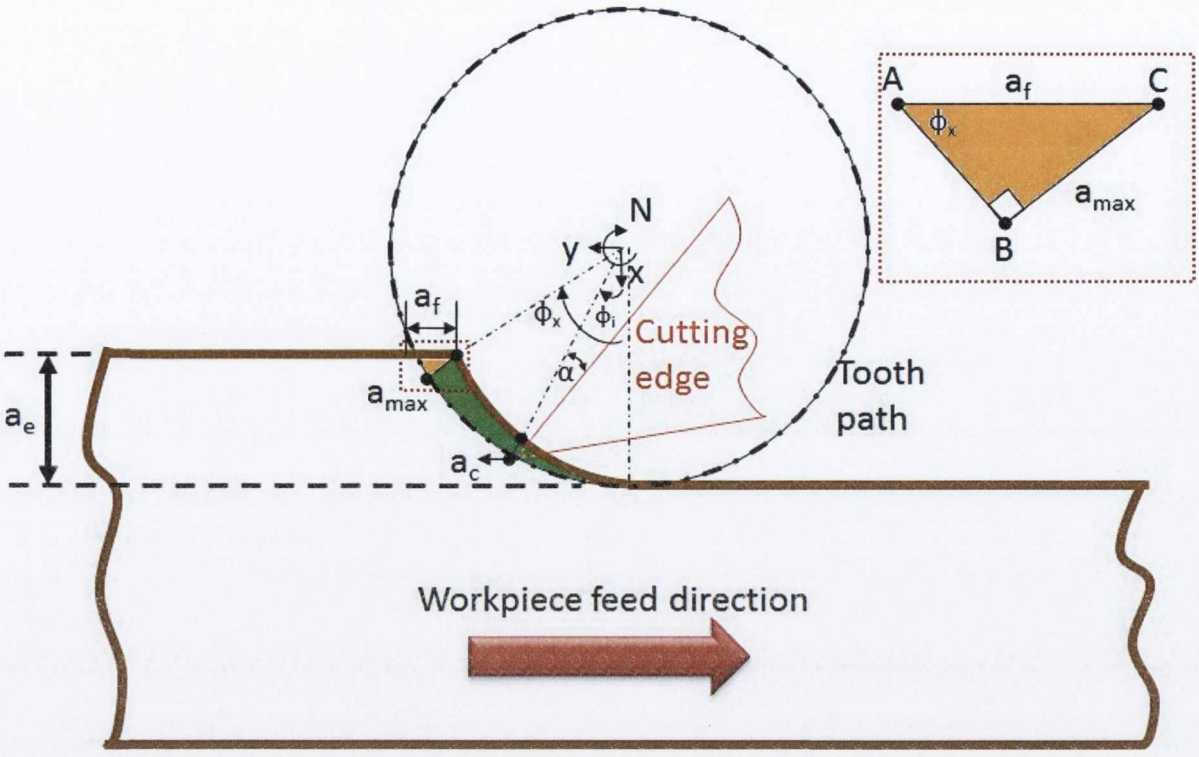

Figure 2.7: Basic cutting geometric factors associated with edge trimming.

Cutting Speed:

$$\mathbf{v_c = \pi \cdot N \cdot D} \qquad 2.1$$

Where v_c is the cutting speed (m/s)

N is the spindle speed (rpm)

D is the tool diameter (m)

Feed Rate:

$$\mathbf{v_f = fN} \qquad \mathbf{2.2}$$

Where v_f is the feed rate (mm/min)

f is the feed per revolution (mm/rev)

Feed per tooth defines the translation of the workpiece between the engagements of successive cutting edges and is expressed as:

$$\mathbf{f_z = \frac{v_f}{C_F \cdot N}} \qquad \mathbf{2.3}$$

Where $\mathbf{f_z}$ is the feed per tooth (mm/tooth)

N is the spindle speed (rev/min)

C_F is the number of flutes

The length of the cutting edge engagement in the workpiece for low feeds compared to spindle speeds as are used in FRP trimming is estimated by:

$$\mathbf{L_c = \frac{D}{2}\cos^{-1}\left(1 - 2\frac{a_e}{D}\right)} \quad \textbf{2.4}$$

Where $\mathbf{L_c}$ is the length of cut (m)

$\mathbf{a_e}$ is the radial depth of cut (m)

The minus sign in Equation 2.4 is used to account for down milling and the plus sign is used for up milling.

The average thickness of the undeformed chip is calculated using:

$$a_{ave} = \frac{f_z a_e}{L_c} \quad \textbf{2.5}$$

Where a_{ave} is the average undeformed chip thickness (m)

In order to determine the full angle of engagement between tool and WP, the following formula is used:

$$\mathbf{\cos \Phi_x = 1 - \frac{2a_e}{D}} \quad \textbf{2.6}$$

Where $\mathbf{\Phi_x}$ is the total engagement angle of the trimming process (°)

The opposing tool rotations for up and climb milling cause different lengths of cut, with up milling producing a longer cut with a smaller average undeformed chip thickness, while climb milling results in a larger average undeformed chip thickness due to a smaller length of cut per tooth. This explains the higher cutting forces, and ultimately cutting power required for down milling.

Due to the nature of this constantly changing theoretical chip thickness during the milling process, the instantaneous uncut chip thickness, $\boldsymbol{a_c}$, at an engagement angle, $\boldsymbol{\Phi_i}$, is determined using:

$$\mathbf{a_c = f_z sin\Phi_i} \quad \textbf{2.7}$$

The material removal rate in edge trimming is calculated by:

$$\mathbf{Z_W = a_e a_p v_f} \quad \textbf{2.8}$$

Where $\boldsymbol{a_p}$ is the workpiece thickness for trimming operations (m)

The effective chip thickness is determined by:

$$a_{eff} = a_e \frac{v_f}{v_c} \quad \textbf{2.9}$$

Figure 2.8 illustrates the forces associated with orthogonal continuous chip formation, from which it is possible to derive relationships between the various forces associated with the cutting process. This model assumes that a continuous chip is formed due to a shearing action along the shear plane, which relates the uncut chip thickness to the post-machining chip thickness through the cutting ratio, defined as:

$$r = \frac{a_c}{a_o} \quad \textbf{2.10}$$

Where r is the cutting ratio

a_c is the uncut chip thickness (mm)

a_o is the chip thickness after machining (mm)

The shear angle can be determined using the relationship with the cutting angle defined as:

$$tan\,(\phi) = \frac{r\,cos(\alpha_o)}{1 - r\,sin(\alpha_o)} \quad \textbf{2.11}$$

Where ϕ is the shear angle (°)

α_o is the rake angle (°)

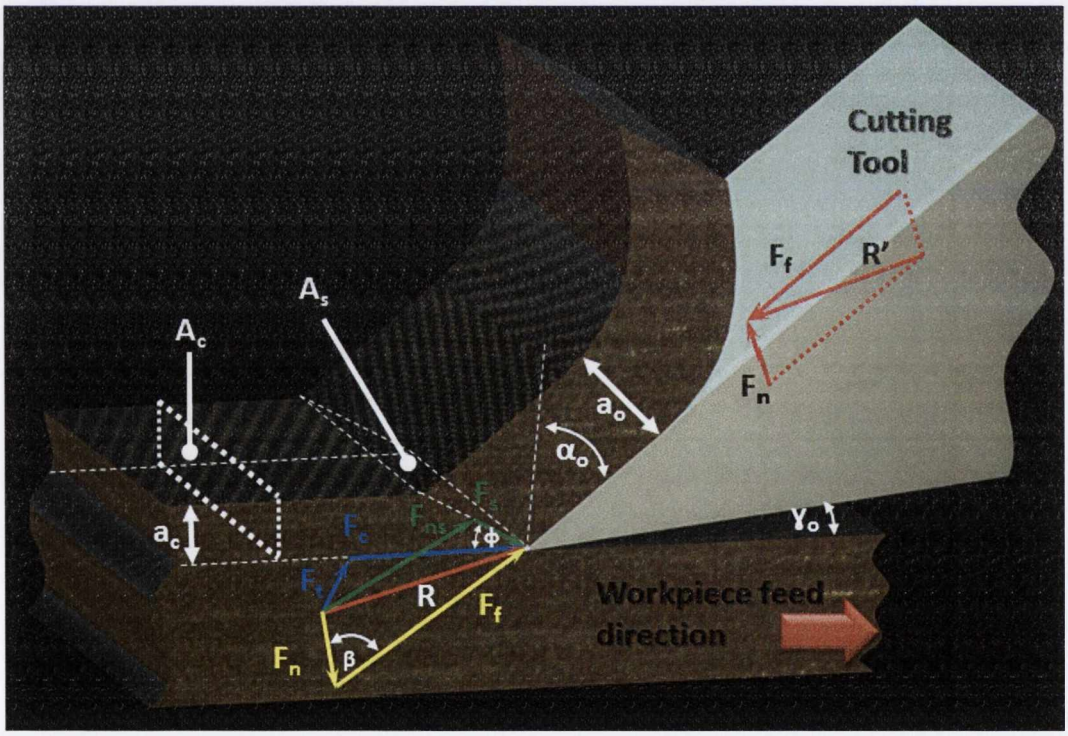

Figure 2.8: 3D representation of orthogonal cutting showing the various forces including, cutting force, F_c, thrust force, F_t, feed force, F_f, normal force, F_n, shear force, F_s, and normal shear force, F_{ns}, which can be determined using some trigonometric principles.

2.3.2 Chip formation during CFRP cutting

While similar tools, machinery and basic setup are employed in order to perform material removal processes on CFRP composite materials as is seen with metals and plastics, the structure of the workpiece (WP) material itself results in a vastly different chip formation mechanism to that established for metal cutting. Correspondingly, the heat generation theory in orthogonal composite machining is significantly different from that of metal and cast epoxy resins.

In a paper by Jahromi *et al.* [35], the idea of chip formation in composites is outlined, whereby in order for the chip to form, both matrix and fibre must be separated from the WP. Thus the matrix should shear and the fibre should break to achieve chip formation.

Wang *et al.* [36] dedicated an entire section of their 1995 journal paper to the chip formation mechanism associated with CFRP composite materials having long fibres. In this section, they indicate that the type of chip produced when using unidirectional laminates of fibres is largely dependent on the fibre orientation of the composite to the cutting tool. Their analysis of the chip formation process for unidirectional fibre arrangements of $0° < \theta < 135°$, utilised a high speed camera. The images obtained from the camera indicated that peel fracture, emanating from the tool point and propagating along the fibre/matrix, was predominant in 0° orientations. This resulted in small but distinct fragmented chips. The ultimate failure of the material to cause the chip was found to be due to advancement of the chip along the tool face until bending fracture occurred under cantilever loading.

Wang *et al.* found that as the orientation degree increased the quantity of distinct chips decreased and were replaced with small discontinuous dust chips. The images of 90° orientation material during edge trimming indicated not only smaller chips, but also the presence of cracks on the machined surface and out of plane displacement ahead of the tool. Wang *et al.* noted that the combined forward and downward compressive tool load resulted in a brooming effect in which the initial surface features generated by the tool point are replaced by an extruded surface due to contact between the clearance face and the workpiece. Difficulty was found in analysing the chip formation in orientations greater than 90° due to the decreasing chip size. However, out of plane displacement and macro fracture were also observed for orientations of 105° to 150°. This chip formation mechanism is described in [37]. Figure 2.9 to Figure 2.12 illustrate the effect of the tool acuity on the mechanism of failure of 0°, 90°, +45° and -45° oriented fibres respectively. In each of the below cases, there is a considerably different interaction between workpiece and tool.

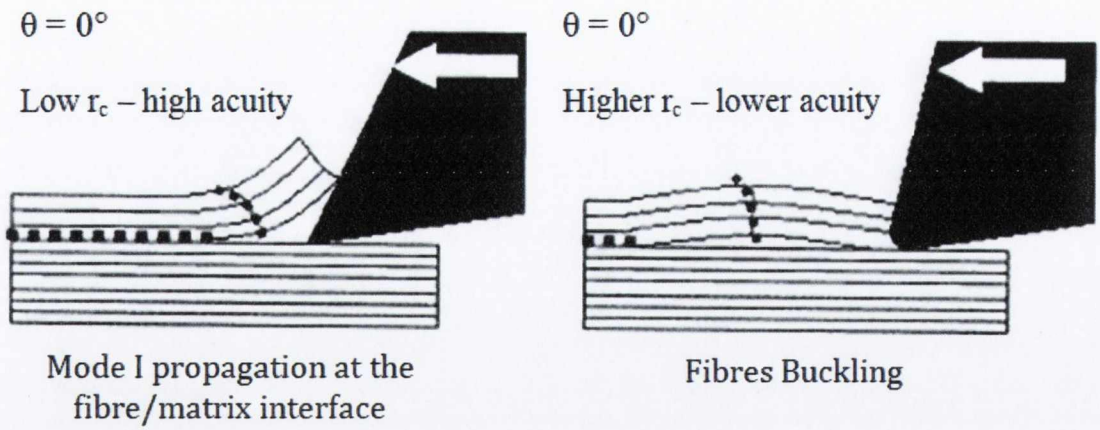

Figure 2.9: Mechanisms of chip formation during the machining of 0° UDFRP with high(left) and low (right) cutting edge acuity tools. (Adapted from [37])

In Figure 2.9, with fibre orientation parallel to the direction of cut at 0°, it should be noted that for high tool acuity there is a rupturing effect at the fibre matrix interface with crack propagation ahead of the tool tip. This causes the chip to separate via brittle fracture at an angle perpendicular to the initial fibre direction.

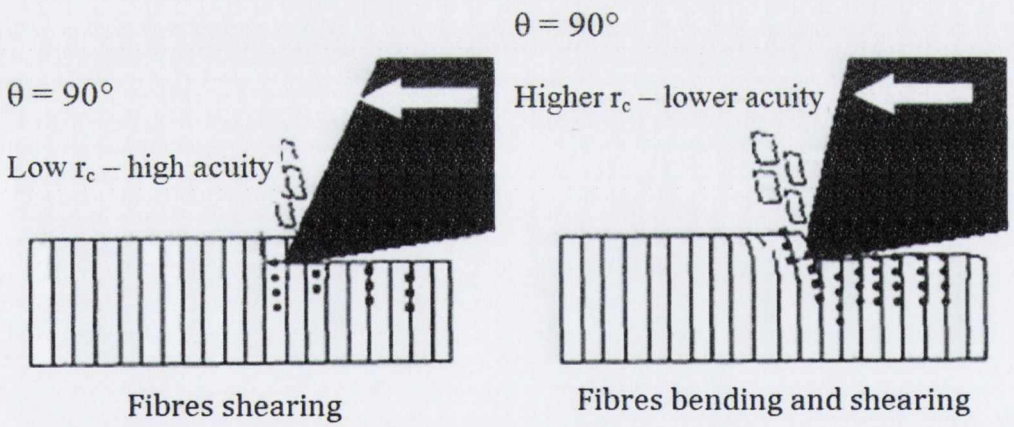

Figure 2.10: Mechanisms of chip formation during the machining of 90° UDFRP with high or low cutting edge acuity tools. (Adapted from [37])

In Figure 2.10, with fibres perpendicular to the direction of cut at 90°, the cutting mechanism appears to initiate with a mode I opening, penetrating the material at fibre-matrix interfaces. This is followed by a secondary rupture at the surface due to the fibres shearing. This orientation of fibres is therefore capable of resulting in long cracks along the depth of cut, particularly as tool acuity reduces [37]. As a result, damage such as delamination can occur due to cutting of this orientation of FRPs.

A tensile deformation of the fibres and a shearing by the cutting edge perpendicular to the fibres appear to make up the cutting mechanism for fibre orientations of 45°, as illustrated in

Figure 2.11. The chip forms by shearing along the fibre/matrix interface to the free surface. [37]. As the cutter moves along the feed direction, fibres tend to spring back to extend above the theoretical machined surface and rub along the clearance face of the tool. Subsurface delamination is also a concern for this orientation, again augmented by low tool acuity [37].

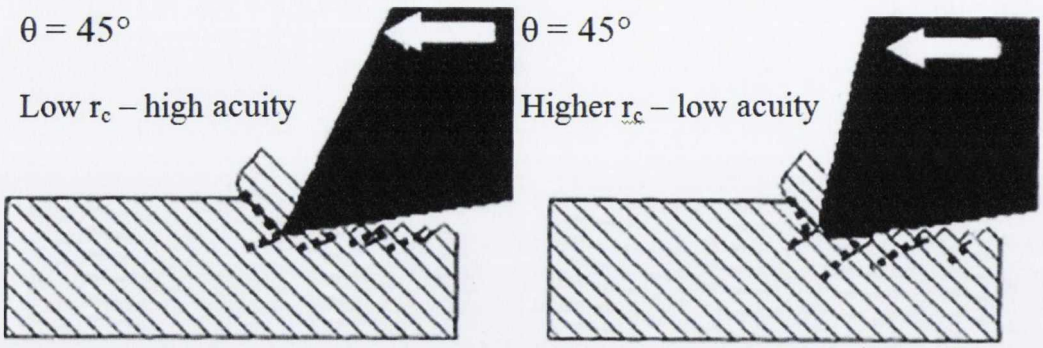

Figure 2.11: Mechanisms of chip formation during the machining of +45° UDFRP with high or low cutting edge acuity tools. (Adapted from [37])

Alternatively, fibre bundle orientations of -45°, shown in Figure 2.12, are pushed by the tool, bent and broken by bending [37]. Damage associated with this type of orientation and cutting mechanism is cracking in the thickness of the material at fibre-matrix interfaces. There is less spring back of the fibres in this orientation than for orientations previously mentioned.

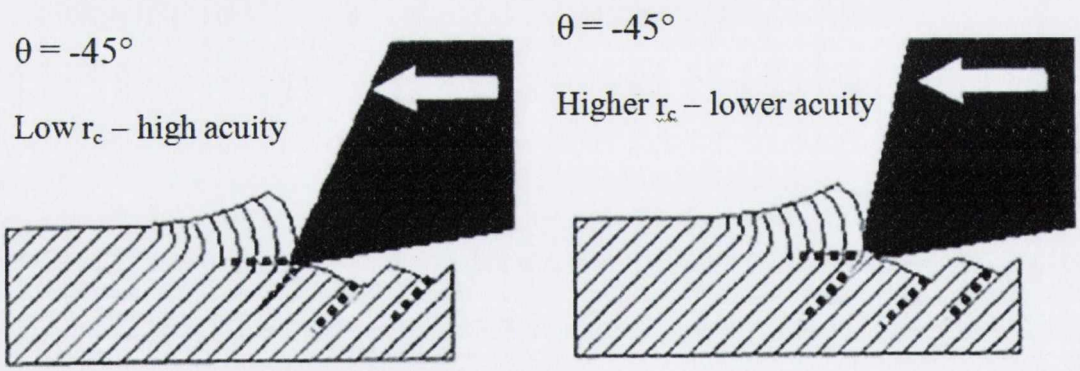

Figure 2.12: Mechanisms of chip formation during the machining of -45° UDFRP with high or low cutting edge acuity tools. (Adapted from [37])

In a later paper by Wang *et al.*[38], it was noted that chip formation in trimming of multi-directional Gr/Ep laminate produced comparable formations to those previously discussed for unidirectional material despite the multiple fibre angles present. However, it was found that plies adjacent to 90° and -45° plies provided support and resulted in less damage to the finished surface than was found in the unidirectional material case. Another finding was that

principal cutting force experienced high fluctuations in the multi-directional material which were accredited to the presence of the 90° laminate plies.

principal cutting force experienced high fluctuations in the multi-directional material which were accredited to the presence of the 90° laminate plies.

2.3.3 Machining parameters used with traditional CFRP cutting investigations

Much research has been done on the turning of CFRP composites and this is useful to consider when determining cutting speed. In chip-formation investigations by Soo Kim *et al.* [39] the turning of carbon fibre-epoxy composites, cutting speeds of 35 m/min to 134 m/min were used to determine aspects such as tool wear in relation to fibre winding orientation. In a more recent paper by Ferreira *et al.* [40], an optimisation methodology was used in rough turning to determine the best cutting conditions for a cemented carbide tool. Ferreira *et al.* found an optimised cutting speed of v_c = 225 m/min.

During the same time period, research was undertaken in Singapore by Sreejith *et al.* [41] relating to the use of polycrystalline diamond (PCD) tools during face-turning of carbon-phenolic ablative composites. In this research, the range of cutting speeds used was 100 m/min to 400 m/min for a range of feed rates of 0.025 mm/rev to 0.1 mm/rev. Later research by Mata *et al.* [42] investigated the effect on thermoplastic rather than thermoset polymers with regards to cutting speed and feed rate during the turning process. Mata *et al.* used cutting speeds of 50 m/min to 200 m/min against feed rates over the range 0.05 mm/rev to 0.2 mm/rev.

In the realm of milling, various types such as end milling, edge trimming and face milling have been investigated for cutting speed influence. Research by Hocheng *et al.* [43] into chip formation mechanics and workpiece damage indicated that cutting conditions should be properly selected to avoid the surface irregularity induced by heat accumulation. Hocheng *et al.* used cutting speeds up to 188.4 m/min for a feed rate of 0.0167 mm per tooth. In the University of Aveiro, Portugal, Davim and Reis [44] presented a study that evaluated the cutting parameters, i.e. cutting velocity and feed rate, in reference to the surface roughness and damage in milling laminate plates of carbon fibre-reinforced plastics, as shown in Figure 2.13.

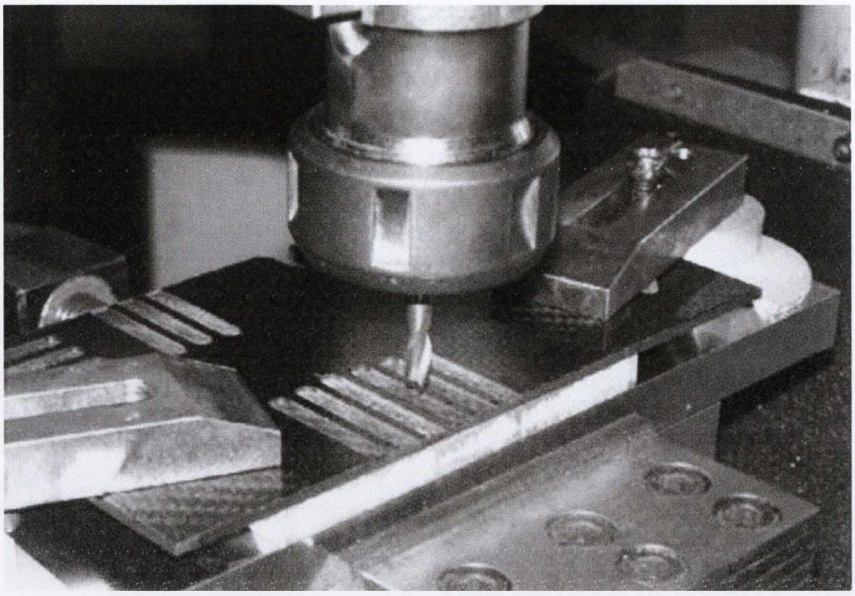

Figure 2.13: Testing setup of the Davim and Reis end milling experiment [44].

Using a multiple regression analysis, Davim and Reis used three levels of cutting speeds, 28 m/min, 38 m/min and 47 m/min, with corresponding feed rates of 200 mm/rev, 410 mm/rev and 860 mm/rev. Interestingly, in another study published at approximately the same time as [44], Davim *et al.* used the same experimental setup and tooling in order to determine the effect of cutting parameters during the milling of glass fibre reinforced plastics . In this instance, cutting speed levels were raised to 47 mm/min, 79 mm/min and 110 mm/min for corresponding feed rates of 0.04 mm/rev, 0.08 mm/rev and 0.12 mm/rev. The conclusions made by Davim *et al.* [44] were again that feed rate is the cutting parameter which has the greater influence on machining force in the workpiece and delamination factor, whilst the cutting parameters used produced an Ra value of 1-2.02 μm for the two materials tested. This is a relatively high precision surface finish.

In a thorough review of composite machining practices, Teti [45] determined that as regards process parameters selection in the milling of FRP composites, due to the multiplicity of possible composites, recommendations can only be given for specific machining applications. In most cases, however, a high cutting speed ranging from 800 to 1200 m/min with a low to moderate feed per tooth proved advantageous. This reference was in relation to glass fibre reinforced polymer (GFRP) composites using PCD tools, which as seen from the works previously mentioned, require significantly more cutting speed to achieve the same surface finish as tungsten carbide tools.

In a paper on high-speed drilling of CFRP composites, Gaitonde *et al.* [46] investigated the amount of delamination experienced due to a range of parameters, including cutting speeds. Using a cemented carbide grade K20 twist drill of 5mm diameter with 25° helix angle and an aerospace headstock at 40,000rpm by air turbine tools, cutting speeds of 60, 120 and 600 m/min were examined in conjunction with various feed rates and point angle. A key finding in

this investigation was that high-speed cutting plays a major role in reducing damage at the entrance of the hole [46]. It also states that the combination of low feed rate and point angle is essential in minimising delamination during drilling of CFRP composites.

The cutting speed has been shown by Kobayashi [47] to have two opposing effects on the machining of polymers. Firstly, as the cutting speed increases, the strain rate will increase, causing the material to fail at a lower strain in the form of brittle chips. Secondly, the heat generated in the cutting zone will increase the long-range mobility of the FRP's molecular chains and therefore increase ductility. The glass transition temperature and polymer molecular weight would therefore dictate which effect became dominant in the process.

2.3.4 Health and safety aspects in CFRP machining

In attempting to investigate the phenomenon of CFRP milling, it is important to take into consideration the potential hazard. According to Sheikh-Ahmad [31], hazard is the potential that a material, process or equipment will cause an adverse health effect under the conditions in which it is produced or used.

Sources of Hazards

In relation to polymer-based composites, the sources of such hazard are found during handling of the material, at prepreg stages, as well as due to dust and gaseous emissions generated during machining. However, once fully cross-linked, thermoset polymer composites can be considered inert and skin exposure does not pose a threat. In fact, according to Ramakrishna *et al.* [48], due to the high inertness and potential mechanical properties of carbon fibres, these fibres are currently the most widely used reinforcement material in the development of biocomposites. However, dust from conventionally cut epoxy resin was found by Malkusch *et al.* [49] to result in significant lung cell damage during in-vitro investigations on target cells from the washed lung fluid of guinea pigs. Sheikh-Ahmad [31] produced a general list of hazards generated from the machining of composites, shown in Table 2.1. It is also stated by Sheik-Ahmad that pitch-based fibre dust particles may be connected with an increased threat of cancer, while the PAN based equivalent does not produce any risk.

Table 2.1: Hazards and routes of exposure in machining FRPs [31].

Hazard	*Operation*	*Exposure Route*			
		Inhalation	Skin contact	Eye contact	Injection
Exposed protruding fibres	Handling	-	-	-	X
Dust	Traditional machining	X	X	X	-
Fumes	Laser machining, EDM, traditional machining	X	X	X	-

It is also widely accepted that while dust is damaging to the human respiratory system, it is also a serious irritant to skin and eyes. The American Conference of Governmental Industrial Hygienists (ACGIH) has issued a recommended exposure limit of 3mg/m^3 for *Particles Not Otherwise Specified* (PNOS) – a category that includes composite dust [50].

Another source of hazard, similar although on a smaller scale to dust, is aerosols. These can occur during excessive heating, in which the polymer matrix begins to decompose. This results in the production of airborne, potentially toxic substances. The recommended

exposure limits (RELs) from the National Institute for Occupational Safety and Health (NIOSH) for such aerosols are shown in Table 2.2 [51].

Table 2.2: NIOSH recommended exposure limits for hazardous agents [51].

Hazardous Agent	*NIOSH REL*	*Health Effect*
Benzene	Ca; 0.1 ppm (0.32mg/m3), 8-h TWA 1 ppm (3.2mg/m3) ceiling (15 min)	Cancer (leukaemia)
Fibrous glass	3 million fibers/m3 TWA (fibers ≤ 3.5μm in diameter and ≥ 10μm long); 5mg/m3 TWA (total fibrous glass)	Eye, skin and respiratory effects
Ethyl benzene	100 ppm (435mg/m3) TWA 125 ppm (545mg/m3) STEL	Eye, skin, and upper respiratory irritation
Indene	10 ppm (45mg/m3) TWA	Mucous membrane and lung irritation; in animals, liver and renal necrosis, spleen injury
Naphthalene	10 ppm (50mg/m3) TWA 15 ppm (75mg/m3) STEL	Hemolysis and eye irritation that causes cataracts
Phenol	5 ppm (19mg/m3) TWA (skin) 15.6 ppm (60mg/m3) ceiling (15-m) (skin)	Skin, eye, CNS, liver, and kidney effects
Styrene	50 ppm (215mg/m3) TWA 100 ppm (425mg/m3) STEL	Nervous system effects, eye and respiratory irritation, reproductive effects
Toluene	100 ppm (375mg/m3) TWA 150 ppm (560mg/m3) STEL	CNS depression
M, p-Xylene	100 ppm (435mg/m3) TWA 150 ppm (655mg/m3) STEL	CNS depression, respiratory and eye irritation

Research into dust particles produced during milling operations of thermosetting plastics has shown that mostly coarse, non-respirable particles are produced. Significant factors on dust particle size are cutting tool geometry, cutting parameters and number of tool cutting edges [52]. Literature suggests that aerosol emissions are primarily associated with laser machining due to the heat intensity generated during the process [53].

2.4 Damage caused during the machining of CFRP

A primary reason for many machining investigations is to develop an understanding of the process that will allow maximised productivity and throughput, whilst producing a safe and high quality product. Secondary machining processes in the manufacturing of a composite component are particularly well studied due to the high level of value already added to the near-net shaped product to be machined [15]. Damage, of any kind, would therefore be highly counter-productive and hinder the overall throughput, while using too cautious a set of machining parameters would hinder the productivity. It is this balance that has ultimately spurred interests in such investigations. As a result, it is necessary to understand the types of damage associated with CFRP machining.

Prior to machining, during the initial stages of composite product manufacture, defects can occur in the form of surface scratches, edge chips and mould marks. The formation of voids is also possible, caused by trapped volatiles which expand during the early stages of the curing process [54].

Taking a philosophical perspective, the act of machining in itself is deleterious and destructive, as the outer layer of material is removed, or destroyed, in a dramatic sense from the original structure and an alternative, *machined* outer surface takes its place. Therefore, as a destructive process, the level of damage inflicted onto either the workpiece or the tool itself is driven by the manner in which material is removed. The quality of this *revised* outer surface is dependent on numerous factors including tool geometry, tool material, cutting parameters, workpiece material and mechanical properties and material removal method which results in a specific chips being formed. This was explored initially by Konig *et al.* [15] in one of the earliest documented works on FRP machining and has since been studied extensively.

The primary indicator used for damage quantification in cutting processes is surface roughness measurement. Yet there are numerous types of damage that are not suitably characterised by such measurements, referred to as defects. The decisiveness of defects is typically only qualitatively surmised via inspection or geometric inferences.

In defining the damage caused to workpiece materials during machining processes it is important to note the difference between what is and is not acceptable to find as part of the final product. Surface roughness related variations such as the difference in Ra value between 0° and 90° fibre orientations, or between various lay-up configurations in multi-directional ply configurations are a necessary iniquity in terms of the final product, whereas fibre pullout, delamination, linting, cracking, burning and chemical damage are defects which should either be prevented or removed from the final product before being released for application.

Several factors, such as fibre orientation relative to the cutting tool, tool acuity, cutting speed, feed rate and depth of cut, have been noted in numerous investigations over the last three decades to cause various types of quantitative and qualitative damage to the CFRP workpiece when incorrectly selected. Since Konig's initial investigations, copious research spanning damage caused by orthogonal cutting and turning, [36, 38-40, 55-76] , drilling, [46, 58, 77-96] , milling, [43, 44, 97-100], and alternative methods of machining such as laser, abrasive water jet (AWJ) and ultrasonic-vibration (USV) machining, [97, 101-106], have been undertaken. These investigations have considered types including thermal, [39, 43, 46, 58, 62, 65, 70-74, 78, 79, 81, 82, 84, 86, 87, 90, 94, 95, 99-103, 105-107], mechanical, [36, 38-40, 43, 44, 46, 55-71, 78-93, 97-99, 101-104], and to a small extent chemical damage, [55, 77, 101, 102], caused during a machining process.

These damage-related research works are categorised by machining method, date and damage type in Table 1. This table indicates the relatively small number of investigations which have been performed on the CFRP milling process, and further, the lack of thermal damage investigations within the realm of milling.

Table 2.3: Literature review summary of CFRP machining damage works.

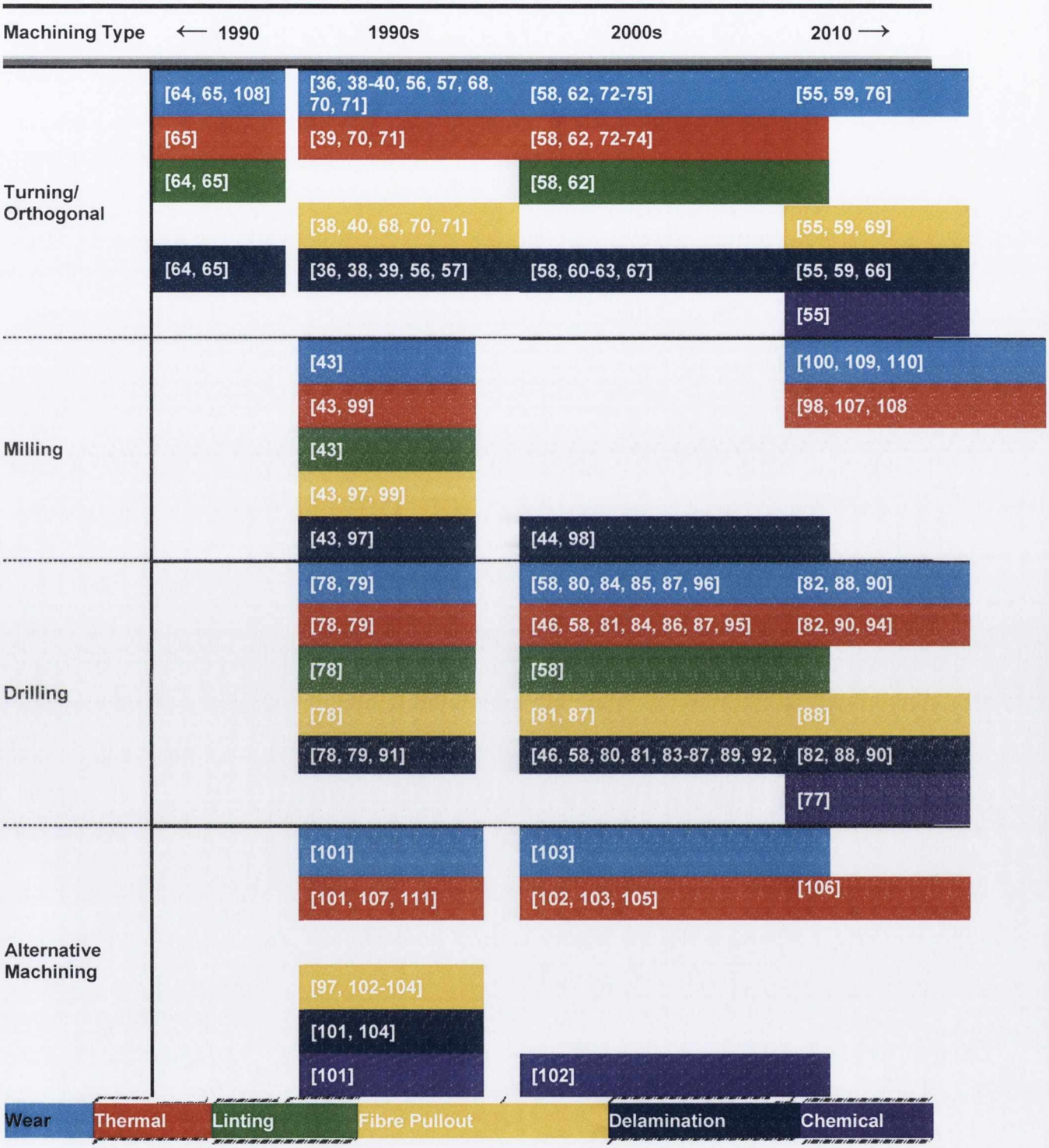

2.4.1 Thermal damage

According to Konig *et al.* [15], in spite of the high heat resistance of the fibres in CFRP composites, the temperature level is limited to the melting or decomposition temperature of the matrix. Burning is enforced by heat chocking due to poor thermal conductivity of matrix and fibre. Therefore FRPs may only be cut by thermal process of high power density and short interaction time. Carbon fibres are not suited for thermal cutting [15].

Rahme *et al.* [86] stated that during drilling investigations into FRP drilling damages a significant increase in temperature can cause degradation of the matrix resulting in significant thermal degradation in the thickness of the material. This is as a result of the heat generated during the cutting process. This type of damage is unique to FRP composites, due to the range-dependent thermal stability associated with thermosetting polymers for which significant factors are the glass transition temperature, T_g, prior to actual burning and molecular structure, type of curing agents and curing schedule for the duration of pyrolysis [112]. It was stated by Lee [112] that pyrolysis of epoxy composites occurred at 450°C as low-boiling volatiles including 13.4 mol-% ethane of MNA-cured epoxy resins were detected. It is noted however, that types and amounts of volatiles, such as ethane, found at various temperatures are highly dependent of the bisphenol type used to make the epoxy, curing agents employed and reaction conditions utilised. This point is illustrated through the results obtained by Chatterjee [113] in which it is stated that during a degradation analysis the epoxy system was stable up to 270°C after losing only 1% of its weight. At 353°C, 5% weight loss was observed, and at 523°C, 5% of the weight remained in the system. A detailed look at the curing conditions indicates that the former epoxy [112] was mixed with a catalyst at 90°C initially, then cured at 55°C for 16 hours, 125°C for 2 hours and 175°C for 2 hours, while the latter epoxy [113] was mixed and cured at room temperature for 12 hours and 121°C for 4 hours. This indicates the impact of curing schedule alone on the resultant thermal degradation of the material.

Typically, the potential extent of heat damage is evaluated using mechanical, destructive analysis [113]. Chatterjee analysed the thermal degradation in several different ways. Dynamic Mechanical Analysis (DMA) was used to measure the temperature dependence of the viscoelastic modulus (E') and Loss Modulus (E"), Thermogravimetric Analysis (TGA) was used to identify the thermal degradation patterns under an air environment and Dielectric Analysis (DEA) was used to evaluate the bulk dielectric properties and infer a linear relationship with thermo-mechanical properties from DMA and TGA.

During machining, although it is possible to maintain measured process temperatures below the pyrolytic threshold, there remains the possibility of thermal damage to the epoxy matrix of the composite for two reasons. Firstly, temperatures from the glass transition

range up to the point of pyrolysis leads to the formation of a rubbery structure, which ultimately affects the manner by which such thermoset-based composites undergo chip formation during machining [65]. Secondly, there is often a difficulty in measuring the ultimate maximum temperature (UMT) within a cutting process due to positioning of thermocouples, or infrared sensor emissivity errors. Therefore, the actual temperature to which a CFRP workpiece is exposed can be underestimated.

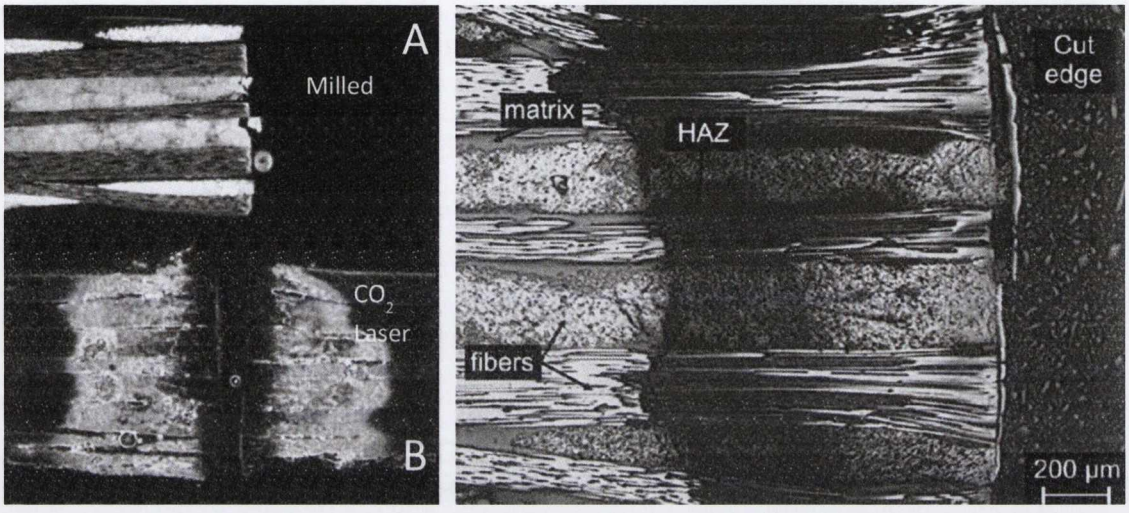

Figure 2.14: (A) Comparison of trimmed edge of CFRP composite using milling and laser ablation and (B) CO_2 Laser thermal damage to a CFRP workpiece during laser. (Adapted from [103])

During orthogonal machining investigations on GFRP, Santhanakrishnan *et al.* [65] noted that differential expansion and thermal conductivity between the fibres and matrix was problematic when laser machining such materials, resulting in damage. This was identified more recently via an image presented by Herzog *et al.* [103] as seen in Figure 2.14. This led to a general, yet temporary shift in the literature, away from laser machining techniques and focusing more intently on traditional machining methods of cutting. In later research by Santhanakrishnan *et al.* [71], it is stated that the thermal conductivity of CFRP composites is very much greater than that of the GFRP composites. This statement has implications for the tool wear associated with the cutting process. It also has implications for the role of the workpiece in the removal of heat from the cutting process. In works by Rahman *et al.* [70], the relationship between cutting speed and temperature in the drilling of CFRP is briefly mentioned and it is stated that the location of maximum cratering on the tool and maximum chip-tool interfacial temperature coincide with each other. Thus cratering of the tool during machining can lead to tool damage, which ultimately reduces the quality of the workpiece surface.

Palankumar *et al.* [62] indicate that with increasing cutting velocity, abrasion, diffusion and deformation due to thermal plasticity effects become pronounced. This statement was

made in relation to turning of GFRP composites at cutting speeds of 75 m/min and 175 m/min.

Beckwith noted that in the event of workpiece overheating during the drilling or cutting of composites, damage scenarios could include fibre-resin micro-cracking, delamination at edges, thermal degradation of the resin mechanical properties and unacceptable colour changes. Thus, there is a link between the effect of thermal changes to the process and the mechanical damage resulting in the workpiece. This is due to the variation in coefficient of thermal expansion between the fibre and matrix material.

Recent works by Pecat *et al.* [110] investigated the surface integrity and process forces associated with a slot milling process performed at a variety of temperatures on unidirectional CFRP. The authors found cracks below the surface up to 200 μm in length associated with temperatures below the glass transition (T_g) region of the epoxy matrix. When the machining process was elevated to above the T_g point, such cracks did not occur. The authors state that the disappearance of cracking is related to the less brittle nature of the matrix when above the T_g. The authors also discovered thermal damage in the sub-surface regions when milling at 120°C.

2.4.2 Mechanical damage

Fibre linting

According to Davim [37], this type of damage is characterised by poor fibre cutting by the tool and is illustrated in Figure 2.15. Mainly found during the cutting of aramid fibre-based composites, this type of damage consists of frayed fibres with a flaking of the surface during drilling and milling. The main cause of such defects is an incorrect definition of the tool geometry and non-optimal machining conditions. This type of damage was noted experimentally by Santhanakrishnan *et al.* [64] in their turning investigations of machinability characteristics of various FRP composites. Santhanakrishnan *et al.* state in their conclusions that Kevlar FRP machined surfaces exhibit poor surface finish due to the fussiness caused by delaminated, dislocated and strain ruptured tough kevlar fibres.

It is stated by Beckwith, [58] that an effective method of reducing or preventing this method of damage is by ensuring high acuity of the cutting edge of the tool.

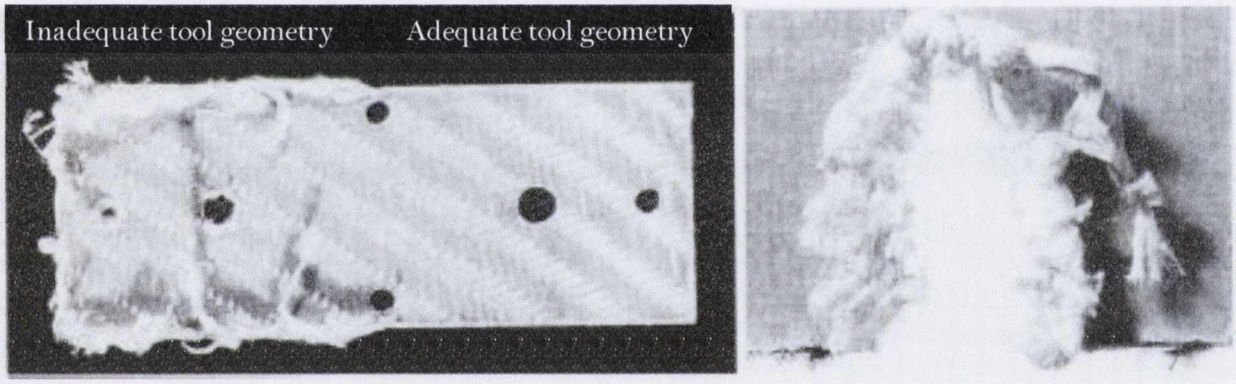

Figure 2.15: Examples of fibre linting of aramid fibres due to inadequate tool geometry. (Adapted from [37])

Fibre pullout & matrix decohesion

The former occurs when the unbroken fibres detach from the matrix. This type of damage is caused by flexion of fibres under cutting edge influence which leads to a relative displacement of fibres relative to the matrix. The angle range at which pullout is seen to occur is -15° to -75° for fibre orientation with respect to tool displacement [37].

Shyha [114] demonstrated the effects of variable drilling parameters on matrix decohesion and compared these to pre-existing voids in the workpiece material. Examples of the types of damage mechanisms focused on by Shyha are shown in Figure 2.16.

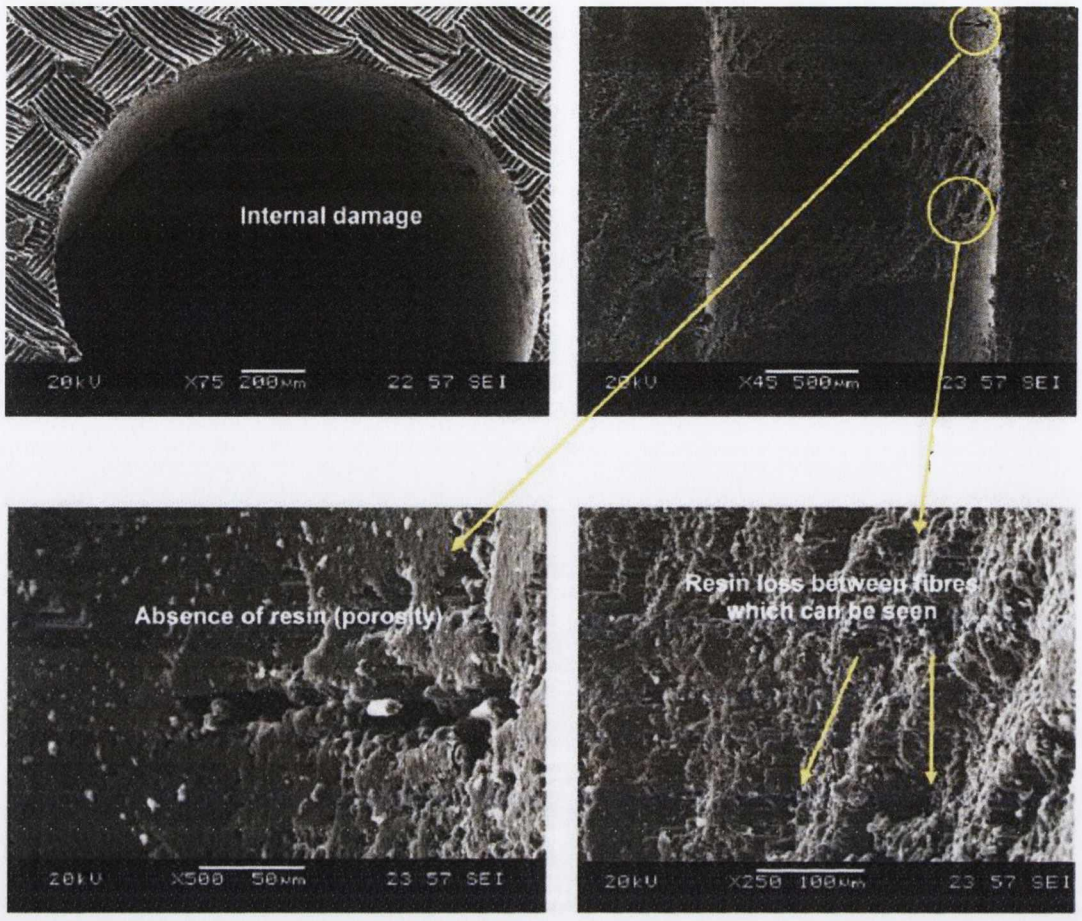

Figure 2.16: Internal hole damage determined by Shyha due to porosity and layer separation [114].

Delamination

Defined as the separation of plies in the thickness of the composite and the formation of interlaminar cracks in the material [37] delamination is mentioned as early as 1983 by Koplev *et al.* [108] as a major difficulty and primary reason for what many consider to be the earliest research into the CFRP cutting process and chip formation. As stated by Abrate *et al.* [78], delaminations cause severe reductions in the load carrying capabilities of the part and must be avoided.

This type of damage is typically seen in drilling at the initial entry and exit surfaces as shown in Figure 2.17, and in milling due to certain tool geometries which can cause separation of superficial plies of the central layers. As well as this between-ply separation, intralaminar cracks can also occur due to the effect of fibre orientation with respect to tool displacement during machining.

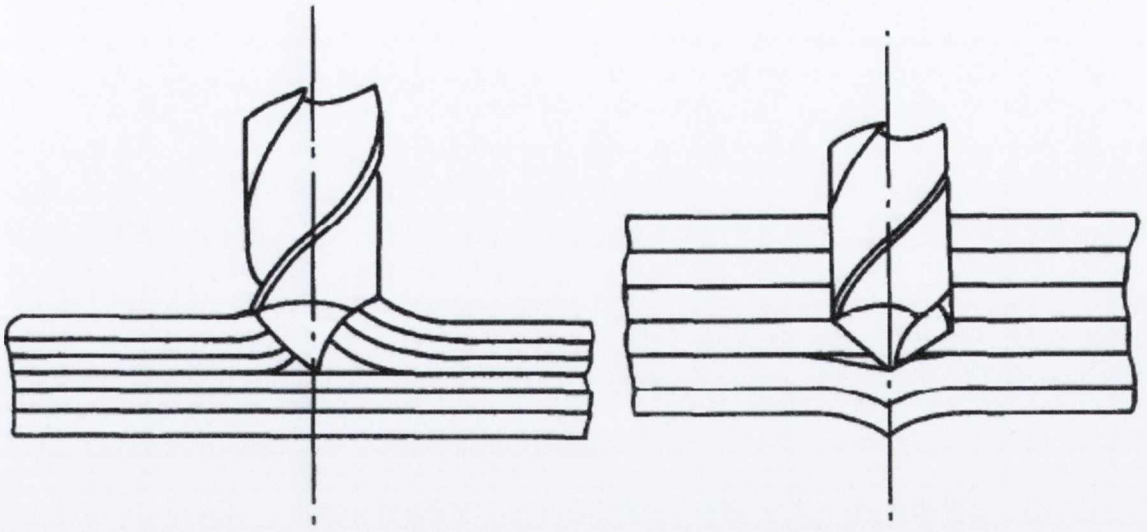

Figure 2.17: (Left) Entrance or peel delamination and (Right) exit or push-out delamination [78].

Shayha [114] found that similar results in delamination occur for both UD and woven laminates, even when using new tools during drilling of CFRP composites. However, a difference was noted by the author between entry and exit delamination as shown in Figure 2.18.

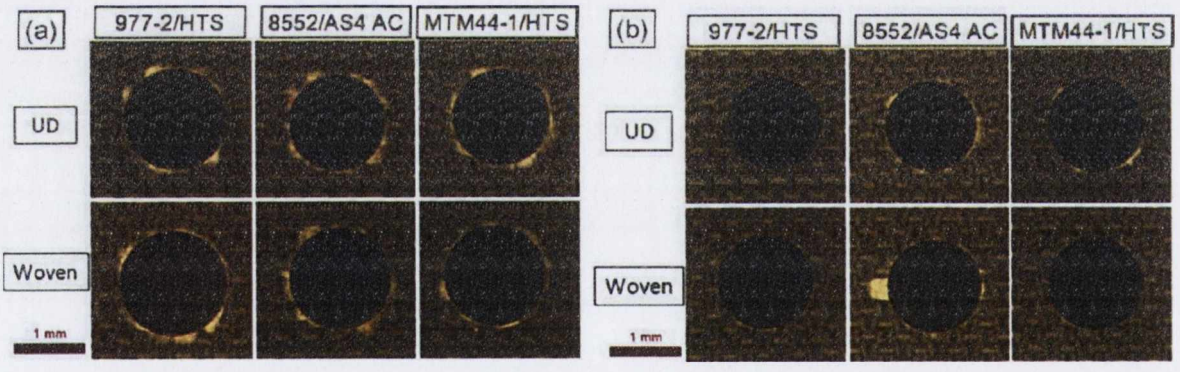

Figure 2.18: Delamination for: (a) hole entry and (b) hole exit at 0.2 mm/rev feed rate for first drilled hole. (Adapted from [114])

In milling investigations on CFRP composite damage, Davim *et al.* [98] used a delamination factor, illustrated in Figure 2.19, in order to determine the effect of machining parameters on the resulting damage caused by delamination to the workpiece. It was concluded by the authors that the feed rate was the highest statistical and physical influence on the delamination factor, and that the use of a two-flute end mill produced less damage than a six-flute end mill.

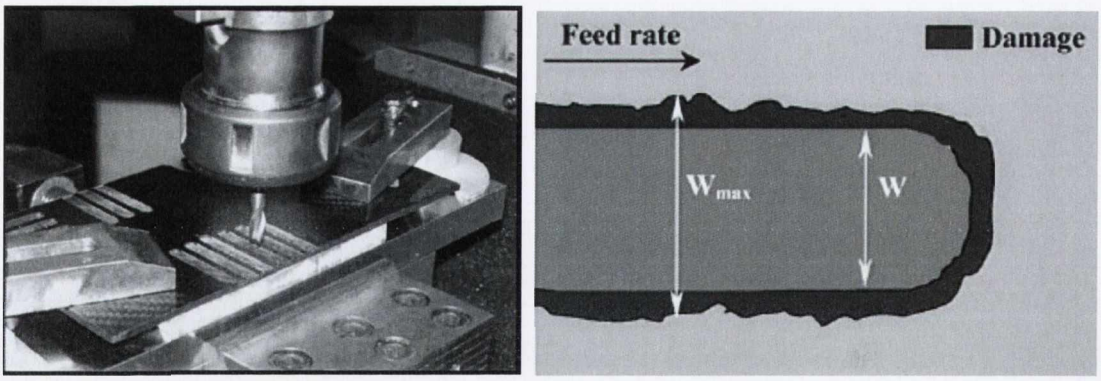

Figure 2.19: (left) Setup used for end milling and (right) delamination factor. (Adapted from [98])

Sheikh-Ahmad *et al.* [109], describe the various types of mechanical and visible damage associated with the edge trimming of CFRP. The authors determined that surface roughness increased with increasing effective chip thickness in the longitudinal direction but could not predict a trend in the traverse direction when using the R_z metric as recommended by Ramulu. [99] Other findings included the presence of Type I/II and I delamination in the surface plies and that average delamination depth increased with increasing effective chip thickness.

2.4.3 Chemical damage

As described in [37], chemical damage can occur when lubrication is used. This type of damage is proportional to the type, i.e. water or oil based, pH characteristics and contact time, when using water due to water recovery by the composite which can result in the destruction of molecular bonds between fibre and matrix.

The typical result of such damage is to cause decohesion at the matrix/fibre interface that can produce cracks or delamination. Solutions employed in order to prevent such damage are dry machining, gas cooling and micro-lubrication systems. In research by Konig *et al.* [15] it is stated that limited force implications result from the addition of lubrication.

2.5 Edge trimming of CFRP composites

Figure 2.20 illustrates the effect of trimming operations to a high value add component in moving from post-mould status to a ready-to-fit, finished component.

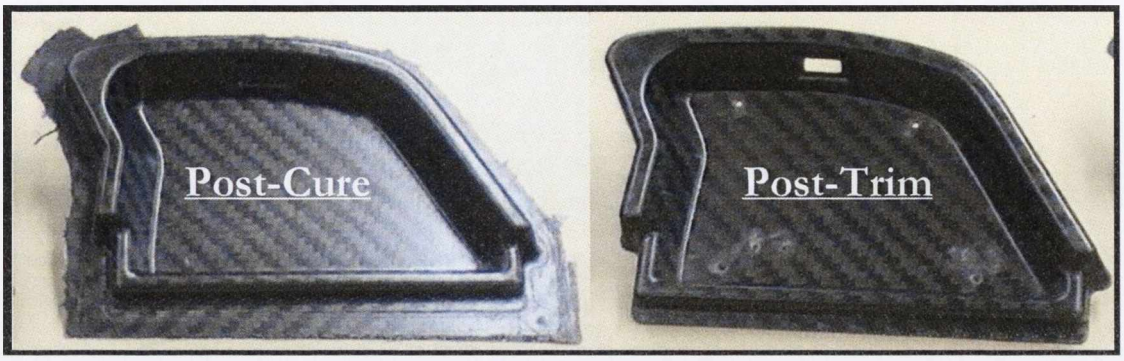

Figure 2.20: A CFRP cushion support typically found on-board commercial aircraft. (Left) Post-cured component and (Right) finished component post-trim.

2.5.1 Competing technologies and state-of-the-art

A number of different process technologies appear to produce reasonable results when trimming CFRP. The two main competitors are abrasive water jet (AWJ) machining and traditional milling incorporating CFRP-customised tools. While AWJ is found to produce reliable two dimensional parts [115], particularly for large laminate thickness, the use of cutting technologies such as milling and drilling are state-of-the-art in nearly every application for CFRP processing [116], but particularly in 3D milling. Such machining techniques provide the potential to allow the use of a single machine for part completion.

2.5.2 Tool design and selection for CFRP milling

According to Teti *et al.* [45] a key factor in selecting the material for CFRP machining tools is the hardness of the carbon fibres within the workpiece material, which results in rapid wear in the form of rounding of the cutting edge. Therefore the cutting edge should be resistant to both abrasion and chipping. Teti *et al* therefore recommended that fine grade K10 carbide or polycrystalline diamond (PCD) are appropriate tool materials. Only solid carbide offers the flexibility of different cutter geometries, accompanied by reasonable cost [117]. In addition to preservation requirements for the tool itself, with regards to the removal of imperfections and damage to the workpiece, Chatelain and Zaghbani also indicated the following key geometric characteristics of the tool [117]:

- Rake angle: Increased rake angle improves the overall quality of the machined edge.
- Clearance angle: Controls the bouncing of fibres on the clearance face.

- Tool nose radius: May be large for high strength operations needed during roughing parts.
- Helix angle: Generate lower in-plane cutting forces and higher axial forces, resulting in delamination and fuzzing during FRP machining. Introducing a second, opposing helix generates an opposing axial force causing compression from both sides of the laminate, thus preventing delamination.

Solid carbide router burr tools, such as that depicted in Figure 2.21, incorporate opposing helices ground into the green-state tool to generate pyramidal flutes. The orientation of the flutes to the workpiece delivers a shearing action, while the opposing helical flutes cause the fibres to be pulled in tension, ensuring no fibre pull-out [6]. While such deburring tools are prevalent in industry, few studies have been conducted on the use of such tools in CFRP machining [117]. Sheihk-Ahmad *et al.* [109] performed investigations on a range of tool designs, including that depicted in Figure 2.21, concluding that best machined surface was achieved for smallest effective chip thickness used, i.e. lowest feed rate and highest cutting speed. The range of cutting speeds and feed rates used in this investigation were 100 – 300 m/min and 2.54 – 10.16 m/min.

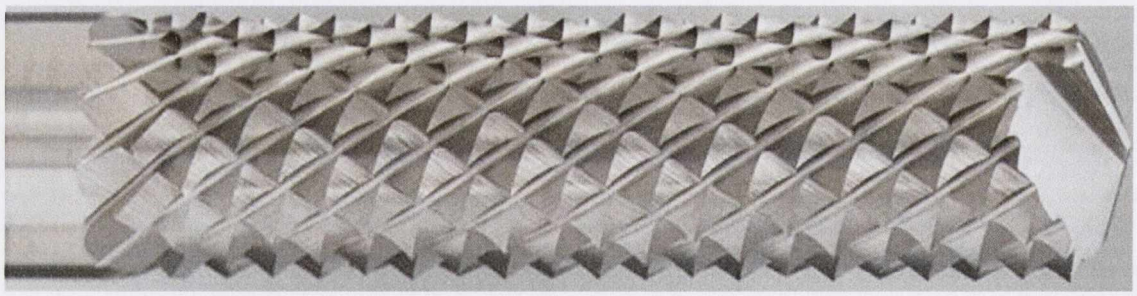

Figure 2.21: Deburring Router cutting tool.

An alternative tool design was studied by Leung Soo *et al.* [118] in which single layer electroplated diamond and cubic boron nitride (CBN) grinding points on an edge routing tool replaced traditional cutting edges. This tool design treated the trimming process more as a grinding process than a milling process, using a variety of grit sizes directly brazed onto the fluted/grooved cutter body and using significantly higher cutting speeds. The conclusions of this work indicated that the CBN version experienced greater levels of tool wear than the diamond abrasive, while the workpiece experienced no obvious delamination, minor edge cracking and limited voids in roughing investigations.

2.6 Heat transfer in CFRP machining processes

2.6.1 AEQUAT CAUSA EFFECTUM

Ever since the famous *Mechanical Equivalent of Heat* experiments performed by James Prescott Joule and Robert Mayer simultaneously in the mid-nineteenth century, the law of conservation of energy has indicated that there is a relationship between mechanical energy and thermal energy [119]. Indeed, in experimental investigations performed as early as 1798 by Count Rumford, aka Benjamin Thompson, it was noted that the mechanical action of a bore driving down a gun barrel could cause water to boil as a result of the heat produced by friction. Interestingly, before this time, it was thought by all scientists that heat was an invisible, weightless liquid called *caloric* [120].

In 1953, Bever *et al.* published works [121] exploring the energy stored in a gold-silver alloy chip formed by orthogonal cutting. This paper is one of the earliest journal references to state that a significant amount of the mechanical work in a cutting process is changed into heat. Since Bever's article this theory has been stated in a number of works [122-125].

It was the development of *The Moving Heat Source Theory,* by Rosenthal [126], which became a significant driving force in machining temperature investigations. This theory relates to the relative static effect of a constant heat flux moving at a uniform velocity and an observer moving at the same speed and is examined in detail in [127].

2.6.2 Heat generation in composite cutting

According to Grzesik, Four main sources of heat in traditional cutting have been identified, as outlined in Figure 2.22 [128]:

- Heat sources due to intensive plastic deformation (Q_1 on the shear plane 1-2-3-4)
- Frictional heat sources (Q_2) localised at the tool/chip interface (1-2-5-6)
- Heat (Q_3) at the contact between the workpiece and the flank (1-2-7-8)
- Heat from interface (Q_4) which transfers to sub-layers of the workpiece

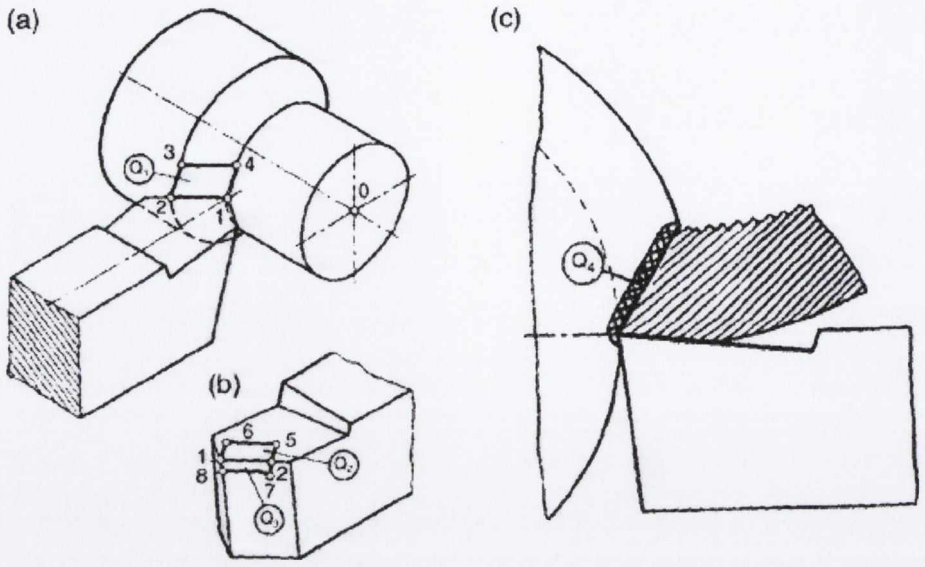

Figure 2.22: Machining sources of heat generation (Q) in metal cutting; (a) Q_1 due to intensive plastic deformation on the shear plane, 1-2-3-4, (b) Q_2 and Q_3 due to frictional heat at tool/chip interface, 1-2-5-6 and WP/tool flank, 1-2-7-8, respectively, (c) Q_4 due to interface heat transferred into WP. (Adapted from [128])

Usually, Q_3 only becomes important when the tool is worn and Q_4 is such a small heat source that it is often neglected in metal cutting.

CFRP composite orthogonal cutting have the additional complexity to metals of being affected by the thermal properties and orientation of the fibres [31].

Koplev et al. [108] in 1983, was the first to state that the primary material removal mechanism, during machining of CFRP composites, is via brittle fracture of the fibre. Therefore, very little heat is generated as a result of plastic deformation in the shear zone. Sasahara *et al.* [100] state that carbon fibre hardly deforms plastically and the amount of heat generation is smaller than the case of conventional metal cutting.

It was again Koplev who determined that the effect of the tool downward pressure on the composite below is the production of cracks approximately 0.1 – 0.3 mm deep into the specimen [108]. This is noted particularly during machining perpendicular to the CFRP fibres as occurs in edge trimming process. Koplev also found that smaller cutting depths usually produce fewer and shorter cracks. The implication of having the matrix material of the composite create a higher plane of surface than the carbon fibre reinforcement is that extrusion is potentially taking place only at the polymer matrix-tool flank face interface. This interaction would produce significant friction and heat along this interface, potentially resulting in matrix smearing in such areas and increased wear along the flank face.

While the mechanisms of heat generation would seem to be substantial, particularly when considered in high speed machining applications, it is important to note that edge

trimming is an intermittent machining process. In an intermittent process, short tool/WP contact times and chip lengths are expected due to the nature of the cutting tool, e.g. multiple flutes, rotational effects and rake angle [129]. A result of short contact times is the cooling of the tool as it is exposed to the ambient air between contacts with the WP. It was determined by Kitagawa *et al.* [129] that as a result of these process characteristics, the intermittent cutting process has an inherent time associated with heat generation mechanisms when compared to continuous processes. Armendia *et al.* [8] determined that in metal intermittent cutting processes the temperature amplitude variations are significantly larger than in continuous cutting. However, in cutting of FRP composites, particularly carbon with chip formation by fracture, the increased speeds and reduced feeds needed to obtain the requisite surface finish are hypothesised to reduce this amplitude variation.

2.6.3 Heat dissipation in composite cutting

The following methods of heat dissipation exist during traditional cutting processes, as illustrated in Figure 2.23 [124]:

- The discarded chip carrying the heat away from plastic shear plane, q_{1c}, and frictional at the tool rake/chip interface, q_{2c}. Temperature is found to decay along the length of the chip. In addition, natural convection and radiation at the outer surface cause a temperature gradient across the thickness of the chip that is greater than that along the chip length. [37]
- The WP acts as a heat sink for heat generated by both plastic shear, q_{1w}, and frictional heat at the tool flank/WP interface, q_{3w}.
- The cutting tool acts as a heat sink for heat generated by friction at both the tool rake/WP interface q_{2t}, and the tool flank/WP interface, q_{3t}.

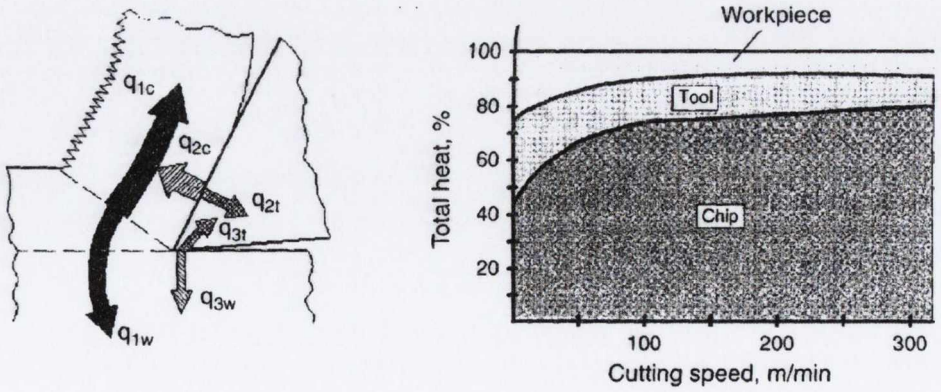

Figure 2.23: Heat flow scheme (left) and percentage of the heat generated going into the workpiece, tool and chip, as a function of cutting speed. (Adapted from [128])

Coolant, where used, will help to draw away heat from all areas. This is not relevant for composites due to the damaging effect of water-based fluids on interlaminar bonds in CFRP materials and abrasive wear in the tool, and the potentially carcinogenic nature and detrimental machine tool effect of carbon dust particles dissipated by air-based cooling methods.

It is widely recognized that the vast majority of mechanical energy is converted into heat by friction and plastic deformation. Grzesik [128] states that the amount of heat transmitted to the tool and the WP depends on the condition of the tool as well as the thermal properties of the workpiece material. A sharp tool will incur less friction on the flank face than a worn tool where the flank face rubs along the WP.

Of the numerous differences between CFRP composite materials and metals as workpiece materials, Palankumar and Davim [62] stress that the thermal conductivity variation between matrix and fibre and differential thermal expansion coefficient are both important factors in relating to the dissipation of heat during the machining of CFRP composites.

Typical thermal conductivity values for carbon fibres, epoxy, steel and carbon-epoxy composite are shown in Table 2.4. As can be seen from this table, the longitudinal conductivity of the carbon fibres is substantially higher than steel and even Tungsten Carbide. As a result, the possibility for heat to travel away from the cutting zone is increased via the presence of such highly conductive fibres, which potentially run in numerous directions away from the cutting interface. Simultaneously, the highly insulating properties of the epoxy polymer cause a thermal constriction in the matrix material surrounding the fibres.

Table 2.4: Comparisons of thermal conductivities of various materials

Material	*Thermal Conductivity (W/m K)*	
	Longitudinal	**Transverse**
Carbon Fibre (10μm) (PAN)	250 – 300	50 – 100
Epoxy	0.346	
Steel	15.57 - 46.71	
Tungsten Carbide	84	
PCD [111]	120 – 560	
Carbon-Epoxy Composite High modulus	48.44 - 60.55	0.865

In metal cutting, Fleischer *et al.* [130] performed an extensive review of heat partition ratios in the literature.

Table 2.5: Comparison of heat partition ratios in machining processes [130].

Component	*Drilling (%)*	*Turning (%)*	*Milling (%)*
Tool	5 - 15	2.1 – 18	5.3 – 10
Workpiece	10 – 35	1.1 – 20	1.3 – 25
Chip	55 – 75	74.6 – 96.3	65 – 74.6

The results of their investigation are presented in Table 2.5. This table shows the substantial variation in results, particularly in drilling and turning investigations. The majority of uncertainty in any of the material removal processes studied is found in detecting the thermal energy released into the WP, as shown in Figure 2.24. This research also indicates that it is not possible to determine the WP heat input from the cutting energy. This is in agreement with the later findings by Courbon *et al.* [131], in which the discrepancy was found to relate to the presence of a thermal contact resistance at the interface which is highly application specific.

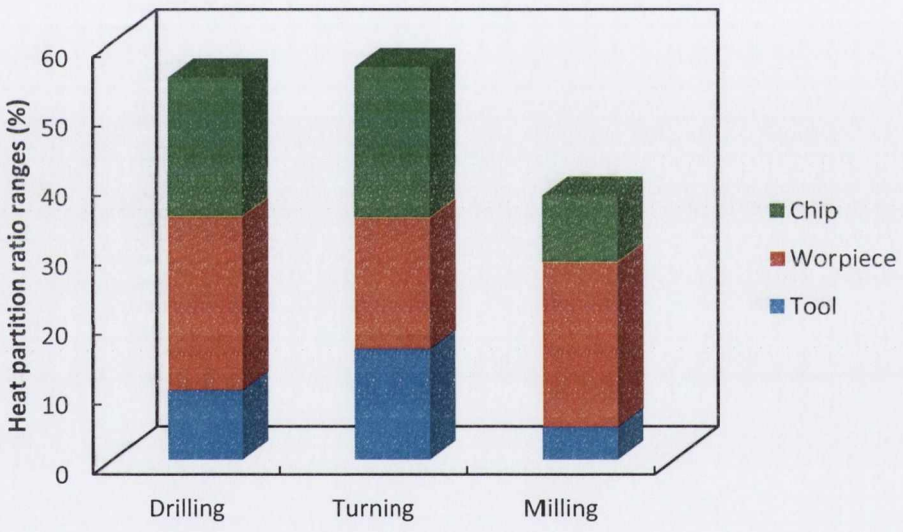

Figure 2.24: Range of variations associated with results from Table 2.5.

Abrate and Walton [78], stated in a review of FRP drilling that there is a substantially different dissipation ratio to that experienced in metal drilling. In CFRP cutting, the authors state that the ratio is approximately 50% to tool and the rest dissipated equally between the workpiece and chip. Since there is a similarity between the partition ratios of drilling and milling in metal cutting, it seems plausible that other CFRP machining ratios should be similar to CFRP drilling ratios. The comparison is enhanced when the radial depth of cut is maximised as in roughing edge trimming operations. Through such a large addition of heat energy potentially entering the workpiece during roughing operations, the importance of temperature awareness during CFRP machining therefore cannot be underestimated.

Recent works into modeling the milling process as a transient thermal system were performed by Pabst *et al.* [132]. The authors identified a general lack of information regarding the heat fluxes on the WP side of a grey cast iron face-milling operation. Experimental temperature data was obtained using thermocouples in the workpiece. The results showed the effects of the intermittent nature and axial depth of cut on the heat dissipation mechanisms associated with the milling of metal. As illustrated in Figure 2.25, heat generated at the bottom of the tool is able to conduct downwards and outwards into the WP. However, heat generated at the top of the tool requires more time to conduct into the surrounding workpiece. The radial zone of increased temperature close to the cutting interface is then removed, causing a large majority of the heat to be removed with the chip. Additionally, the authors found that greater energy densities were found in greater radial depths of cut.

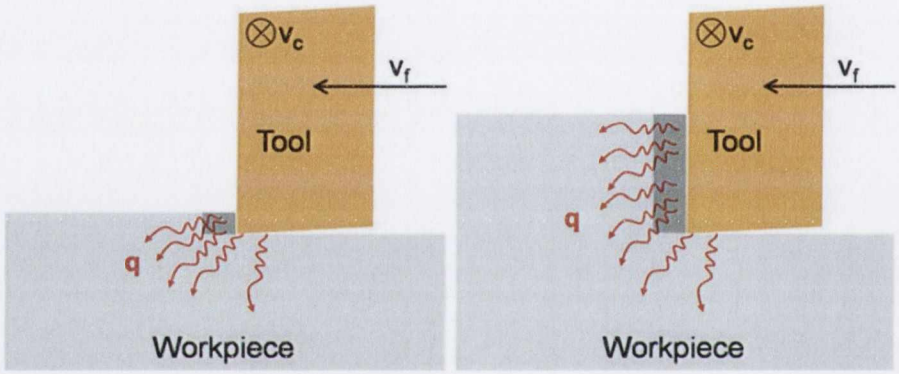

Figure 2.25: Heat dissipation routes for different depths of cut [Adapted from [132]].

2.7 Temperature measurement techniques used in machining

Temperature measurement has been a focus during material removal processes since approximately 1798, when Count Rumford completed and documented a set of calorimetric experiments during a stint as a superintendent in a horse-driven, boring factory for brass cannons in Munich [5]. Since then, a significant amount of research has been done on temperature analysis within metal cutting machining processes. Temperature is known to critically influence machining aspects. These include accelerating tool wear thus shortening tool life, causing thermal deformation of the workpiece, cutting tool and machine tool thus lowering the overall accuracy, affecting the subsurface of machined parts through phase transformation, thermally induced residual stresses and increased thermally activated defects [123].

The existing methods for measuring temperature during machining are shown in Figure 2.26.

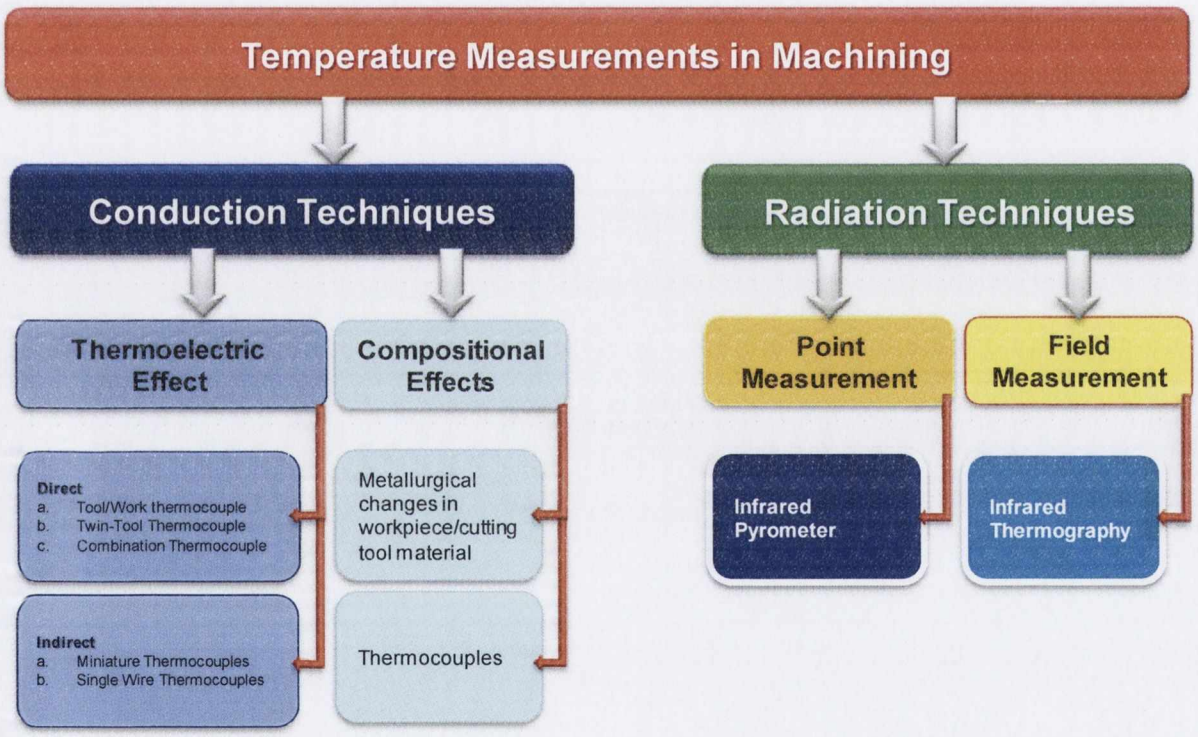

Figure 2.26: Existing measurement methods in temperature monitoring of machining processes. (Adapted from [128])

However, as mention by Davies *et al.* [5], the main barrier to the understanding of thermal behaviour in material removal is the inability to measure temperatures accurately, consistently, and with high resolution and high band-width. Also mentioned by Davies *et al.* are the types of measurement methods that have historically been utilised for temperature measurement during the machining process, which are shown in Figure 2.27. According to Davies *et al.*, as we move

further into the 21st century the most popular methods include Thermophysical (1943), Dynamic TC (1924), Thermocouple (1920), Micro-Resistance Thermometer (2001), Spectral Radiance Thermometry (1986) and Ratio Thermometry with optical fibres (1995).

Interestingly, of the 234 references reviewed by Davies *et al.* only 11 citings refer exclusively to temperature measurement during the milling process, which is the focus of this research.

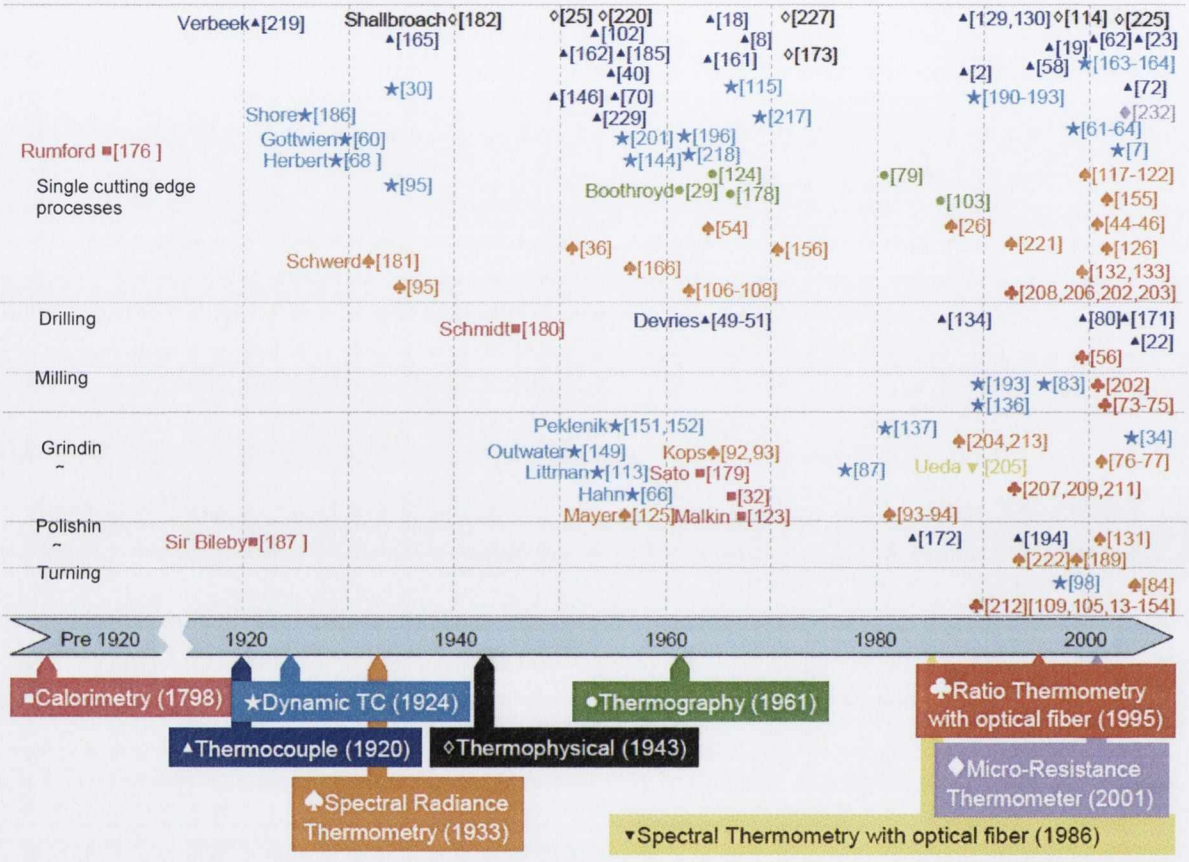

Figure 2.27: Historical outline of important work in the field of thermal measurement techniques in material processes as generated in Davies *et al.* review [5]. The diagram is categorised by material removal process, temperature measurement method and date.

According to Childs [133], the main factors which should affect the choice of temperature measurement method selected for any application are; temperature range, sensor robustness, temperature field disturbances by the sensor, signal type/sensitivity to noise, response time, and uncertainty.

These factors should be weighed against ease of calibration, availability, cost and size in order to determine the most realistic and accurate method for thermal analysis.

In machining, referring back to Figure 2.26 and Figure 2.27, the main types of temperature measurement applied currently can be divided into conduction and radiation techniques. An

alternative means of grouping measurement methods, as indicated in Figure 2.28 is contact and non-contact methods.

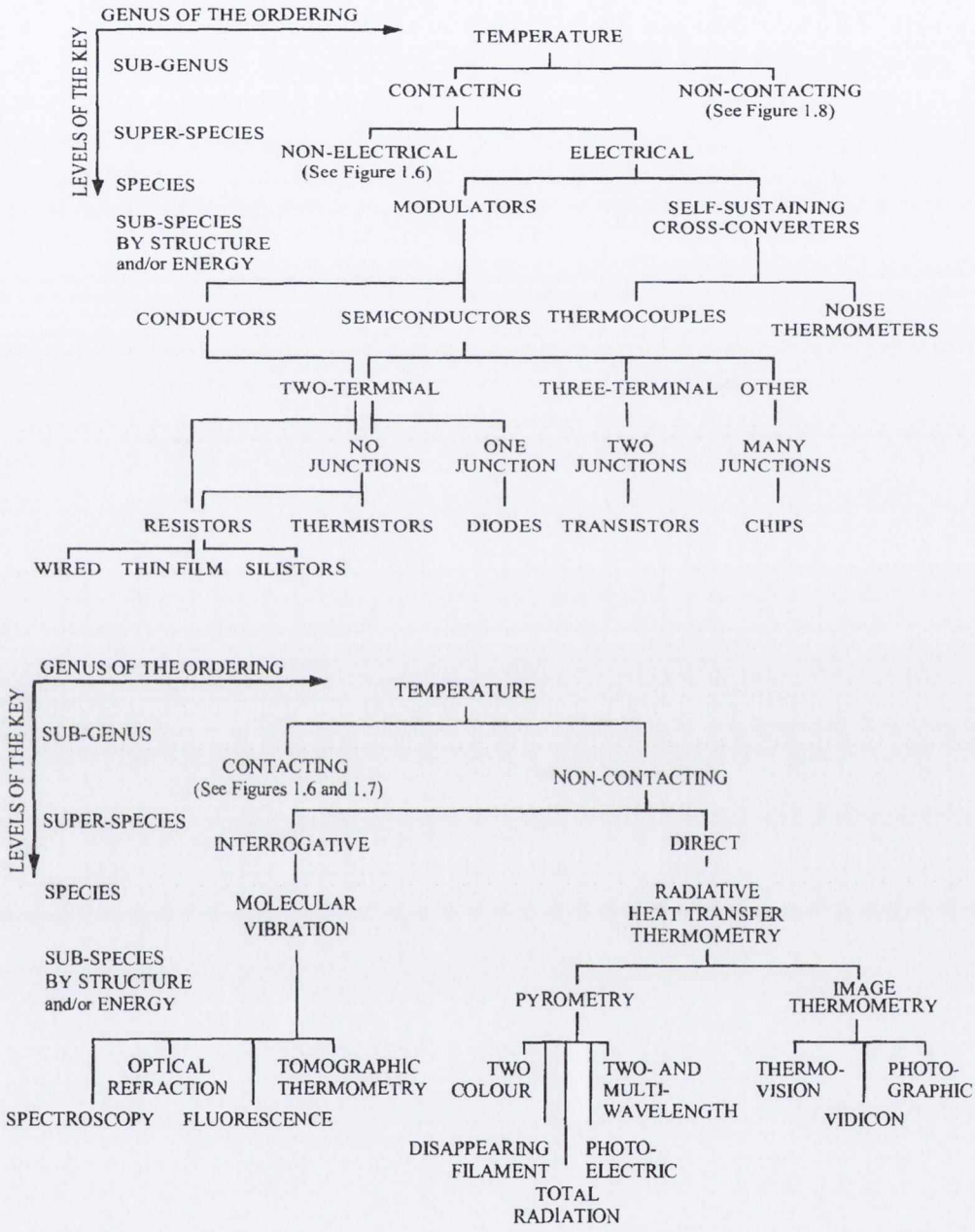

Figure 2.28: Classification of the (top) contacting and (bottom) non-contacting methods used in temperature measurement [134].

2.7.1 Conduction techniques

In order to understand a sensor based on conduction temperature measurement, it is necessary to understand the basic idea of conduction.

Conduction relates to the concepts of atomic and molecular activity, and can be considered as the transfer of energy from the more energetic to the less energetic particles of a substance when interaction takes place between the particles. [135] A means of quantifying heat transfer processes is in the form of a rate equation, i.e. the amount of energy transferred per time unit.

Equation 2.12 represents Joseph Fourier's statement: [135]

"The heat flux, q (W/m^2), resulting from thermal conduction is proportional to the magnitude of the temperature gradient and opposite to it in sign." [136] Using the constant of proportionality, k, then in one-dimensional form gives:

$$q = -k\frac{dT}{dx} \qquad 2.12$$

In Equation 2.12, k is the thermal conductivity, in W/m·K, of the material through which conduction is taking place. Equation 2.12 indicates that if temperature, T, decreases with distance, x, then the heat flux, q, will be positive, i.e. it will flow in the x-direction. As a result, q will always flow from areas of high temperature to areas of low temperature.

In machining, conduction takes place between the tool, workpiece and chip at multiple locations during the process. Thus, when setting out to measure the temperature of a process, it is necessary to specify which of these temperatures is intended to be measured. There are a number of thermoelectric conduction based methods; thermocouples, resistance thermometers and thermistors; which are used in the literature to measure the temperature during machining, which will be outlined below.

When two wires composed of dissimilar metals are connected at both ends and one end is heated there is a continuous current, which flows in the thermoelectric circuit. This is known as the Seebeck effect. Once this circuit is broken at the centre, the net open circuit voltage is a function of the junction temperature and the composition of the two metals. [137]

In a thermocouple, a pair of thermoelectrically dissimilar metals is joined together at one end and a voltage measuring instrument is connected to the other two ends. The response signal of the thermocouple is due to the temperature difference from one end of the pair of metals to the other, as shown in Figure 2.29. In order to accurately determine the temperature at the end of interest from the voltage, the temperature at the 'reference junction' end must be known.

Different material combinations are used in a thermocouple for varying temperature range applications, as described in Table 2.6. Thermocouple signals are DC voltages in the ranges from microvolts to tens of microvolts per degree Celsius.

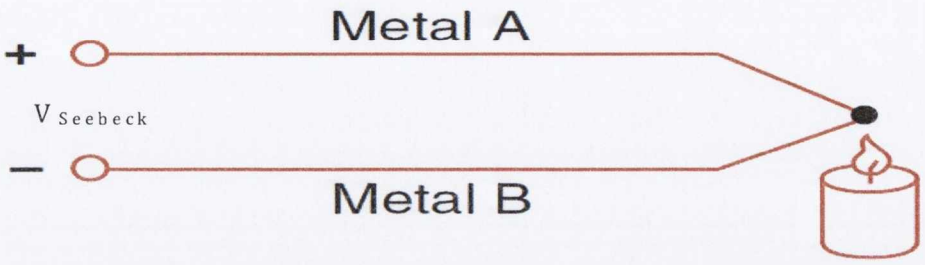

Figure 2.29: Seebeck Voltage effect with dissimilar metals [138]

Micro-thermocouples have recently been used for high sensitivity analyses in temperature measurement. [139] This unit consists of a sensing element assembly of two wires of dissimilar metal, a protecting tube and termination points to get the signal from the sensor. A non-ceramic insulation is used to protect and insulate the sensing assembly from the external atmosphere. In order to obtain the measurement junction of the thermocouple, wires are attached to a bank of condensers. The two wires approach each other at the same time and the beaded junction is made by the sparking method. The energy releases produced by the couple voltage-capacitance is sufficient to weld the wires together. An advantage of this technique of manufacturing is the junction diameter is of the order of the wire diameter and as a result the wire diameter can be used to calculate time constants.

Measurements within a volume are generally much easier to obtain than on surfaces and errors are usually smaller. However, their analysis is more difficult to carry out due to 1) the interaction between the connection wire and the medium and 2) a cavity must potentially be created within the medium that will change the conduction paths of heat travelling through it. As well as this, it is almost impossible to generate a perfect match between sensor and cavity walls resulting in thermal resistances due to residual space filled with air, glue, grease, etc. The error of such resistances is of the same order as errors associated with surface measurements. [139]

A summary of thermocouple types used in machining processes was presented by Garnier *et al.* [139] and is shown in Table 2.6.

Table 2.6: Examples of Thermocouple Types. [139]

Type	*Metal A (+)*	*Metal B (-)*	*Temperature Range (°C)*	*Seebeck Coefficient σ (μV/°C) at T°C*	*Standard error (%)*	*Minimal error (%)*	*Comments*
B	Platinum-30% Rhodium	Platinum-6% Platinum	(0 - 1820)	5.96 μV at 600°C	0.5	0.25	Idem R type (glass industry)
E	Nickel l0% Chromium	Copper-Nickel alloy (Constantan)	(-270 - 1000)	58.67 μV at 0°C	1.7 - 0.5	1 - 0.4	Interesting sensitivity
J	Iron	Copper-Nickel alloy (Constantan)	(-210 - 1200)	50.38 μV at 0°C	2.2 - 0.75	1.1 - 0.4	For reduced atmosphere (plastic industry)
K	Nickel-Chromium alloy (Chromel)	Nickel-luminium alloy (Alumel)	(-270 - 1372)	39.45 μV at 0°C	2.2 - 0.75	1.1 - 0.2	The most widely used because of its wide temperature range, supports an oxidising atmosphere
N	Nickel-Chromium-Silicium alloy (Nicrosil)	Nickel-Silicium alloy (Nisil)	(-270 - 1300)	25.93 μV at 0°C	2.2 - 0.75	1.1 - 0.4	New combination very stable
R	Platinum-13% Rhodium	Platinum	(-50 - 1768)	11.36 μV at 600°C	1.5 - 0.25	0.6 - 0.1	High temperature applications, resists oxidation
S	Platinum-10% Rhodium	Platinum	(-50 - 1768)	10.21 μV at 600°C	1.5 - 0.25	0.6 - 0.1	Idem R type
T	Copper	Copper-Nickel alloy (Constantan)	(-270 - 400)	38.75 μV at 0°C	1 - 0.75	0.5 - 0.4	Cryogenic applications
W	Tungsten	Tungsten-26% Rhenium	(20 - 2300)	58.67 μV at 0°C			Sensitive to oxidising atmospheres, linear response and good performance in high temperatures
W3	Tungsten-3% Rhenium	Tungsten-25% Rhenium	(20 - 2000)	58.67 μV at 0°C			Idem W type
W5	Tungsten-5% Rhenium	Tungsten-26% Rhenium	(20 - 2300)	58.67 μV at 0°C			Idem W type

Embedded thermocouples

These are stated as a regularly used method [124] and one of the earliest thermocouples used [140] in cutting temperature measurement. In this method, the thermocouple is placed in a hole drilled typically in the static part of the process, i.e. the tool for turning and the workpiece for milling and drilling. [124] An example of such a workpiece-embedded thermocouple was used by Richardson *et al.* [141] during experiments to validate a temperature model for the milling process. However, Garnier indicates that there is significant importance on the position and direction in which the thermocouple is embedded. The thermocouples should always be mounted along isothermal lines, as shown in Figure 2.30 [139].

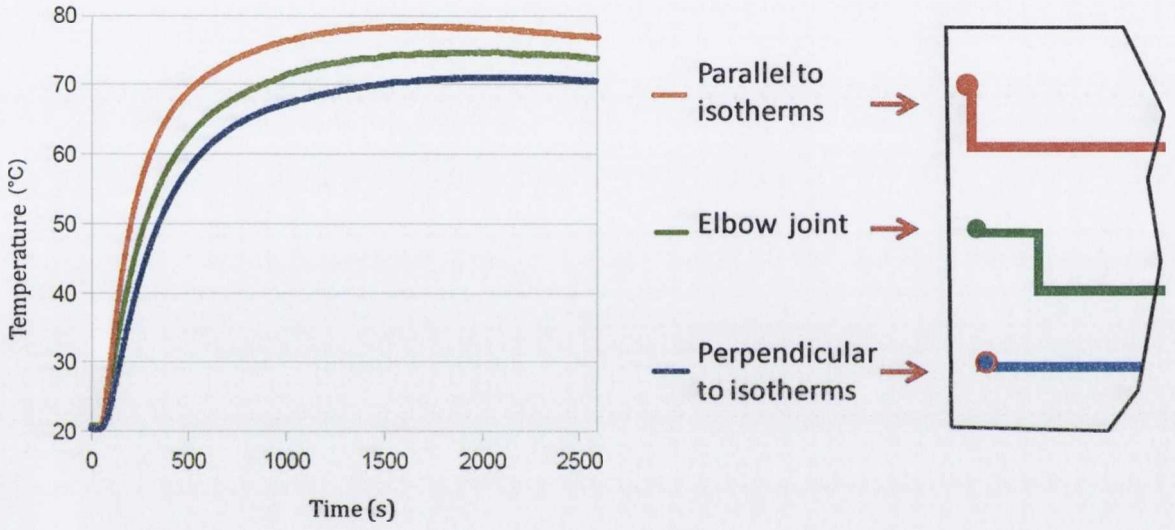

Figure 2.30: Effect of thermocouple placement on temperature. (Adapted from [139])

Additionally, Arriola *et al.* [142] placed the temperature sensitive tips of such embedded thermocouples approximately at the tool-chip contact zone in an orthogonal steel cutting experiment to take advantage of smaller gradients in the direction perpendicular to chip flow and ensure precise, repeatable locations for the thermocouples. The authors also stated in this research that while both thermal camera and embedded thermocouple provided similar temperatures for the process, thermocouples provided a cheaper and less sophisticated option than the thermal camera alternative.

A more complex method of embedding thermocouples comes from placing them into the rotating part of the cutting process. Hillery and Shuaib, [143], placed thermocouples into human and bovine bone and stainless steel drills as shown in Figure 2.31, in order to investigate the temperatures experienced by the bone during drilling. Kusters [144] used the EDM technique to

drill thermocouple holes into a cemented carbide tool in order to assess the temperature distributions in the tool to a distance of 0.2mm from the surface of the tool.

Kitagawa *et al.* [129] went a step further than Kusters, embedding a tungsten wire, of 20 µm diameter, into a Si_3Ni_4 tool during a pre-sintering process, which was then sintered with the tool matrix before an edge of the wire was exposed on the rake face by grinding. This was done in order to obtain local temperatures on the rake face of the tool.

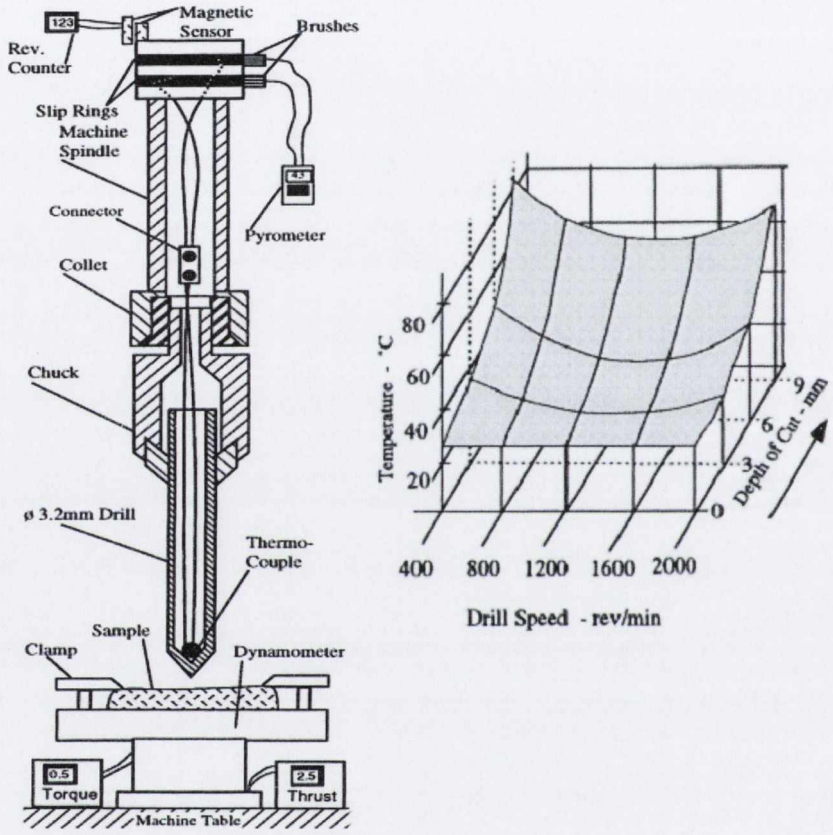

Figure 2.31 Experimental setup and results using thermocouple embedded in drill [143].

These techniques introduce additional technologies to the embedded thermocouple measurement method. Hillery and Shuaib used a slip ring mechanism to overcome the issue of obtaining a signal from a rotating tool. This mechanism has been employed by other researchers, [145] although alternative methods of wireless temperature data have also been employed [146].

The accuracy obtained during the placement of embedded thermocouples from the cutting interface is known to be limited [139]. The use of various methods ranging from basic extrapolation to inverse problem techniques must be incorporated into such temperature measurement solutions in order to achieve accurate results of tool surface temperature [139].

Methods such as the inverse heat transfer technique [147] have been applied in machining applications to estimate the temperature at the cutting interface based on measurements taken from sensors within the cutting tool [148, 149]. Numerical solutions of the heat equation are typically employed, in conjunction with the inverse technique as a tool to supply the heat flux boundary input to the model. In cutting tool temperature modelling works, Samadi *et al* [150] solved the theoretical inverse problem for the finite element method using the sequential function specification method (SFSM). In this case, cutting face temperatures were solved for using simulated sensory information was based on modelled temperatures at an embedded position within the tool model. The simulated embedded temperature information was obtained through a direct numerical analysis using a known temperature at the surface. The inverse problem was solved by obtaining an approximation of the heat flux input boundary through a 7-step procedure [150]:

- Make a guess at the heat flux, q^*
- Call the direct solver (ANSYS APDL was used) to calculate temperature at the sensor location using q^*.
- Calculate the step sensitivity coefficient for q^* for r future time steps.
- Estimate the m^{th} heat flux component as the new q^* using an estimator formula.
- Compare the estimated heat flux with the old q^* using convergence criteria
    - If the convergence criteria are not satisfied, return to step 2.
    - Otherwise, accept the estimated heat flux at that time step as q_M.
- Perform a single time step temperature calculation to determine the initial condition for the following time step.
- Increase M by one and go back to step one.

The use of such methods to solve for a surface temperature in the tool from an embedded thermocouple sensor allows for an accurate approximation of the tool surface temperature to be achieved. However, Courbon *et al.* [131] state that more attention should be paid to thermal contact resistance if accurate temperature fields in the tool are sought after. Thermal contact resistance, TCR, occurs when there is an imperfect contact between the tool and a continuous chip in metal cutting. Due to the very small chip size in CFRP machining [108], and the revised multi-point tool design to cope with such chip formations [6], further investigations are required to determine the influence of TCR on the CFRP partition ratio.

Dynamic thermocouple

One version of this type of sensor is the tool-work/chip thermocouple. This was developed by Gottwein, Shore and Herbert [151] in the 1920's and is still used as a viable measurement method. In this method, the contacting tool and workpiece materials are used to generate the EMF, which is translated into temperature as illustrated in Figure 2.32. Stephenson *et al.* [151] indicated that tool-work thermocouple methods were the most promising of all techniques for measuring temperature during cutting. The critical requirement of this method, therefore, is electrical conductivity of the tool and workpiece.

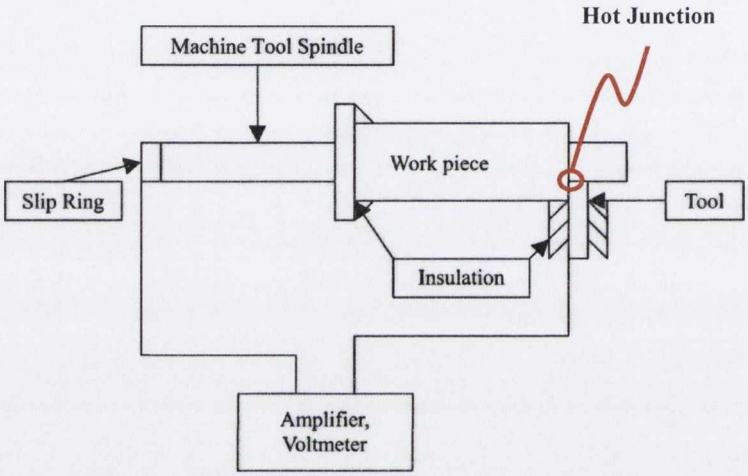

Figure 2.32: Conventional tool-work thermocouple circuit. (Adapted from [151])

As a result of this requirement, Narutaki [152] state that the tool-work thermocouple method cannot be applied with the natural diamond tool to measure the cutting temperature. Uncertainty remains regarding what the temperature recorded represents. Stephenson states that for tungsten carbide tools, the difference between the EMF generated in the tool-work thermocouple and the average interface cutting temperature are small [151]. In addition, another limitation of this tool is the requirement for insulation of the tool and work from surroundings and therefore no cutting fluid can be used during investigations with this sensor [153], although this issue can be solved by grounding the workpiece to the machine. [151] According to Stephenson *et al.,* the electrical isolation of the chuck and tailstock greatly reduces the stiffness of the workpiece/machine system and increases the likelihood of chatter during heavy cuts [151]. This insulation is also often difficult to achieve with a high chip volume which leads to chip shorting noise [154]. The necessity for an accurate calibration of the thermocouple pair is also an essential part of this type of thermocouple [124].

Sasahara *et al.* [100] investigated CFRP temperatures using the tool-work thermocouple technique, by incorporating a carbide rod, shown in Figure 2.33 and using electro-conductive

grease, contacting the rotating carbide tool during machining, while the hot junction was formed at the cutting interface. The CFRP end of the thermocouple was insulated from the machine table using epoxy sheet.

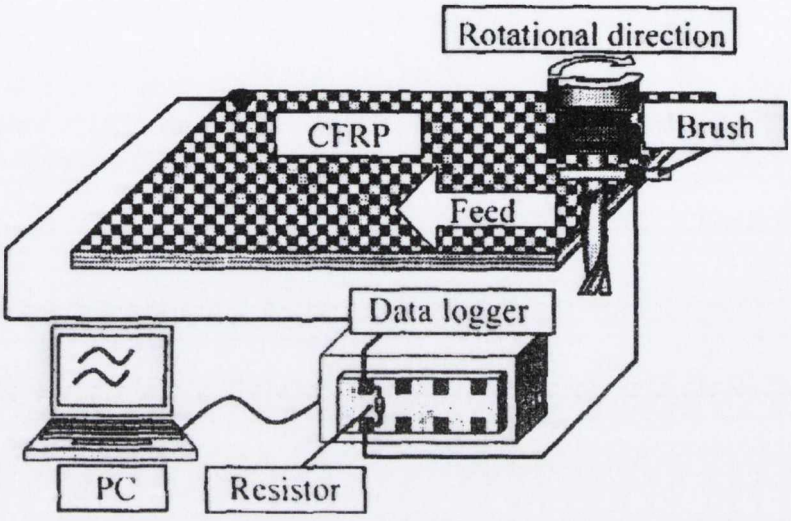

Figure 2.33: Tool-workpiece method used by Sasahara *et al.* [100]

In works by Babic *et al.* [155] during grinding investigations, a dynamic method known as the single pole thermocouple technique was employed to measure grinding temperature during dry and mist jet cooled versions of the process. This technique, set up as shown in Figure 2.34, utilises the material removal process to smear a thin constantan wire over a steel workpiece, thereby forming a hot junction, which is highly precise and highly responsive.

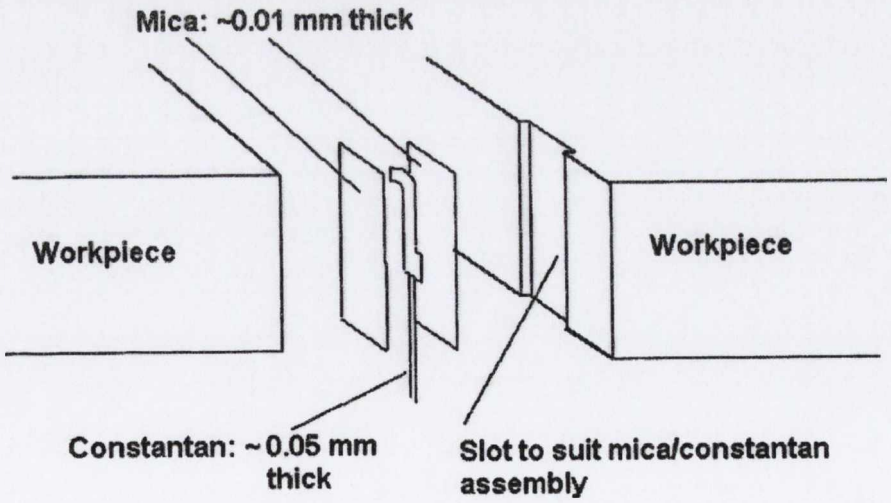

Figure 2.34: Single pole thermocouple technique used by Babic *et al.* [155]

Thin film thermocouples (TFTs)

These are small sized, fast response, low cost and flexible design thermocouple sensors. The concept of such sensors is to get right into the cutting interface in order to measure the exact temperature during tool-workpiece interaction. However, such devices must succumb to trade-offs between durability, sensitivity and realistic machining [5].

Choi and Li fabricated and applied such a thermocouple to the laser machining process in order to measure the transient surface temperature in nanosecond pulsed laser micromachining, shown in Figure 2.35 [156]. It was determined from these experiments that TFTs could produce a response time of 28 ns which is significantly superior to other conventional thermocouples [156].

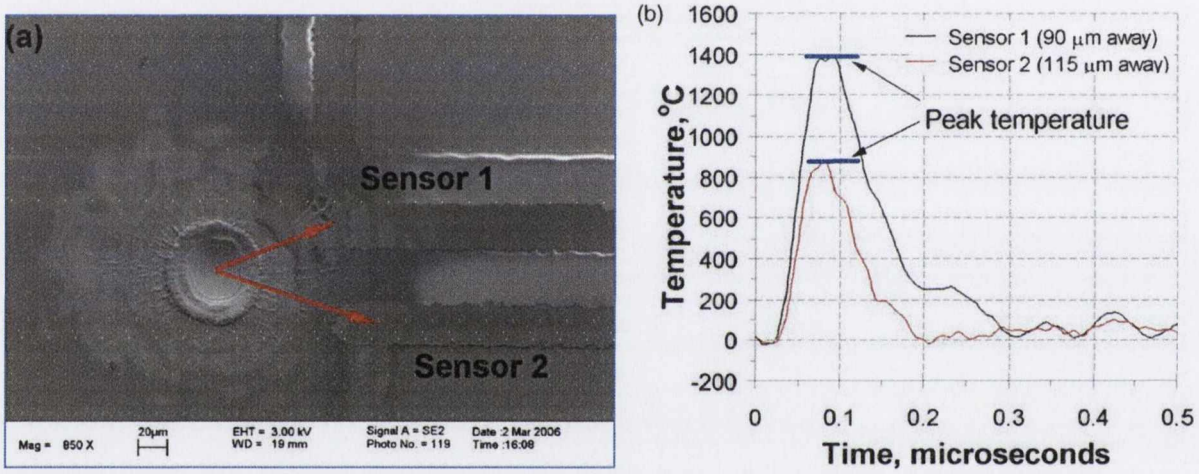

Figure 2.35: (a) Laser spot mark in close proximity to the TFTs and (b) the effect of proximity of the sensors to recorded temperatures [156].

In another experiment, Basti *et al.* [123] used a cutting tool insert with a built-in TFT, as shown in Figure 2.36. It is stated that there were some stability issues in obtaining measurements due to built-up edges right up at the cutting edge. However, with sensors outside of this zone measurements relating to the cutting force were generated. It is not stated to what degree of accuracy or resolution these measurements were made.

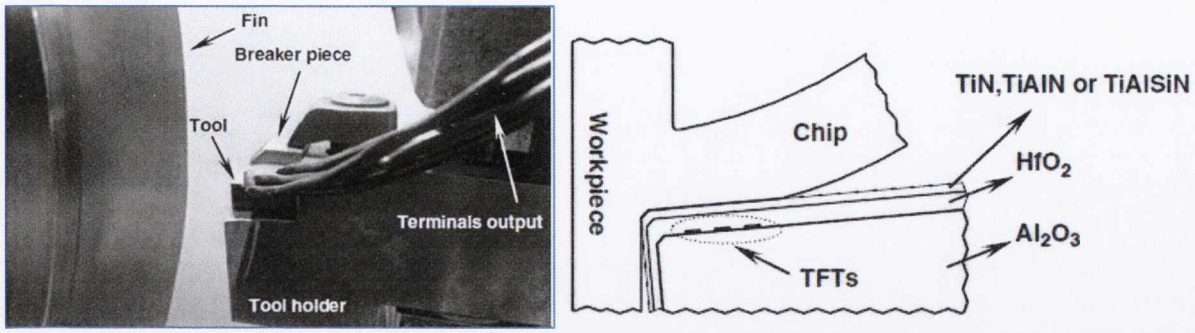

Figure 2.36: (Left) Experimental setup of the sensored insert and workpiece and (Right) the concept of tool with built in TFT. (Adapted from [123])

In a grinding process by Brinksmeier *et al.* [157], a TFT was compared to two other designs of K-type thermocouples. The results indicated that the TFT provided a much shorter response due to the extremely small volume of material to be heated, yet failed to match the other sensors in durability.

Brinksmeier *et al.* [157] state that a major difficulty in temperature measurement is the realisation of the signal transfer from the rotating tool to a data acquisition system (DAQ). However, this problem was overcome by Le Coz *et al.* [158], using a wireless data transmission system for drilling and milling applications.

Resistance thermometers

In general, resistance thermometers are devices that change their electrical resistance with temperature. Also known as thermo-resistors and resistance thermometer detectors, these sensors require the supply of energy to sustain the flow of acquired temperature data [134]. The physical principle of these devices is based on the behaviour of conductive bodies, typically metals, under temperature. In this scenario, as the temperature increases the amplitude of the excited atomic nuclei vibrations increases. This also results in an increase in the probability of collisions between free electrons and bound ions. Therefore, due to the interruption of the motion of free electrons caused by crystalline collisions, the electrical resistance of the material increases [134].

Resistance thermometer detectors

Also known as RTDs, these sensors consist of a resistance thermometer conductor on an insulating support. The nominal resistance, R_0, in industrial applications is commonly between 50 Ω and 100 Ω. [134] The resistance of an RTD is measured by passing a current through the detector. These devices are used extensively in calibrations of other temperature measurement sensors due to low cost and high accuracy. However, errors associated with submersion

requirements have restricted the use of such sensors in machining monitoring [5]. It is recommended by Davies *et al.* that such sensors be used in conjunction with simulation and alternative measurement techniques to fully quantify measurement uncertainties.

2.7.2 Radiation techniques

Like other energy forms, such as sound and light, heat propagates away from its source in waves. Heat is omitted from an object as a type of infrared radiation. Heat radiation can be described as an electromagnetic (EM) wave of periodic wavelength through space as a function of time. The wavelength, λ, represents the spatial periodicity and the period of oscillation represents the transient periodicity – its reciprocal is the frequency, ν. The wavelength and frequency of a wave are connected by the speed of propagation, c, of the wave as shown in Equation 2.13.

$$c = \nu \cdot \lambda \qquad 2.13$$

EM waves, such as infrared heat waves, travel at the speed of light (299 792 458 m/s) in a vacuum and close to this in air – depending on the index of refraction. Via a process called polarisation, a process whereby disturbances from the source oscillate in many different directions, EM wave disturbances are in the form of electrical and magnetic fields. These fields are perpendicular to each other and the direction of propagation as shown in Figure 2.37.

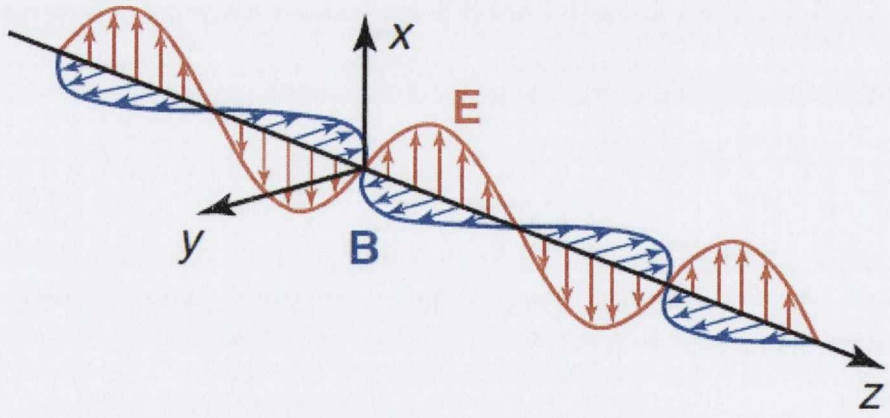

Figure 2.37: Electric fields (E) and magnetic induction fields (B) perpendicular to each other and the direction of propagation [159].

EM waves are typically classified according to their wavelength in the electromagnetic spectrum (EMS). As shown in Figure 2.38, the visible light spectrum accounts for a small portion of this EMS, from 380 nm to 780nm [159]. Relating to infrared imaging, long-wave (7 –

14 μm), mid-wave (3 – 5 μm) and short-wave (0.9 – 1.7 μm) ranges have been defined and commercial cameras have been developed for all three. An important idea for the measurement of such devices is that EM thermal radiation is emitted by all bodies at a temperature > 0 K (-273.15 °C). The amount of radiation and how it is distributed as a function of wavelength depend on temperature and material properties.

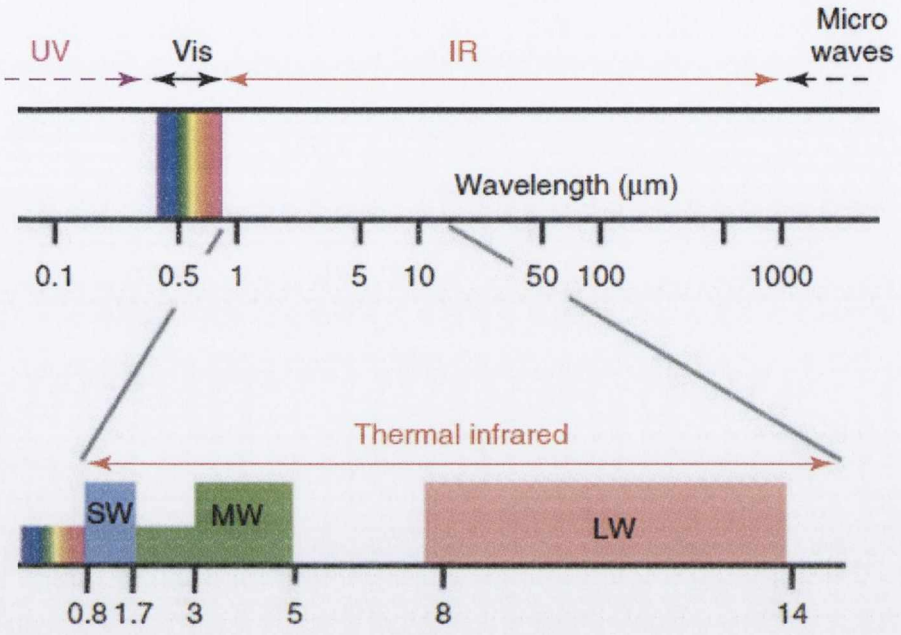

Figure 2.38: Infrared and adjacent spectral regions. (Adapted from [159])

Plank's law

Considering an element of surface area *dA*, as shown in Figure 2.39, the total energy flux, $d\Phi$, from this element into the hemisphere is called radiant power or flux, measured in watts (W). It is only possible to measure this quantity directly if the detector is able to collect radiation from the hemisphere completely, which is not normally possible. Therefore, using a relationship between the emitting surface area and the power, the emittance or exitance, *M*, in W/m^2 is determined using Equation 2.14. This characterises the total radiant power within the hemisphere. Irradiance is measured by the same units as emittance, but refers to the energy received by the element.

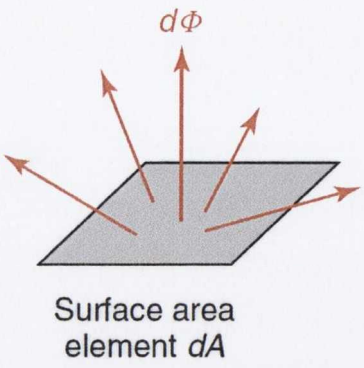

Figure 2.39: Total energy flux [159].

$$M = \frac{d\Phi}{dA} \tag{2.14}$$

Considering the wavelength of the emitted energy for the same element, the spectral density is defined as:

$$\Phi_\lambda = \frac{d\Phi}{d\lambda} \tag{2.15}$$

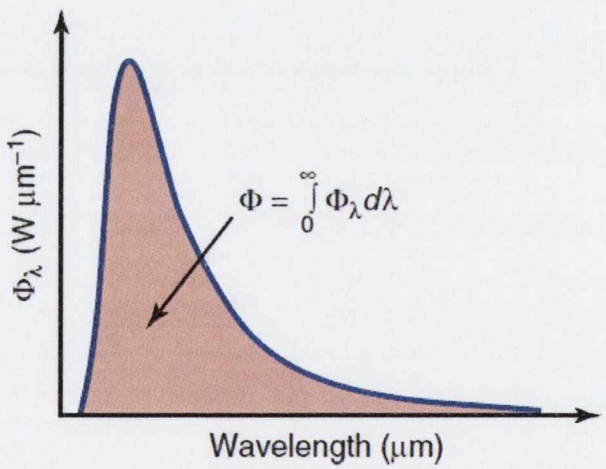

Figure 2.40: Relation between radiant power, Φ, and its spectral density [159].

The spectral radiant exitance, i.e. for the full spectrum of wavelengths, for a black body is defined by Plank's law, represented in Equation 2.16 [160].

$$M_b(\lambda, T) = \frac{2\pi hc^2}{\lambda^5 \left[e\left(\frac{hc}{\lambda kT}\right) - 1\right]} \tag{2.16}$$

Where c = 299 792 458 m/s the speed of light in a vacuum, h = 6.626 176 x 10^{-34} W s^2 the Planck constant and k = 1.380662 x 10^{23} W s/K the Boltzmann constant.

Emissivity

According to Minkina *et al.,* [160] the most important feature of a surface that affects the amount of energy radiating from it in stationary thermal conditions is its emissivity. Detailed research into the application of radiation thermometry in machining temperature measurements by Pujana *et al.* [161] determined that emissivity of the tool during machining is a function of temperature, wavelength, surface roughness and metal oxidation, over the time span of a cutting process measurement. The authors determined behaviours for P10 and P20 grades of WC in terms of each of these factors. It is interesting to note that over relatively small scales, as are necessary in CFRP machining, i.e. 0 - 200°C, the effect of such factors is relatively low in comparison to the effect associated with higher temperature metal cutting processes.

Minkina *et al.* go on to state that total emissivity of a body, i.e. over the full radiation range is defined as the ratio of full-range radiant exitance M(T) of that body to full-range radiant exitance $M_b(T)$ of a black body at the same temperature:

$$\varepsilon_\lambda = \frac{M(T)}{M_b(T)} \qquad \textbf{2.17}$$

Although there are numerous methods described by Minkina [160] for evaluating the emissivity of an object, the following are options which, when combined, are suitable for the evaluation of the emissivity of a cutting tool.

- Use a sticker or paint of high and accurately known emissivity, e.g. ε =0.95, and measure the temperature of this section of the surface. Then focus the camera on the original surface and adjust the emissivity until the temperature readings are the same - steady state conditions must be used for this.
- Using an alternative measurement device calibrated previously, such as a thermocouple, in order to determine the temperature of the point [162].

Thermal imaging cameras

The basic idea of a thermal imaging camera is that an object emits radiation in the direction of the camera where it is focussed onto the detector. The detector system then acts as a transducer, converting radiation into electrical signals that can be measured quantitatively [159]. Detectors are divided into [139]:

- **Photon detectors:** Absorption of photons of infrared radiation by the detector element leads to changes in charge that can be detected by the system.
- **Thermal detectors:** First, incident radiation is absorbed to change the temperature of the material. Next, the electrical output of the thermal sensor is produced by a change in the physical properties of a material – temperature-dependent electrical resistance in a microbolometer shown in Figure 2.41.

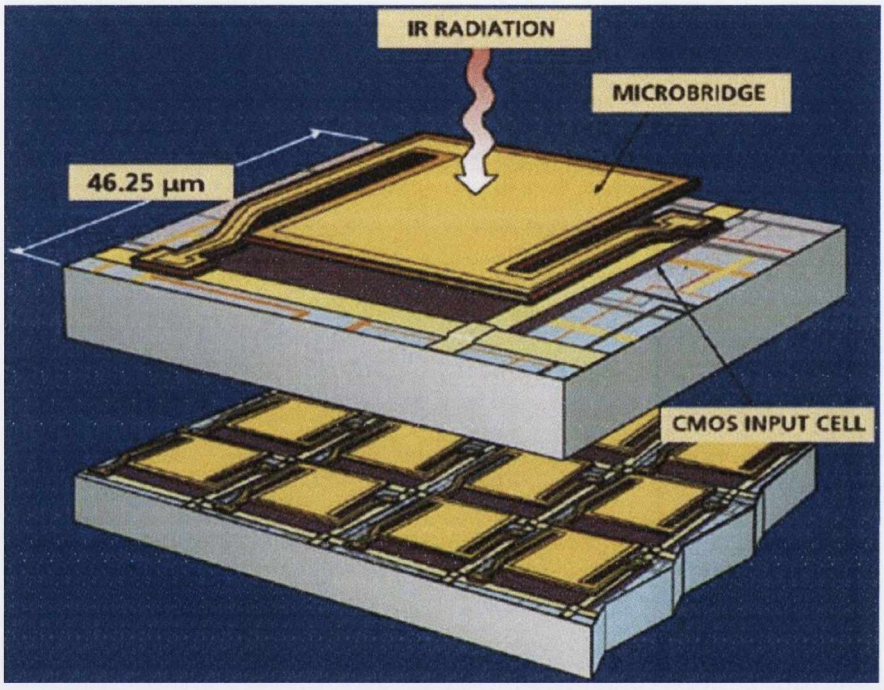

Figure 2.41: Schematic overview of a microbolometer detector [163].

An alternative method of characterising such cameras is:

- **Single point detectors:** The image is generated point-by-point at consecutive time instances [160].
- **Linear and array detectors – Focal Plane Array (FPA):** These devices are built up as matrices consisting of individual detectors.

There are two other ways in which to divide thermal cameras: 1) by wavelength scale and 2) by the presence of cooling.

Thermography has been used in a number of works in order to measure the temperature during material removal processes. Muller-Hummel *et al.* [162] presented a measurement system, shown in Figure 2.42, for measuring the rake face of diamond-coated inserts during dry turning. This allowed for a correlation between temperature and wear to be determined. The authors state that this method could be translated to interrupted cutting.

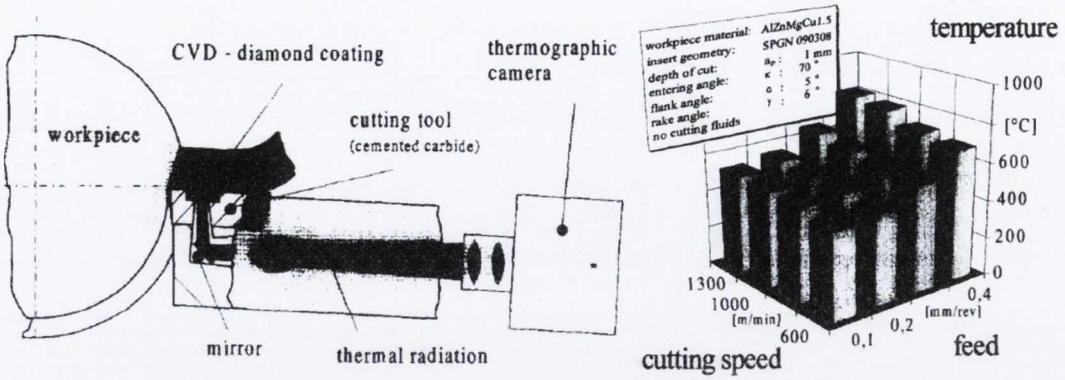

Figure 2.42: Model of thermographic measurement system with a tool face borehole and results obtained from system [163].

Investigations by Dewes *et al.* [153] into milling of hardened steel incorporated an Agema Thermovision 900 IR camera as shown in Figure 2.43. In this research it is not stated how the emissivity value was determined nor what orientation the camera was set to the measurements.

Figure 2.43: IR camera setup used by Dewes et al. [153].

The maximum chip temperature was obtained from this method and it was found to be lower than that obtained by thermocouple method. The reasons cited for the lower IR value are a combination of too small a target hot zone of the process and software issues. It is also stated by the authors that the thermocouple is considered to be intrinsically superior for milling applications [153].

Sugita et al. [164] investigated the cutting temperature in end milling of cadaver bones using thermography to investigate the damage caused to osteocytes during cutting. The authors compensated the emissivity of the cutting tool by painting it black to give it an emissivity of 0.98 and took temperate results immediately after the end of the cutting process. However, only approximate values were obtained in this research.

Del Campo *et al.* [165] developed a new devise for IR spectral directional emissivity measurement for temperatures up to 1050 K. A fourier transform infrared (FTIR) spectrometer was used for signal detection. Results were obtained as a function of temperature, emission angle and surface state. Their experimental results, shown in Figure 2.44 indicate a very good fit with theoretical values.

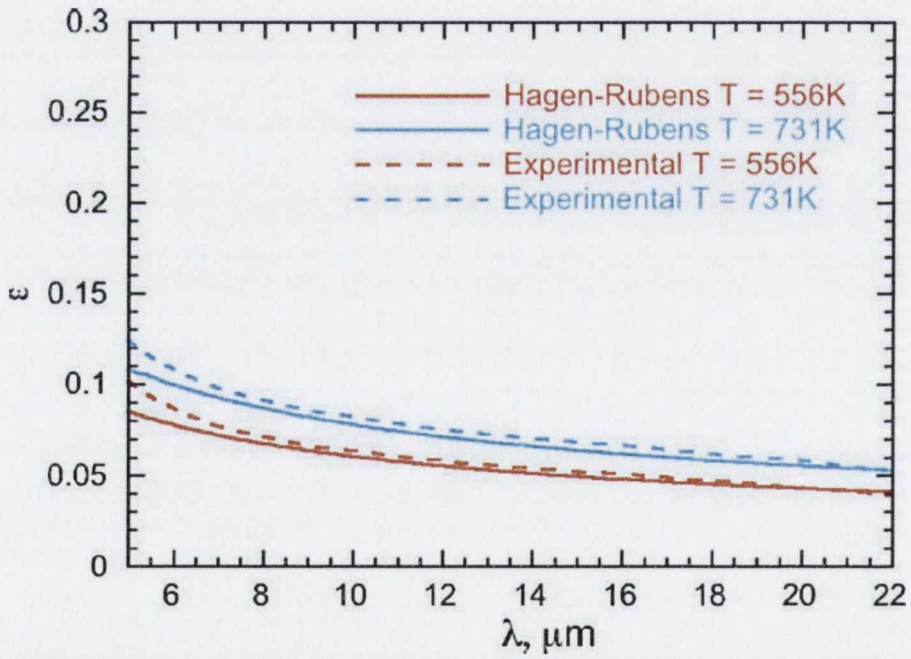

Figure 2.44: Good fit between experimental & theoretical emissivity values at various wavelengths [165].

The device developed by Del Campo *et al.* [165] was utilised by Armendia *et al.* [8], in a study in which the high speed milling process was monitored using a micro-thermal imaging system to

determine interrupted cutting temperatures of Ti6Al4V and AISI 4140 steel. In order to emulate the milling process, teeth were machined into the end of cylindrical tubes which was placed into a specially adapted tool holder section. This allow the workpiece, rather than the cutting tool, to rotate. The setup for this experiment is illustrated in Figure 2.45. The measurements were taken using a high bandwidth, 40 Mpixels/s, infrared microscopic imaging system focused on the edge of the cutting tool. Thermal radiation in the narrow range of 3.97 – 4.01 μm was measured by a cooled FPA with germanium lens for protection. The emissivity of the workpiece and tool materials as a function of wavelength and temperature were measured with an FTIR spectrometer, however the narrow range of accepted radiation removed the need for the wavelength function. Each pixel in the array was assigned a unique emissivity value in the range 0.2 to 0.3.

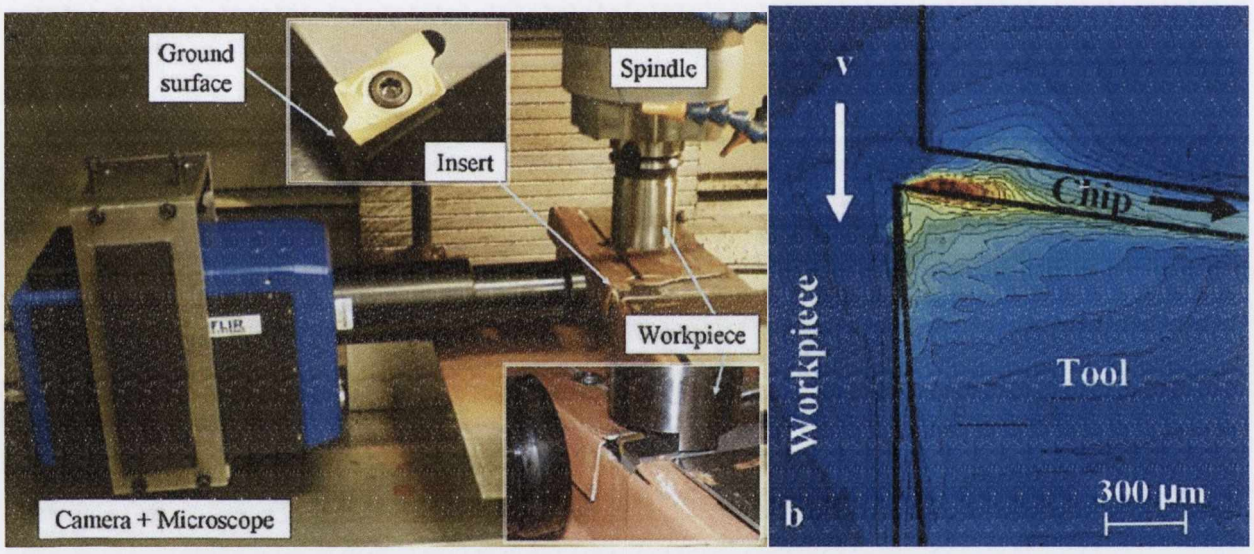

Figure 2.45: Milling process simulation with different configurations. (Adapted from [8])

The conclusions of this research indicate that interrupted cutting results in lower temperatures due to the effect of cooling periods between engagements as depicted in Figure 2.46.

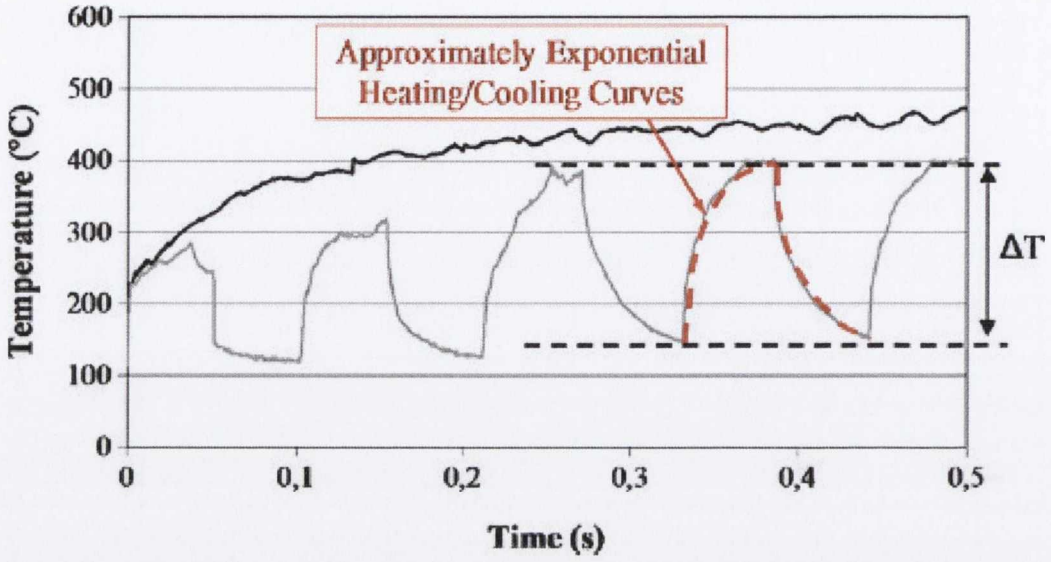

Figure 2.46: Comparison of continuous and intermittent cutting. (Adapted from [8])

In terms of machining composites, Sasahara *et al.* [100] used a thermal imaging camera as a validation tool for a tool-work thermocouple investigation of CFRP milling. This investigation used a basic estimation of the emissivity using the paint method. The results indicate that the camera produced variable validation that was highly dependent on temperatures with values up to 30% lower than those obtained via the tool-work thermocouple method.

Pyrometers

These devices work on the same principle of measuring the emitted thermal radiation of a body. In recent works, Brinksmeier *et al.* [94] used a pyrometer in order to measure the direct workpiece temperature close to the tool-workpiece contact area in the drilling of CFRP. The pyrometer used had a range of -18°C to 870°C and measured the workpiece temperature 0.2mm away from the hole being drilled, as illustrated in Figure 2.47. The authors concluded that using an orbital drilling strategy rather than a conventional strategy reduced the temperature during cutting.

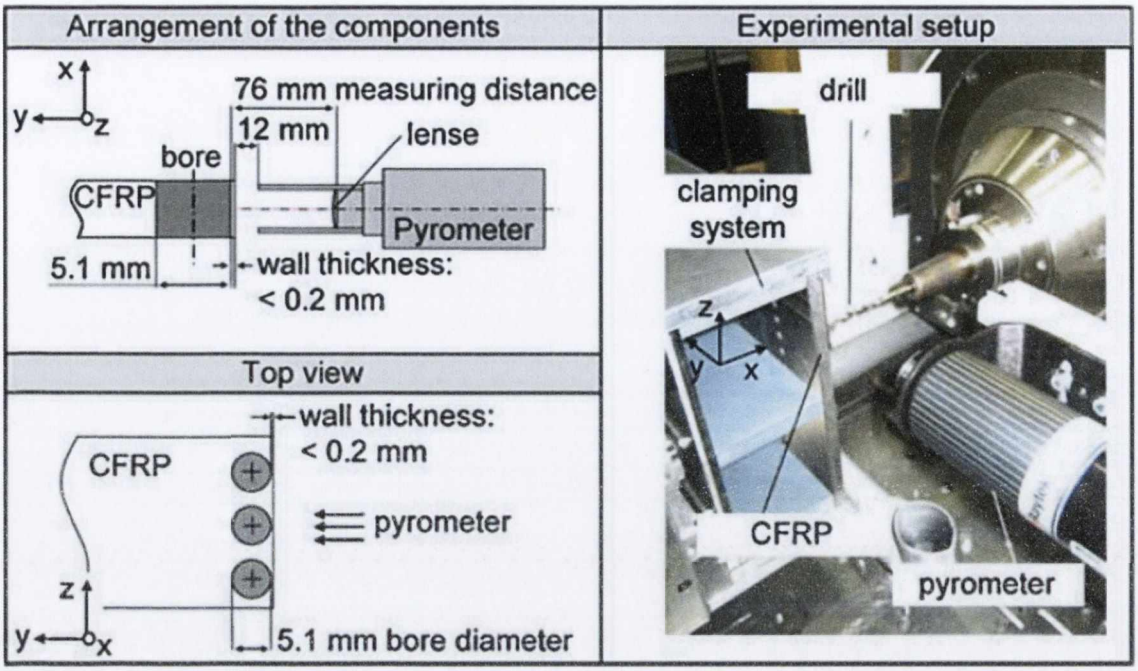

Figure 2.47: Experimental setup used by Brinksmeier in pyrometer drilling tests. (Adapted from [94])

Ueda *et al.* [166] used a two-colour pyrometer in conjunction with optical fibres to measure the temperature during drilling of carbon steel as illustrated in Figure 2.48.

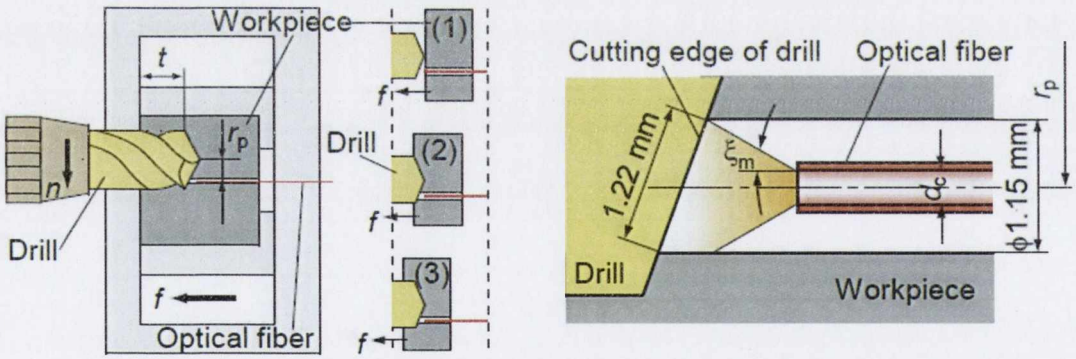

(a) Optical fiber setting. (b) Detail of temperature measurement.

Figure 2.48: Arrangement of optical fibre in drilling temperature measurement used by Ueda *et al.* [166].

The pyrometer used had a high response speed and remained a fixed distance of 1mm away from the cutting edge through the drilling process. This method allows for a highly accurate measurement without contact.

Following on from this, Ueda *et al.* [167] went on to apply the fibre-coupling transmission technique to the measurement of temperature of a CBN insert from a point 0.65mm from the rake face on the flank of the tool surface using a two-colour pyrometer. This was done, as illustrated in Figure 2.49, by implanting a fluoride glass fibre optics cable into the cutting tool up to the under surface of the CBN tip. Infrared rays radiating from the tip travel through the optical fibre, through the coupling to the two colour detectors where the ratio of the voltage outputs, in conjunction with calibration data produce the temperature.

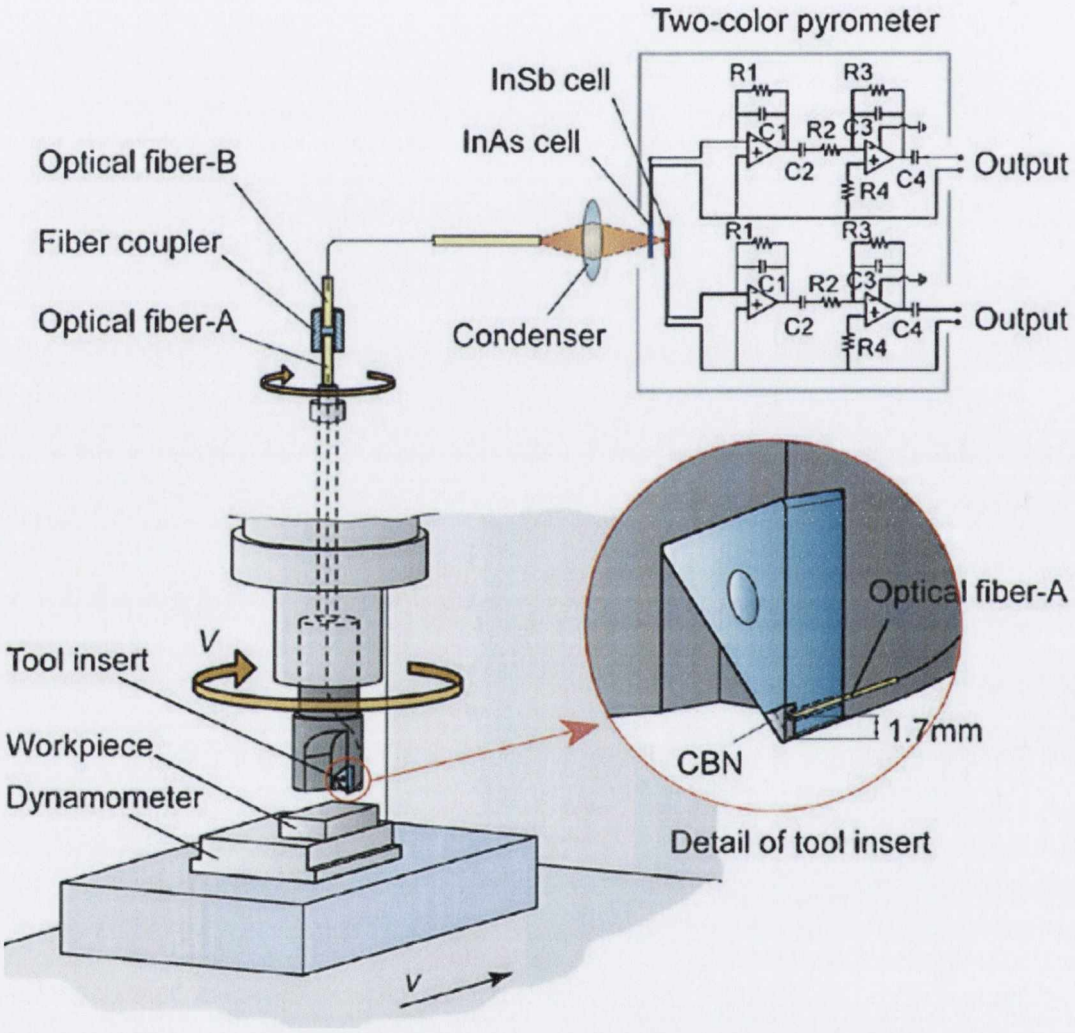

Figure 2.49: 2-colour pyrometry temperatures in milling measured by Ueda *et al.* [167]

2.7.3 Temperature measurement techniques suitable for CFRP machining monitoring

Chen [79] performed experiments on the drilling of CFRP composites using the embedded thermocouple technique. In this experiment, Ni-Cr and Ni-Al wires of 0.1mm were used for thermocouples embedded via the EDM process into a 0.5mm groove in a 9 mm diameter carbide tool, as shown in Figure 2.50. The issue of obtaining the signal from a moving tool was negated by placing the CFRP workpiece into the drill chuck and fixing the drill bit onto the work table.

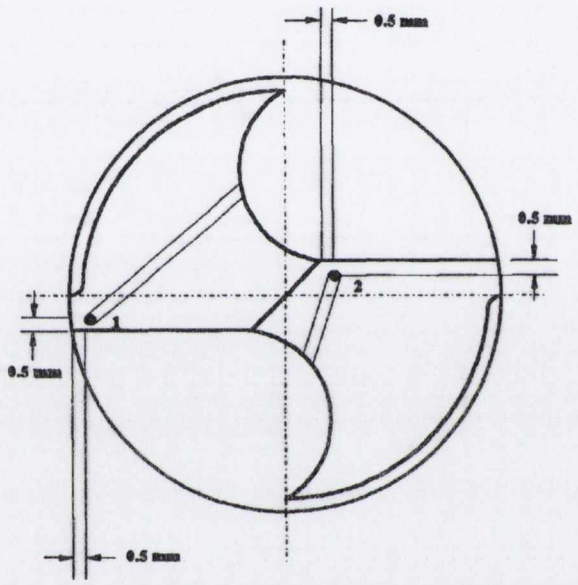

Figure 2.50: Thermocouple locations on the flank surface of a drill used by Chen.

As mentioned previously, Sasahara [100] used a tool-workpiece thermocouple setup in order to obtain temperatures from a CFRP composite-Ti-AlN-coated carbide tool milling process. Results indicated temperatures approaching 500°C for a highly worn tool using cutting speeds within the limits of those recommended for typical CFRP materials. However, the tool-work thermocouple relies on a single junction temperature at the interface of tool and workpiece. In composite milling, chip forms as dust particles and interactions with the tool could increase the error associated with the result. In addition, during the lay-up of CFRP composites, butt joints are used to reduce the amount of prepreg wasted during lay-up. This process involves pushing prepregs into a jig-saw type arrangement in order to complete the layer. The tool-work thermocouple relies on the conductive path through the highly conductive carbon fibres. The

presence of such butt-joints in the laminate structure could cause issues in accuracy of the temperature.

The non-contact, radiation methods presented by Ueda *et al* [167] could provide a viable solution in CFRP milling investigations. Since the presence of chip particles could affect the temperature measured, the fibre-coupling should be sealed from the dusty chip not extracted from the CFRP trimming process.

2.8 Surface roughness measurement

In the medical device industry, where surface roughness can be both beneficial, for promotion of integration for bone implants, and a hindrance, in blood stream implants, significant focus is placed on the parameter selected for surface metrology analysis. This is indicative of the application-specific nature of such analyses and is highly relevant to surface analysis of machined composite components. Wang *et al.* [38] state that standard surface roughness parameters were not capable of accurately distinguishing the surface quality of the multi-directional laminate composite due to the inherent damage of the -45° plies. Instead, it is suggested by Wang *et al.* that a more comprehensive description of the machined surface can be obtained from a combination of average surface roughness parameters and statistical parameters from profiles taken traverse to the trimming direction.

A CIRP paper by Ramsden *et al.* [168], states that at the lowest level of sophistication, the root mean square roughness or interface width can be used. This is defined as:

$$R^2 = \sum_{i}^{N} \frac{(h_i - \bar{h})^2}{N}$$

Where h_i is the *i*th of N small contiguous areas into which the surface is divided and $\bar{h}$ is the mean height. Ramsden *et al.* also state in this paper that more sophisticated measures quantify texture such as the power spectral density of surface features (S) which encapsulates information about the lateral distribution of asperity, can be used.

According to the literature, [72, 99, 169-173] there are a number of surface roughness (SR) amplitude parameters currently used in industry, such as roughness average (R_a), root-mean-square (rms), roughness (R_q) and maximum peak-to-valley roughness (R_y or R_{max}). The most commonly used of these parameters in determining surface quality is roughness average (R_a). This term is defined by Çolak *et al.* [169] as the area between the roughness profile and its mean line, or the integral of the absolute value of the roughness profile height over the evaluation length as shown in Figure 2.51.

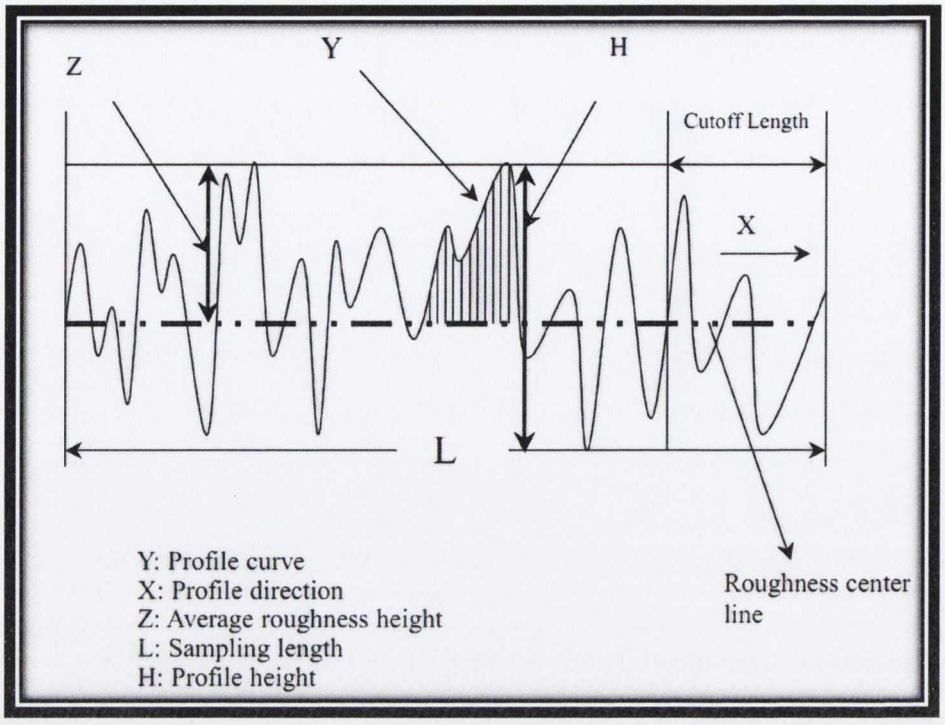

Figure 2.51: Surface roughness profile [171]

The average roughness of a surface is therefore expressed by the equation:

$$R_a = \frac{1}{L}\int_0^L |Y(x)|dx$$

Various surface irregularities are described in DIN standard 4760 and illustrated in Figure 2.52. It should be noted that a machined surface of a CFRP composite is most likely to exhibit 3rd and 4th order surface irregularities with 2nd orders as possibilities given specific cutting parameters.

Surface irregularity (as a contoured cut presented reinforced)	Examples for the kind of deviation	Examples for the reason of formation
1st Order: Deviation of form 	unevenness noncircularity	Error in the guidance of the machine tool, deflection of the machine or of the workpiece, chucking error, hardening distortion, wear
2nd Order: Waviness 	waves	Eccentric clamping or form defect of a cutter, vibration of the tool machine or of the tool
3rd Order: 	grooves/scratches	Form of the tool cutting edge, feed rate or infeed of the tool
4th Order: 	ridges ripples knobs	Process of the chip formation, (tear chip, slear chip, built-up edge), material deformation while sand blasting, gemnation during the galvanically treatment
5th Order: impossible to visualize in a simple manner	structure	Process of crystallization, modification of the surface through chemical affection e.g. pickling), corrosion mechanism
6th Order: impossible to visualize in a simple manner	lattice structure of the material	Physical and chemical process in the synthesis of the matter, tensions and shear within the crystal lattice
	Superposition of the surface irregularities 1st - 4th order	

Figure 2.52: Classification of surface roughness formation related to DIN 4760 Standard.

2.8.1 Surface roughness parameters

According to a review by Peters *et al.* [170], in 1952, at the CIRP General Assembly in Leuven, General P. Nicolau stated that the choice of the most appropriate (SR) parameter and optimal value for specific applications was left to the design engineer. Since this time numerous papers have been published relating to surface roughness of composites [75, 99, 173-176].

According to Çolak *et al.* [169] surface quality of a machined part depends on stability of CNC, cutting parameters, cutting tool, workpiece material and tool path. As illustrated in

the Ishikawa diagra in Figure 2.53, there are numerous factors which are known to affect the surface roughness of a component. Therefore, when selecting a method of SR measurement, it is essential to consider as many of these factors as possible. Some key relationships which have been found to exist in relation to cutting parameters and the cutting tool are:

$$Surface\ Quality \propto Cutting\ Speed; Cutting\ edge\ sharpness$$

$$Surface\ Quality \propto \frac{1}{Depth\ of\ Cut}; \frac{1}{Feed\ Rate}; \frac{1}{Tool\ Wear}$$

As stated by Çolak *et al.,* [169] there are many methods of measuring surface roughness, such as image processing, microscopes, stylus type instruments and profile tracing instruments. In their investigations of surface roughness, for end milling operations using a 10mm HSS cutting tool on Aluminium 6061 T8 workpieces, a Pocket Surf stylus instrument was used, produced by Hommel Werke T500. While their results indicate poor empirical predictions in comparison to experimental results for low spindle speeds and smaller depths of cuts, there is a good correlation when using high speeds >1500 rpm and large depths of cut >1.27mm.

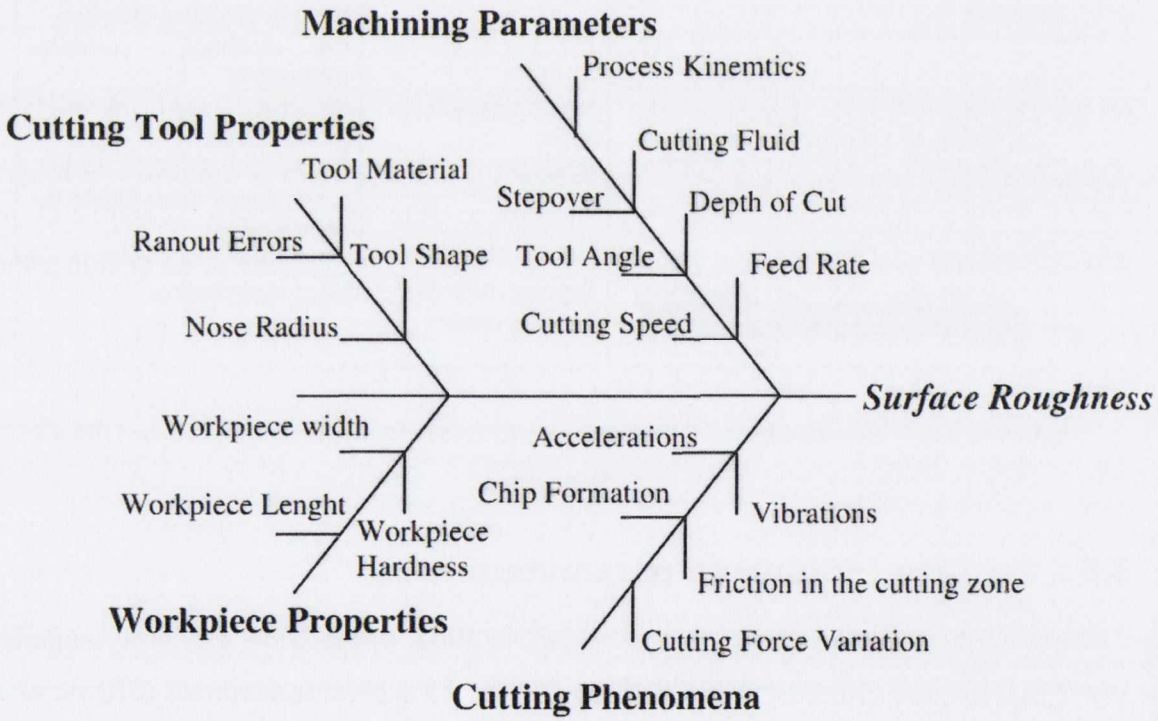

Figure 2.53: Ishikawa diagram with parameters affecting surface roughness [172].

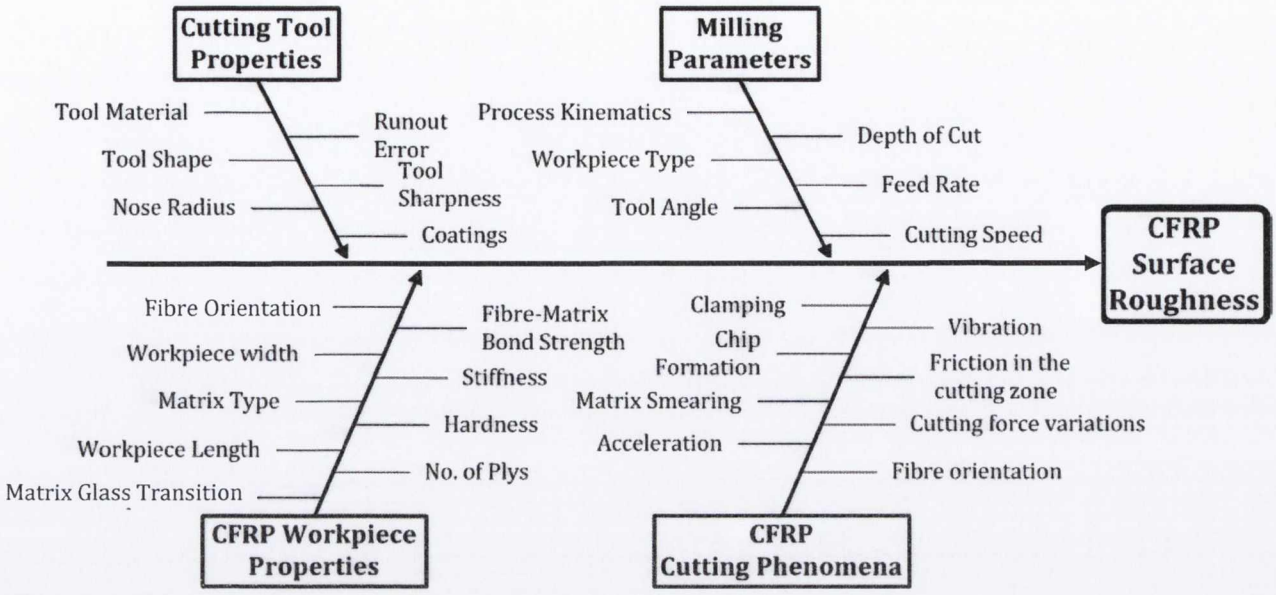

Figure 2.54: Ishikawa diagram with factors affecting CFRP surface roughness.

In addition to the factors identified in Figure 2.53 for general cutting, particularly in the areas of Workpiece Properties and Cutting Phenomena, CFRP composites require the consideration of other parameters as shown in Figure 2.54.

In earlier research performed on surface roughness by Hocheng *et al.* [43], unidirectional CFRP materials were milled and the resulting surfaces examined using a stylus-type Mitutoyo Surftest-201 device and an optical microscope. Different cutting parameters; cutting speed: 31.4, 94.2 and 188.4 m/min; feed rate: 50 to 150 mm/rev; depth of cut: 1mm, were used in conjunction with an OSG-Walter F2037 single square carbide insert tool with 20mm cutter head diameter.

In works performed by Ramulu *et al.* [99], it was stated that a more appropriate measure of the surface roughness of a composite, specifically graphite/epoxy type, are the parameters R_Y and R_Z due to the high dependence of SR in composites on the fibre orientation and measurement direction. Findings by Koplev *et al.* [108] reinforce the idea that the machined surface of a fibre reinforced polymer (FRP) composite is highly dependent upon the chip formation process and the fibre orientation with respect to the cutting direction. In the works of Ramulu *et al.* mentioned, the experiments were performed at relatively low cutting speeds in relation to those used for more recent research efforts; 3.1, 3.8 and 5.6 m/min for a cutting tool of radius 12.7mm. This is quite possibly due to the fact that the authors were using cutting speeds typically associated with the machining of more conventional materials. It is stated by Ramulu *et al.* that optical surface roughness techniques have an advantage of no contact between the sample and the instrument, and quick measurements can be obtained. Nonetheless, their results are obtained using the most common industry standard device – a stylus type

Surfanalyzer System 000 with an EPT-01049 diamond stylus probe with radius 2.54 μm. Surface roughness heights were measured at intervals of 1.25 μm and SR characteristics were evaluated using a cut-off length of 0.8mm. As a qualitative validation to the stylus measurements, the authors used a Joel JSM-T330A scanning electron microscope (SEM). An important finding of Ramulu *et al.* was that maximum peak-to-valley roughness (R_Y) and ten-point-height (R_Z) parameters were able to distinguish the surface profiles of different fibre orientations, and quantify the amount of micro geometric variations such as fibre pull-out. The authors therefore state that these are the parameters of choice described on a machined CFRP surface. It is stated, and shown in Figure 2.55, that R_A and R_Q are unsuitable and do not fully describe the irregularities of the surfaces studied.

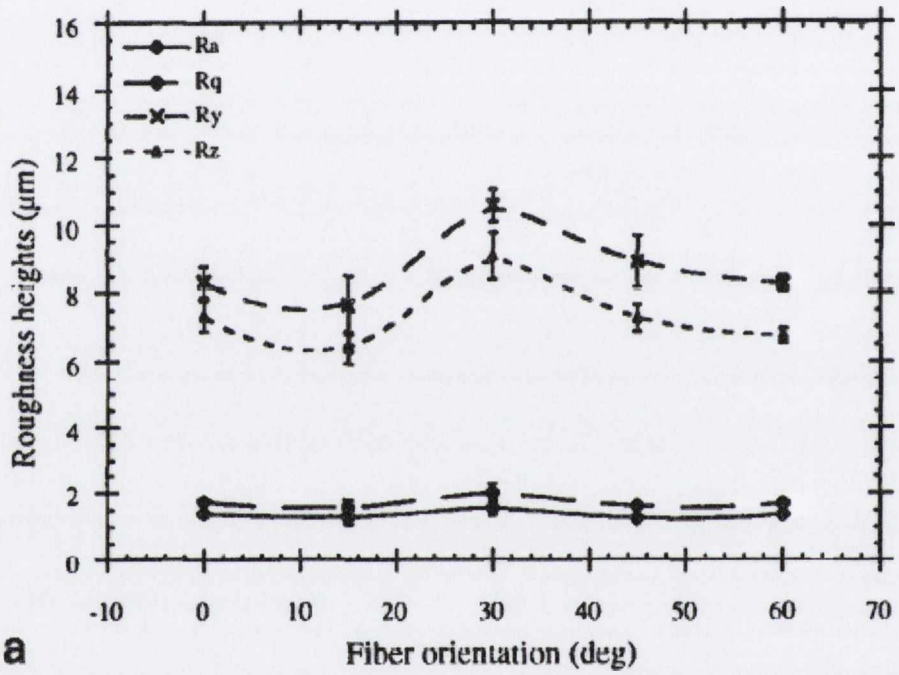

Figure 2.55: variation of surface roughness heights as a function of fibre orientation with respect to the cutting direction: (a) longitudinal direction; (b) transverse direction. Cutting speed = 3.1 m/min, depth of cut = 0.381 mm, error bars correspond to one standard deviation [99].

Similar SEM validation has been used in the dental field by Kohles *et al.* [177], who used two common surface characterisation instruments, an interferometer and a stylus profilometer, to measure the SR (R_A) of dental implants. Their results indicated that the interferometer produced more accurate results in predicting the SEM-based roughness. However, as a measure of aggregate precision over all measurements, the most repeatable instrument was the stylus.

Basheer *et al.* [175] used an FEI Quanta 200 HV SEM to perform a qualitative analysis type validation of the machined surface of a 9mm sample length of Al/SiCp composites

after turning. The machined roughness was measured along the feed direction using a Mahr Perthometer having a 2 μm stylus tip radius with cut-off length of 0.8mm. An explanation is given by Basheer *et al.* regarding the qualitative validation of SR measurement using the SEM images [175]:

"SEM photographs of machined surfaces on Al/SiC/20p composites showed the evidence of fracture as well as the particle pull-out, see Figure 2.56 (a) and Figure 2.56 (b). The size of the reinforcement and the corresponding areas of fracture or pull-out could be significantly more than the radius of the stylus tip. Hence the variation in the surface roughness due to the particulate pullout and fracture could be captured by the surface roughness measurement."

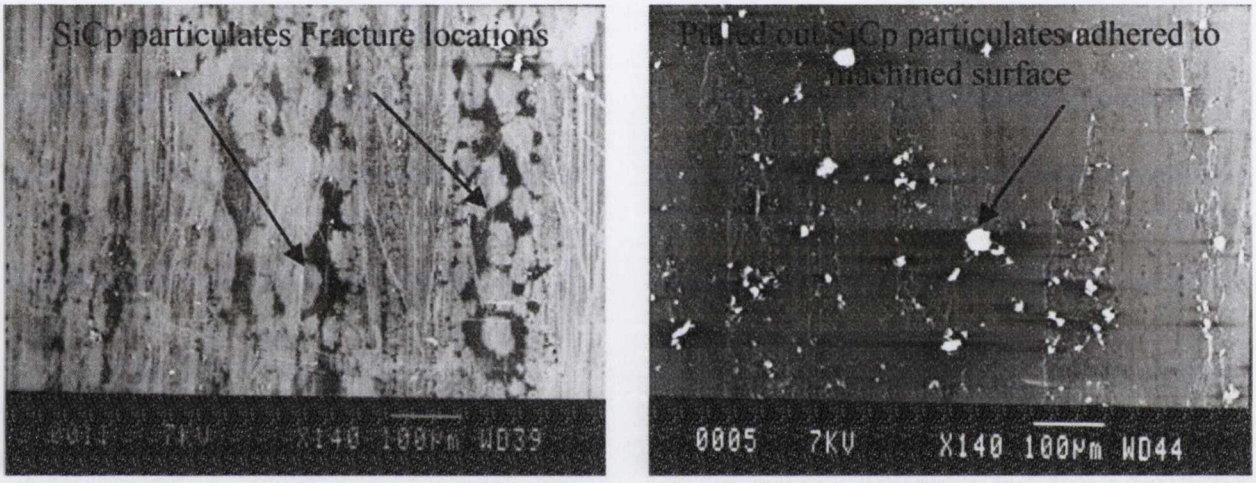

(a) (b)

Figure 2.56: SEM pictures of machined surface on Al/SiC/20p/220 showing evidence of (a) SiCp fracture and (b) SiCp pull-out [175].

Research carried out by Killçkap *et al.* [173] on the turning of metal matrix composites, utilised Taylor-Hobson Subtronic 3+ equipment in order to obtain surface roughness (R_A) values of the composite material under different cutting parameters; cutting speeds of 50, 100, 150 m/min; feed rates of 0.1, 0.2, 0.3 mm/rev; and depths of cut of 0.5, 1, 1.5 mm. However, there is no indication as to the accuracy of the results obtained for SR in these experimental efforts and conclusions appear speculative at best.

Palanikumar *et al.* [72] assessed the factors influencing surface roughness during the turning of GFRP composites, which had been manufactured via filament winding. It is stated in this work that the average surface roughness (R_A), which is mostly used in industries, is taken for this study. The use of R_A by both Killçkap *et al.* [173] and Palanikumar *et al.* [72] seems to counter the statement made by Ramulu *et al.* previously regarding the use of SR parameters R_Y and R_Z due to the unsuitability of R_A in representing the real SR of fibre reinforced composites. In the experiments performed by

Palanikumar *et al.*, a Taylor-Hobson Subtronic 3+ stylus type instrument was also used to obtain the R_A values. Their ANOVA results were used to determine effects and interactions between cutting parameters and surface roughness. An optimisation procedure for predicting the surface roughness for turning GFRP composites within the ranges is also supplied. Interestingly, the authors state that the validity of the procedure is limited to the range of factors considered for the experimentation. However, no indication is made towards any form of validation or calibration with regards to the surface roughness measurements, with the consequence that all results produced are subject to an unquantifiable amount of uncertainty.

El-Sonbatty *et al.* [81] investigated surface roughness occurring in the drilling of GFR/epoxy composites using the same stylus-type instrument as Palanikumar *et al.* [72] and Kilıçkap *et al.*. [173] The authors are quoted as having used standardised roughness parameters (R_A) in order to the assess surface microstructure. The cut-off and traversing length values were 0.8mm and 2.4mm respectively. The values of surface roughness are the average of three measurements taken at the middle of the hole wall and parallel to the hole axis.

Pramanik *et al.* [176] performed surface roughness analysis on metal matrix composites using a Mitutyo Surftest 402 stylus-type instrument. The parameters used by these authors were the R_A and R_{MAX} , while the cutting conditions were: depth of cut = 1.0 mm; feed = 0.025, 0.05, 0.1, 0.2 and0.4 mm /rev; and cutting speed = 100, 200, 400, 600 and 800 m/min.

In a paper by Azmir and Ahsan, [178] investigations were performed to determine the surface roughness parameter R_A for abrasive water jet machined glass/epoxy composites. In their experiments to verify a proposed surface roughness prediction model, the authors used a SURFPAK SV-514 stylus-type device equipped with a cone-shaped diamond stylus having a diameter of 10 µm and a tip angle of 90°. Quoting Azmir and Ahsan, "The surface roughness was measured over the edge of the cut specimen. It was obtained across the thickness of the test sample surface. The surface roughness profiles were taken from 0.5mm above the bottom surface to 0.5mm below the top surface to avoid the effects of jet exit and entry respectively. All measurements were acquired using 0.8mm cut-off length." The machining test was repeated four times and for each repeated test the average surface roughness was obtained as mentioned. However, only a linear section of the specimen thickness was used in order to obtain such a value for the complex composite structure as shown in Figure 2.57. Without considering other surface roughness parameters such as R_Y and R_Z their conclusion that cutting orientation is insignificant in influencing R_A cannot be considered comprehensive.

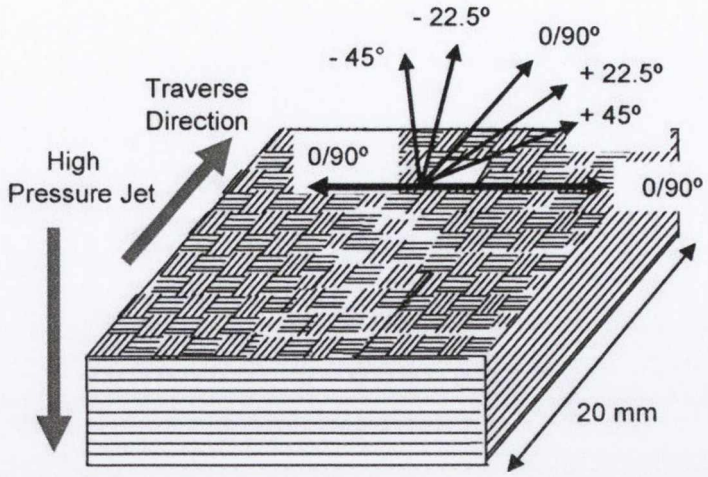

Figure 2.57: Cutting layout and orientation as discussed by Asmir [178].

In a study performed as recently as 2009, Davim *et al.* [179] used a Hommelwerke T1000 profilometer, a relatively old technology stylus-type device. An arithmetic mean roughness value (R_A) of AISI 1045 carbon steel was obtained in order to determine the wear of PEEK polymer when in long dry sliding contact with steel. Therefore, the SR data acquired from the profilometer became the basis of the conclusions within the study. In a number of papers, relating to the study of glass/carbon FRP composites, published by the same author, [44, 62, 98, 179, 180], the same T1000 profilometer is used in order to gain an R_A value according to ISO 4287/1.

Davim found that the measured roughness (μm) of the machined CFRP WP surface followed a repeating trend, whereby a sharp increase in roughness was noted as the fibre orientation approached 90° for a range of depths of cut (DOC). After 90°, the roughness varied significantly depending on DOC. It was found that the roughness spiked sharply from 90° to 120° and then decreased for a DOC smaller than the fibre diameter. However, for DOCs greater than the fibre diameter, the chip formation mechanism changes, and surface roughness did not decrease after 120°. In this situation, the rake angle was found to have a greater effect on the resulting roughness and a sharper tool was found to produce a rougher surface. This phenomenon was explained by Davim as being due to the variation of deformation mechanisms in the cutting zone when the DOC and fibre orientation change and is illustrated in Figure 2.58.

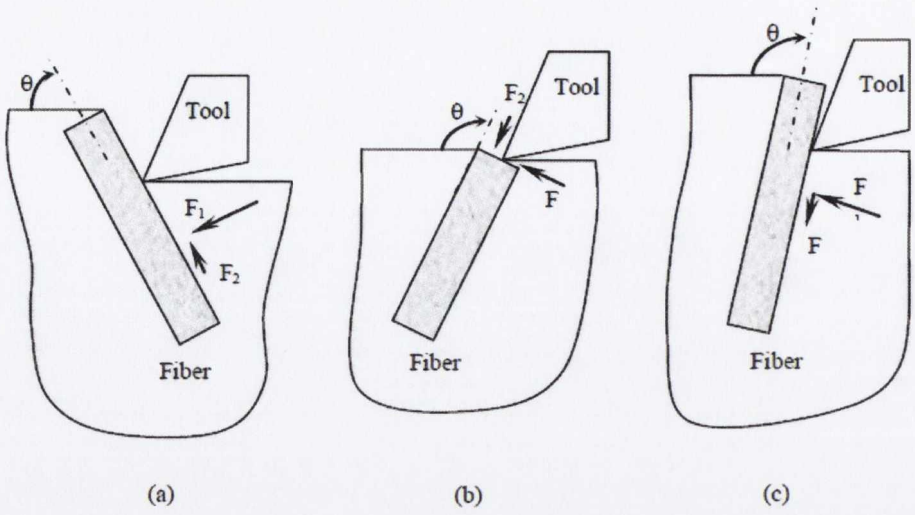

Figure 2.58: Schematic cutting models [37].

A recent investigation by Soo *et al.* [118] into the use of superabrasives for edge routing of CFRP composites utilised the stylus profilometer to obtain a 3D surface map. The authors used the R_A metric in this investigation, stating that measurements were obtained in the transverse direction to feed at regular intervals from start, middle and end. In addition to the 3D maps generated, the authors also utilised a scanning electron microscope to make conclusions regarding this study.

2.9 Statistical design of experiments

Experimental design was invented by R.A. Fischer during his investigations into agricultural data at Rothamsted Agricultural Experiment Station in 1918 [181]. According to Montgomery [182], we can define an experiment as a test or series of tests in which purposeful changes are made to the input variables of a process or system so that we may observe and identify the reasons for changes that may be observed in the output response. Statistical terminology refers to the input variables, such as cutting speed (v_c) and feed rate (v_f), as *factors* and the settings, such as v_c = 100; 150; 200 m/s, as *levels.*

Different methods allow the investigation of numerous factors, at the correct levels, simultaneously and economically in order to identify their effects on the experimental results. Such results can then be used to determine the best combination of factors under specific experimental conditions.

Consider the signal-to-noise analogy illustrated in Figure 2.59. What is observed during the experiment must be divided into signal and noise components. The signal is the key variable of interest and the noise represents the random factors associated with the experiment. The goal in the design of the experiment is to maximise the signal to noise ratio. This can be done via two methods: signal enhancement and noise reduction.

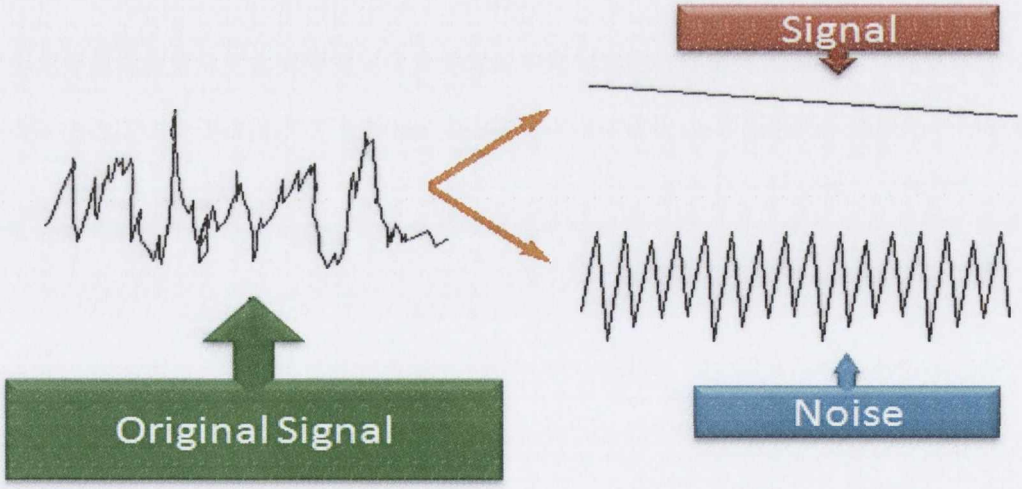

Figure 2.59: Analogous representation of the problem facing experimental designers. (Adapted from [183])

1. **Signal-enhancing experimental designs:** Full and fractional factorial. A full factorial design is one where the levels of one factor are evaluated against each level of every other factor, and the arrangement provides all possible effects and interactions, however the scale of testing can be prohibitive. [114]
2. **Noise-reducing experimental designs:** Covariance (ANCOVA) and blocking designs.

2.9.1 Using residuals plots to validate a statistical model

A residual is defined as the difference between the mean of a set of observations and an individual observation [184]. Such residuals can be used to graphically determine whether a statistical analysis is appropriate for the data available.

Due to the relatively low sample size taken in statistically based results, it is often difficult to assess the validity of the underlying statistical methods used in analysing the data. The statistical model in this research is that the data obtained is independently randomly scattered around some mean [184]. The randomness of the data can be assessed graphically using residuals versus fitted values plot, shown in Figure 2.60, in order to determine if there are any unexpected systematic errors within the process. The residuals should be distributed randomly about the zero line. This method clearly identifies outliers in a process response.

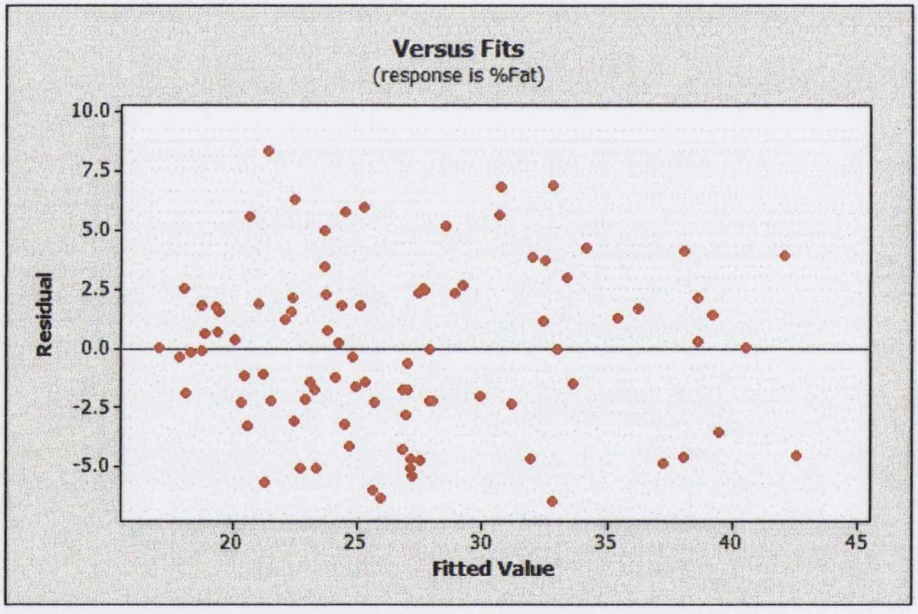

Figure 2.60: Example of a residuals vs fits plot used to determine random variation.

Additionally, the random scatter corresponds to that which would be expected from a Normal distribution. A Normal distribution exists if 100 % of the data is enclosed by the bell-shaped curve described in Figure 2.61. This curve plots the frequency magnitude of data points on the y-axis and variation between data points on the x-axis. Therefore the majority of the data points should lie at the centre of the bell curve, producing a centrally located mean, μ, with lesser frequent data points towards the tails of the curve. It must be noted that 99.7, 95 and 68 % of the data points lie within 1 times, 2 times and 3 times the standard deviations, σ. The standard deviation is often used as a measure of the precision of a process, as the greater this value the less precision exists within the process.

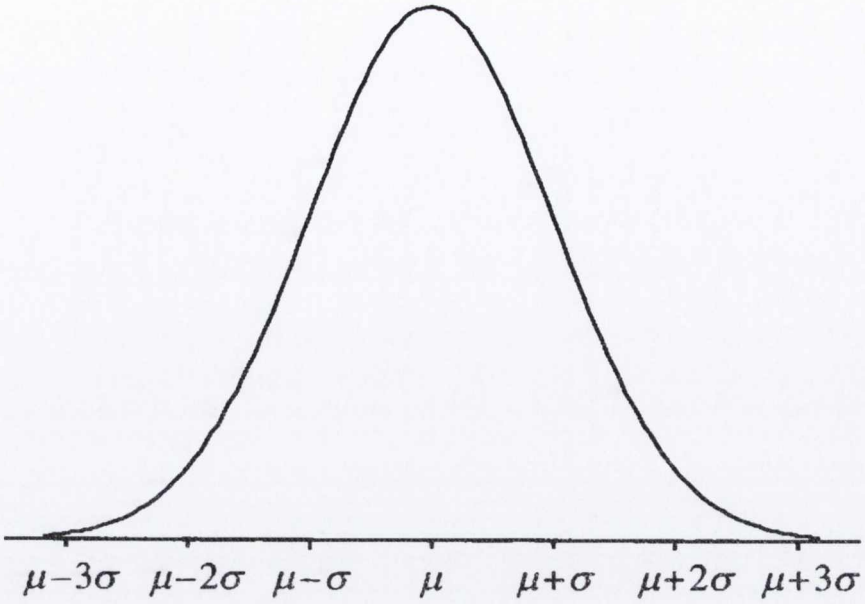

Figure 2.61: Normal distribution curve.

There are a number of methods which can be used to validate the Normal assumption. The most obvious method is to observe a histogram of the frequency vs residuals, as shown in Figure 2.62. This plot also provides details of the general characteristics of the residuals, including spread and and shape.

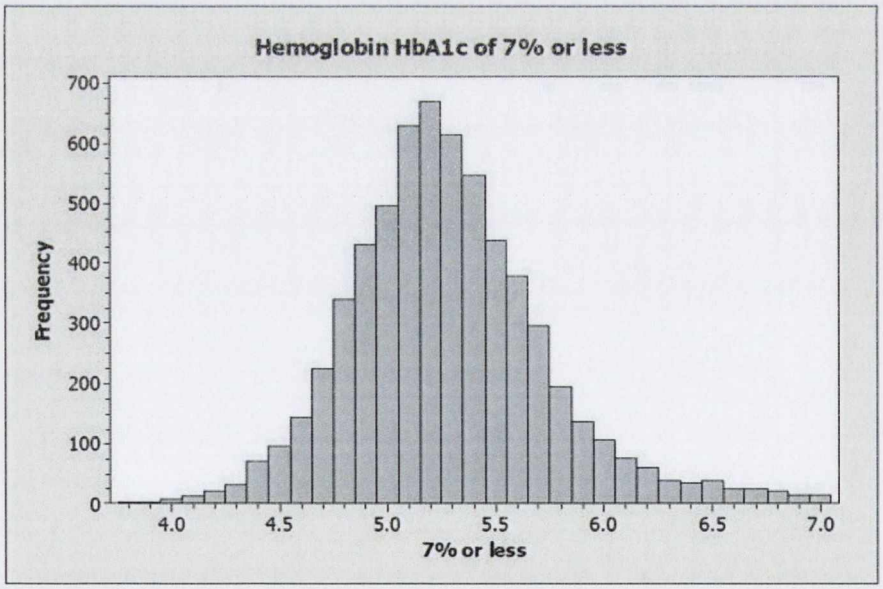

Figure 2.62: Example of a histogram plot of frequency vs residuals.

Another graphical method involves examining a normal probability plot, which plots the ordered data values against rankits or nscores. Nscores are completely independent of the data points which are calculated as the expected values distributed evenly around a normal distribution plot with a mean of 0 and a standard deviation of 1. The number of

nscores must be the same as the number of data points. As shown in Figure 2.63 if the data points follow a linear trend line, the data may be assumed to be Normal.

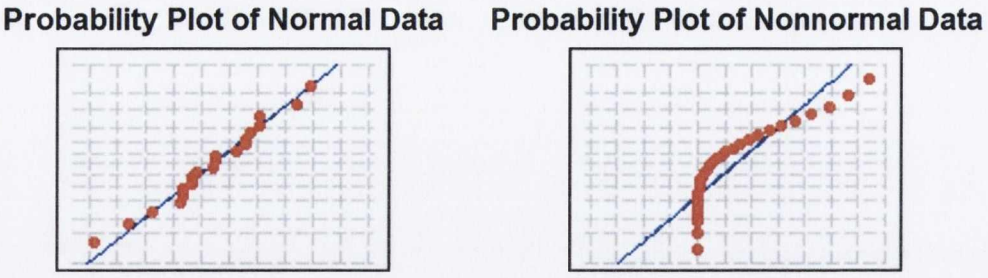

Figure 2.63: Graphical analysis used to assess the assumption of Normality.

Time-based non-random error can be determined from the plot of residuals versus observation order, shown in Figure 2.64. In this plot, there should again be random variation around the zero line.

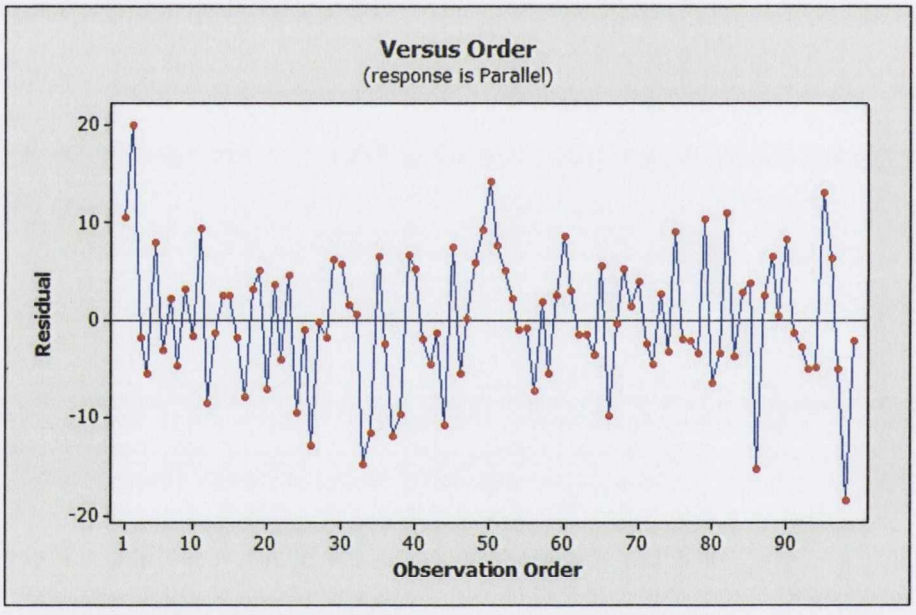

Figure 2.64: Example of residuals vs observation order plot.

2.9.2 Analysis of variance (ANOVA)

Variance is defined as the square of the standard deviation associated with a mean of several measurements [184]. Analysis of variance (ANOVA) is a statistically based, objective, decision-making tool [114]. This technique uses tests based on variance ratios to determine whether or not significant differences exist among the means of several groups of observations, where each group follows a normal distribution [185]. In order to understand the ANOVA table it is necessary to understand residuals and how such residuals are obtained, as these values form the basis for calculating the various factors in Table 2.7.

Table 2.7: Example ANOVA Table

Source	*DF*	*SS*	*MS*	*F*	*P*	*PCR*
Variable 1	X	X	X	X	X	X
Variable 2	Degrees of freedom	Sum of squares	Mean squares	F ratio	The p-value	Percentage contribution ratio
Variable 3						
Error						
Total	X	X				

In an ANOVA table, there are a number of techniques which transform basic data points into formal statistical conclusions about the variance associated with a process, these are:

- The degrees of freedom, DF, represent the number of independent observations in a set of data that are available to estimate the parameter in focus from the overall data set from which the observations are drawn. For ANOVA analyses, the degrees of freedom for a specific set is n-1, where n is the number of observations in the set.
- The sums of squares (SS) value is a means by which to assess variation from the mean of a parameter. The SS of a particular source in Table 2.8 takes the square of each residual in the set related to the source term, and computes the sum of those squared values. The calculation of the total sum of squares considers both the sum of squares from the factors and from random chance or error.
- The mean squares (MS) are calculated as the ratio of the SS and DF, thus averaging the variance for each source term.
- The F-ratio is calculated as the ratio of the MS of each individual factor and the MS of the chance variation error, i.e. Error source term. Therefore, the F-ratio represents the average variance of each factor relative to the chance variation in the process. The higher the F-ratio is for a given factor, the more probable it is that the means of the factor levels are statistically significantly different.
- The p-value is a test of the statistical significance of a test statistic, in this case the F-ratio. It represents the probability ($0 < p < 1$) of obtaining an F-ratio, that is at least as large as the calculated F-ratio if the null hypothesis is true.
- The null hypothesis for the ANOVA table is always that the population means, i.e. factor level means, are equal, while the alternative is that at least one is different. Thus, if the p-value is less than the accepted risk level defined for the analysis, typically 5 % or 0.05, the null hypothesis is rejected as the probability is acceptably low.

- Percentage contribution ratio indicates the relative amount of variance a particular source contributes to the process. It is only necessary to consider this number for factors with a p-value < 0.05.

More details of this approach can be found in the reference by Mullins [184].

2.10 Literature review findings

- In terms of damage, there is a significant body of research regarding the mechanical damage mechanisms associated with CFRP machining. However, the sensitivity of the CFRP workpiece to thermal damage during edge trimming remains largely unexplored.
- Previous literature has indicated that thermal degradation in epoxy thermosets can begin at a temperature as low as 270°C, although exposure time is also a key factor. However, recent works have indicated that incipient sub-surface damage can occur when the workpiece temperatures is as low as 120°C. Numerous works have highlighted the sensitivity of polymer matrix material to thermal effects, with little exploration of the phenomenon.
- The primary mechanisms of chip formation in CFRP milling have been found to be matrix fracture and polymer shearing, producing extremely small chip sections in stark contrast to metal cutting material removal theory. It is also noted that there is potentially a significantly different heat partition ratio in CFRP machining compared to metal cutting, with a larger portion of heat dissipating into the workpiece.
- Previous works investigating milling used lower speeds of 28 – 110 m/min for a carbide tool. It is noted that the tool material has a large role in defining the optimal machining parameters, with PCD tools allowing for a higher cutting speed to be realised for the same quality. Previous literature also states that feed rate has a higher influence on cutting forces than cutting speed for FRP materials. Industry recommended cutting parameters are typically used in the literature for comparison.
- Temperature measurement techniques used in machining previously include thermal imaging, two-colour pyrometers, dynamic thermocouples and thin film thermocouples. The majority of investigations appear to monitor the temperature of the tool at the interface, while some infer the interface temperature through inverse techniques. Of the techniques mentioned, telemetric embedded thermocouples, micro-thermal imaging and two-colour pyrometry with coupled fibres appear to show the most potential for temperature process monitoring which do not destructively interfere with the process. Of these methods, the telemetric embedded thermocouple technique provides a potentially robust, repeatable alternative in conjunction with a method by which to iteratively determine the surface temperature.
- Although the literature suggests that techniques have been used in order to enhance the perception regarding the temperature response of a sensor during machining processes, the area of heat flux shape functions, i.e. the time-series magnitude of the heat flux associated with the cutting process, remains relatively unexplored. An

understanding the heat flux shape function at the cutting interface is fundamental to viewing a machining process as a thermal system, particularly when dealing with thermally sensitive workpiece materials, such as polymer-based composites.

- Literature suggests that surface roughness measurement performed on CFRP machined surfaces are typically done with stylus profilometer contacting the workpiece. It has been found that R_Z is more adept than R_A at distinguishing surface profiles of different fibre orientations and quantifying micro geometric variations such as fibre pull-out., however, it is stated by numerous authors that non-contact methods provide significant advantage in terms of accuracy and ease of use. The primary reason for the use of stylus based methods is cost, with WLI and MeX introducing significant expenditure. The best results appear to be achieved through the validation of surface roughness values obtained, either by SEM investigation or 3D profile generation.

3 INTEGRATED TELEMETRIC TEMPERATURE SENSOR CHARACTERISATION

As a result of a review of previous studies, the design of a sensor which incorporates the embedded thermocouple, in conjunction with the transmission of wireless signals, becomes the focus of this research. The sensor used was developed by ACTARUS. This design incorporates all transmission modules on the tool and tool holder section of the rotating system. The goal of this design was the measurement of tool temperature during milling operations at high speed spindle frequencies. [158]

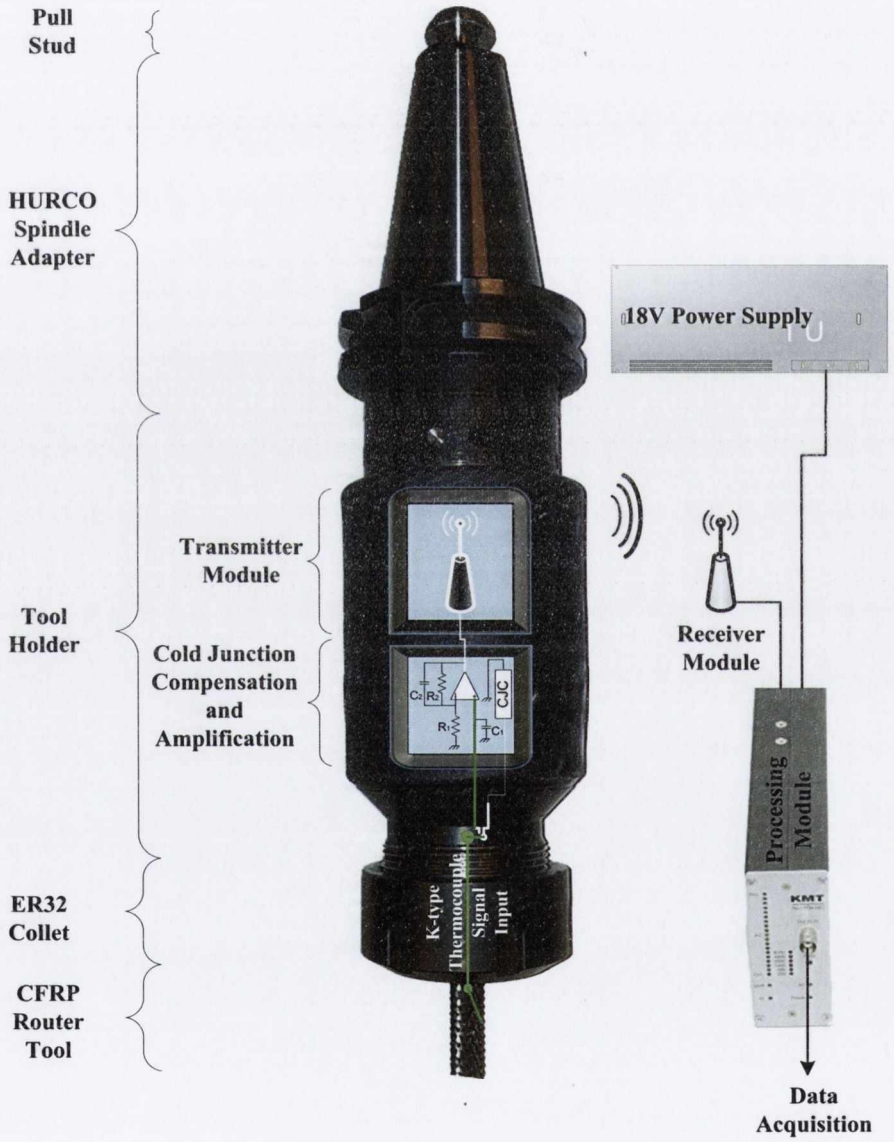

Figure 3.1: Telemetry system and components required to deliver thermocouple signals from the cutting tool to DAQ.

3.1 Sensor design

3.1.1 Wireless temperature via inductance

The components of the wireless telemetry system which enable the transmission of voltage, produced by way of the Seebeck effect, from a spindle and tool rotating at speeds of up to 10,000 rpm are outlined in Figure 3.1. The principle components of this telemetric transmission design are:

- Signal input and conditioning
- Transmission module
- Receiver Antenna module
- Processing module

As described in Figure 3.2, the signal received from the input thermocouple sensor embedded in the tool is connected to an electronic thermocouple module embedded into the tool holder. This module performs cold junction compensation as well as amplification and filtering of the analogue voltage signal.

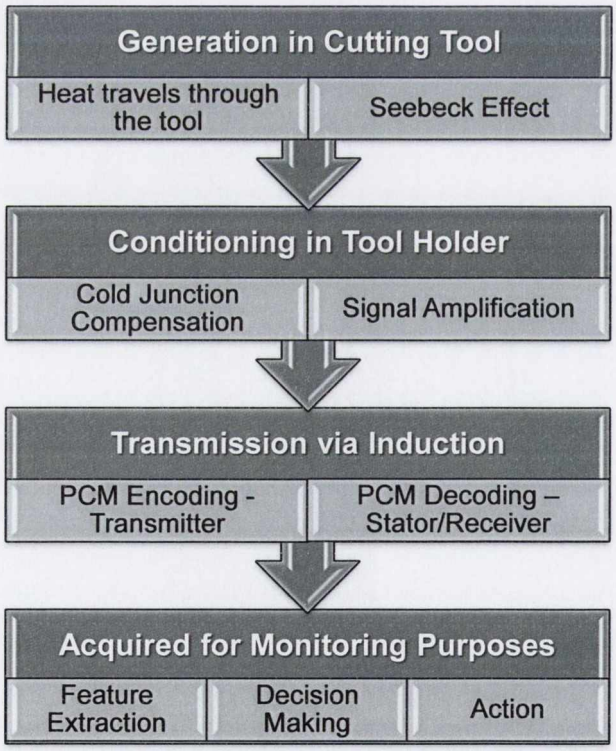

Figure 3.2: Flow diagram of the ITT sensor signal transmission route from heat source through to DAQ system.

The signal is then sent to a transmission (ADC) module which converts the analogue signal to a digital pulse code modulated (PCM) representative signal. This digital signal is

conveyed to an induction coil which transmits the voltage signal to the stator. An electromagnetic coil formed from 10 wraps of 0.5 mm copper wire wound around the tool holder shaft acted as the transmitter. Ferrite tape was used to isolate the magnetic field between the shaft and coil in combination with mounting tape. Power is supplied inductively to the transmission modules from the stator. The repeatability of the current wireless transmission system was investigated by Le Coz *et al.* [158] indicating that the dispersion of temperature values was lower than ± 2% in milling. For all sensor applications, the stator distance from the induction coil was fixed at 15mm.

3.1.2 Tool embedded thermocouple

The core of the temperature measuring sensor is a grounded k-type thermocouple (TC), consisting of a nickel-10%-Chromium (+) and Nickel-5%-Aluminium (-) wires, embedded within an 8 mm solid carbide cutting tool. The k-type TC was selected due to its linearity over a large temperature range, from 0°C - 1200°C. The diameter of the thermocouple used is 0.2mm and the nominal rated response is approximately 20ms. The TC is embedded as shown in Figure 3.3 with a precise 0.6mm groove bored into the cutting tool for TC insertion up to a distance of 0.5 mm away from the base of the cutting edge as depicted in Figure 3.3. The path for the insulated TC wires into the transmission module is facilitated by a 1mm channel along the edge of the tool length. The thermocouple was fixed into position using a thermally conductive adhesive material similar in conductance to tungsten carbide. A customised CAPTO C5 tool holder (adapted to fit a HURCO CAT40 spindle) was used to allow access for the TC and accommodate the signal conditioning and transmission module and components.

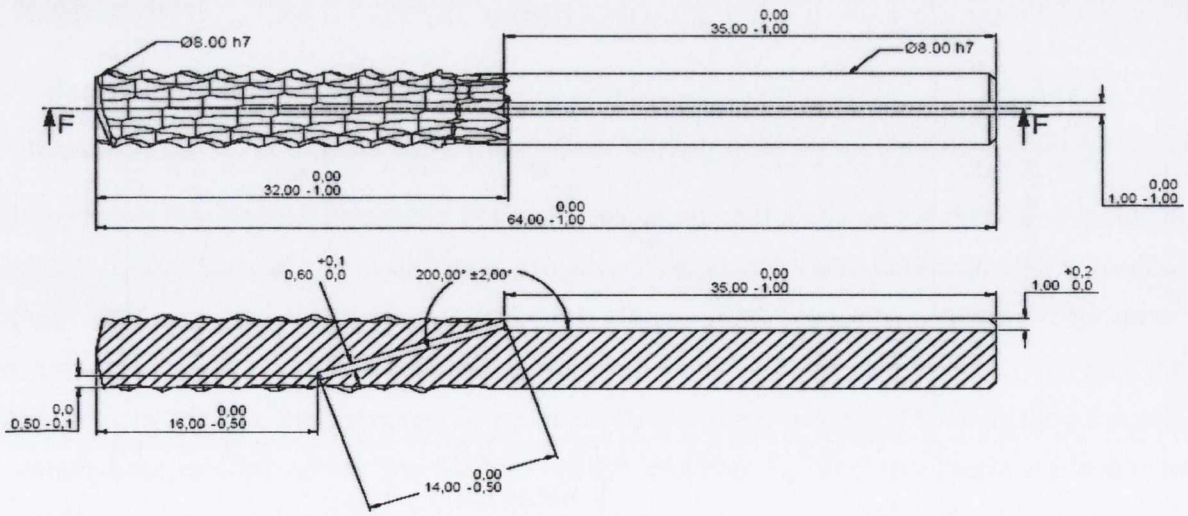

Figure 3.3: Thermocouple embedded position within the CFRP deburring tool.

3.2 Static response and system calibration

In order to begin a full system calibration, the ITT system was connected to an NI DAQ system with a customized LabVIEW program used to control data entry rates during calibration. The system calibration was performed using a highly accurate temperature calibration dry block having a certified uncertainty of 0.02°C over the range of 0°C < T < 600°C.

The tool was submerged quickly into the dry block, containing conductive, heated oil with a flash temperature of 230°C. For each temperature set point in the calibration, the dynamic response of the ITT sensor was recorded. The measurement chain was initiated just prior to the tool surface making contact with the hot oil, as the sensor was moved into position in the dry block. Measurements were acquired over a period of ten minutes in order to ensure steady state results.

The sensitivity of the ITT sensor system under steady state can be calculated as the slope of the linear transfer function relating input response voltage to output calibrated temperature. In this case, the slope is shown in Figure 3.4, representing a sensitivity of approximately 154μV/°C for temperatures in the range of 20°C to 175°C. This is in comparison to a typical sensitivity value for a bare wire k-type thermocouple of 41 μV/°C. It should be noted, however, that in this case the sensitivity of the thermocouple is based on a post-amplification voltage signal, amplified in the electronic module housed in the tool holder prior to wireless transmission. This amplification provides an enhanced resolution to the sensor since it is incorporated into the system calibration of the ITT sensor.

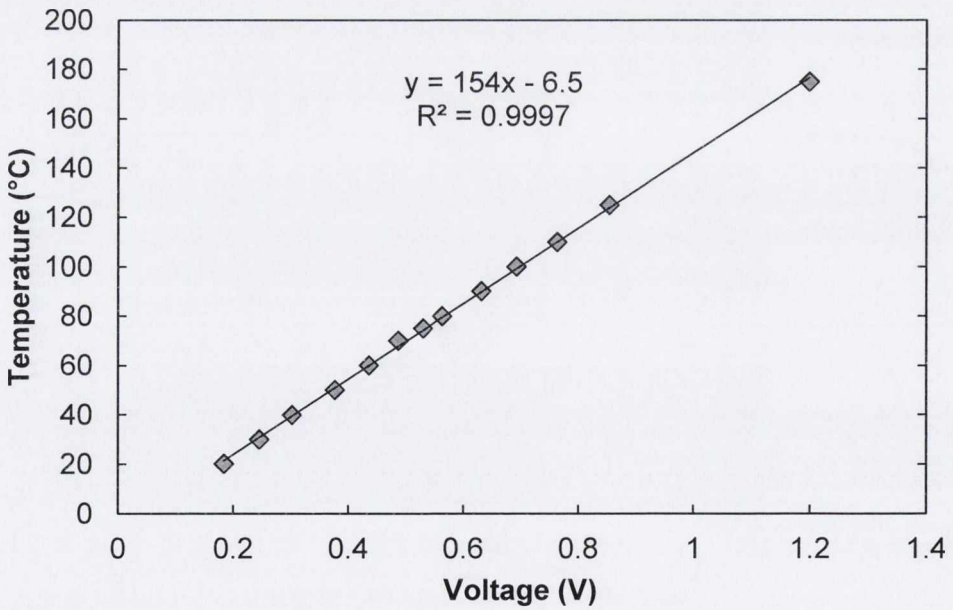

Figure 3.4: Calibration curve of the ITT sensor for steady state conditions.

3.3 Dynamic calibration of the ITT sensor

Fundamentally, all sensors used to produce an electrical response from an input stimulus have a specific response-stimulus relationship. This relationship is dependent upon a number of factors associated with the transfer of energy from the hot body to the sensor. While the steady-state calibration provides an indication of the sensor response when energy exchange becomes negligible, alternative methods must be used to represent the sensor in a dynamic measurement capacity. Some insight of how to obtain an accurate perception of the sensor response in a dynamic, transient thermal environment may be obtained by idealising the system.

In order to determine what affects the accuracy of a temperature measurement, consider the ITT sensor as illustrated in Figure 3.6, where the green dot of the sensor comprises all ITT sensor components. This includes a significant thermal mass in the form of the tungsten carbide of the cutting tool and TC connection material between the point of measurement at the thermocouple head/junction and the cutting zone, where the temperature is generated.

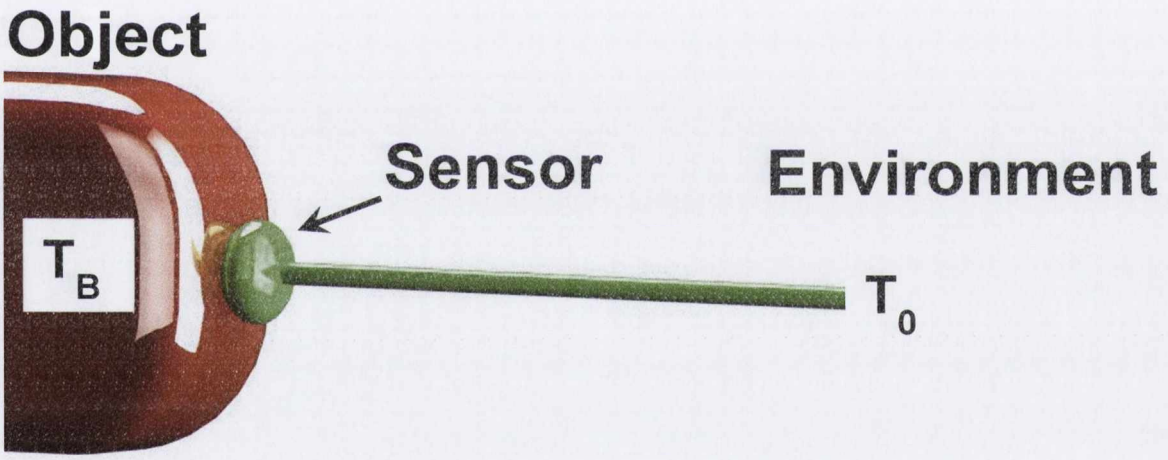

Figure 3.5: Fundamental perspective of thermocouple sensor. A hot body at temperature T_b, in contact with the sensor surrounded by an environment at T_0.

Considering the idealised scenario of Figure 3.5 as an analogous circuit diagram, shown in Figure 3.6, key sections of resistance are identified in the heat flow path from source, through sensor to acquisition hardware for the steady state case. For a steady state case, the amount of heat energy transferred between the hot body, at temperature, T_B, and the thermocouple head at temperature, T_S, is limited by two main factors. These include the rate at which heat energy enters the system, which dictates T_B, and the thermal resistance between sensor and hot body for a steady state case, r_1. Additionally, the system is controlled by the resistance between the sensor and the external environment, r_2. Assuming a steady state scenario, the law of conservation may be applied to this thermal circuit

diagram, whereby the energy transferred from hot body to sensor is equal to the energy transferred from sensor to environment. This results in Equation 3.1:

$$\frac{T_B - T_S}{r_1} = \frac{T_B - T_0}{r_1 + r_2} \qquad \textbf{3.1}$$

Where T_0 is the temperature of the external environment.

This can be rearranged to show the temperature at the sensor for this basic first-order system, as shown in Equation 3.2. From this equation it can be concluded that after the step input is initiated, i.e. after $T_B > T_0$ there will be a difference between the temperature perceived by the sensor and the actual temperature of the hot body. However, such an error can be minimised by reducing the thermal resistance between the sensor and hot body, and maximising the resistance between the sensor and environment.

$$T_S = T_S - (T_B - T_0) \cdot \left(\frac{r_1}{r_2}\right) = T_B - \Delta T \left(\frac{r_1}{r_2}\right) \qquad \textbf{3.2}$$

The design of the current ITT sensor has some inherent resistance associated with the presence of the tool material between the hot body, i.e. the cutting interface. However, the fact that the sensor is embedded and completely surrounded by the tool material increases the thermal resistance with the external environment.

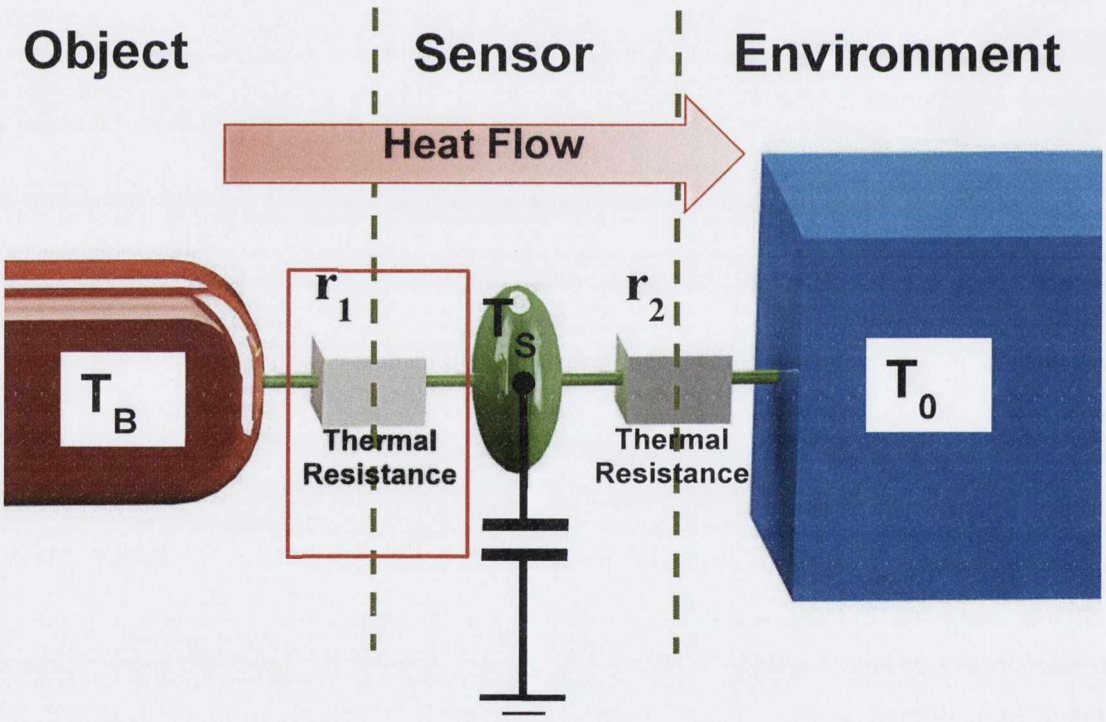

Figure 3.6: A circuit diagram of the ITT sensor with a thermal resistance (r1) between the hot body and sensor and (r2) between the sensor and surrounding conditions.

At this point it is important to consider two heat properties, thermal resistance and thermal impedance. Both of these properties are configuration- and geometry-specific and can

change with material properties and cutting interface interaction variations. Thermal resistance is defined as the ratio between the difference in temperature between two closed isotherms and the total heat flow between them. Thermal impedance is defined as the ratio between two closed isotherms and the heat flow entering the hotter of the two surfaces. Thus thermal impedance is simply thermal resistance without the condition of equal heat flux across both isotherms, i.e. non-steady-state conditions.

For a dynamic conductive boundary between a bulk object transferring thermal energy to a sensor, combining Newton's law of cooling and the specific heat equation produces:

$$dQ = \alpha(T_B - T_S)dt = m \cdot c \cdot dT \qquad \textbf{3.3}$$

Where *m,* the sensor's mass and, *c,* the sensor's specific heat properties are assumed as average values for the sensor. Hence, the heat absorbed by the sensor can be expressed mathematically as the solution to the first order differential equation above as:

$$T_S = T_B - \Delta T\left(e^{-t/\tau_t}\right) \qquad \textbf{3.4}$$

In Equation 3.4, τ_t represents the time constant of the sensor. The time constant for this sensor, based on a unit step input at $t = 0$ for a first-order system, was defined as 63.2% of ΔT, the initial gradient between T_B and T_1. The time constant represents the time taken for the sensor's response to a step input to reach Assumptions for Equation 3.4 to hold are:

- Thermal resistance between the sensor and the environment is infinitely large.
- The object's temperature does not change after the sensor is attached (infinite heat source).

A simple dynamic experiment, in which the ITT sensor system was dunked into a hot oil bath, was performed. The time constant was obtained from this experiment in order to compare the sensor's behaviour to 1st order response theory. Using the experimental setup from the static system calibration described previously, the ITT signal responses were scrutinised for a range of set point temperatures, T_B. Comparing the response of the ITT sensor during these tests with theory indicates an under-performance by the sensor in experiments in achieving bulk temperature, as indicated in Figure 3.7.

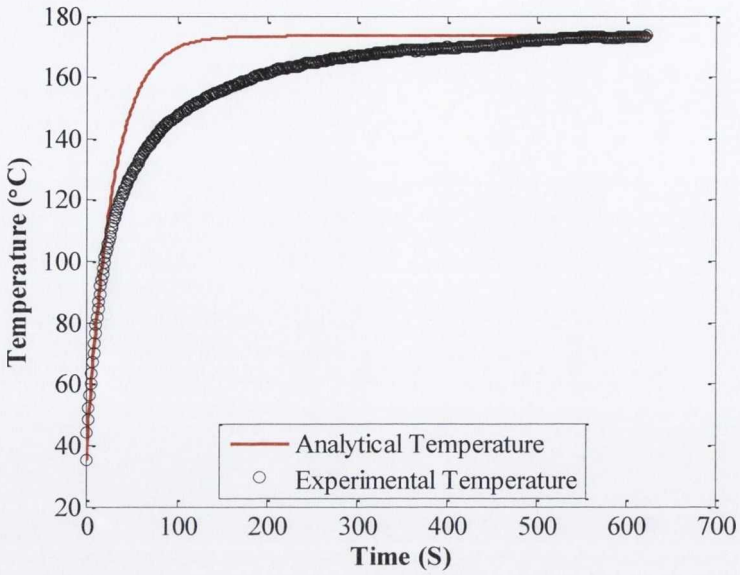

Figure 3.7: Comparison of analytical and experimental response of ITT sensor for a bulk temperature, T_B, of 175°C.

The difference in dynamic response of experimental and analytical results is partially due to the additional thermal resistance added by the tool material, which separates the TC head from the infinite heat source resulting in a time constant in the range 25.2 sec < τ_T < 27.9 sec for a temperature range of 20°C < T_B < 175°C. The response delay is also noted by Rittel, [186], to be due to the liquid-solid interface through which heat transfer must occur in the dipping experiment. The author states that much faster responses are possible for thermocouples embedded in simple solid geometries.

Rabin and Rittel [187] showed that while a thermocouple immersed in a liquid produces an approximately first-order transient response, the response of a thermocouple embedded within a solid material, as is the case of the ITT sensor, "...is far from being similar to that of a first order process." Therefore, further experimental and theoretical investigations were required in order to develop an understanding of a sensor located within a complex geometry under alternative heat input boundary conditions.

The need to understand the dynamic behaviour of the ITT sensor becomes more obvious after investigations into the CFRP machining process performed using the ITT sensor in conjunction with a force sensor. The measurements from the two sensors were acquired simultaneously using a NI PXI DAQ system. Measuring the force and temperature at the same time allowed for an illustration of how the cutting process works, with force being a result of the interaction between workpiece and tool, and temperature being a somewhat unfavourable energy by-product of such forces and friction associated with the cutting interaction. The process of identifying the behaviour of the temperature sensor during a cutting process is outlined in Figure 3.8.

Through this process, an important behaviour of the sensor, **lag**, was identified, in addition to **damping**, which was previously identified. The question following the discovery of such a lag was,

"Can the information from this lagged, damped sensor be used to obtain an accurate history of the tool temperature at the cutting interface?"

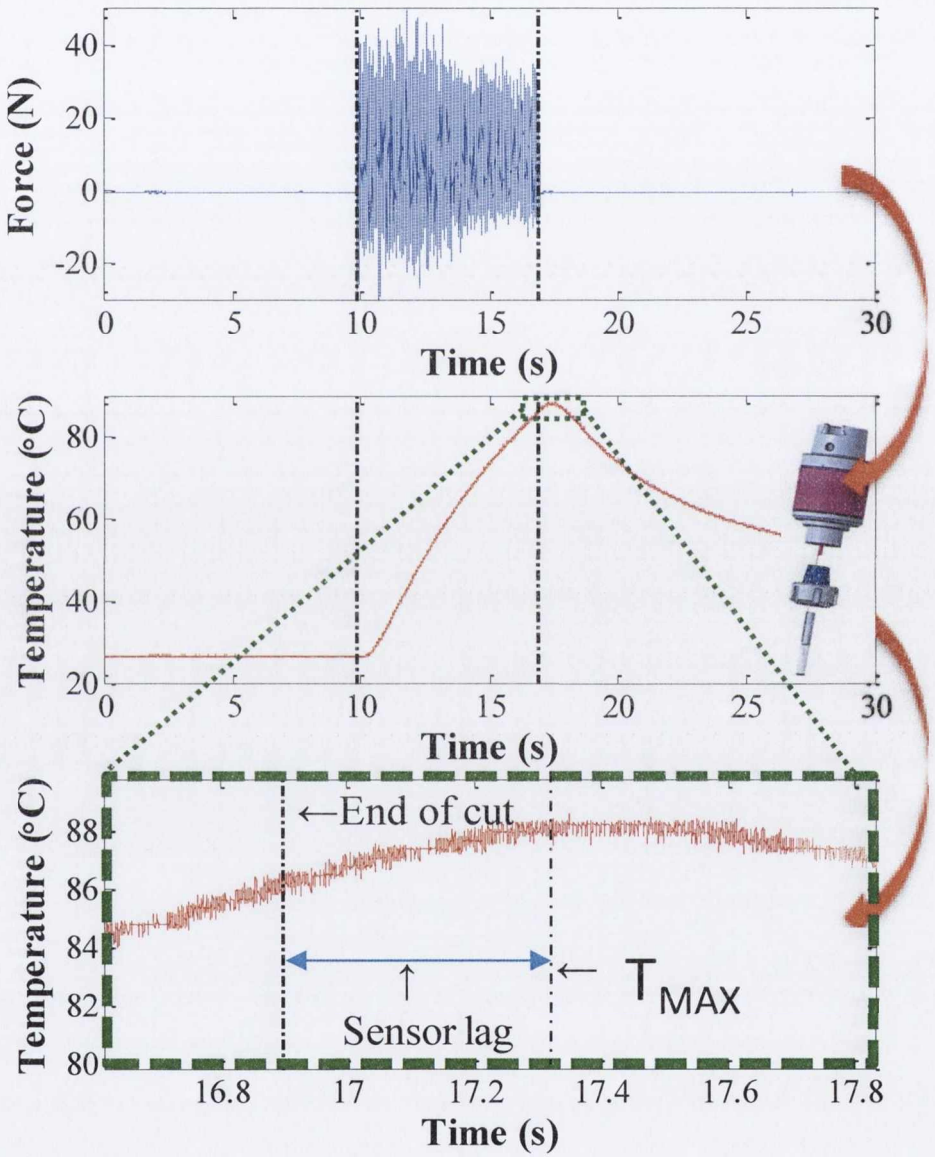

Figure 3.8: Signal Processing Methodology (Top) Force sensor locates the time series of cut, (Middle) Relevant temperature signal extracted and (Bottom) Key feature identified - Lag.

To answer this question, two paths of research were explored with the aim of complimentary results supporting an advanced sensorial perspective on the ITT sensor response:

- A ***cutting tool 3D finite element (FE) analysis*** was performed on the specific tool geometry used in this research. The model was developed to ensure accurate thermal behaviour with mesh-independent and time step-appropriate solutions. The aim of this model was to effectively solve for the heat flux and tool temperature at the cutting junction by matching the results of the simulation to the ITT sensor results obtained during the edge trimming of CFRP composites.
- An ***analogous heat flux*** experiment was setup in which a diode laser became the heat source and a portable rotary station was used to accommodate the ITT sensor and simulate the rotating milling tool as per the edge trimming operation. This use of a known heat flux provides a validation experiment for the FE model aimed towards closing the gap between the ITT sensor response and the actual tool surface temperature.

A comprehensive understanding of the heat transfer process through the cutting tool is essential as this provides the basis by which the ITT sensor acquires thermal data to monitor the process. The use of FE methods to understand heat transfer applications, particularly in machining, is well documented [188, 189] and provides a cost-effective method by which to understand the influence of specific parameters on the thermal behaviour of the system.

From preliminary dynamic calibration experiments, using impinging heated jets, it was discovered that there is a significantly lower temperature recorded at the ITT sensor than by a sensor at the surface of the tool. This is illustrated in Figure 3.9. This amplitude ***damping*** effect must be characterised precisely using a controlled, accurately known heat flux value, to determine the actual tool surface temperature. Once experimental values in a range appropriate for CFRP machining have been obtained, i.e. up to 200°C, the parameters can be used in conjunction with FE methods to more comprehensively characterise the sensorial behaviour and perception. Additionally, such controlled experiments allow for a validation of the FE model by tracking the temperature at the surface and ITT sensor tip locations and comparing with experimental values.

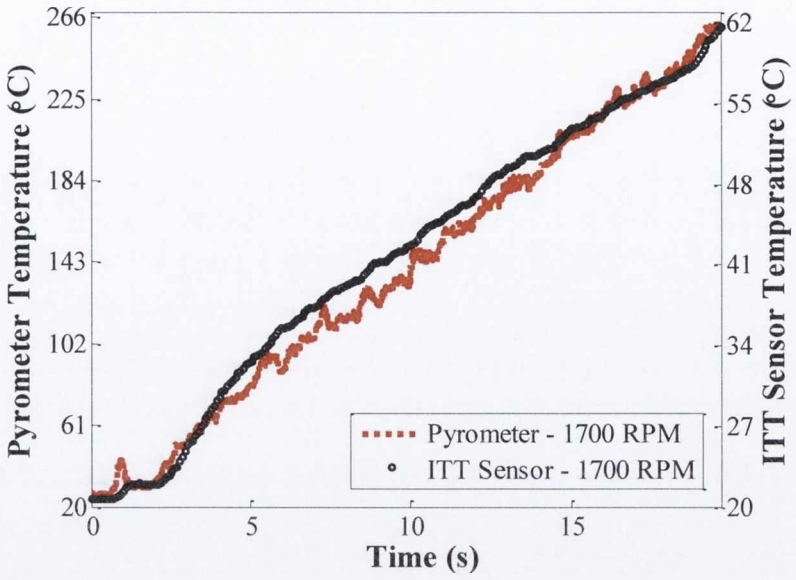

Figure 3.9: Approximate comparison between the surface temperature and ITT sensor temperature measured simultaneously.

3.4 Cutting tool 3D finite element modelling and analysis

In order to fully utilise the ITT sensor's capabilities, a more detailed understanding of the transient conductive behaviour of the tool was undertaken to obtain useful information such as the heat flux during cutting and a 3D temperature profile for a variety of parameters. Finite element analysis (FEA) is commonly used to achieve such an understanding. FEA is a numerical tool that allows for a discretised parametric model to be built and solved for a range of parameter variations up to a desired level of accuracy. As described by Bickford, [190], the finite element method should use several distinct steps:

1. **Discretisation**: generation of an approximate, segmented, discrete model of the real, continuous model.
2. **Interpolation**: replacing the physical model with appropriate, discrete portions, e.g. replacing the continuously distributed elastic properties by linear springs.
3. **Elemental description or formulation**: The mathematical relationship governing the mechanical effect to be solved for, e.g. Fourier's law for conduction.
4. **Assembly**: formation of *global* matrices which includes all of the elemental matrices for a particular physical parameter associated with the analysis, e.g. elemental conductivity matrices are assembled into global conductivity matrix. System equations can then be generated to for governing equations.

5. **Constraints**: application of specific conditions at the global boundary of the discrete model, e.g. prescribed temperature or heat flux at a boundary.
6. **Solution**: Solves the constrained assembly or system of equations matrices associated with the analysis, e.g. for conduction analyses, solves for the elemental temperatures.
7. **Computation of derived variables**: Apply governing equations to calculate further variables at each element, e.g. using Fourier's Law to calculate the fluxes from the temperature gradients of each element.

Ultimately, the model should be developed so as to produce sensible results and reduce computational time. ANSYS FEA software was used to perform simulations for this works. As some of the steps mentioned above are implicit with the nature of the software setup, which uses pre-processing, processing and post-processing phases, summary steps used to build the FEA are described in Figure 3.10.

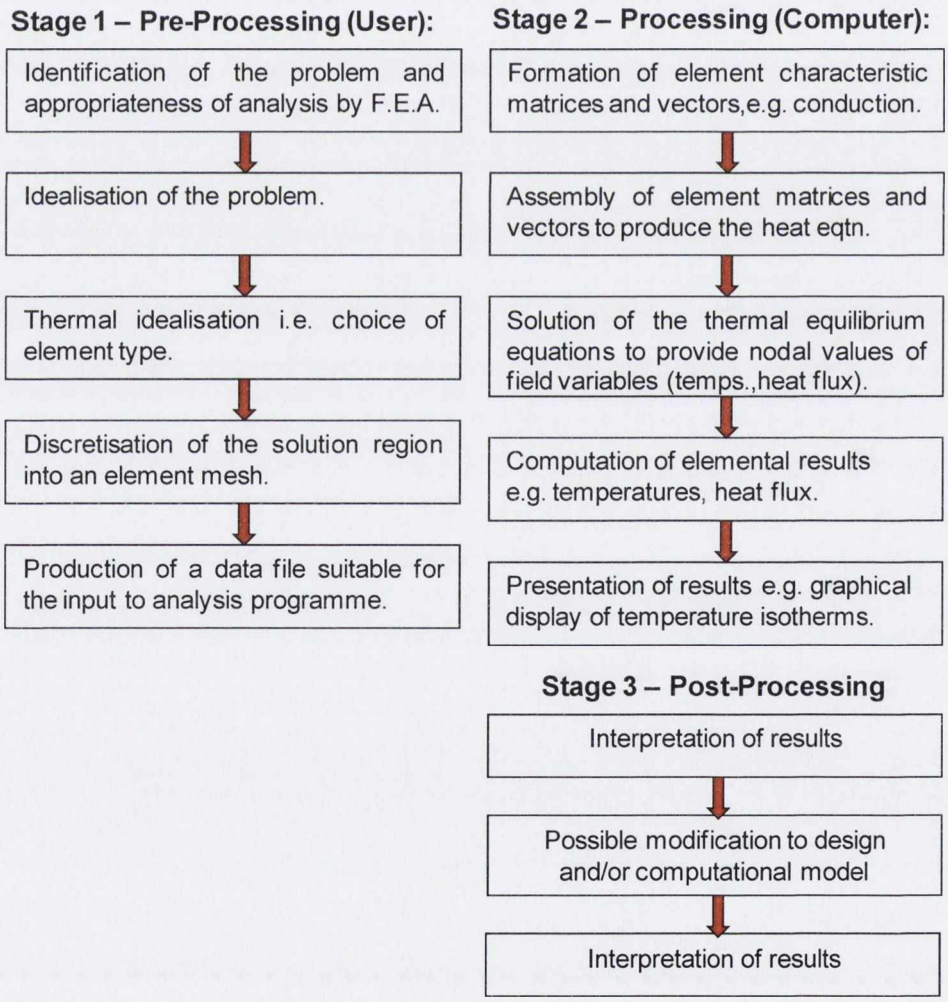

Figure 3.10: Basic stages in the finite element method

In the current investigation, due to the complexity of the tool geometry and the nature of the process, the eventual FE model used was a three-dimensional transient thermal analysis. The overall goal of this chapter is to *recreate* the temperature curve achieved by the ITT sensor during the cutting process and the analogous laser-driven constant heat flux experiments, thus inferring both a surface tool temperature and a tool-side heat flux value for the process. As this is a highly complex physical process, numerous variables need to be included into the model, such as:

- Thermal properties
- Boundary conditions
- Mesh dependencies
- Heat sink contact conduction

Such variables were introduced in phases. The incremental development stages of the FE model of the ITT sensor are therefore discussed in the following sections.

3.4.1 Simplified cylinder with 1-D radial conduction

Since the ultimate goal of this analysis was to approximate a surface temperature and heat flux, based on a temperature radially and axially removed from the source of heat, a number of advancing steps were used to arrive at the final, complex FE modelled solution. The introductory investigation involved a simplified conduction model to assess only radial isotherms of a cylinder as shown in Figure 3.11.

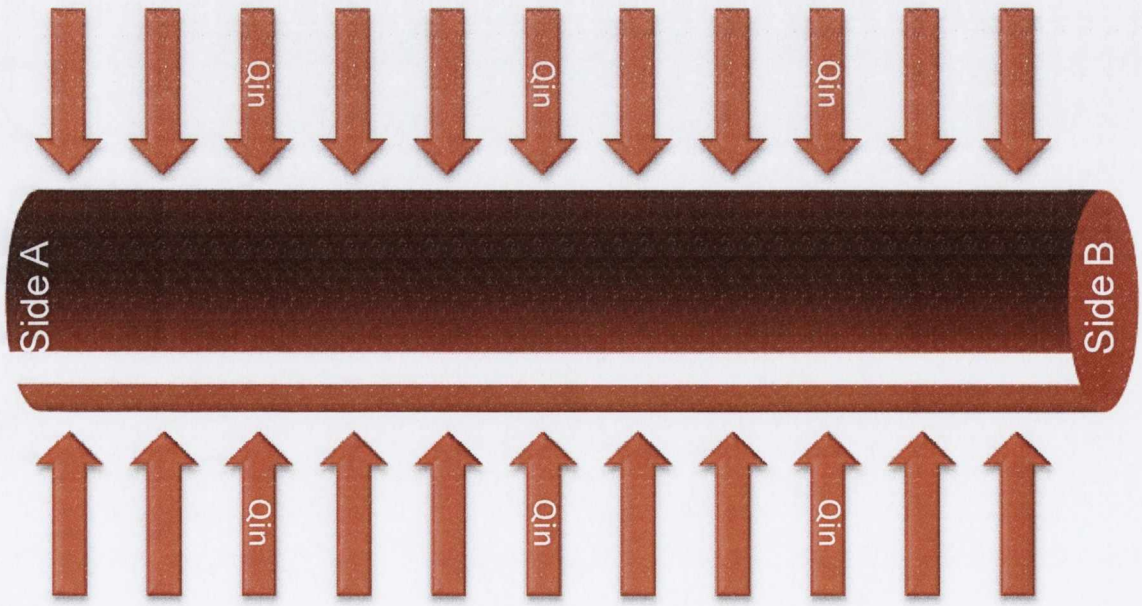

Figure 3.11: Simplified model and boundary conditions used to consider only radial conduction through a cylinder.

In this case, the problem appears to be a two-dimensional setup in the cylindrical co-ordinate system, with both radial and axial conduction possible. However, by making the assumptions that sides A and B are isolated, it is possible to turn this into a one-dimensional scenario which can be solved using analytical methods for comparison.

Pre-Processing Phase

In this phase, the cylinder was modelled with dimensions and material properties in-line with the actual tool under investigation. Element types appropriate for thermal analysis were used and the mesh was controlled by the line segment method. The first type of element, PLANE55 is a 2D plane element with four nodes with a single temperature degree of freedom at each node. The remaining elements in the model were generated from SOLID278 nodes, which are extruded 3D elements each containing eight nodes, with a single degree of freedom, temperature, at each node. In this basic cylinder model, the size of mesh elements was controlled via the use of line divisions. For radial lines, a division size of 0.25mm was used, while a division size of 0.5mm was set to divide the 60mm length of the cylinder. This resulted in 115,797 elements being generated for this 3D model. Details of the parameters used for these steps are shown in Table 3.1. A custom-built modelling tool was developed, using ANSYS APDL code, as described in Appendix 4, to allow for parametric-based analysis to be performed both for sensitivity purposes and so as to investigate key variables once the most appropriate, realistic model had been built.

Table 3.1: Summary data – Cylinder with 1-D radial conduction analysis

Analysis type	**Transient thermal on cylinder**
Geometry	Cylinder
Length (m)	0.06
Radius (m)	0.008
Material properties	Tungsten Carbide (WC)
Density (kg / m^3)	15630
Specific heat (J / kg K)	258
Thermal conductivity (W / m K)	84
Element type	
Areas	PLANE55
Volumes	SOLID278

The mesh for this problem is displayed in Figure 3.12. The line segment size chosen was based on a sensitivity analysis, performed to ensure that the resultant temperature variations between simulations were less than 1.5%.

The heat flux values selected for this phase of modelling were based on approximate laser power values that would be associated with the validation phase to be described in section

1.1. The expected laser power required in order to achieve surface temperatures of between 40°C and 250°C was between 10W and 100W.These values were obtained during a preliminary trial on the laser. In this trial a thermocouple attached to the surface of a static tool, onto which the laser energy was radiated, generated the temperature data. Based on an approximation of the laser spot size and tool circumference, the resulting heat flux values used for the FE simulations are presented in Table 3.2.

Table 3.2: Heat flux calculations for FE simulations

Laser spot thickness (m)	Tool circumference - arc length (m)	Laser contact area (m^2)	Heat power applied (W)	Heat flux (kW/m^2)
0.001	0.0251	2.51E-05	10	397
0.001	0.0251	2.51E-05	50	2000
0.001	0.0251	2.51E-05	100	4000

Figure 3.12: Discretisation process with (left) areal mesh and (right) volumetric sweep of the areal mesh across the model length.

The governing 3D heat diffusion equation was solved during FE analysis, which is represented in Cartesian co-ordinates as:

$$\frac{\partial^2 T}{\partial x^2}+\frac{\partial^2 T}{\partial y^2}+\frac{\partial^2 T}{\partial z^2}=\frac{\rho C_p}{k}\cdot\frac{\partial T}{\partial t} \qquad \textbf{3.5}$$

Where T is the temperature (°C), k is the thermal conductivity (W / m K), ρ is the density (kg / m^3) and C_p is the specific heat (J / kg K).

The initial condition is:

$$T(x,y,z,0)=T_\infty \qquad \textbf{3.6}$$

Where the ambient temperature, T_∞, was set to 20°C.

The boundary condition for the region where heat flux is applied as a result of the interaction between tool and CFRP is represented by:

$$\dot{q}_{in} = -k\frac{\partial T}{\partial n} \qquad \textbf{3.7}$$

Where $\dot{q}_{in}$ is the heat flux representing the energy generated as a result of the cutting process which is proportional to the rate of change of temperature with respect to time in a given direction, n. The range of heat flux values explored in this model was 397 < $\dot{q_{in}}$<4000 kW/m^2

All other surfaces of the model were given the adiabatic boundary condition:

$$k\frac{\partial T}{\partial n} = 0 \qquad \textbf{3.8}$$

Solution phase

The analysis type was set as transient thermal in order to investigate the conduction through the model over time. Two load steps were used for this analysis. An initialisation time step of 0.001 s was used to set the initial boundary conditions of the model. For this first time step, only 5 sub-steps were used as this was found to be sufficient to obtain an accurate solution. The second time step was set to 0.3 s to investigate the initial transient effect on radial isotherm profile and compare to analytical results. The constant heat flux was stepped rather than ramped. For the latter time step, 20 sub steps were used to ensure a high degree of precision in the solution and to guarantee convergence.

The system of equations solved at each sub step within each time step is detailed in the ANSYS APDL user manual. The summary of this procedure is that it is based on using the temperature derivatives at each location in the spacial and temporal domain, the thermal gradients at each integration point can be determined by replacing the vector operator with a shape function derivative matrix which is then evaluated at each integration point.

The sparse matrix direct solver in ANSYS was used for this analysis in the in-core memory mode due to sufficient memory availability. This solver is based on a direct elimination of equations, as opposed to iterative solvers, where the solution is obtained through an iterative process that successively refines an initial guess to a solution that is within an acceptable tolerance of the exact solution. In this particular analysis there were 122,210 equations solved. Direct elimination requires the factorization of an initial very sparse linear system of equations into a lower triangular matrix followed by forward and backward substitution using this triangular system. The space required for the lower triangular matrix factors is typically much more than the initial assembled sparse matrix, hence the large disk or in-core memory requirements for direct methods. Sparse direct solvers seek to minimize the cost of factorizing the matrix as well as the size of the factor using sophisticated equation reordering strategies.

Post processing

Figure 3.13 displays the results of the transient FE analysis for a period of 0.3 s. From this figure it is clear that the surface has achieved a constant, uniform temperature, whereas there exists a thermal gradient of approximately 10°C for an applied heat flux of approximately 0.4 W/mm^2. The results of the comparison between the analytical modelling work, in Appendix 3, and the finite element simulations are presented in Figure 3.14. One of the key features highlighted in Figure 3.14 is the difference appearing between the surface temperature and the temperature at even a relatively small radial distance from the cutting surface, i.e. 0.5mm below the surface – where the ITT sensor is placed. This is also shown in contour plot form in Figure 3.13. There is good agreement between the data from both

analytical and FEA indicating that the correct boundary conditions were applied and the system behaviour is well defined by the developed FE model for the 1-D conduction case.

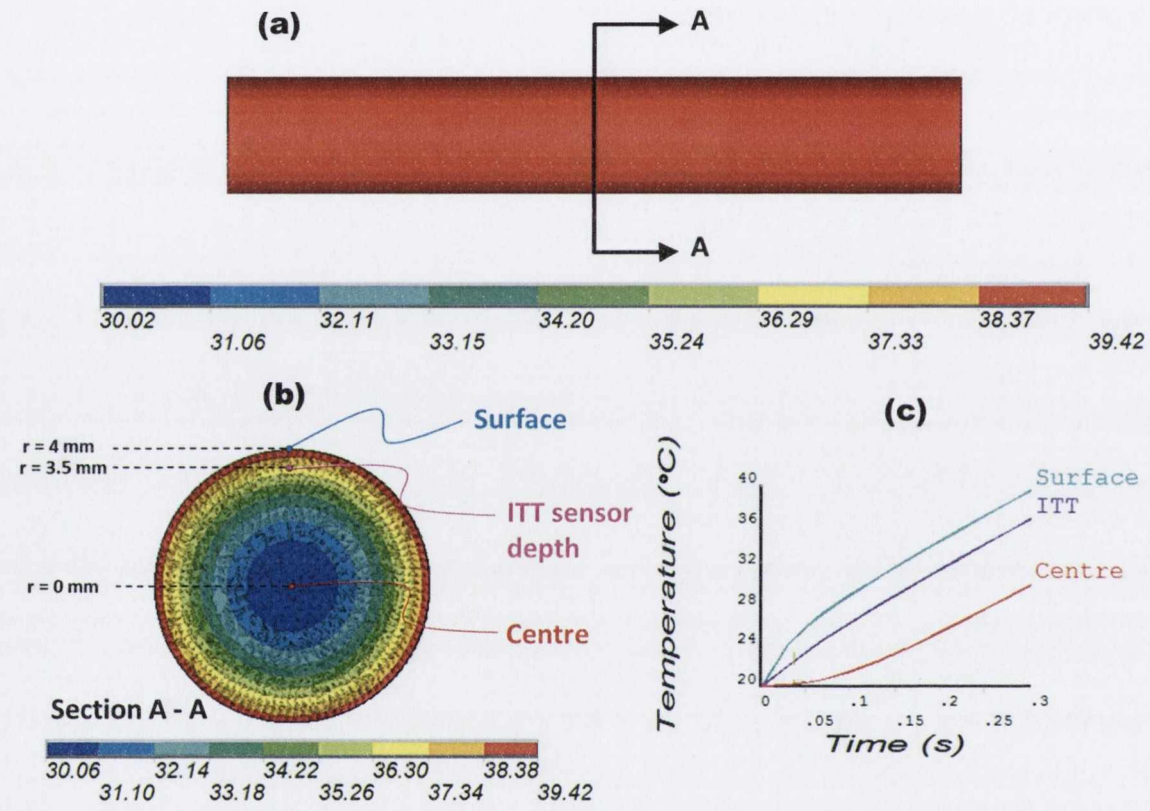

Figure 3.13: Results for FE analysis of a WC cylinder after 0.3 s of 397 kW/m^2 heat flux showing (a) contour plot of the uniform axial temperature profile, (b) contour plot of the concentric variability in the radial direction and (c) the time-dependent variation at different points through the radial cross-section.

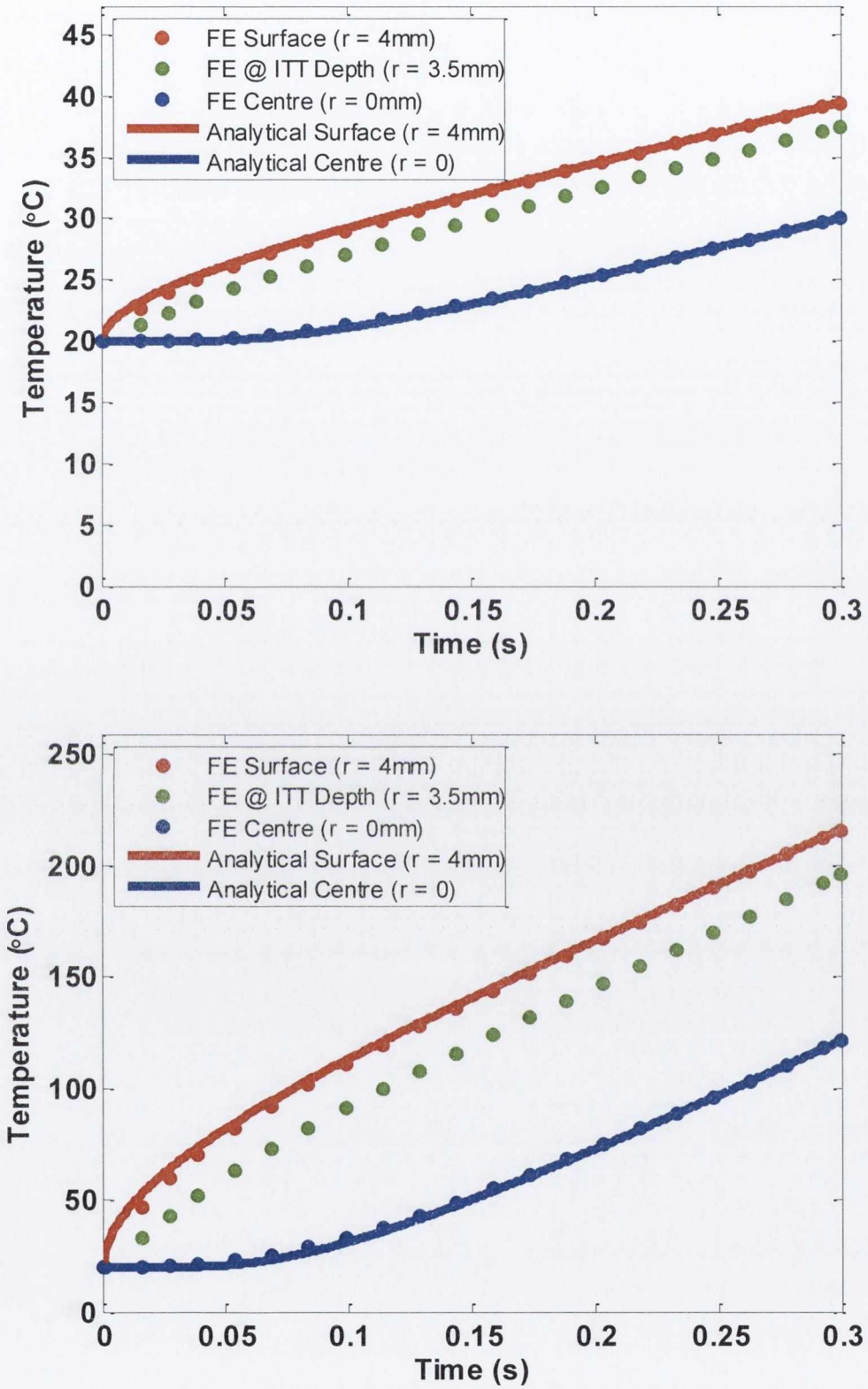

Figure 3.14: Comparative plots of the analytical and FE simulation temperatures in the initial phase of heating of 1-D radial conduction cylinder case for a heat flux of (Top) 397 kW/m^2 and (Bottom) 4000 kW/m^2.

Another interesting phenomenon regarding the transient behaviour of the various radial locations is seen in Figure 3.14. While the increase in temperature at the surface and centre of the cylinder follow a natural log and exponential curve function respectively, at the ITT sensor depth there is an approximately linear time-temperature relationship.

Further tests were performed to determine the effect of mesh resolution on the FEA results and whether mesh refinements provided a solution closer to that obtained using the analytical model. The results are illustrated in Figure 3.15 and Figure 3.16. In Figure 3.15, the low resolution mesh incorporated 28,950 elements and produced results to within 1% of the analytical results for $t < 0.1$ s. However, for $0 \text{ s} < t < 0.1$ s, the FE solution deviation from analytical solution increased to approximately 10%. Increasing the number of elements to 115,797 reduced this initial transient deviation between FE and analytical results, as shown in Figure 3.16, to approximately 1.5% which was determined to be an acceptable estimate for a relatively low computation time exercise.

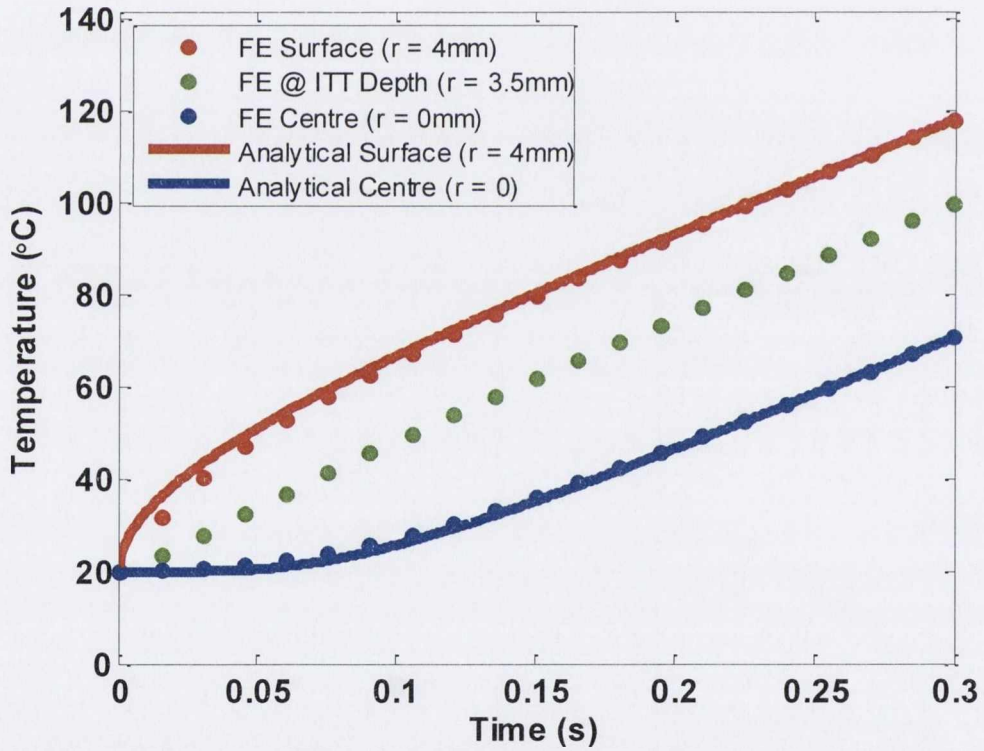

Figure 3.15: Comparative plot using low resolution meshing for numerical computation of the 2000 kW/m^2 case.

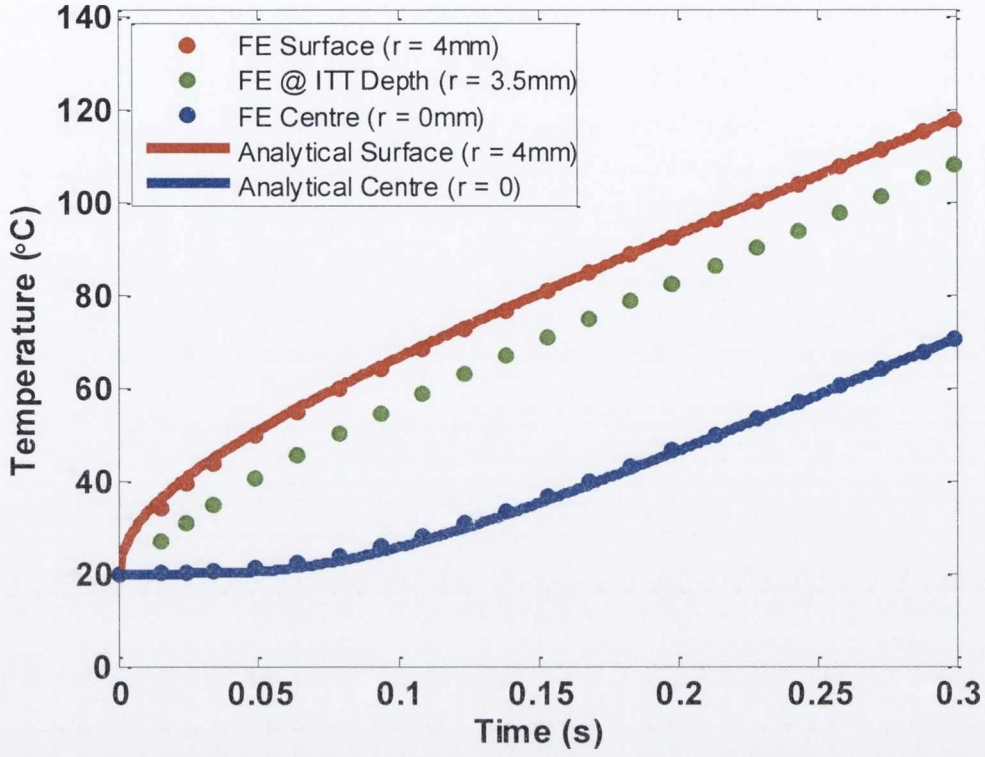

Figure 3.16: Comparative plot using high resolution meshing for numerical computation of the 2000 kW/m^2 case.

3.4.2 Cutting tool geometry

The natural progression from an 'over-simplified' case of 1D conduction in a cylinder is to consider pure conduction through the cutting tool geometry. This cutting tool has a double helix, purposefully designed to ensure asymmetric overlap of cutting edges with the workpiece during heat generation. As a result of this asymmetric geometric design, it is not possible to consider a 2D case and a 3D analysis is therefore a logical step.

Pre-processing phase

The 3D burring router model which represents the ITT sensor system, shown in Figure 3.17, was generated in the 3D solid modelling package, Pro-Engineer Wildfire. The geometry was studied using a Microscope and SEM to obtain geometric values. The .prt file was then imported into the FEA software for analysis. The details of the geometry, elements, materials and mesh are described in Table 3.3.

Figure 3.17: Three-dimensional model of the cutting tool

The mesh, illustrated in Figure 3.18, included high refinement at the heat flux boundaries due to the findings for the simple cylinder and due to the potentially large gradients and small size of the cutting edge. Line controlled refinement was used throughout the model, as determined suitable by a sensitivity analysis similar to that performed for the 1-D simple cylinder case. This resulted in a total of 186,642 elements for the refined model, with approximately 160 elements per pyramidal tooth on the cutting surface. The boundary conditions, also indicated in Figure 3.18, for this analysis were maintained from the previous cylinder analysis, with all external surfaces apart from those at the longitudinal periphery having a constant applied heat flux in the range $397 < q < 4000$.

Table 3.3: Summary Data – ITT cutting tool radial conduction only analysis

Analysis Type	*Transient Thermal on ITT Geometry*
Geometry	ITT Cutting Tool
Length (m)	0.06
Radius (m)	0.008
No. of positive helices	13
Positive Helix Pitch (°)	30
No. of negative helices	10
Negative Helix Pitch (°)	30
Cutting Edge length (mm)	0.0033
Material Properties	WC
Density (kg/m3)	15630
Specific Heat (J/kgK)	258
Thermal Conductivity (W/mK)	84
Element Type	
Volumes	SOLID78
Meshing - Line Segments	
Curved lines	Diameter/32
Straight lines	Diameter/16
Cutting tool opposing circle	Diameter/8
Localised Mesh Refinement	lines < 0.01mm

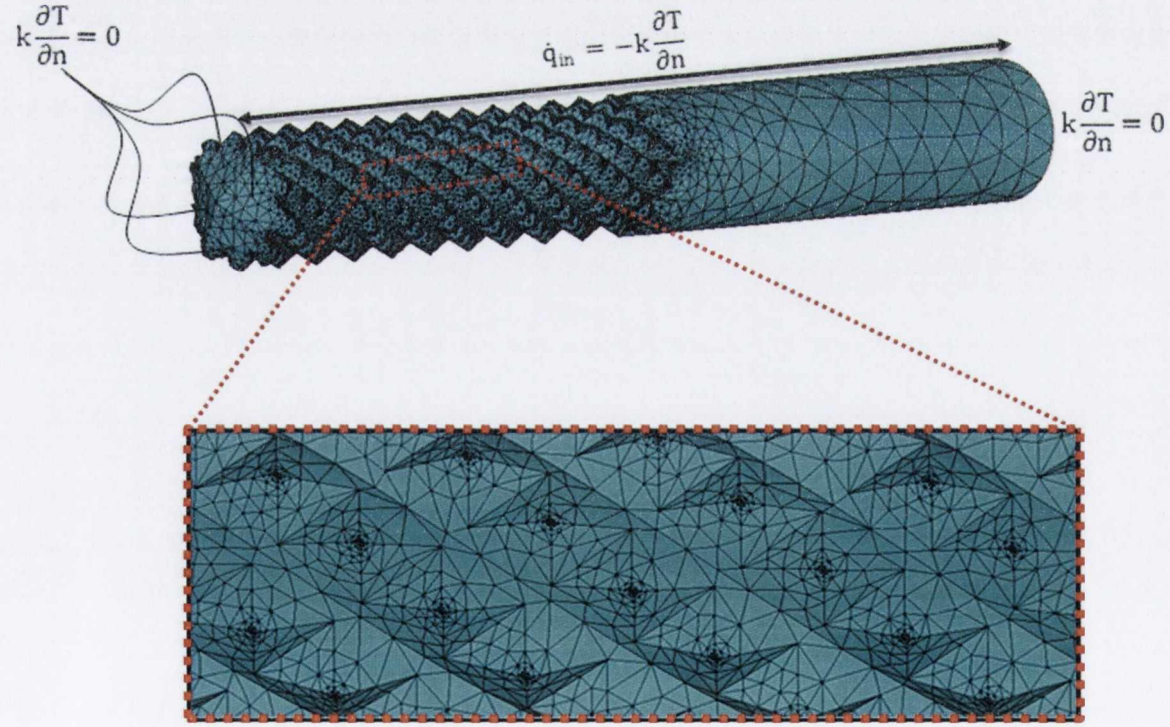

Figure 3.18: 3D Mesh of the ITT cutting tool using tetrahedral elements with enhanced mesh refinement at the cutting edge.

Solution Phase

The solution phase of this analysis was performed in exactly the same manner as described in 3.4.1 with the exception that the number of sub-steps used was increased to 50 sub-steps, due to the increase in elemental complexity.

Post-Processing Phase

The results of the ITT geometry were then compared with those from the cylinder to determine the degree of similarity between results, indicated in Figure 3.19. From the results shown in Figure 3.19, the increased surface temperature response of the ITT geometry is as anticipated, due to the decrease in volume. The increase in surface area caused a greater temperature gradient in the axial zone, with the complex geometry seemingly constricting the path of heat travelling away from the boundary condition and into the centre of the tool. This is seen more clearly from the contour plot shown in Figure 3.20(a), in which the temperatures at the cutting edges are much higher than on the smooth, cylindrical surface of the rest of the tool. The thermal behaviour of the ITT tool geometry is therefore not the same as that for the basic cylinder, with an increase in the maximum surface temperature reached by the ITT geometry of approximately 13 °C after only 0.3 s of exposure to this boundary condition. Therefore future analyses must incorporate the ITT geometry into the model to acquire a realistic result comparable to experimental results.

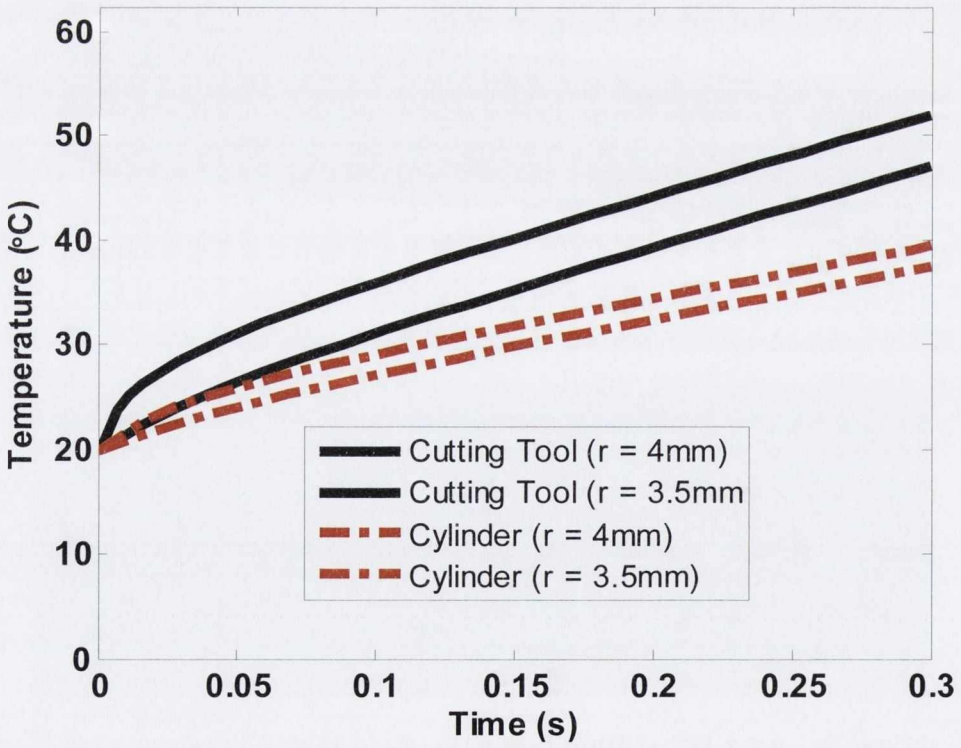

Figure 3.19: Plot of the initial transient response in the radial direction comparing FE results for ITT cutting tool against FE results for a basic cylinder for a heat flux value of 397kW/m^2 for the same constant radial heat flux boundary condition.

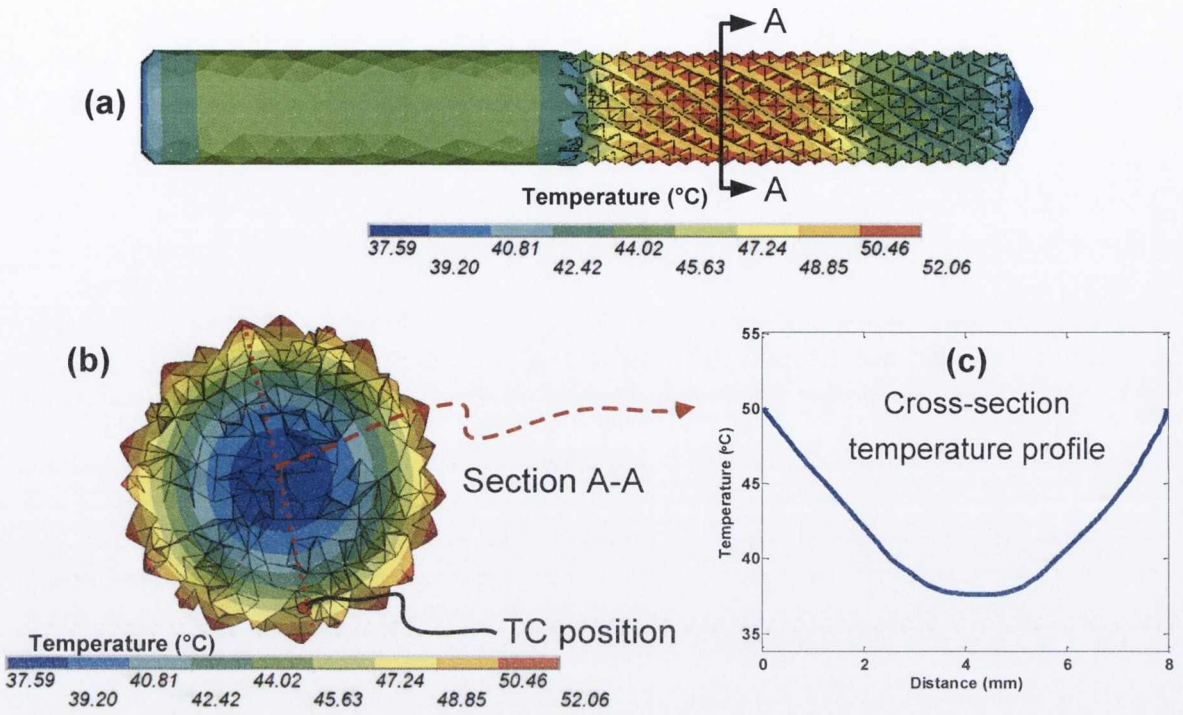

Figure 3.20: Contour plots of ITT cutting tool geometry showing the axial and radial temperature profile after 0.3 s of 397 kW/m^2 heat flux for (a) axial view (b) A – A section view and (c) line plot of temperatures across the cross section.

3.4.3 Cutting tool geometry with localised heat flux

The analysis of a cylinder undergoing radial conduction only gave an introduction to the radial heat flow paths through the tool. However, the issue of axial conduction effects must also be addressed, as axial depth of cut, a_P, varies with workpiece thickness in trimming operations. In order to investigate axial conduction effects, an assumption was made that due to the speed with which the tool is rotating through the cut, there is a constant virtual heat flux on the outer circumference at the axial location of the tool / workpiece interface as shown in Figure 3.21 in the form of a heat ring. This assumption is valid provided the time out of cut is lower than the impedance value of the tool material and the boundary is perfectly insulated. In our case, an assumption is made that rough cutting is being performed, in which the maximum radial depth of cut, a_e, is equivalent to the tool diameter. Under this circumstance, approximately 50 % of the circumferential surface is engaged in the cut at any instant.

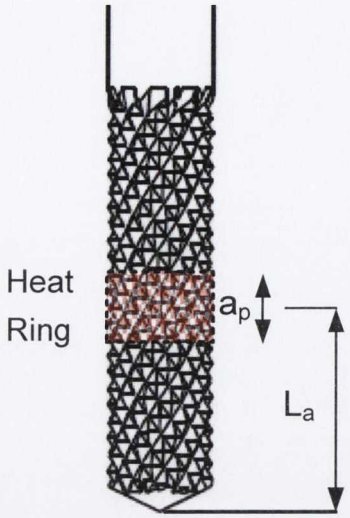

Figure 3.21: Virtual heat flux represented as a heat ring at the cutting interface.

Pre-processing

The setup of the model was identical to that described in section 3.4.2 with the exception of the boundary conditions which are described and illustrated in Figure 3.22. For this problem, rather than the entire outer radial surface of the tool being exposed to the heat flux, only rake face surfaces in the exposed cutting region were selected based on a node selection technique. This technique involves selecting the nodes firstly in the axial direction, therefore specifying the axial location of the cutting interface on the tool, i.e. using the APDL code *NSEL,S,LOC,X,0.0155,+0.0165* to position a 1mm heat flux ring centred at 16mm from the tool tip. However, as this resulted in all of the nodes in this section of the tool being selected, the selection was transferred to only those nodes in the outer surface in contact with the workpiece. This was done using the APDL code *ASLN,S*.

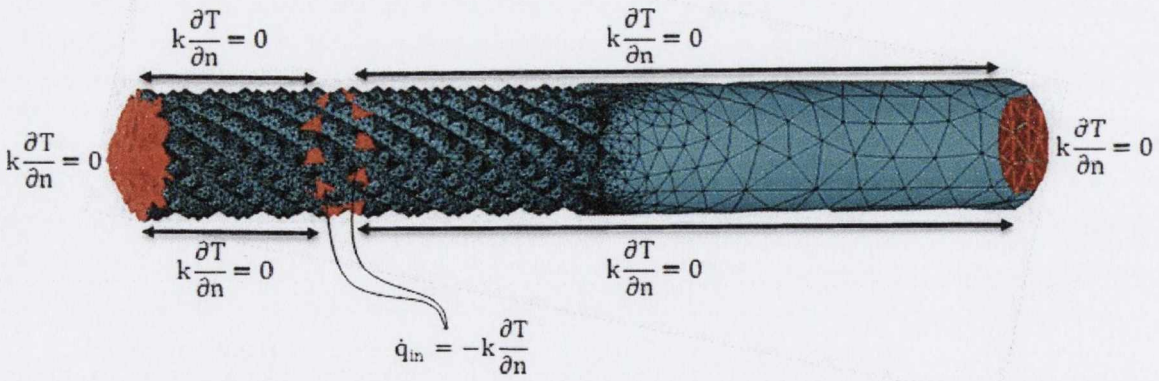

Figure 3.22: Boundary conditions for the localised heat flux analysis on ITT cutting tool.

Solution phase

The solution phase of this analysis was performed in the same manner as described for the previous investigation with the exception that the number of sub-steps used was increased to 50 to accommodate the increase in elemental and boundary condition complexity. Since the comparative experimental data is taken over a period of 7 or 24 s, it was also necessary to increase the second time step and as a result, increase the sub-steps accordingly to ensure that the implicit FE method used achieved an accuracy of 0.05 % convergence for both heat and temperature criteria.

Post-processing phase

The results of interest for the 'localised heat flux' simulation are illustrated in Figure 3.23 and Figure 3.24, where the cross section of the tool at which heat was applied is illustrated. There can be few comparisons made to the 1-D radial conduction only boundary conditions case, as the localisation of heat flux reduces the area to such an extent that axial conduction becomes an inevitable component of the solution. Due to the asymmetry associated with the double-helix design of the tool, the radial isotherms are no longer uniform but rather distorted, as the entry path for thermal energy does not occur evenly around the outside of the tool. Figure 3.23 shows a maximum difference in the time-history plots for the four radial locations selected of approximately 1°C.

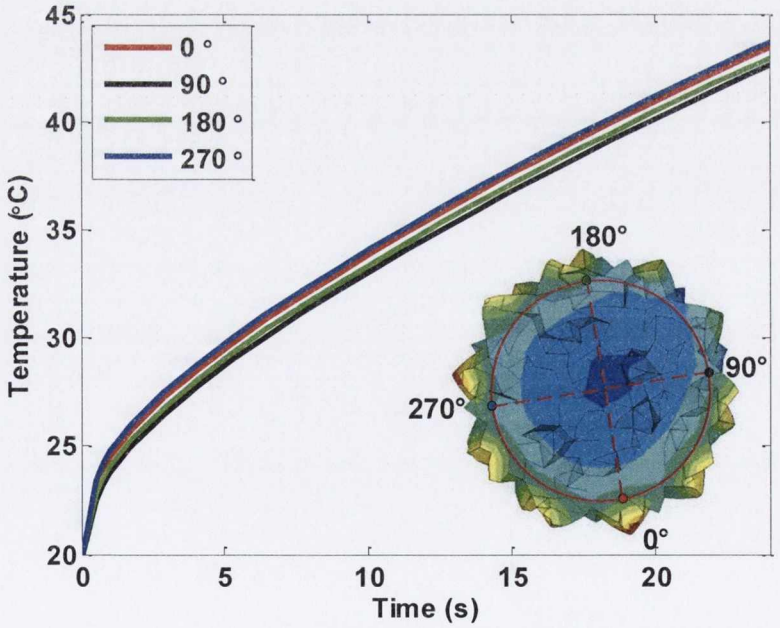

Figure 3.23: Comparison of time-history plots for various radial ITT sensor locations for a_p = 1mm and q_{in} = 397 kW/m^2.

This result indicates that although the double helix design associated with the tool does have some effect on the potential response of the sensor this is not a large effect for the parameters used in this simulation, i.e. 1mm a_p heat ring of 397 kW/m^2. This prompts further investigation of parameter effects which will be discussed in the coming sections.

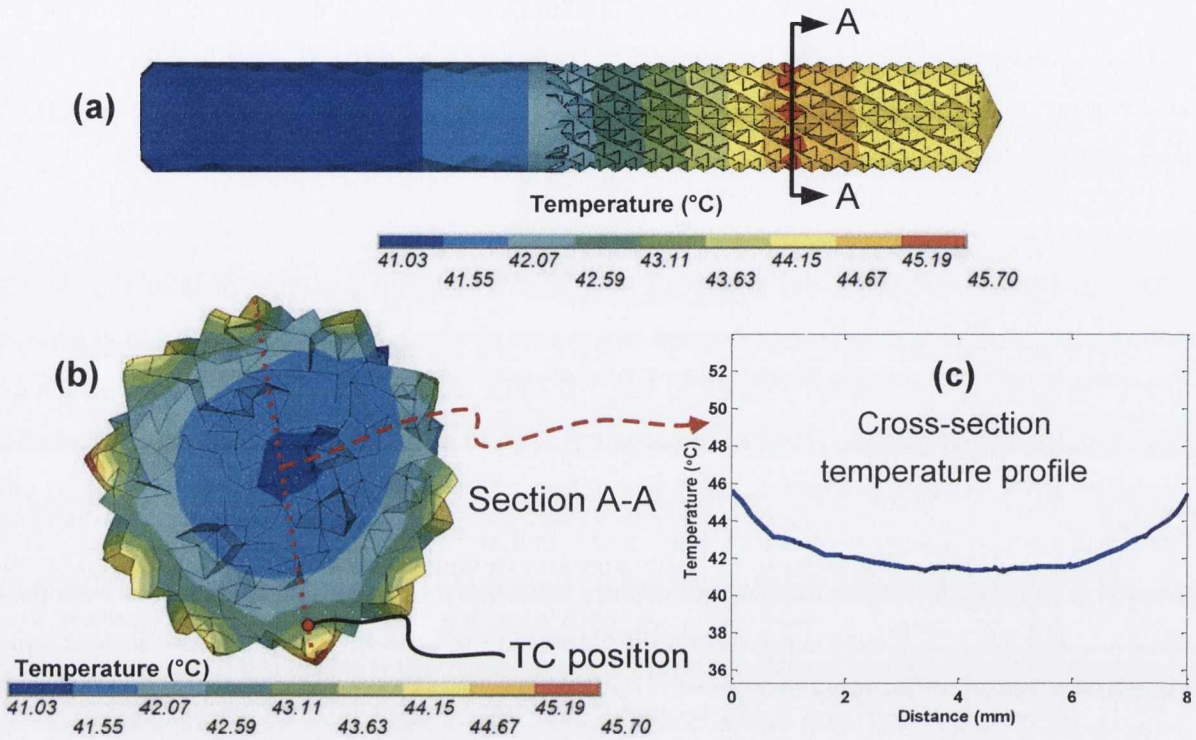

Figure 3.24: Contour plots of ITT geometry with a_p = 1mm showing the axial and radial temperature profile after 24 s of 397 kW heat flux for (A) isometric view (B) central cross section and (C) elevation.

The 0° - 180° temperature profile after an exposure time to the heat flux of 24 s in this simulation is presented in Figure 3.24 (c). This plot indicates the steep gradients at the outer regions of the radial cross section. Such gradients highlight the importance of positioning the sensor as close as possible to the radius of the tool to minimise loss of temperature signal.

Considering the axial variations shown in Figure 3.24 (a), a substantial thermal gradient is also seen in this orientation. The temperature difference between tool tip and ITT sensor location is noted to be approximately 1.5 °C while the gradient in the opposite direction from the ITT sensor location to the tool holder end is approximately 4.5 °C for this case of a 1 mm heat band and constant virtual heat flux ring of 397 kW/m^2.

While this model increases the accuracy of the ITT sensor analysis, further boundary condition effects and material property sensitivities associated with the ITT sensor system are not accounted for in this basic conduction model. Thus, in order to increase the

accuracy of the FE model to represent the real ITT sensor behaviour, the following will be considered:

- Conduction to the tool holder
- Convection to the environment
- The effect of a complex shape function heat flux
- Impedance value of tool, i.e. thermal properties
- Radiation to the environment

Of these variables, the most obvious starting point for investigation was conduction to the tool holder. It has been seen from this investigation that there is substantial axial conduction through the tool, which infers that some of the heat will reach the section of the tool in contact with the tool holder and diffuse via this material. In conjunction with this, an easily implementable variable is a convection coefficient on the outside of the unexposed cutting tool surfaces rotating at high speeds through the air. These two variables were the first investigated.

3.4.4 Cutting tool geometry with localised heat flux and dissipative conduction

The analysis of the ITT geometry indicated that while the initial transient phase for radial dissipation was clearly defined, when the model was extended to include transients beyond the first 0.3 s, the model reaches an asymptotical slope and temperature increase becomes linear with time regardless of radial location within the tool. From previous experimental data it is known that this is not a realistic scenario and decay in sub-surface temperatures occurs as the conduction path of the heat is partitioned 1) radially inwards, 2) axially along the tool and 3) outwards as discussed previously. To model this conductive behaviour, a simplified tool holder geometry of a tool steel cylindrical heat sink, in contact with the smooth cylindrical shaft of the ITT cutting tool was included in the FEA.

Pre-processing

The model, illustrated in Figure 3.25, was setup as previously described in section 3.4.2, with both of the volumes – tool and tool holder – imported from Pro-Engineer Wildfire. The mesh of the tool was described in section 3.4.2, while the holder was meshed with fine elements of the same order of magnitude as those used for the tool at the internal holder diameter, and a relatively course mesh at the outer diameter, resulting in 16,970 additional elements which formed the tool holder component. For comparative purposes, a time step of 24 s and heat flux value, of 397 kW/m^2 were applied with consideration to conduction heat transfer only. Convection values were introduced onto the surfaces of the tool outside of the theoretical 'cutting zone' as will be discussed in the post-processing section. Since the tool and holder use different material models, described in Table 3.4, it was necessary to indicate to the FE software that surface-to-surface contact existed between the elements at the boundary of these two volumes.

Table 3.4: Material properties of the tool and tool holder used in simulations

Material Properties	***WC [191]***	***AISI 4140 Tool Steel [192]***
Density (kg/m^3)	15800	7850
Specific Heat (J/kg K)	210	473
Thermal Conductivity (W/m K)	84	42

This was done by generating a contact pair, as shown in Figure 3.25, in which the outer surface of the tool was meshed as the contacting surface and the inner surface of the holder as the target surface. Contact-specific elements, TARGE170 and CONTA174 were used which allow for the closed-contact surface-to-surface thermal conduction equations to be incorporated into the resulting non-linear solution. This was done with the inclusion of a

thermal contact conductance (TCC) value set to the largest possible value between the tool and tool holder, calculated as:

$$TCC = \frac{q}{(T_t - T_c)} \qquad \textbf{3.9}$$

Where:

TCC	-	Thermal contact conductance (W/m^2K)
q	-	Heat flux (W/m^2)
T_t	-	Temperature of the contact point on the target (K)
T_c	-	Temperature of the contact point on the contact (K)

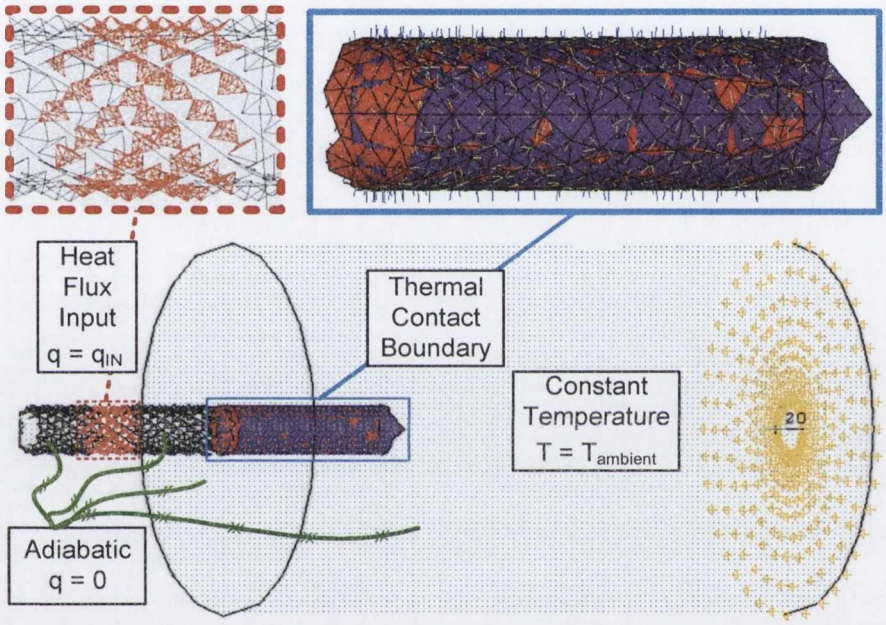

Figure 3.25: Development of the model from [A] the solid model imported from Pro-Engineer, to [B] the FE elemental model with boundary conditions including [C] surface-to-surface contact for tool and simple tool holder.

The ANSYS APDL code used to generate the FE model geometry, mesh style, elements, material properties and contact properties are detailed in Appendix 5.

Solution phase

The introduction of the second volume and the necessary thermal contact conduction converts this analysis from a basic linear transient model to a non-linear model in which two separate material models exist for each volume. A sample of the ANSYS APDL code used to generate the time steps for the iterative process, along with the details of the analysis type and solver requirements is provided in Appendix 6. Convergence criteria must be closely inspected for both temperature and heat. The critical convergence values were set to 1×10^{-11} for the residual value for each factor. A typical convergence plot, shown in Figure 3.26, illustrates the converging solution via graphical solution tracking.

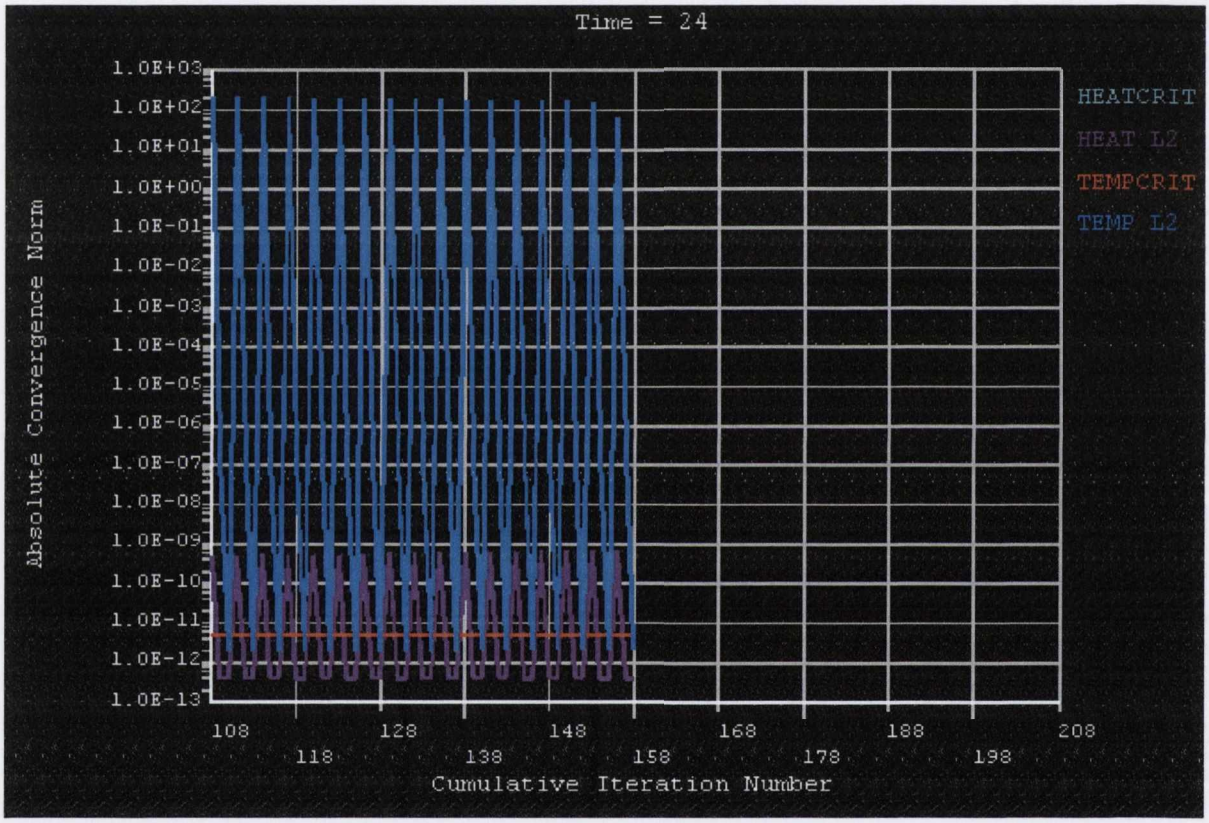

Figure 3.26: Cumulative iteration plot showing the solution convergence route per sub-step.

This particular 'snapshot' of the graphical solution tracking plot was taken at the end of the simulation, at t = 24 s. The x-axis of this plot, labelled 'Cumulative Iteration Number' shows the length of the analysis. As ANSYS steps through non-linear analyses, it uses a solver, in our case the Newton-Raphson method, that iterates to find a solution. If the problem is relatively linear, very few iterations will be required and thus the length of the graph will be small. However, if the solution is highly non-linear, or is not converging, many iterations will be required.

As can be seen from Figure 3.26, the solution completed after the cumulative iteration number reached 158. This is based on the number of time steps and sub-steps which were used in this simulation. These were pre-defined in order to ensure a highly accurate result.

The y-axis of Figure 3.26, labelled Absolute Convergence Norm, refers to non-normalized values which for this transient non-linear thermal analysis are absolute values.

The main point of the graph shown in Figure 3.26 is to relate the temperature to the heat flux. These values are graphed because they are the corresponding values in the solution vector for the degrees of freedom (DOF's) that are active in the element being used.

For both temperature and heat flux there are two parameters graphed. The 'HEATCRIT' and 'TEMPCRIT' curves represent the convergence criteria heat flux and temperature values respectively. These values are calculated as the product of the square root of the sum of squares of the applied load and the tolerance which was set to 0.05 % for all simulations. The 'HEAT L2' and 'TEMP L2' curves represent the square root of the sums of squares of the difference between the calculated internal heat flux and temperature values respectively at a particular degree of freedom and the corresponding external heat flux / temperature in that direction respectively. For each substep, the software iterates until the 'HEAT L2' and 'TEMP L2' values are below the 'HEATCRIT' and 'TEMPCRIT' values respectively. Thus, the sharp spikes upward in the curve represent the start of a new sub-step.

Post-processing phase

The databases generated during the iterative transient thermal analysis were investigated using the post-processing component of the FE software. Details of the ANSYS APDL code used to extract the information from the generated databases are provided in Appendix 7.

Initial investigations to determine the extent of the losses from the tool to holder via conduction were performed. Figure 3.27 illustrates axial and radial conduction for a_p values of 1mm with a focus on tool conduction only. This plot illustrates the interaction between the tool and holder in the thermal system, as the temperature of the tool as it reaches the contact point with the holder is significantly warmer than the outer ambient section of the tool holder.

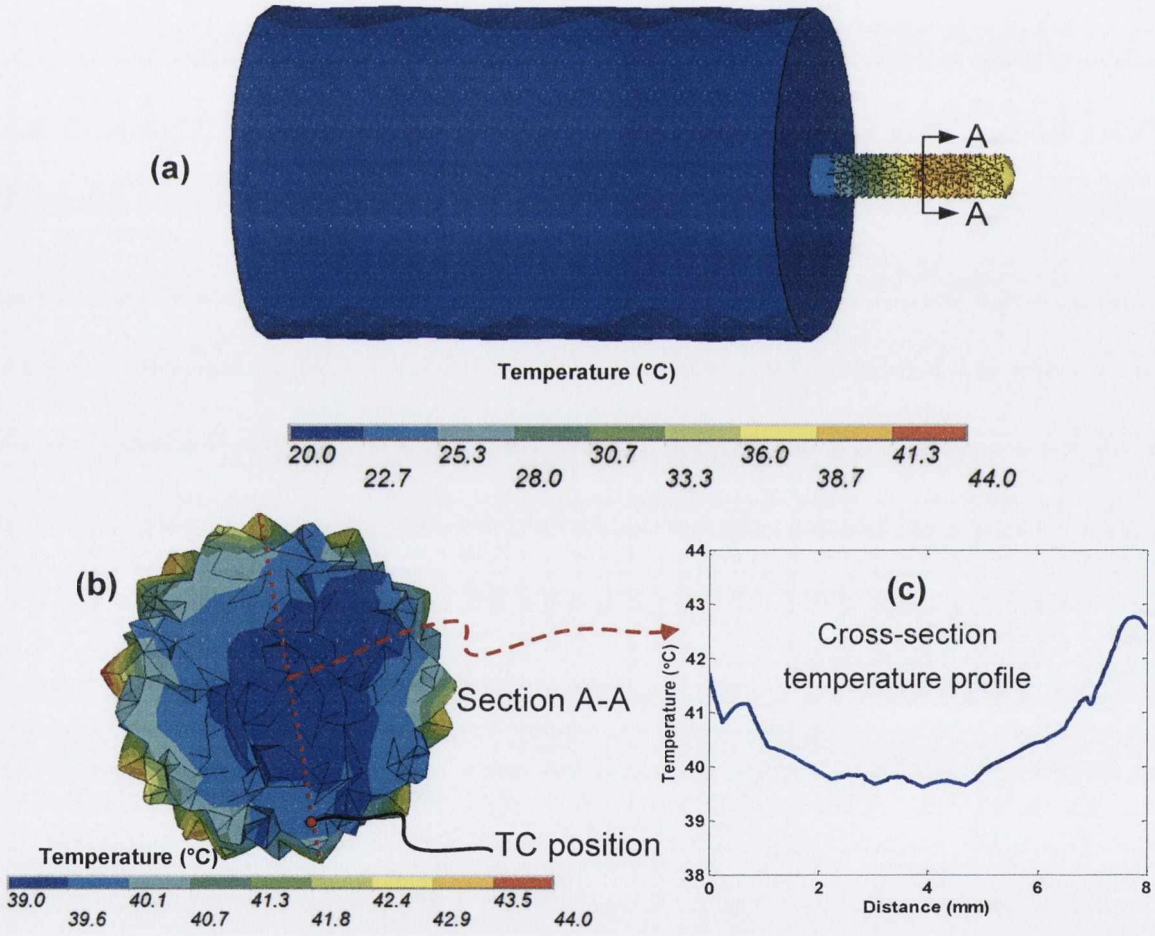

Figure 3.27: Contour plots of ITT geometry with conduction to tool holder for a_p = 1mm showing the axial and radial temperature profile after 24s of 397kW/m^2 heat flux for (a) overall model (b) ITT thermocouple tip cross section and (c) elevation.

Conduction to the holder is illustrated in more detail in Figure 3.28 to Figure 3.30. While the results of this simulation show comparable results to those noted for the simple ITT model described in section 3.4.3, there is a clear effect associated with the introduction of the tool holder. Details of the time-history temperature at the heat flux input boundary on the tool surface are shown in Figure 3.28. In this plot, there is evidence that the holder begins to act as a heat sink after a period of approximately 11 to 13 s, causing the temperature within the tool to curve further away from the almost asymptotic shape of the *without holder* model's curve. This is further shown in Figure 3.29, where the heat flux entering the tool holder is seen to increase even before the temperature at the surface is affected, at 3 - 4 s. Figure 3.30 provides further evidence of the penetration of thermal energy into the holder. All of this indicates that the addition of the tool holder provides a realistic heat sink, which should not be ignored. Therefore, for future simulations, the holder was kept and other possible boundary conditions, which could increase the realism of the problem, were investigated. These included convection effects, thermal contact conductance value used and heat flux applied.

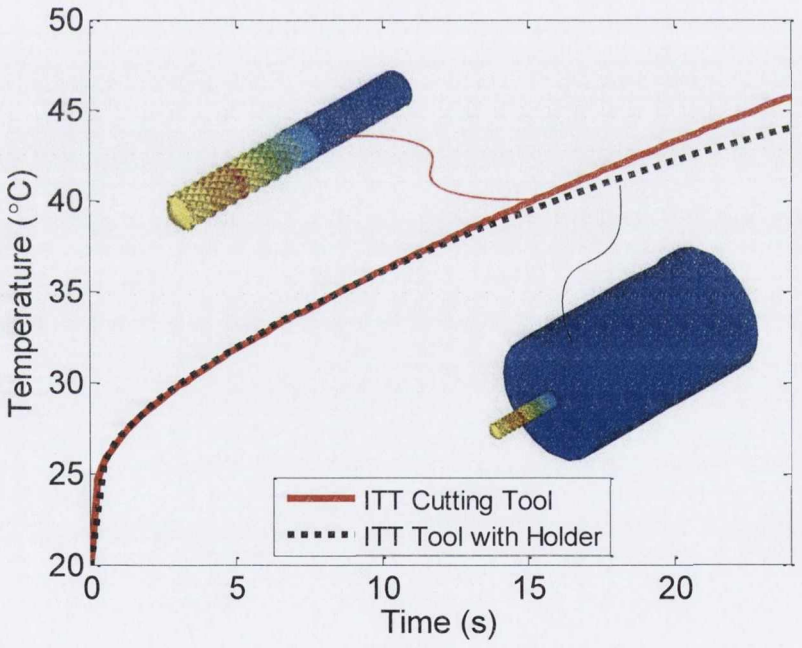

Figure 3.28: Comparative plot of the time-history for the surface temperature at the heat flux input boundary for the model without conduction (solid lines) and with conduction to tool holder (dotted lines).

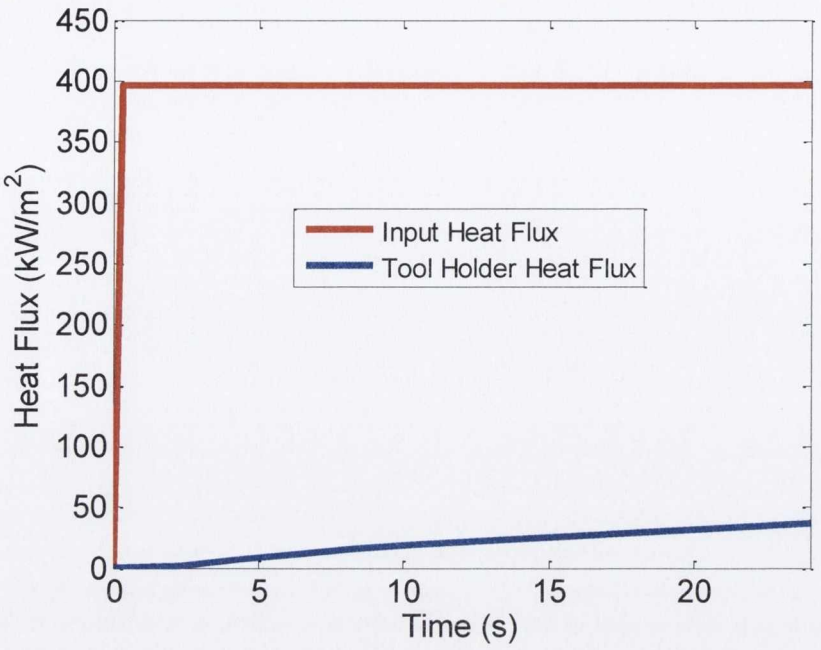

Figure 3.29: Comparison of heat flux input versus heat flux at the tool holder.

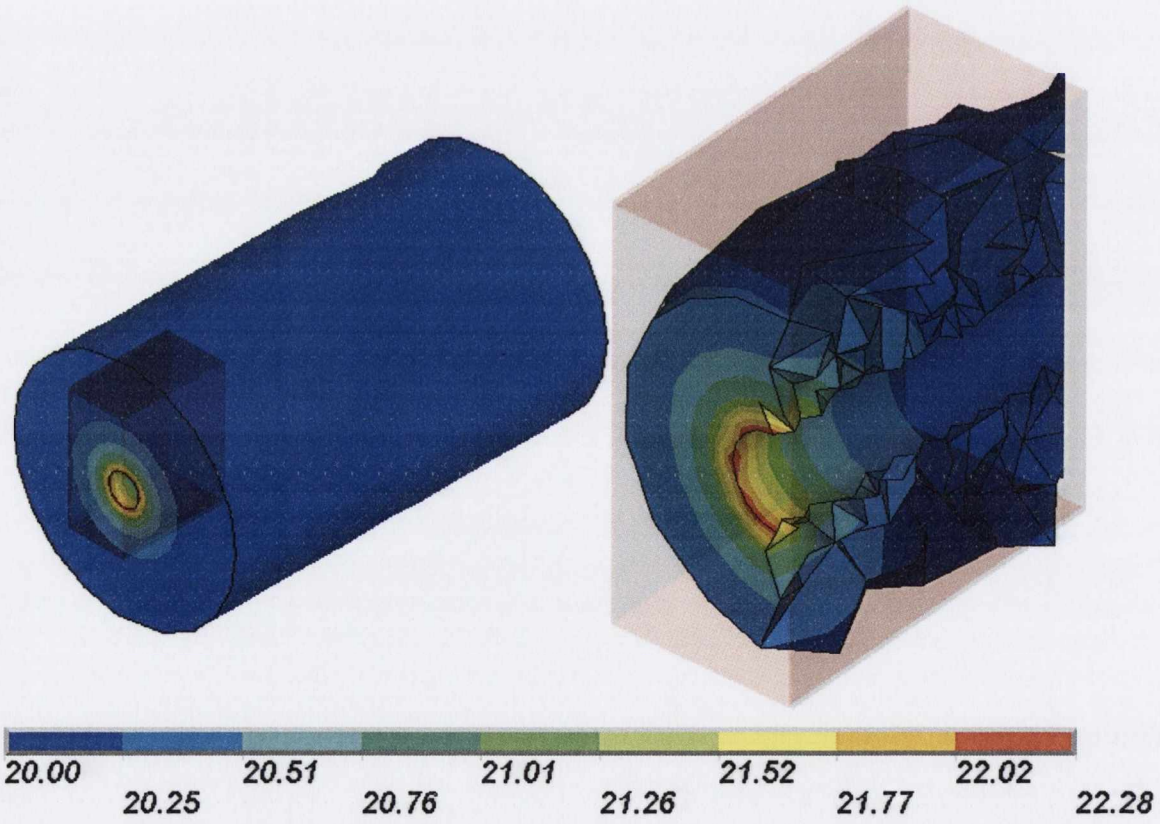

Figure 3.30: Heat conducting into the tool holder from ITT tool (q = 397 W/m^{2}K).

3.4.5 Sensitivity analysis of boundary conditions

It was determined in the previous section that the additional heat sink, i.e. the tool holder, produced increased realism to the mode. In order to determine the effects of other factors in the thermal system under study a sensitivity study was undertaken. The factors were applied to the model in the form of boundary conditions. The applied boundary conditions are shown in Table 3.5. The choice of level for each condition was varied for each factor.

Table 3.5: Boundary condition factors varied during sensitivity study

	Factor Levels		
Boundary Condition Factor	Low	Medium	High
Convection film coefficient - h (W/m^2K)	0	100	1000
Thermal Contact Conductance - TCC (kW/m^2)	0	100	4000
Heat Flux - q (kW/m^2)	50	397	1000

For the convection boundary condition, the literature suggests that forced convection caused due to the rotation of a cylinder is of the order of 10 -100 W/m^2K, [193], and therefore, 100W/m^2K was used as an approximate value, with the high factor level set an order of magnitude higher than this to confirm the boundary condition, as the additional tool surface complexity may cause further increased convection.

For TCC, the default value given by the FEA software, 4000 kW/m^2, defines the contact between surfaces to be perfect. In reality, this is seldom the case, with contact on a micro-scale occurring at finite points along the roughness of both the contact and target surfaces. Therefore, a conservative value of 100 kW/m^2 was used as a mid-point between perfect contact and no contact due to its relatively similar magnitude to the heat flux applied. It was expected that if the model were sensitive to this value, it would be due to the relationship between TCC and heat flux.

The heat flux was therefore partially chosen to attempt to uncover the above-mentioned relationship with TCC. However, the primary reason for the selection of the heat flux was based on the experimental values achieved during machining with comparable geometric boundary conditions, i.e. a_p = 1mm, v_f gives 24s cut, cut took place at the ITT axial location.

A full factorial design of experiments (DOE) was performed on the three factors using a 3^3 design resulting in a single replicate of the analysis consisting of 27 runs. Due to the reliability and repeatability of the simulation software and meshed model, determined previously via a sensitivity analysis, only a single replicate was used for this design of experiment analysis. Thus in this case, the chance variation associated with the real-world process is assumed to be zero and the significance of the variables is assessed

independently of chance variation. The full time-history simulation results were analysed for each design point of the 27 run DOE. The effect of variation of each of the factors independently of the other factors is displayed graphically in Figure 3.31, Figure 3.32 and Figure 3.33. From these figures, heat flux appears to show the greatest effect.

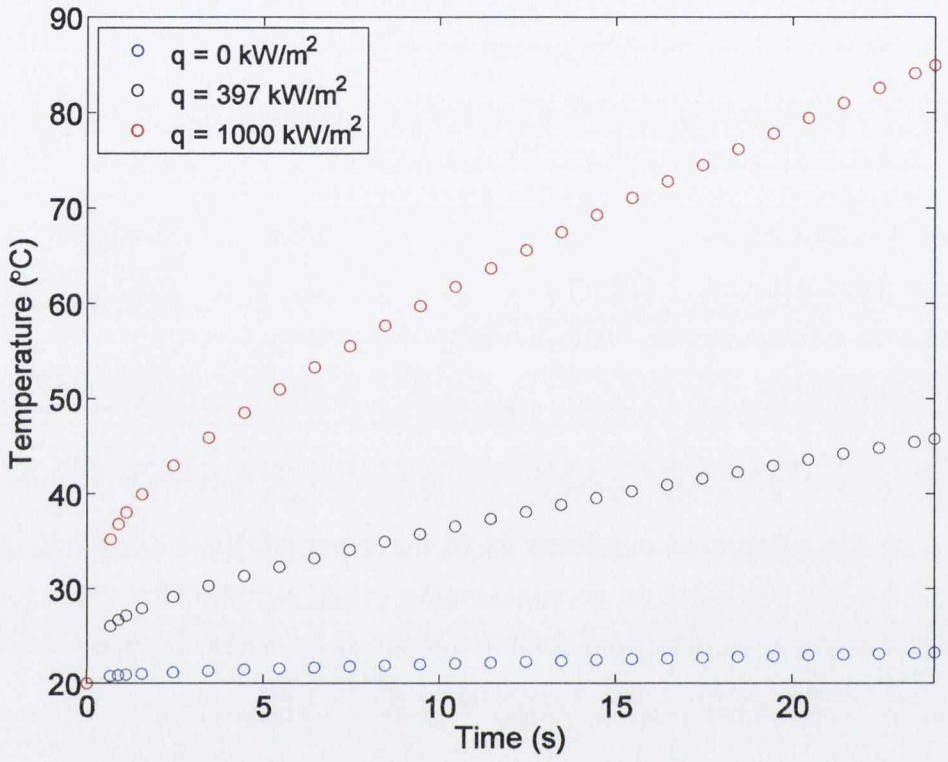

Figure 3.31: Heat flux effect for a constant convection coefficient of h = 0 W/m^{2}K and thermal contact conductance of TCC = 0 kW/m^2.

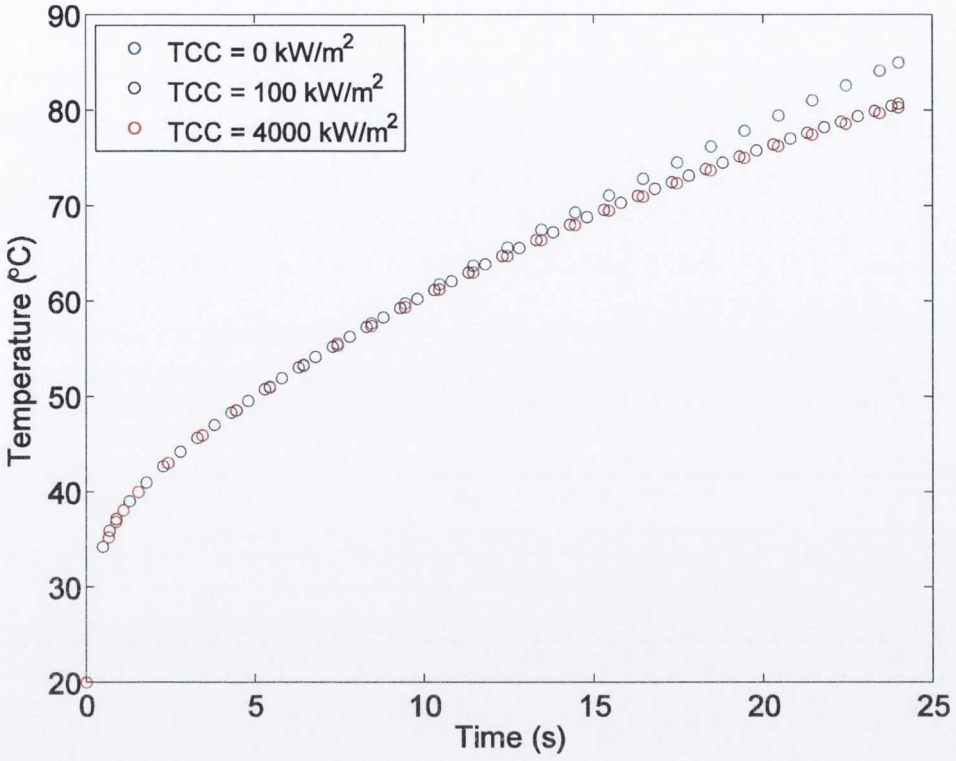

Figure 3.32: Thermal contact conductance effects for constant convection coefficient of h = 0 W/m^{2}K and heat flux of q = 1000 kW/m^2.

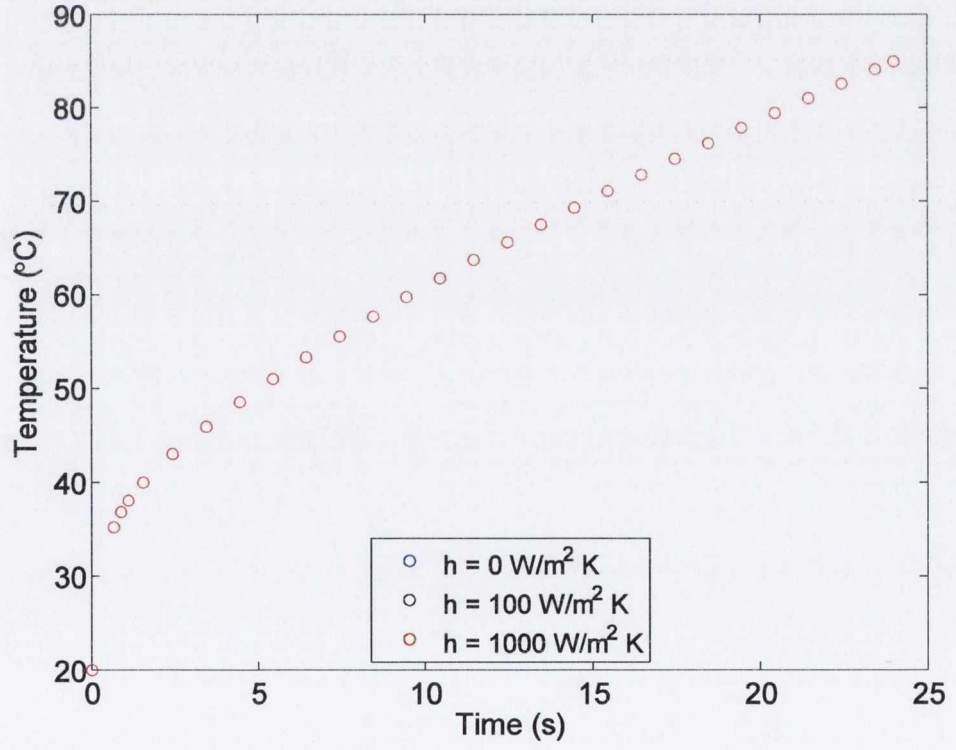

Figure 3.33: Convection film coefficient effect for a constant thermal contact conductance of TCC = TCC = 0 kW/m^2 and heat flux of q = 1000 TCC = 0 kW/m^2.

This visual inspection of factors at specific levels provides insight into the sensitivity of the FE model response to each factor. However, in order to compare the overall significance of all factors the maximum surface temperature achieved after a simulated exposure time of 24 s was used as a response to perform an overall effects analysis.

Figure 3.34 is the main effects plots for this sensitivity analysis. This plot indicates that the primary factor causing the maximum surface temperature to change is the heat flux, whilst variations in both convection and TCC are approximately an order of magnitude less. Convection values fluctuate closely about the mean for the range tested, and TCC values reduce slightly due to the removal of a small portion of the heat by the tool holder.

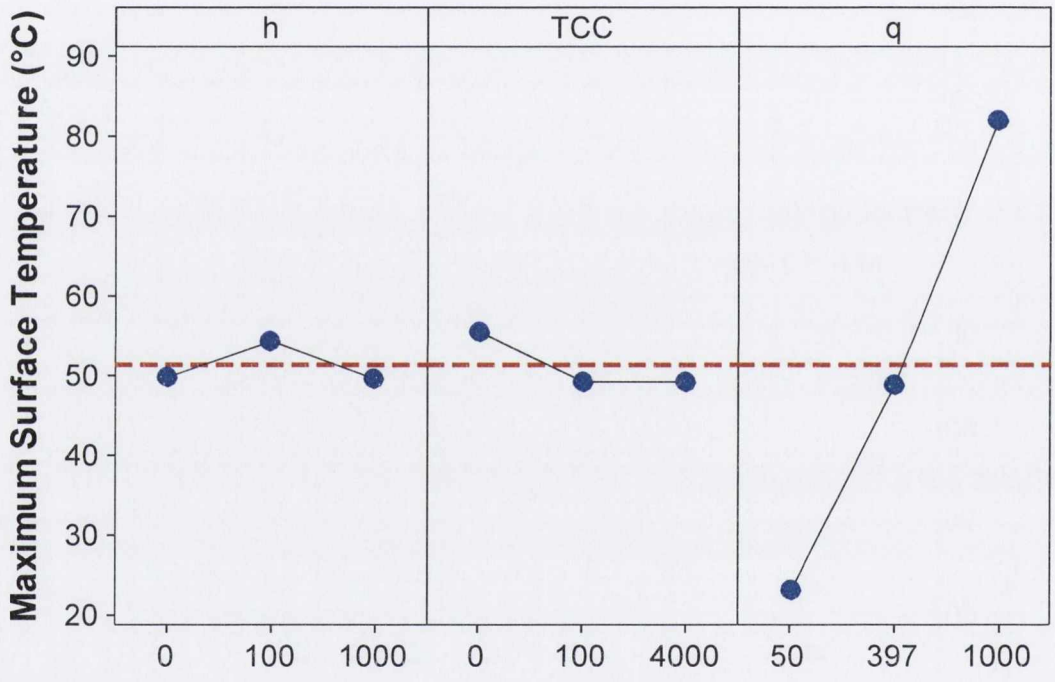

Figure 3.34: Main effects plot for max surface temperature results from the sensitivity analysis.

3.4.6 Thermal Property Sensitivity Analysis

A sensitivity analysis was performed to determine the effect of thermal properties of the cutting tool on the behaviour of the model over a period of time less than the time constant of the material. The factors investigated in this study were thermal conductivity, k, specific heat capacity, C_p, and density, ρ. These values combine to provide the thermal diffusivity of a material, α, which is defined as:

$$\alpha = \frac{k}{\rho C_p} \qquad 3.10$$

Thus, of primary interest in this analysis is to determine the magnitude of The primary values used to build the previous models were taken from literature, as tungsten carbide [191] is a commonly used material. In order to determine the sensitivity of the FE model response to such parameters, these literature values were used as the centre point for the design. The upper and lower factor levels are 10 % greater and lower respectively than the centre point values. The factors and levels used to investigate the thermal property sensitivity are shown in Table 3.6.

Table 3.6: Thermal property factors varied during sensitivity study.

	Factor Levels		
Thermal Property	Low	Medium	High
Density - ρ - (kg/m^3)	14220		15800
Specific Heat - C_p - (J/kg K)	189	210	231
Thermal Conductivity – k - (W/m K)	76	84	92

In order to constrain the model as much as possible for this sensitivity analysis, a specific simulation setup was used, shown in Figure 3.35. The heat exposure period was set at 7 s in order to investigate short-term behaviour effects of the thermal properties. Maximum iterations and mesh resolution were used as previously determined in order to ensure that the effects seen were specific to thermal properties.

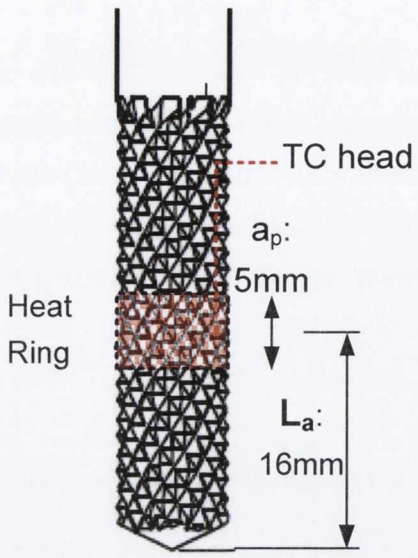

Figure 3.35: Geometric constraints used for thermal property sensitivity analysis.

Density

The density of a solid is defined as the mass per unit volume of material, thus it is important to understand the chemical composition of the solid. Tungsten carbide (WC) is an inorganic compound containing approximately equal parts of tungsten and carbon atoms. The reliability of the literature value for density is dependent upon the manufacturing process used to generate the WC.

Figure 3.36 shows the effect of reducing the density by 10 % from the literature value of 15800 kg/m^3 with all other thermal properties remaining at literature recommended values. From this plot it is clear that a reduction in density has a general inverse effect and a divergent effect over time on the temperature profiles at both surface and ITT sensor locations. After a period of 7 s, there is a temperature divergence of approximately 12 – 13 % across the density range analysed. This divergence is reduced to less than 2.5 % for the initial 1 s of the simulation. An approximate density measurement was performed on the ITT cutting tool using a calibrated digital weighing scale, with ±0.05g uncertainty, in order to obtain a mass of the un-worn cutting tool of 43.3 g. A volume of 2.75 x 10^{-6} m^3 was approximated using Pro-Engineer to calculate the 3D modelled approximation of the tool. This resulted in a density value of 15,745 kg/m^3 which is within 1 % of the literature value. Since the calculated density is based on an approximation of the geometry, and due to the small difference between calculated and quoted densities, the literature value of 15800 kg/m^3 was maintained in the FE model.

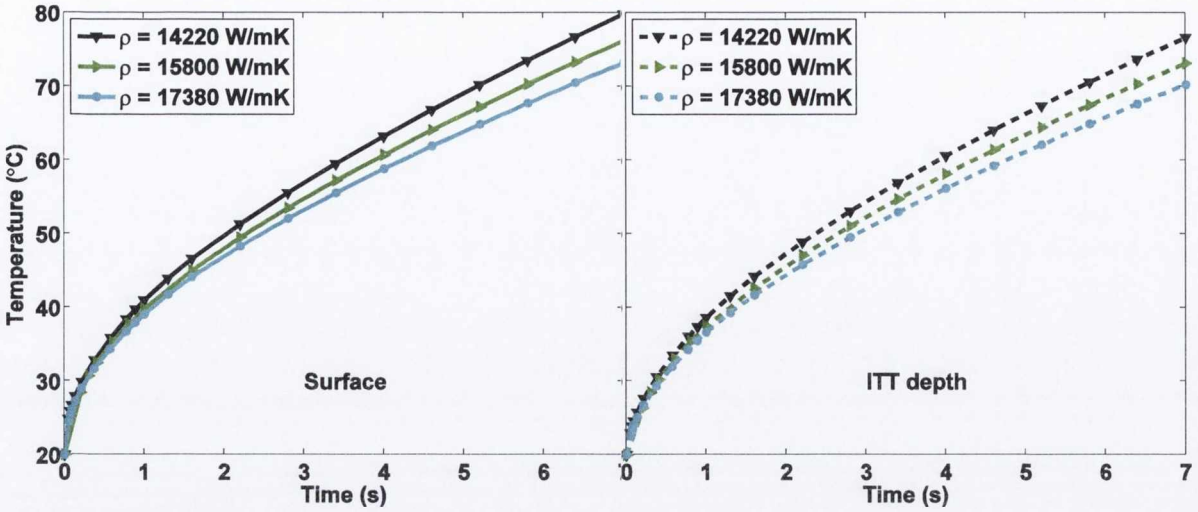

Figure 3.36: Time-series temperature plots of (left) the surface profile and (right) ITT depth profile for a ±10 % variation in density from literature values.

Specific heat capacity

The specific heat capacity is defined as the heat energy required to change the temperature of a unit mass of substance by a unit temperature interval [194]. This process is closely related to the thermal time constant of the substance. As described previously, the time constant is used to compare the dynamic response of a substance to a change in the internal environment from a position of equilibrium. Variations in temperature response due to the specific heat capacity for the FE model results in trends of approximately the same magnitude and inverse nature to those noted for density. These trends are shown in Figure 3.37.

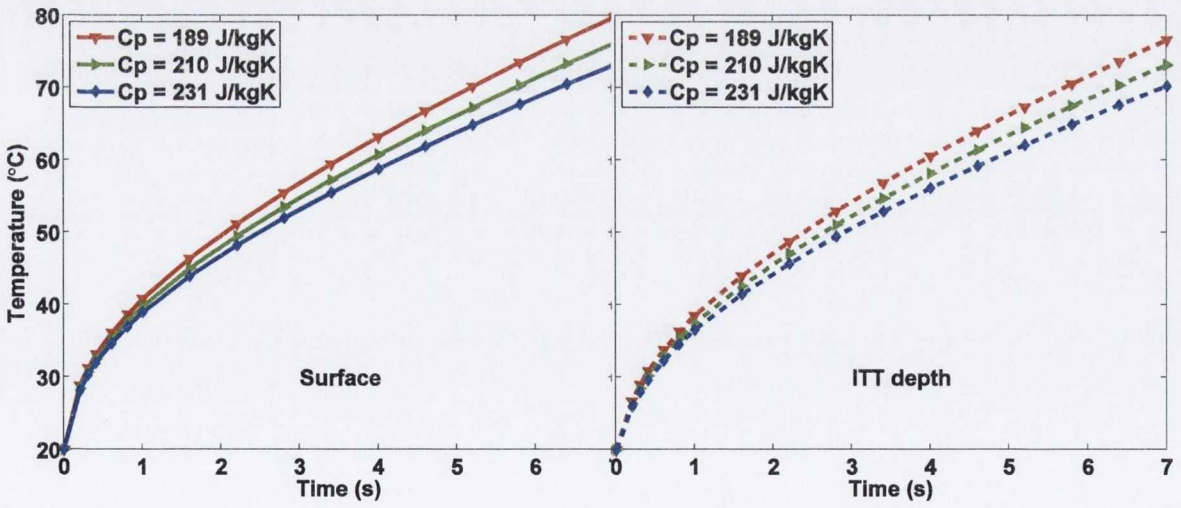

Figure 3.37: Time-series temperature plots of (left) the surface profile and (right) ITT depth profile for a ±10 % variation in density from literature values.

Thermal Conductivity

The thermal conductivity of a substance is defined as the property which describes the ability of a material to conduct heat. As mentioned in 2.7.1, it is the constant of proportionality which links the temperature gradient experienced by a material to the heat flux which caused such a temperature gradient. Thus the larger the thermal conductivity constant of a material, the lower the temperature gradient will be across the material for a given heat flux magnitude.

Figure 3.38 shows the time-series temperature response under different thermal conductivity settings within the FE model. The magnitude of temperature response divergence after 7 s is approximately 6 – 7 %. This is approximately half the magnitude of both density and thermal conductivity.

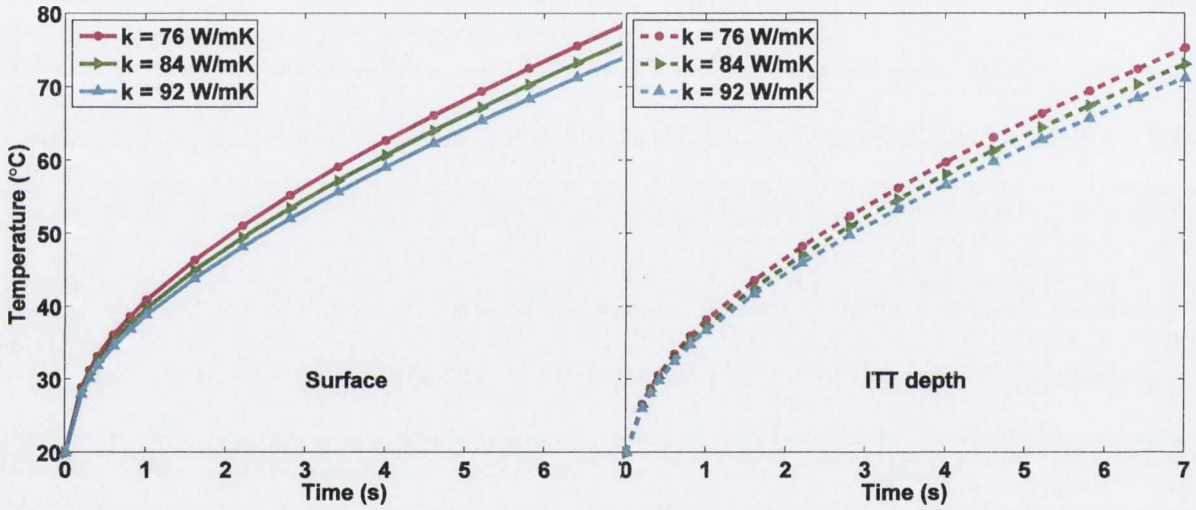

Figure 3.38: Time-series temperature plots of (left) the surface profile and (right) ITT depth profile for a ±10 % variation in density from literature values.

Thermal property effects comparison

The results of the overall sensitivity analysis are detailed in _. The data of this table was supplied to Minitab in order to make comparisons between the effects of each parameter.

Table 3.7: Thermal property sensitivity analysis results

Density (kg/m3)	*Specific heat capacity (J/kgK)*	*Thermal conductivity (W/mK)*	*Surface max. temp. (°C)*	*ITT max. temp. (°C)*	*Percentage divergence (%)*
14220	189	76	86.3	82.8	4.1
14220	189	84	83.6	80.3	3.9
14220	189	92	81.3	78.2	3.8
14220	210	76	82.3	79.0	4.1
14220	210	84	79.8	76.7	4.0
14220	210	92	77.6	74.6	3.8
14220	231	76	79.0	75.7	4.1
14220	231	84	76.6	73.5	4.0
14220	231	92	71.2	68.5	3.9
15800	189	76	82.3	79.0	4.1
15800	189	84	79.8	76.6	4.0
15800	189	92	77.6	74.6	3.8
15800	210	76	78.6	75.4	4.1
15800	210	84	76.2	73.2	4.0
15800	210	92	74.2	71.3	3.9
15800	231	76	75.6	72.4	4.2
15800	231	84	73.2	70.3	4.0
15800	231	92	71.2	68.5	3.9

Main effects plots are presented for surface temperature, ITT temperature and percentage divergence after 7 s of heat exposure in Figure 3.39, Figure 3.40 and Figure 3.41 respectively.

Figure 3.39 and Figure 3.40 show a summary of the trends previously seen for each property over a wider scale of variable settings. These graphs show that the response occurring at the location of the ITT sensor is of the same magnitude for all factor levels investigated. A general trend of a reduced maximum temperature is noted for each of the property main effects plots.

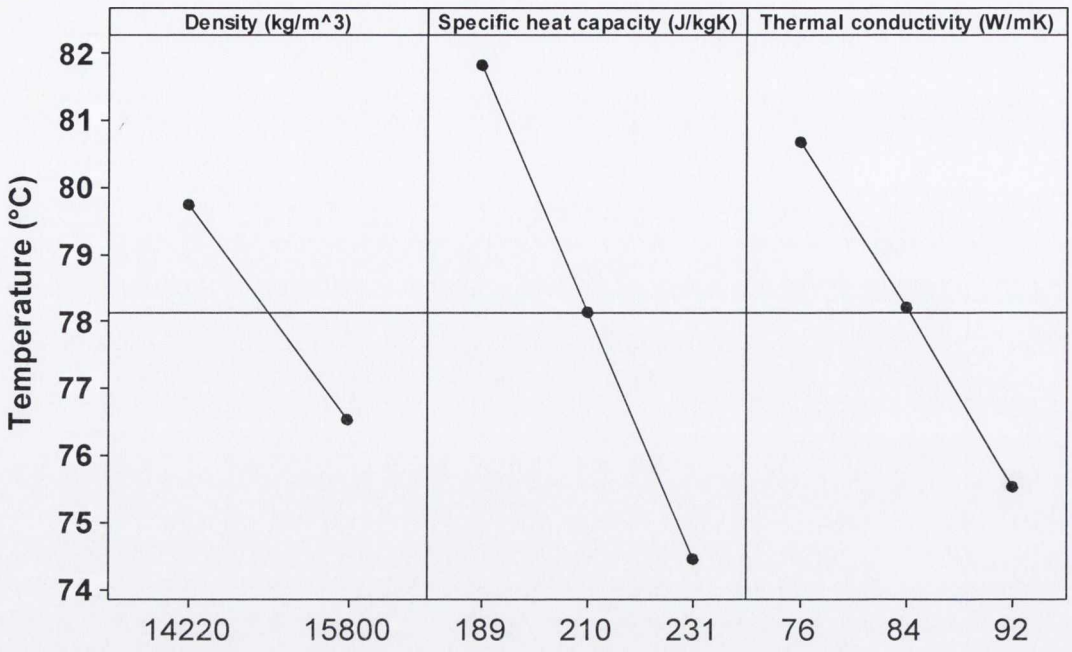

Figure 3.39: Main effects plot of the simulated surface temperatures after 7 s for thermal property variations.

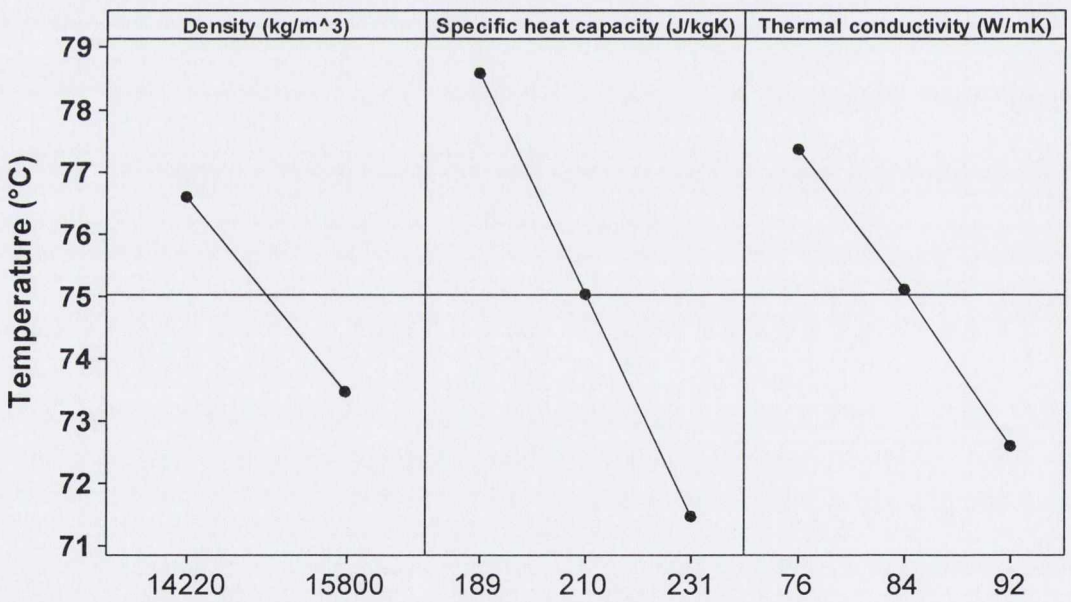

Figure 3.40: Main effects plot of the simulated ITT location temperatures after 7 s for thermal property variations.

Figure 3.41 describes the main effects of property variations on the percentage divergence of the temperatures after 7 s. The divergence is calculated as:

$$\%\, Divergence = \left(1 - \frac{T_{ITT}}{T_{Surface}}\right) * 100 \qquad 3.11$$

As expected from the diffusivity equation, equation 3.10, there is an increase in the diverging effect between surface and ITT sensor location associated with density and specific heat capacity, while there is a larger inverse effect due to an increase in the thermal conductivity. The magnitude of the thermal conductivity effect as this property is changed from 76 to 92 W/mK is relatively small in percentage terms at 0.22 %. This is due to the locality of the heat flux to the sensor location in this constrained simulation. However, the fact that the simulation is able to detect the various direct and inverse trends associated with these divergence effects confirms that the FE model is sensitive to thermal property changes.

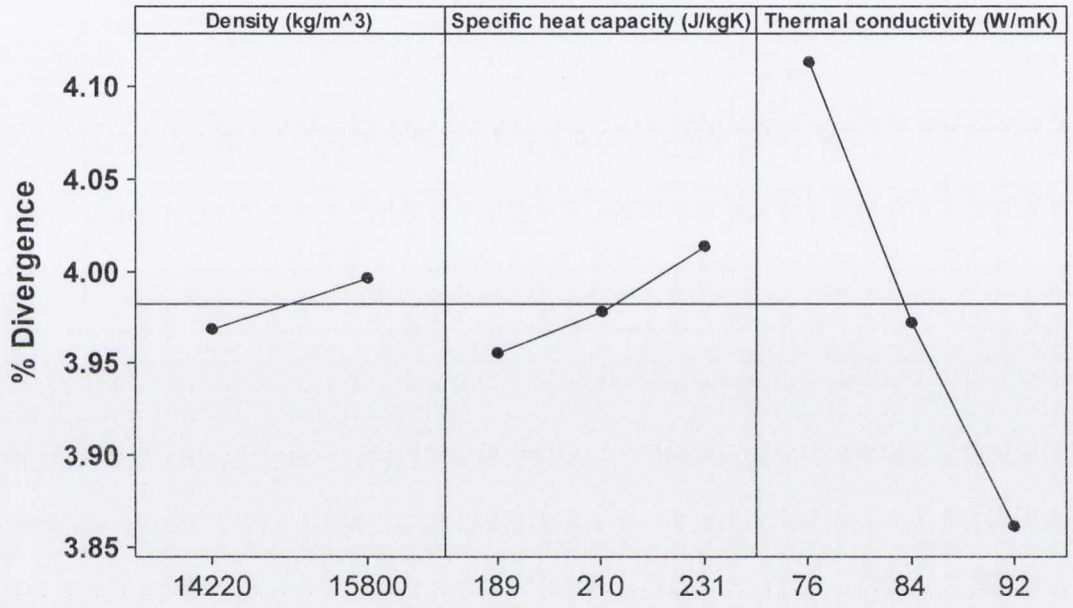

Figure 3.41: Main effects plot of the percentage divergence between surface and ITT temperatures after 7 s for thermal property variations.

This sensitivity analysis shows the various effects of the thermal properties on the response behaviour of the FE model. There are a number of interesting points to note from this study:

1. The thermal properties are more sensitive to longer time interval simulations, with short term response variation, < 1 s, appearing to be negligible.
2. The largest divergence effect is noted for changes to thermal conductivity, whereas the density and specific heat capacity variations produced response changes of similar magnitude.
3. The FE model should maintain the literature recommended parameters, however, these values should be validated through physical experiments

3.5 Validation of the ITT sensor FE model using a controlled heat flux

In order to validate the FE model of the ITT sensor in the temperature zone associated with CFRP cutting processes, heat simulation experiments were designed over the same time durations as dictated by the feed rate in a cutting operation, i.e. for a cutting distance of 150 mm at a feed rate of 375 mm/min results in a cutting duration of 24 s. A constant laser-generated heat flux was adjusted to approximately match the amount of heat energy delivered to the sensor in a real cutting experiment.

3.5.1 Experimental goals and objectives

The overall goal of this investigation is to validate the FE thermal model of the ITT sensor under rotary conditions using a known heat flux and known surface temperature.

Ultimately, the FE model, validated via the results of these experiments, in conjunction with ITT sensor data from actual CFRP cutting experiments will be combined to form an enhanced perception of the CFRP cutting process, by allowing for temperatures and heat flux values at the cutting interface surface of the tool from the remote location of the ITT sensor.

3.5.2 Experimental design

Experiment 3.1: Heat flux variations

The goal for this experiment was to validate the FE model by comparing the resulting temperature data produced by the model with experimental data for both the surface and at the ITT sensor's embedded location. This experiment involved the variable factors and levels displayed in Table 3.8. The factors held constant throughout experiment 3.1 are shown in Table 3.9.

Table 3.8: Variable factors and levels used in experiment 3.1.

Laser heat rate (W)	*Equivalent heat flux (kW/m^2)*
10	~600
50	~1200
100	~2800

Table 3.9: Constant factors used in experiment 3.1.

Factor	*Fixed Level*	*Units*
Ambient temperature	21 ±1	°C
Heat input axial location	16 (above tip)	mm
Heating Period	24	s
Rotation Speed	2000	RPM

Experiment 2: Surface temperature response for heat flux, heating period and rotation speed

Having validated the FE model's ability to predict the surface temperature to a reasonable degree of accuracy, the goal for this experiment was to quantify the effect of heat flux, heating period and rotation speed on the adjusted ITT sensor response. This experimental design involved the variable factors and levels displayed in Table 3.10. The factors held constant throughout experiment 2 are shown in Table 3.11. The factorial table used for experiment 2 for each design point, is shown in Table 3.12.

Table 3.10: Variable factors and levels used in experiment 2.

Heating period (s)	*Laser heat rate (W)*	*Rotational speed (RPM)*
7	50	20
24	100	200
		2000

Table 3.11: Constant factors used in experiment 2.

Factor	*Fixed Level*	*Units*
Ambient temperature	21 ±1	°C
Heat rate location	At the ITT sensor	

Table 3.12: Experiment 2 design points and corresponding factor levels for 1 of the 3 repetitions of the factorial design.

Std. order	*Run no.*	*Heating period (s)*	*Heat rate (W)*	*Rotational speed (RPM)*	*Std. order*	*Run no.*	*Heating period (s)*	*Heat rate (W)*	*Rotational speed (RPM)*
11	1	24	10	200	15	10	24	50	2000
7	2	7	100	20	10	11	24	10	20
16	3	24	100	20	8	12	7	100	200
6	4	7	50	2000	1	13	7	10	20
9	5	7	100	2000	2	14	7	10	200
14	6	24	50	200	18	15	24	100	2000
12	7	24	10	2000	4	16	7	50	20
3	8	7	10	2000	5	17	7	50	200
13	9	24	50	20	17	18	24	100	200

3.5.3 Experimental Setup

A rig was custom built that could mimic the movement of the spindle in a typical milling process, as shown in Figure 3.42. The rig can be described as a two-element system with each element driven by a precision servo motor.

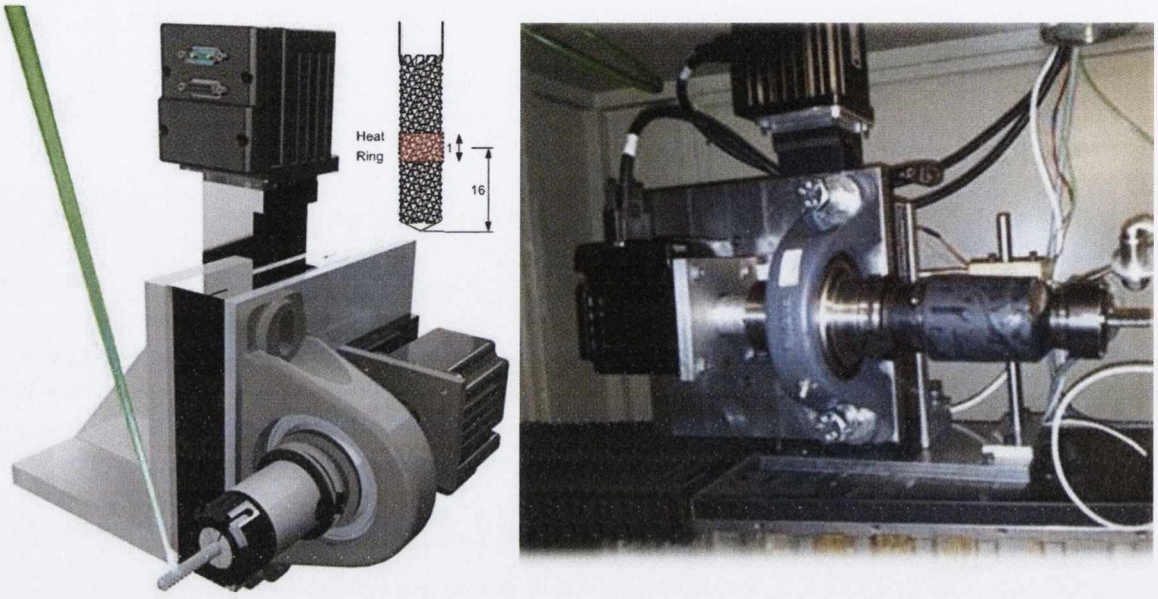

Figure 3.42: (left) Laser rig conceptual design and (right) the actual laser rig with 2-axis motion.

The first element consists of a conical tool holder mount, inserted into a ball bearing pillow block. The ITT system, i.e. cutting tool and tool holder, inserts via the CAT40 shank of the tool holder into the mount and is bolted into position using a customised bolt-shaft. This bolt-shaft has a machined shaft in the opposite direction to the tool holder. A customised motor coupling connects the shaft of the motor to the bolt-shaft to enable highly accurate velocities to be maintained with minimal eccentricity in the system.

The second element consists of a vertical linear mechanical bearing, ball-screw stage, driven by a second motor. Attached to this is a base plate onto which the housing for the tool rotation motor is fixed.

The combination of these two elements is seen via the connection of the tool rotation motor from the first element to the motor housing on the second element.

The experiment was setup as shown in Figure 3.43. A Laser Line IS3000W diode laser was used to perform the dynamic characterisation tests on the ITT sensor. A continuous wave of photons of 800 to 980 nm wavelengths was used as the heat source contacting an area of 1mm x 0.35mm on the tool surface at a focal length of 200mm. The horizontal 2-axis CNC stage and the vertical axis on the customised rig comprised the 3-axis system used to

locate the cutting tool at the laser focal point in 3D space. Due to the wavelength of the photons being beyond that of visible light, a positioning system, comprising a cap and class 2 laser pointer in a precise vertical orientation, was fitted to the head of the laser to locate the 2D horizontal position of the spot, while the focal length was taken from the technical documentation of the laser.

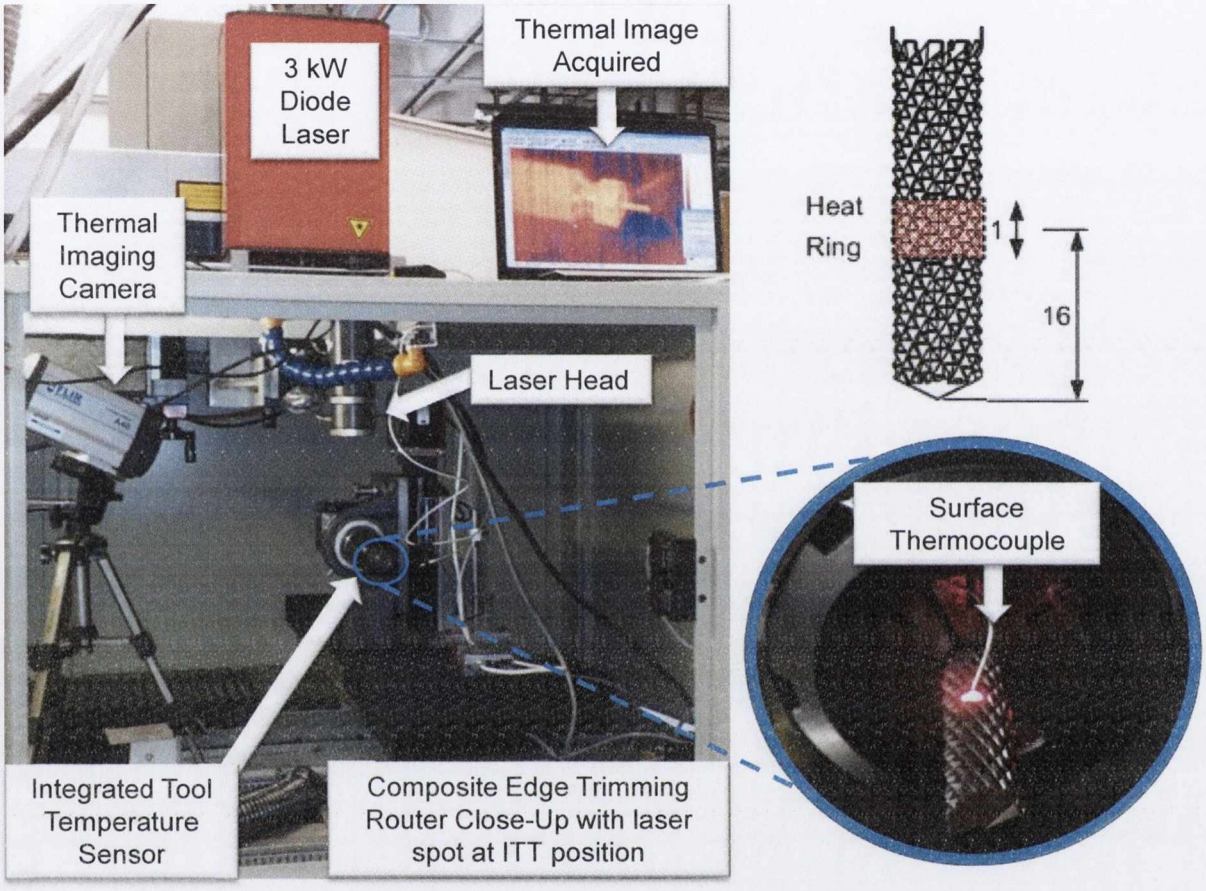

Figure 3.43: Setup for the experimental characterisation of the ITT sensor using a controlled heat source from a diode laser.

Careful attention was paid to locating the laser spot on the cutting tool in order to precisely quantify the effect of the location of the heat source (Q_{in}) along the axial length of the tool. A K-type sheathed thermocouple was placed at the boundary of the laser spot area in order to obtain an approximation of the tool surface with which to compare the ITT sensor result in initial setup tests. This is extremely useful for determining the perception capabilities of the ITT sensor for varied axial cutting strategies, i.e. changing the surface of the tool in contact with the workpiece, throughout the cutting process.

The measurement equipment used during this experiment is listed in Table 3.13.

Table 3.13: Measurement Equipment used in this experiment

Tool surface sensors used	Internal tool sensors used
K-type Sheathed thermocouple (0.075mm diameter) Thermal IR camera (position = 700mm from tool surface; ε = 0.25)	ITT sensor

3.5.4 Data acquisition and signal processing

The data was acquired through two main channels of data acquisition (DAQ) system:

- **NI 9213 thermocouple module:** Used to acquire the data signals for the *wired* thermocouples used in the static testing phase and for ambient measurements in all experiments.
- **KMT PCM module:** Used to acquire the voltage data from the *wireless* ITT thermocouple sensor.

The software used to synchronise and acquire the signals was LabVIEW SignalExpress using a sample rate of 40Hz. This sample rate was selected specifically in order to ensure that maximum information was obtained, i.e. conforming to the Nyquist criterion, whilst avoiding the effects associated with electrical noise found at 50Hz.

A systematic approach, illustrated in Figure 3.44, was taken to convert the *raw data* into meaningful information via calibration fitting, signal conditioning and feature extraction from individual experimental runs and combining the results of such features into a statistical summary plot to describe the overall behaviour of the sensor response.

Customised feature extraction and analysis tools were generated using Matlab in order to obtain quantitative data relating to the associated response variables for specific phases in testing.

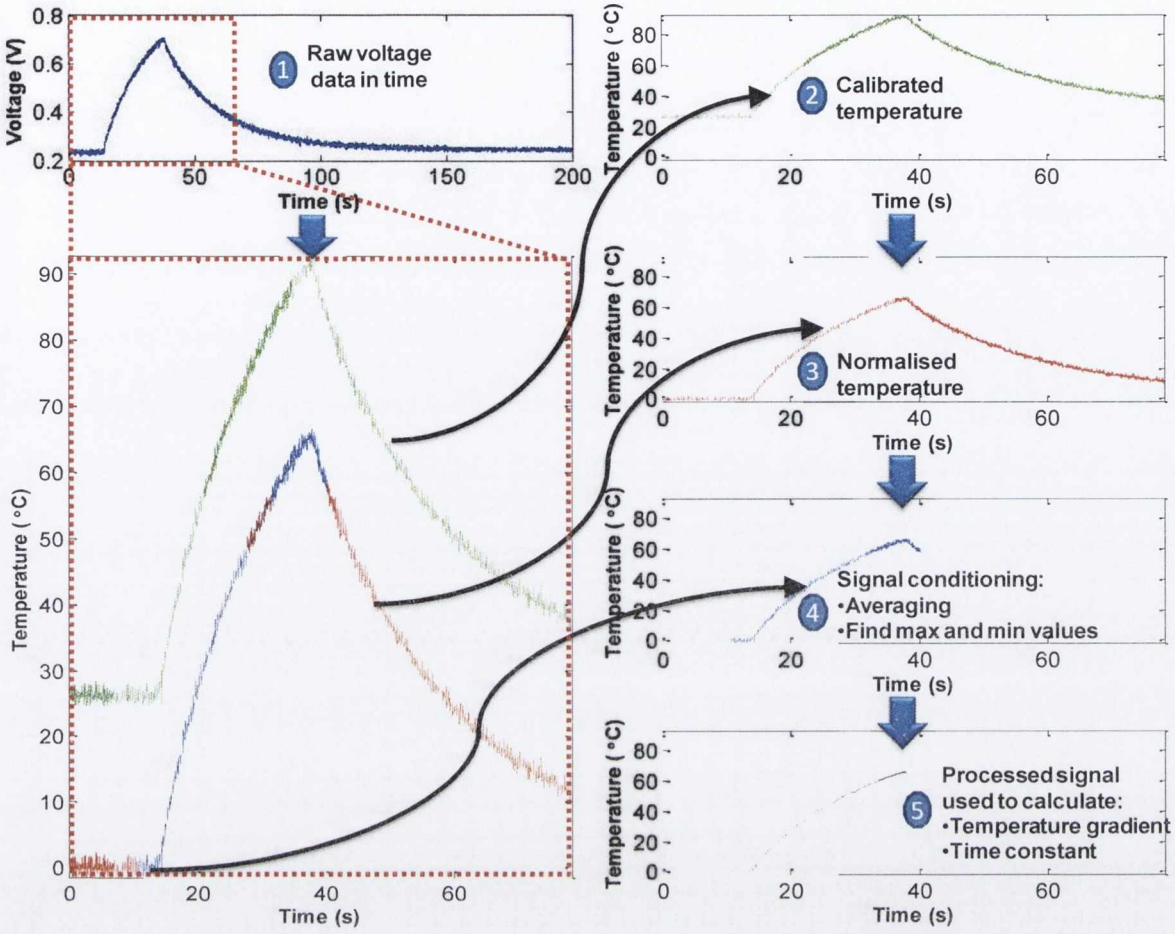

Figure 3.44: Signal processing method used to extract response data.

3.5.5 Results and discussion

Validation of finite element model

In order to begin validation, laser power values used in experiment 3.1 were converted into heat flux values, where:

$$Q = \frac{P}{A}$$

Where Q is the heat flux W/m^2, P is the heat power and A is the area over which the heat is applied. In the initial experimental plan, values of 10W, 50W and 100W were to be used for the experiment. However, when these values were submitted to the LaserLine diode laser as nominal values, the recorded power from the experiment varied from the input values entered. The actual power supplied by the laser the uncertainty of the sensor recording the power was ±1% indicating reliable power and heat flux data. Due to the complex, non-linear nature of the cutting tool, an approximation for the area was obtained using the model generated in Pro-Engineer. This approximation is based on the assumption of infinite rotation speed, i.e. an effective heat flux is experienced over the entire external circumference of the tool within the heat ring simultaneously due to the high rotation speed used. This assumption is made due to the high cutting speeds used in CFRP milling, typically between 5000rpm – 10,000rpm, for this cutting tool. The axial thickness along the length of the heat exposed surface area is determined by the laser spot width, oriented perpendicular to the tool axis to produce a 1mm width for this experiment. Although the previous heat flux calculations were based on the circumference of the tool using the diameter to approximate a value, the actual surface area value was calculated using the built-in area calculator in Pro-Engineer was 3.8×10^{-5} m^2.Table 3.14 shows the values of expected and actual power generated during experimentation, as well as the resulting heat fluxes.

Table 3.14: Experimental laser heat power values and corresponding heat fluxes.

Laser Heat Power (W)	*Heat Flux (kW/m^2)*
23	600
45	1200
107	2800

Heat flux values within the ranges stated in Table 3.14 were applied as an input boundary condition to the FE model. The uncertainty of the sensors was assessed experimentally using repeated runs of the same conditions to obtain the mean and standard deviation of the response. The deviation is clearly displayed in Figure 3.45. From the data in this figure, it

was determined that an approximation of ± 5 % would represent the uncertainty for the range of temperatures being investigated. The uncertainty is shown to reduce as the heat flux into the tool increases, dropping to approximately 4 % for the 2800kW/m^2 case. The same uncertainty level of approximately± 5 % was determined for the IR camera response.

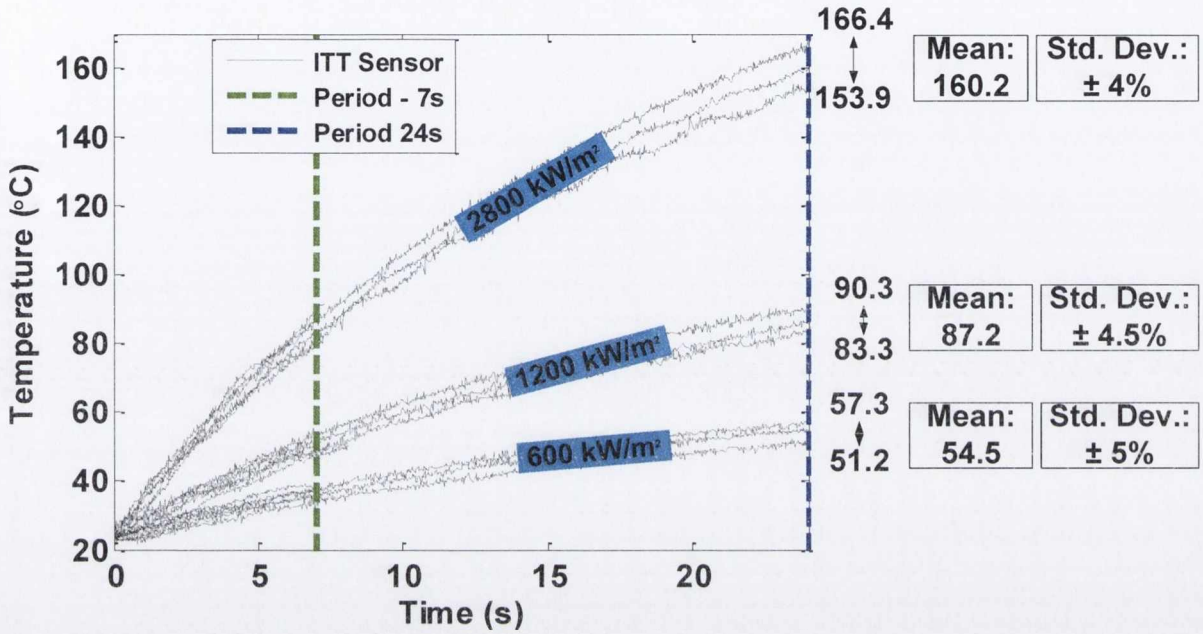

Figure 3.45: Plot of the ITT sensor experimental results for repetitions to determine the sensor uncertainty.

The laser experimental data from the 2000rpm rotation level was obtained for the ITT sensor and the IR camera in combination with uncertainty data as shown in Figure 3.46. The temperature results of the simulated temperature response from the developed FE model were also obtained at both the tool surface and ITT sensor position within the tool, as shown in Figure 3.47. These temperature profiles were then compared Comparing the results of the experimental and modelled time-history curves, shown in Figure 3.46 and Figure 3.47 respectively, there is an indication that for a heat flux boundary condition of 1200 kW/m^2 applied to the model, the simulation result shows a 1.2 % deviation from the ITT sensor response at t = 24 s. The difference at the surface is greater at approximately 10 %. While these graphs show the comparison between FE simulation and laser experiment for a heat flux boundary condition of 1200 W/m^2, the comparison was performed across the broader range 600 W/m^2 < q < 2800 W/m^2. The summary plots for the range of heat flux boundary condition values for experimental and FE are presented in Figure 3.48 and Figure 3.49 respectively.

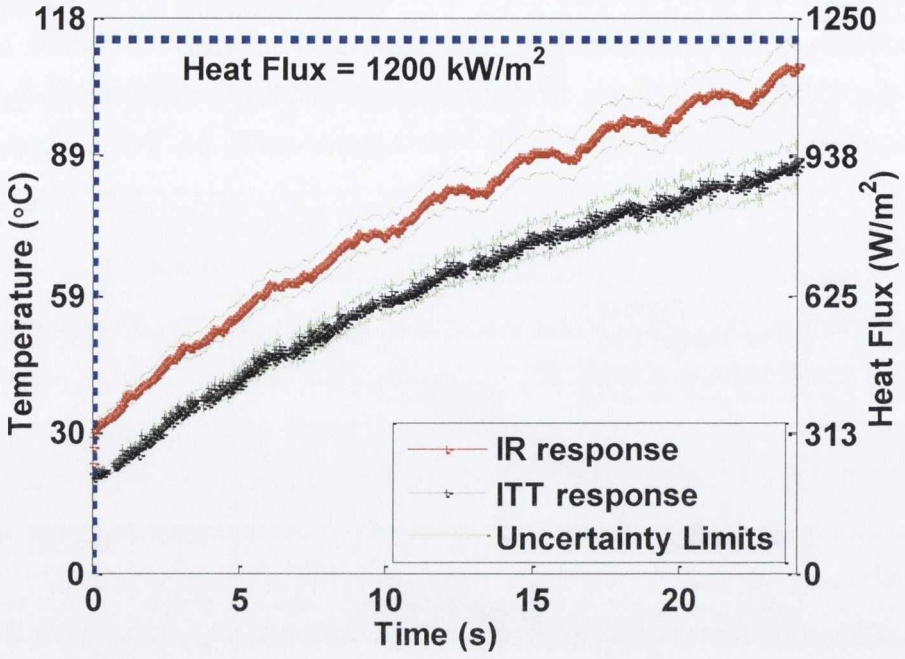

Figure 3.46: Laser experiment temperature response of IR and ITT sensors to a heat flux stimulus of 1200kW/m^2.

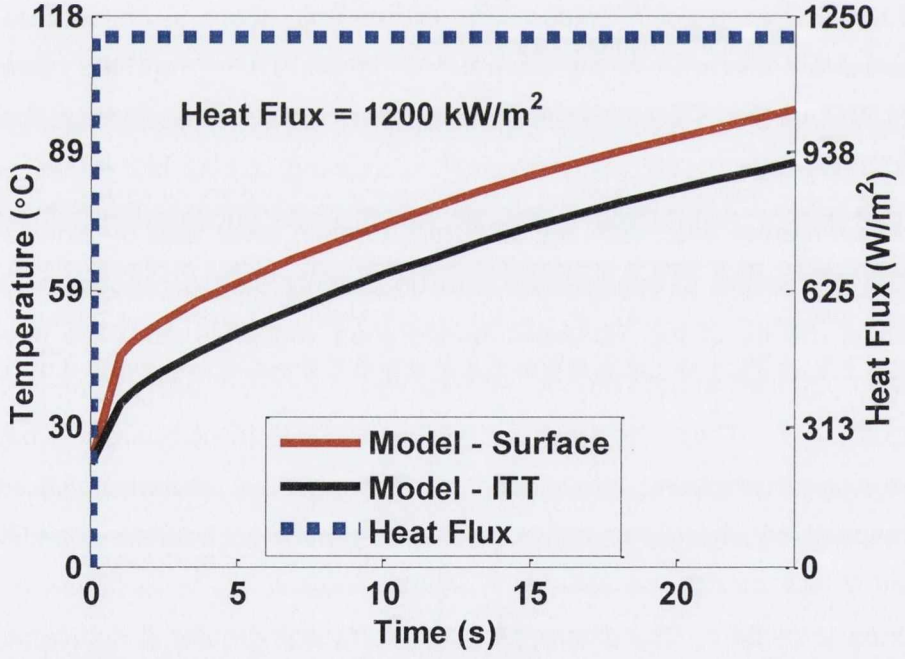

Figure 3.47: FE simulated temperature response at surface and ITT location within the cutting tool to a heat flux stimulus of 1200kW/m^2.

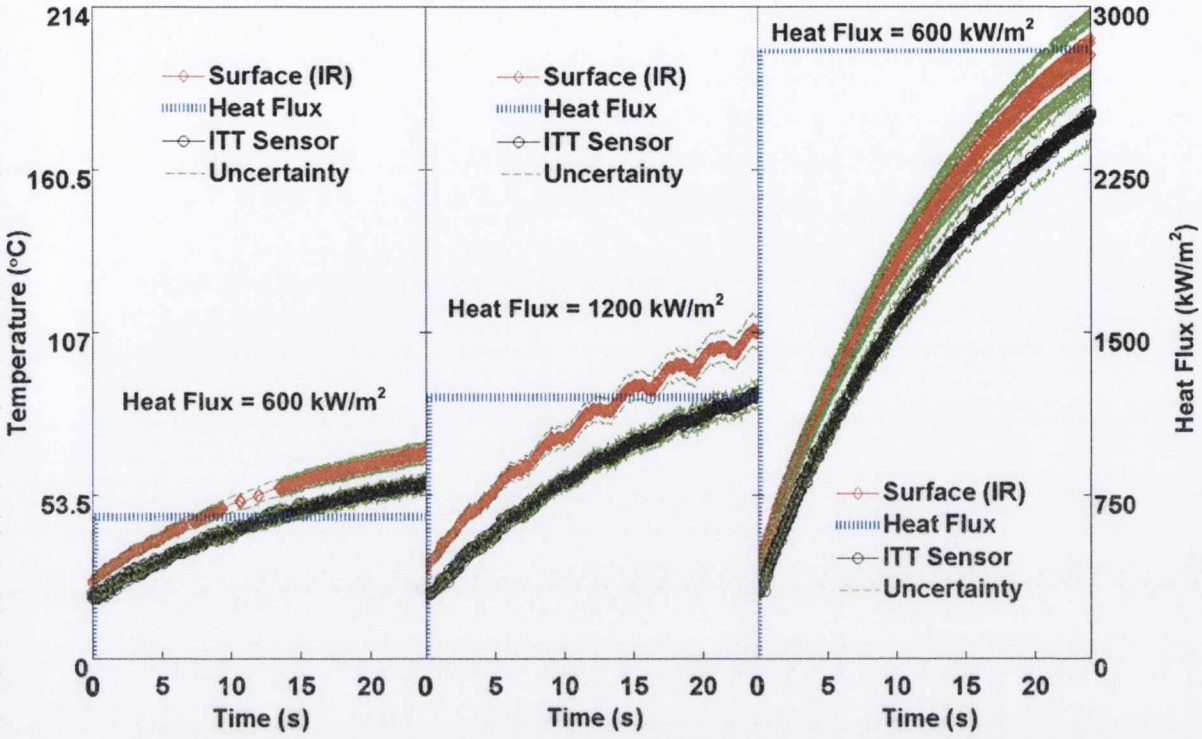

Figure 3.48: Comparison between experimental time-history results for (left) 600kW/m^2, (middle) 1200kW/m^2 and (right) 2800kW/m^2 heat fluxes.

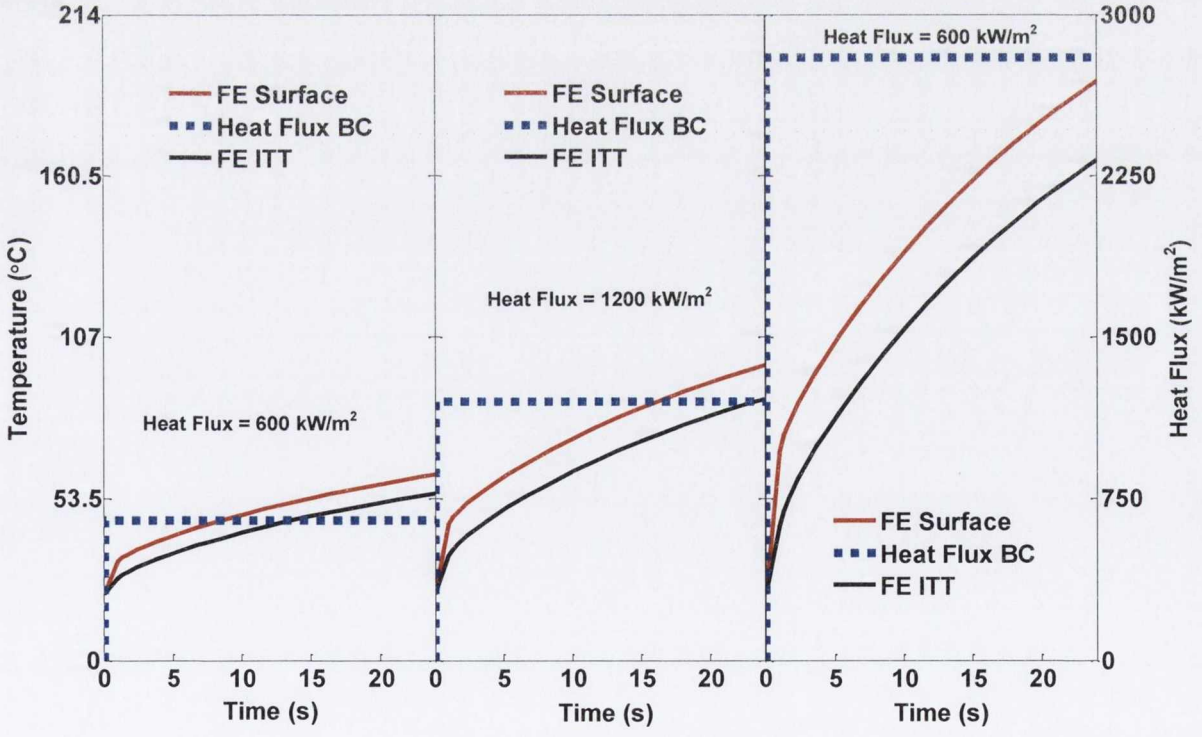

Figure 3.49: Comparison between FE simulation time-history results for (left) 600kW/m^2, (middle) 1200kW/m^2 and (right) 2800kW/m^2 heat fluxes.

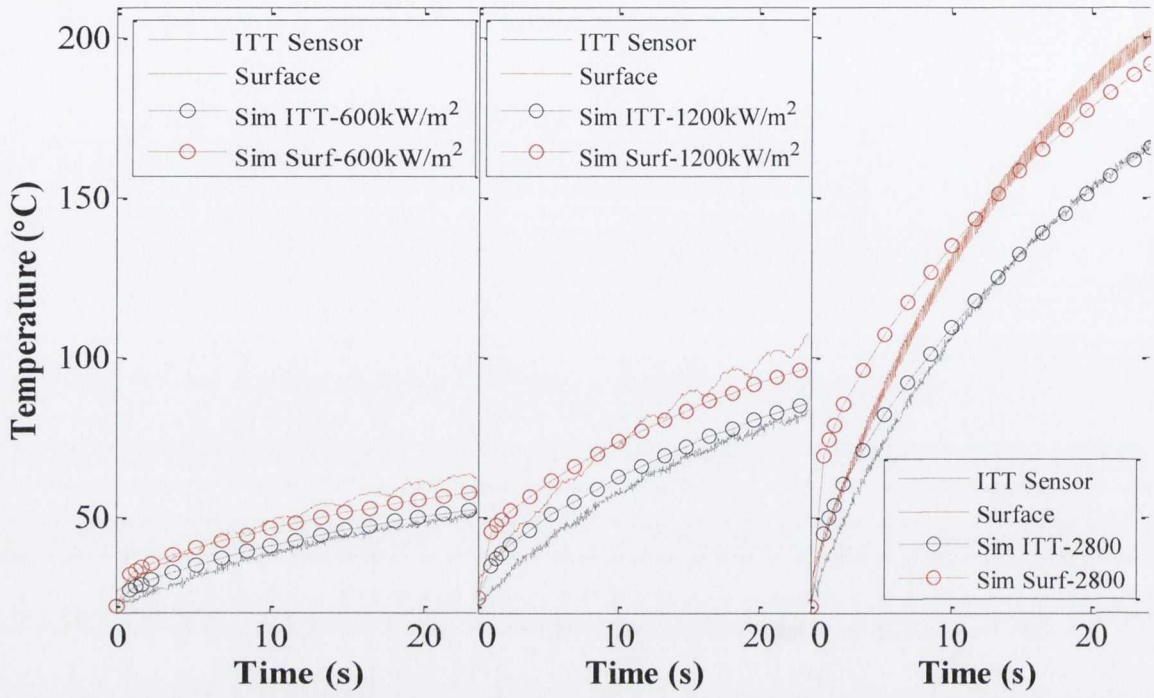

Figure 3.50: Comparison between experimental and FEA results for (left) 600kW/m^2, (middle) 1200kW/m^2 and (right) 2800kW/m^2 heat fluxes.

From Figure 3.50, it is noted that there is strong agreement between experimental and FEA, indicating the validity of the model and boundary conditions used for this range of heat flux boundary conditions. Interestingly, the simulation time-history consistently over-predicts the temperature from the sensor at both the surface and the ITT sensor for $t < 5s$. This behaviour is potentially due to the thermal properties of the tool which dictate both the heat capacity of the tungsten carbide and heat diffusion through this material.

Heat flux, heating period and rotation speed effects

The average results of the 3 repetitions of the experiment are provided in Table 3.15.

Table 3.15: Results from experiment 3 – rotation and heat variation – 1 rep shown.

Experimental parameters				*Uncalibrated and calibration results*		
Design Point	**Heat Period (s)**	**Heat Rate (W)**	**Rotation (rpm)**	**Max. ITT Temp. (°C)**	**Adjusted FE Temp. (°C)**	**Diff in Temp. (°C)**
1	7	10	20	42.3	54.6	12.4
2	7	10	200	38.3	46.8	8.6
3	7	10	2000	42.9	53.0	10.1
4	7	50	20	54.3	72.2	17.8
5	7	50	200	55.7	62.9	7.2
6	7	50	2000	53.2	62.2	9.0
7	7	100	20	96.0	119.9	23.9
8	7	100	200	92.9	121.1	28.3
9	7	100	2000	89.9	105.2	15.3
10	24	10	20	59.2	68.9	9.7
11	24	10	200	58.7	64.9	6.3
12	24	10	2000	61.3	74.4	13.1
13	24	50	20	88.9	109.5	20.7
14	24	50	200	99.0	111.8	12.8
15	24	50	2000	90.4	111.3	20.9
16	24	100	20	160.0	195.0	35.0
17	24	100	200	162.6	203.3	40.7
18	24	100	2000	173.5	205.6	32.2

Figure 3.51 depicts the set of residual plots for maximum surface temperature predicted. In these plots, there is strong evidence showing that the data fits the criteria associated with Normality. Therefore the Normal assumptions underlying the statistical models used for the analysis of such a factorial design are accepted and any statistically significant results can be accepted as plausible. There is a point of interest when focusing on the *Versus Order* plot. In this plot, the initial observations appear to have negative residuals, while later residuals appear more positive. This gradual trend, while on a small scale, is potentially indicative of an increase in temperature during initial conditions. However, this upward shift in the data is countered by the randomisation used during experimentation.

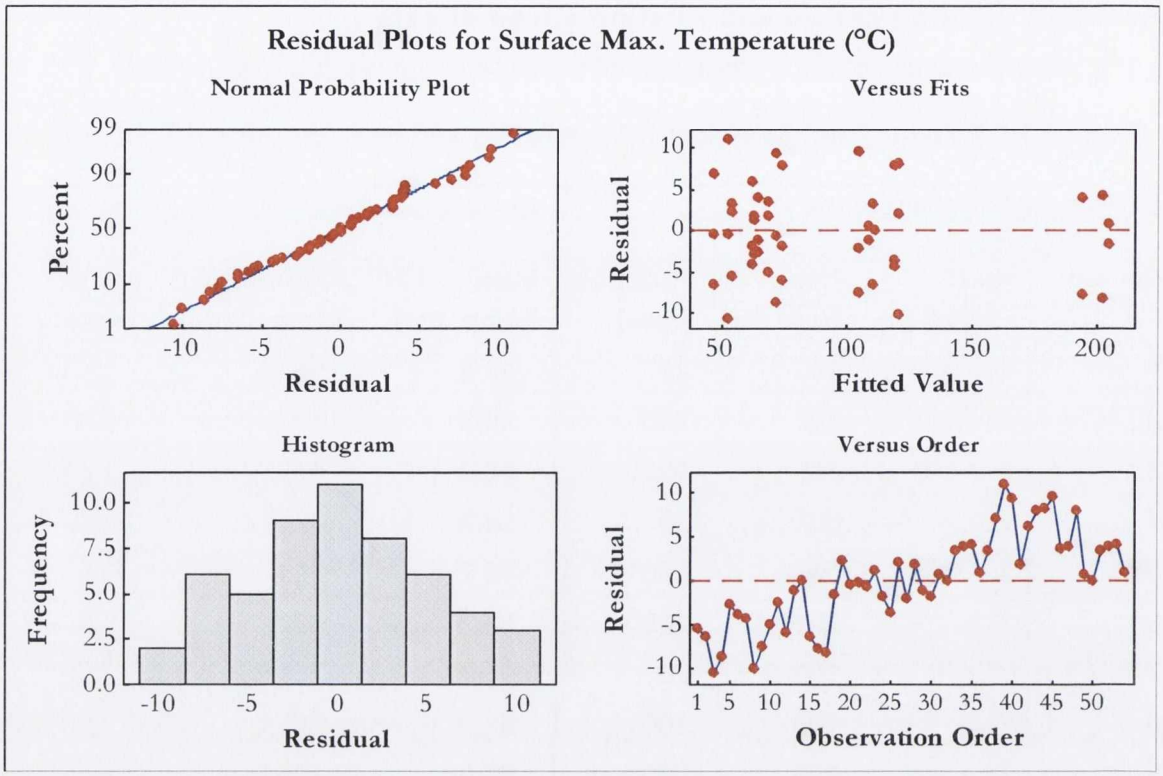

Figure 3.51: Residuals plots for maximum surface temperature on ITT sensor.

The main effects are presented in graph form in Figure 3.52, with supporting statistical information in Table 3.16.

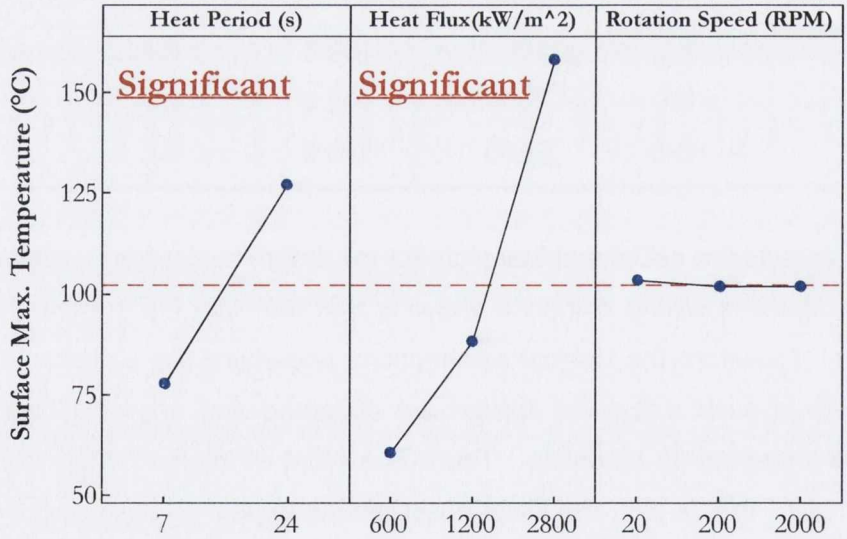

Figure 3.52: Main effects plot for the maximum estimated surface temperature.

Table 3.16: ANOVA results for the maximum estimated surface temperature.

Source	*DF*	*SS*	*MS*	*F*	*P*	*PCR*
Heat Period (s)	1	33250	33250	122.18	0.000	23.86
Heat Flux(kW/m^2)	2	91616	45808	168.33	0.000	32.75
Rotation Speed (RPM)	2	26	13	0.05	0.953	0.00
Error	48	13062	272			43.40
Total	53	137954				

The results indicate that heat flux has the most significant influence on temperature, with a percentage contribution ratio (PCR) of nearly 33%, and an almost linear relationship formed over the range investigated. As expected, the period over which heating takes place is also seen to cause significant change in the maximum temperature experienced by the cutting tool. Interestingly, there is no statistically significant effect on the maximum temperature achieved for the range of rotation speeds tested. The level of confidence on this statement is 95%. The overall standard deviation, across all data for this analysis, was 16.5°C, while the R-sq value of 90.5% indicates that the variance within the process is suitably explained by the factors and chance variation components of the ANOVA table.

An analysis of the data on a more detailed level using an individuals plot, shown in Figure 3.53, provides further evidence as to the behaviour of the sensor. Figure 3.53 presents all of the data points obtained during the experiments. The data is separated into two separate curves, for the two different heating periods used, 7 s and 24 s. For each of these periods, the data points corresponding to the heat flux levels applied are plotted. The variation between repeats is clearly displayed, along with the mean value for each level, which is represented by a blue dot. While there is some variance in these results, there are also visible trends of increasing temperature with increases in heat flux and heating period.

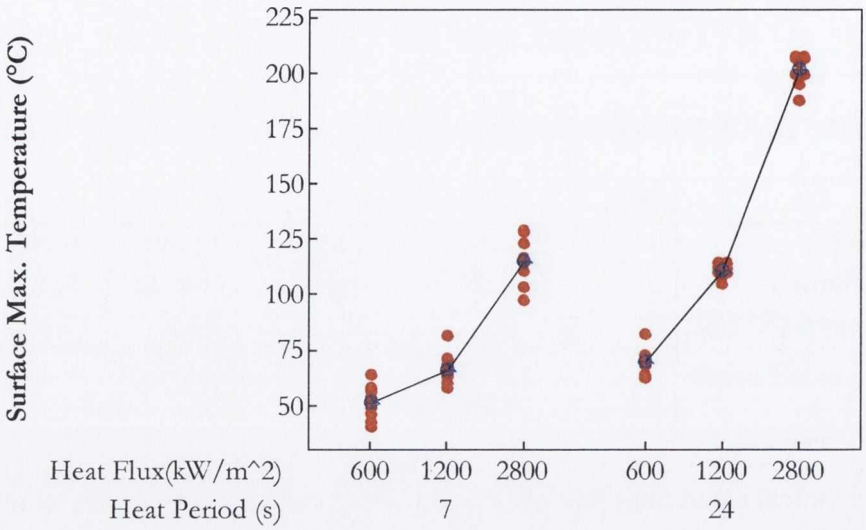

Figure 3.53: Individuals plot of surface maximum temperature vs heat period, heat flux.

This plot indicates the magnitude of the trend associated with both variables and the repeatability associated with each trend. The relationships of the measured temperatures and significant variables in this investigation, was approximated using a linear regression formula generated in Minitab as:

$$T_{Surface\ Max}\ (°C) = -10.9 + 2.92*\text{Heat Period (s)} + 0.0444*\text{Heat Flux (kW/m}^2)$$

In line with the overall ANOVA results, the average uncertainty of this prediction curve is ±16°C and the degree of fit with the current data produced an R-sq value of 90.5%, indicating a reasonable representation and potential for use in temperature prediction.

The main findings of this experiment are:

- The FE model provides a validated representation of the heat transfer process associated with the ITT sensor, as perceived by both a thermal imaging camera at the cutting edge surface and the embedded thermocouple within the tool.
- The effect of rotation on the response of the ITT sensor is negligible and therefore, the assumption of a constant heat ring boundary condition is a valid approximation of the heat transfer process.
- The thermal properties utilised in the FE model provide a good approximation of the real heat transfer process.

As a result of these findings, further investigations into the behaviour of the ITT sensor under a variety of conditions were undertaken, which are described in the coming section.

3.6 Parametric investigations of geometric factors on heat diffusion

A parametric ANSYS APDL code, based on the validated FE model from the previous chapter, was generated in order to determine the relationship between key factors such as axial depth of cut and axial location with respect to the sensor. Considering a heat ring applied at the axial location of the cutting interface along the length of the tool, i.e. L_a = 16mm, Figure 3.54 and Figure 3.55 illustrate the temperature response at the tool surface where such a heat ring is applied, T_S, and the response at the embedded location of the ITT sensor within the tool, T_{ITT}. The T_S and T_{ITT} time history curves match to within 5 % of each other for the case L_a = 16mm; a_p = 5mm, shown in Figure 3.54.

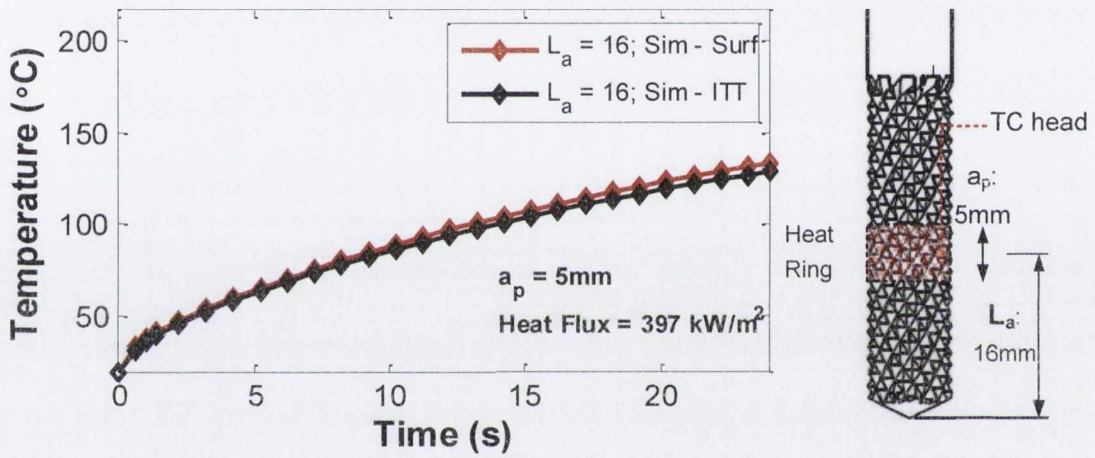

Figure 3.54: FE modelled response of the ITT system for L_a = 16 and a_p = 1mm.

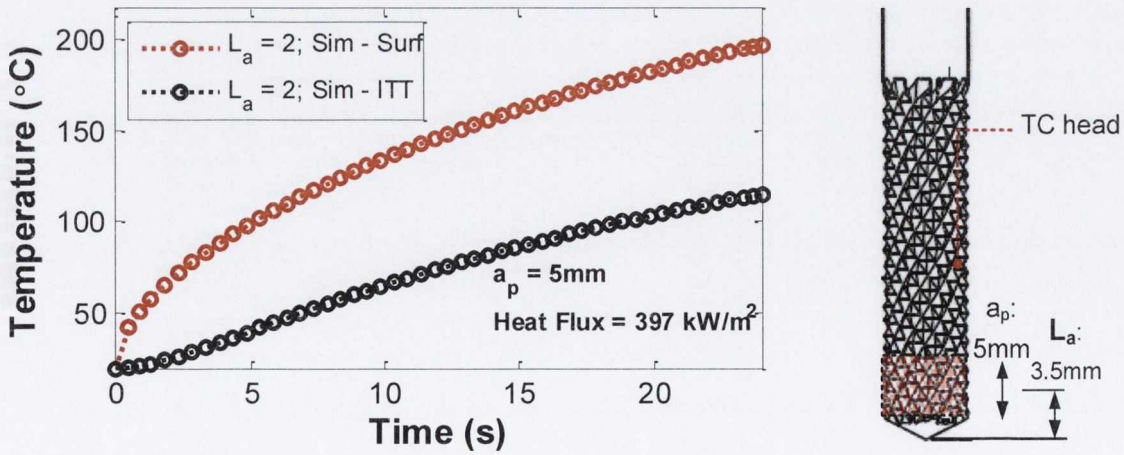

Figure 3.55: FE modelled response of the ITT system for L_a = 3.5 and a_p = 5mm.

In contrast to this, there is substantial deviation between the time-history temperature curves for the case of L_a = 3.5mm; a_p = 5mm, shown in Figure 3.55. In addition to the large deviation between T_S and T_{ITT} in Figure 3.55, there is also an increased surface temperature when the heat ring is located at the tip of the tool. This is hypothesised to be due to the flow of thermal energy through the cutting tool. Interestingly, for the case shown in Figure 3.54, where L_a = 16mm, the heat flux applied at the boundary is able to spread in both axial directions through the 3D structure of the tool. However, for the case shown in Figure 3.55, where L_a = 3.5mm, as the heat must be conducted upwards only. The result of this is that if the heat cannot travel quickly enough away from the source of generation at the cutting interface, a heat choking effect can occur, raising the temperature in the area where the energy is impeded.

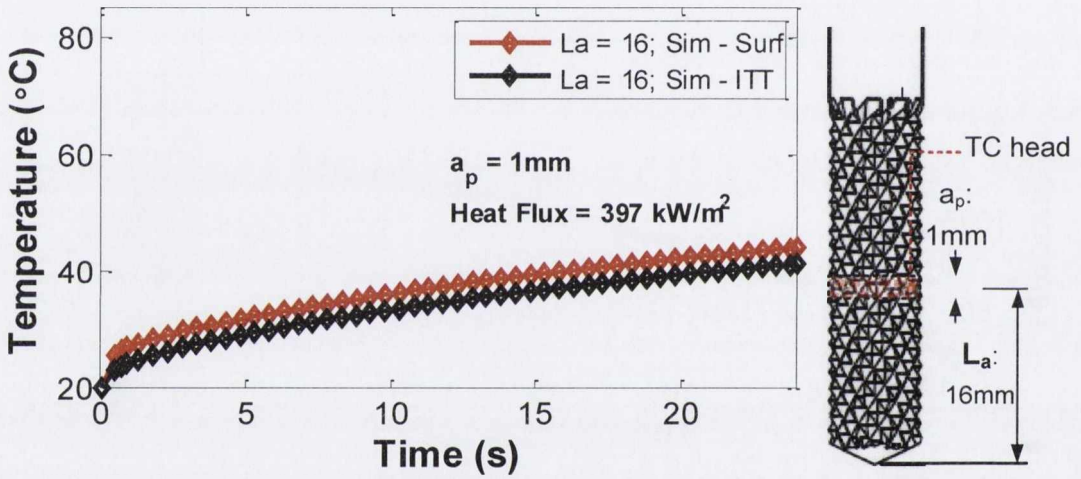

Figure 3.56: FE modelled response of the ITT system for L_a = 16 and a_p = 1mm.

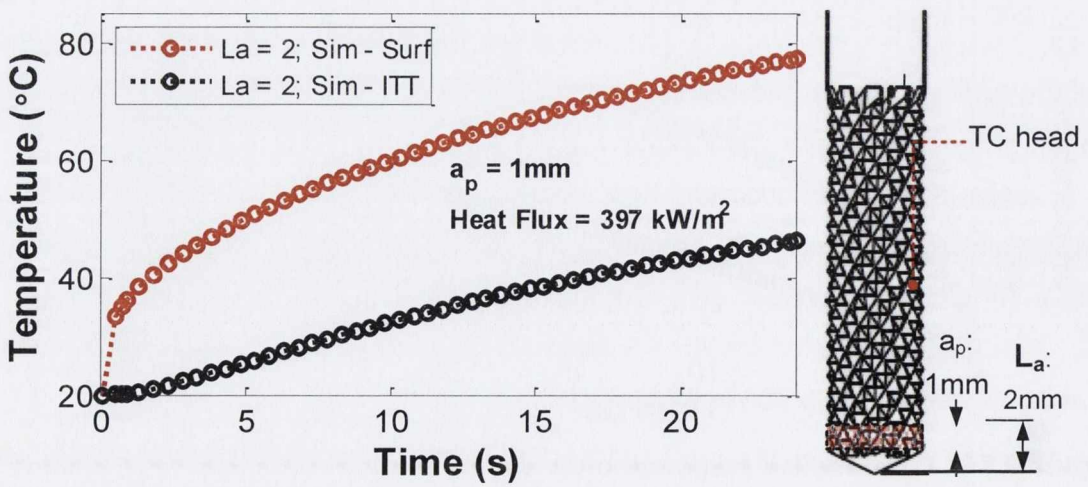

Figure 3.57: FE modelled response of the ITT system for L_a = 3.5 and a_p = 1mm.

Figure 3.56 and Figure 3.57 show the same trends of large deviations between T_S and T_{ITT} and a substantial increase in the magnitude of T_S as a result of tool tip location. Also interesting to note is the effect of variation of a_p. As a_p is increased from 1mm to 5mm there is an increase in the maximum surface temperature reached of approximately 100°C - 120°C. This is in comparison T_{ITT}, which experiences slightly lower temperatures for the case when the heat ring is centred at the tool tip, i.e. L_a = 2 / 3.5mm as opposed to the sensor location, i.e L_a = 16mm.

3.6.1 Effective heat flux – Is this enough?

In modelling this problem until now, it has been assumed that there is a constant, annular heat flux boundary condition at the cutting zone. However, in reality, due to the large number of cutting edges on the complex tool geometry, only a small portion of the tool is in contact with the workpiece at any one time. To counter this, the tool is rotating at such a rapid speed that it is unlikely that any single tool cutting edge will cool down significantly, via any form of heat transfer, before once again being exposed to the workpiece. From this it is noted that while the tool is not technically under constant flux exposure, a negligible amount of energy is being lost by an individual point on the exposed surface during this process before further heat is supplied upon rotation of the tool to the same point. Therefore, the question is "Is it enough to know the effective heat flux value of the process, or will a different heat flux shape result in the same ITT sensor response?" From the results obtained in this research it appears that this is not the case. However, being pragmatic about it, comparisons must be made with the alternative boundary condition in order to ensure that there is no such issue.

In previous literature, investigations have been performed to determine the heat flux associated with numerous cutting operations. At the basal level, Samadi *et al.* [150] considered the orthogonal turning of steel and the associated heat flux. In this investigation, the authors used an assumption of a triangular shape for the heat flux, while in an earlier investigation, Yvonnett *et al* [195] used a similar inverse heat conduction technique (IHCT) to the technique employed by Samadi *et al*, to predict the temperatures during the turning of Aluminum Alloy 6060-T5. In this work, the heat flux and resulting isotherms were restricted using the divided tool technique and the temperature in this restricted zone was measured using a 1mm diameter k-type thermocouple, placed 2.25 mm from the cutting interface.

A key point of interest from the latter described results of the sensor calibration experiments is to determine an appropriate shape for the heat flux associated with the

edge trimming of CFRP, for the specific tool geometry associated with such a process. This is not clearly established in literature and would yield the three dimensional temperature distribution throughout the tool, allowing for a surface and ITT temperature location value to be determined accurately. Therefore, in the following section, the approximation of a constant heat flux is investigated through the use of CFRP edge trimming experiments.

3.7 Temperature perception and the CFRP trimming process

From the previous sections of this chapter, a tool has been developed in order to obtain an advanced perception of a temperature on the outer section of a cutting tool from an embedded location. This was achieved through the use of an FE model tuned to the specific requirements of a dynamic heat transfer process. Such an advanced perception of the temperatures in a rotating cutting process is advantageous as there is potential to gain further understanding of the role of heat in the energy distribution during cutting. In a process such as CFRP milling, where the workpiece is particularly susceptible to thermal damage, such temperature and energy information could be used to develop a relationship between machining parameters, process temperatures and workpiece surface integrity. This will be explored in the following chapter.

4 APPLICATION OF ITT SENSOR IN CFRP MILLING INVESTIGATIONS

The application investigations focussed on the machining of CFRP materials and examined the performance of the sensor system in detail. Aspects investigated include:

- In-cut heat flux boundary conditions
- Axial depth of cut variations
- Axial cutting location variations
- Feed rate variations

Initially real cutting data was gathered via the ITT sensor and a well-established surface temperature technique, thermography, simultaneously to assess the validity of the FE model (FEM) in predicting the temperature at the tool surface. The validated FEM was incorporated in conjunction with real cutting data to explore the validity of hypotheses developed regarding the behaviour of the cutting tool as a thermal system during cutting. It is also used in order to determine the effect of the aforementioned parameters on the workpiece surface integrity.

Since the laser investigations, used to validate the model for a known heat flux, are based on the assumption of a near constant exposure to the heat source, the decision was made to maintain cutting speed at the maximum possible based on tool manufacturer recommendations and industrial practice.

To further ensure the FEM assumption of a *constant heat ring*, a roughing cut was used to maximise the surface area exposed at the heat input boundary. In a roughing cut, the entire cutting tool is submerged into the workpiece, therefore making the radial depth of cut equal to the diameter of the cutting tool. This maximises the tool engagement and minimises any errors associated with the assumption of a constant heat ring boundary condition for simplicity during modelling.

4.1 Cutting tool selection

The cutting tool selected for this research was based on recommendations from industry. The low cost, acceptable quality and reasonable tool life were cited as the primary reasons for using the uncoated deburring style router, shown previously in section 2.5.2. An 8 mm SGS router was selected for this research as this was also a standard size used for edge trimming, particularly in aerospace applications. The recommended machining parameters for this tool are cutting speed: 150 – 200 m/min; feed rate: 1500 – 2000 mm/min.

4.2 CFRP Workpiece materials and material analyses

The CFRP material used in this research is called LTM12, detailed in Appendix 8 and is manufactured by Advanced Composites Group (ACG). LTM12 is a tooling prepreg capable of curing at low temperatures to form an epoxide based resin system, which can be post-cured to produce high temperature (200°C) composite tools for moulding applications [9]. The method used to manufacture the test panels used in this investigation is described in Appendix 9.

Analysis of key parameters governing the temperature-dependent properties of a material was performed to determine sensitivity to thermal damage. In the case of CFRP composites, the glass transition temperature is an important parameter in understanding the behaviour of this material through temperature change. Dynamic mechanical analysis and thermal degradation analysis were therefore employed to study and characterize various properties of the materials provided by Lola Composites for machining investigations in this research.

Dynamic mechanical analysis (DMA)

DMA is used to study the viscoelastic behavior of polymers and polymer-based composites. [196] The general method associated with this technique involves applying a small deformation to a sample in a cyclic manner. This allows for the material's response to stress, temperature, frequency and other values to be studied. [196] The results of a DMA can indicate changes in stiffness (modulus) and damping (Tan δ) and such data is used to obtain modulus information.[196]

A DMA machine operates by applying a sinusoidal deformation to a sample of specific geometry (40mm x 8mm x 1mm in this case). The sinusoidal wave, which causes the deformation, is generated using a force motor and transmitted to the sample using a drive shaft. [196] The applied mechanical load (stress) brings forth a corresponding strain (deformation) whose amplitude and phase shift can be found as shown in Figure 4.1.

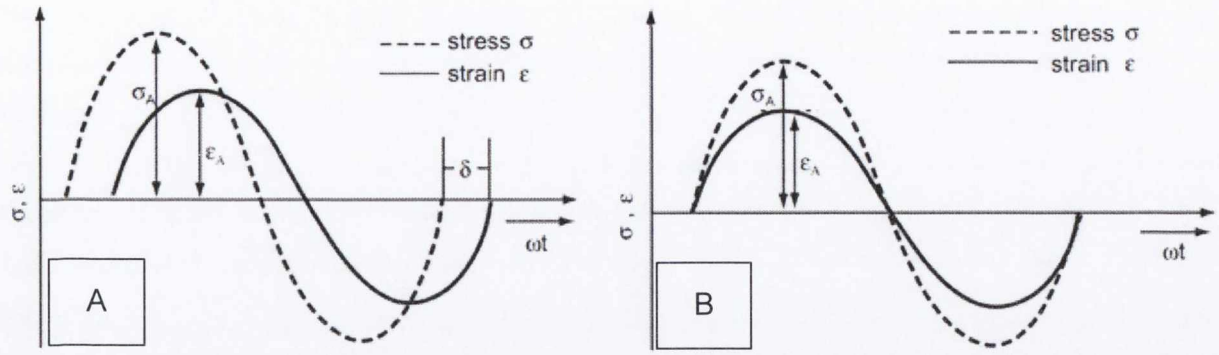

Figure 4.1: A) Stress-Strain curve of an elastic material and B) Curve of the sinusoidal oscillation and response of a linear-viscoelastic material.

Due to the use of the sinusoidal wave, the resulting modulus is expressed as an in-phase component (storage modulus – E' or G' depending on the mode of deformation) and an out of phase component (Loss modulus – E" or G"). The storage modulus represents the stored energy in a viscoelastic solid, i.e. the elastic portion whilst the loss modulus represents the energy dissipated as heat in a viscoelastic solid, i.e. the viscous portion. The ratio of the loss modulus to storage modulus is the Tan δ and is often referred to as damping. It is a measure of the energy dissipation of a material.

The complex modulus, E* is the ratio of the stress amplitude to the strain amplitude and represents the stiffness of the material:

$$|E*| = \frac{\sigma_A}{\varepsilon_A} \qquad \textbf{4.1}$$

The complex modulus is composed of the storage modulus E' (real part) and the loss modulus E" (imaginary part) as outlined in the following formulae:

$$|E*| = \sqrt{[E'(\omega)]^2 + [E''(\omega)]^2} \qquad \textbf{4.2}$$

$$E'(\omega) = |E*| \cdot \cos\delta \qquad \textbf{4.3}$$

$$E''(\omega) = |E*| \cdot \sin\delta \qquad \textbf{4.4}$$

$$\tan\delta = \frac{E''(\omega)}{E'(\omega)} \qquad \textbf{4.5}$$

The storage modulus, E', is representative of the stiffness of a visco-elastic material and is proportional to the energy modulus for a single, rapid stress at low load and reversible deformation. The loss modulus, E'', on the other hand is defined as "being proportional to the energy dissipated during one loading cycle. It represents, for example, the energy lost as heat, and is a measure of vibrational energy that has been converted during vibration and which cannot be recovered. " [197] Within these two definitions, the real part of the modulus

is used to review the elastic properties, and the imaginary part is used to evaluate the viscous properties.

The phase angle, δ, is the phase variation between the dynamic stress and the dynamic strain in a visco-elastic material subjected to a sinusoidal oscillation. In association with this, the loss factor, $\tan\delta$, is the ratio of loss modulus to storage modulus, measuring the energy lost in terms of recoverable energy. Therefore, this term represents the mechanical damping or internal friction in a visco-elastic system. The higher the $\tan\delta$ value is, the higher the non-elastic strain component of the material.

An example of a DMA analysis curve is shown in figure 3.14. At low temperatures, the molecules of this amorphous thermoplastic are so immobile that they are unable to resonate with the oscillatory loads, as the C-C bonds maintain rigid crosslinks, and therefore remain stiff. At higher temperatures, the molecular segments become readily mobile and have no difficulty resonating with the load. Interestingly, weakly cross-linked rubber has one crosslink for every 1000 atoms, while cured, brittle thermosets have one for every 20 atoms.

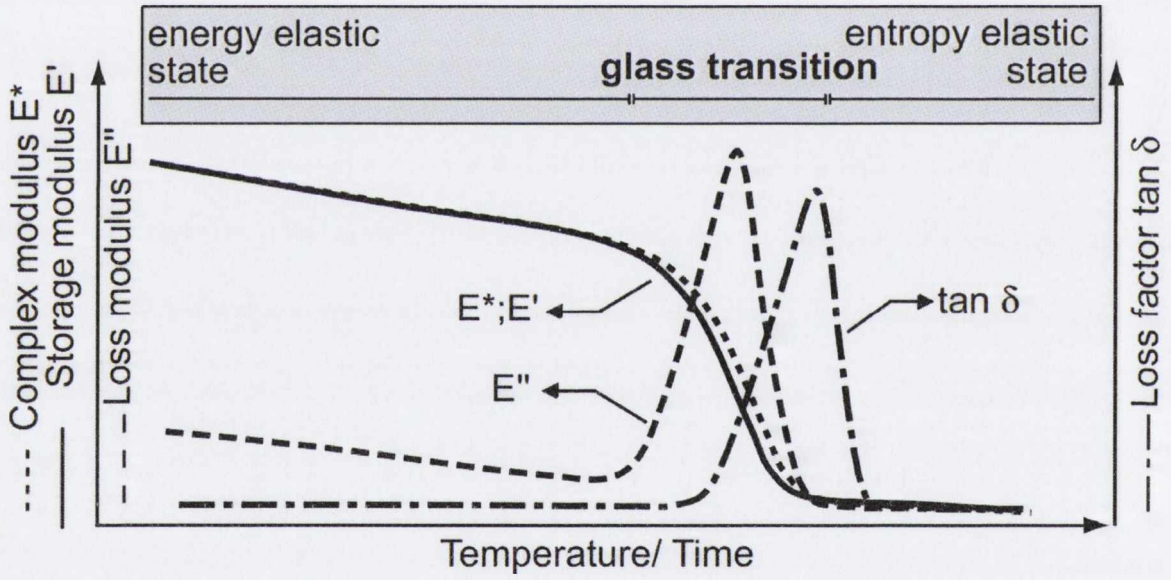

Figure 4.2: Plot of the typical DMA curves for an amorphous polymer such as rubber.

The material is described as *being in a glass state or energy elastic state* at the low temperatures, and in a *rubber* or *entropy elastic state* at elevated temperatures. The change from the glass state to the rubber-elastic state is called the glass transition. Unlike melting, the glass transition is not sharp, and as such a region known as the glass transition region (temperature range) is defined as that below which the material is glassy (i.e. hard and strong), and above which polymer becomes soft and loses its dimensional stability.

The glass transition temperature, T_g, is important from an engineering design, and indeed processing perspective, as it is directly related to the degree of cross-linking which exists within the thermoset matrix of the material. It is difficult to identify the T_g in thermosets

due to the effect of cross-linking on relaxation in the transition region. However, unlike elastomers and rubbers, thermosets such as epoxy have T_g values higher than room temperature.

The DMA results of this research are shown in Figure 4.3 for the LTM12 material. The storage modulus, representing the stiffness or elastic properties of the visco-elastic material, is shown in green on this plot. The material stiffness experiences a gradual decline between 30°C and 193°C from 40 to 35GPa. At 193°C, a more rapid decline in the material stiffness begins to occur. By the time the temperature reaches 235°C, the stiffness has reduced to 24GPa. Since the elastic property change is associated with the transition from a glass state to a rubber state, the glass transition region is estimated to begin at 193°C.

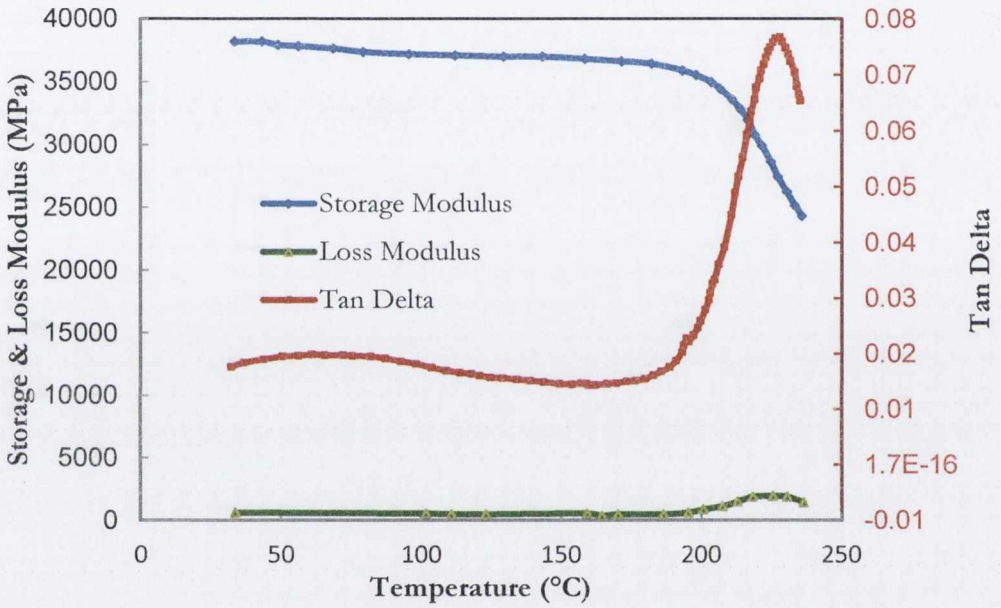

Figure 4.3: DMA provided by ACG Composites Ltd. for LTM12 prepreg system.

The loss modulus is used to evaluate the viscous properties of the material. The low steady-state of the loss modulus up to approximately 200°C indicates constant material properties prior to this point. However, beyond this temperature there is an increase in the vibrational energy, or the energy lost as heat during the loading cycle associated with the DMA test, within the material which peaks at a temperature of 224°C.

The ratio of the storage modulus to the loss modulus, represented in figure 4.24 as the Tan delta series plot, gives an estimate of the internal friction in the visco-elastic system. This value peaks at 224°C, which means that at this temperature the material experience its largest non-elastic strain.

Thermogravimetric Analysis (TGA)

TGA is a technique in which a constant static force is applied to a material. The material mass changes due to temperature increases, while time variations are monitored. This technique is used to determine the coefficient of thermal expansion (CTE) of a material and, as it shows the change of weight with relation to temperature, it can also be used to determine critical degradation temperature associated with a polymer.

A TGA was performed on the LTM12 CFRP specimen by the physics department in Trinity College Dublin. A Perkin Elmer Pyris 1 TGA thermo balance was used to perform the analysis. The TGA experiment involved heating the specimen from 30°C to 900°C at 10°C/min under air flow.

Figure 4.4 shows the results of the TGA, indicating that initial weight losses due to the release of volatiles and moisture within the specimen occur from approximately 140°C. Initial burning temperature is noted at 315°C, potentially due to the degradation of the curing agents and hardeners used in the polymerisation process, with 100 % weigth loss achieved at 750°C.

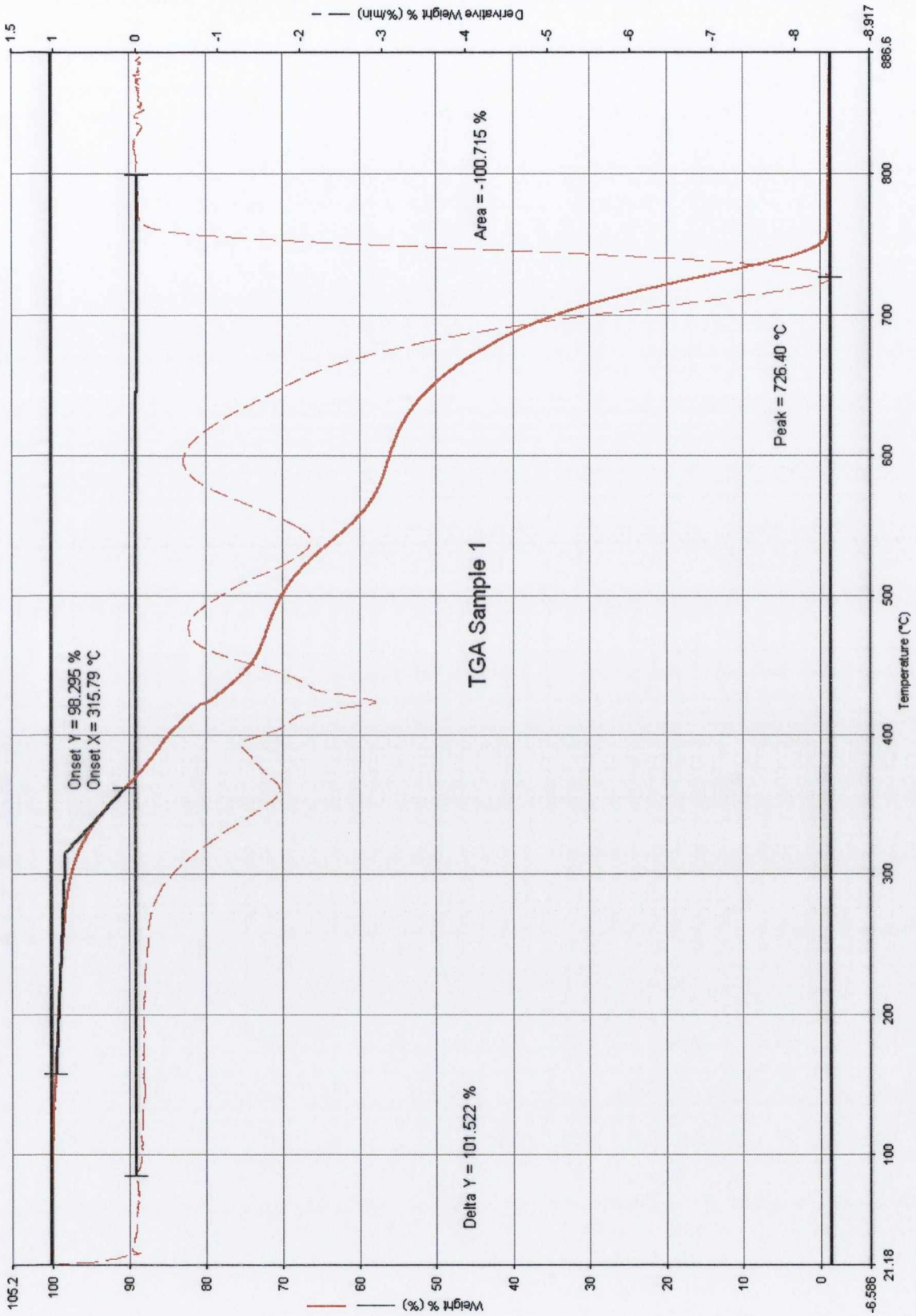

igure 4.4: TGA Results for LTM12 CFRP composite specimen. The solid line indicates % weight loss and dashed line represents the derivative weight %.

4.3 Equipment

The equipment and sensor used both during machining investigations and post machining to analyse the workpiece and tool are identified and briefly described in this section.

4.3.1 HURCO VM2 3-axis milling machine

The HURCO VM10 3-Axis milling machine, in the Advanced Manufacturing Technology Laboratory at Trinity College Dublin, was used in order to undertake experimental works. The work envelop capacity of this one-piece machine is 660mm x 406mm x 508mm. The maximum spindle speed is 10,000 rpm and this is controlled via HURCO's own-brand Max controller. As this machine is not typically designed for composite machining, it was customised by installing a chip extraction system and protective coverings for the moving parts of the machine axes. In addition, the machine was further customised with the fitting of mounting posts at carefully selected locations to allow the installation of sensors, i.e. the ITT sensor inductor/receiver and the thermal imaging camera.

Spindle Drive	11 kW
Spindle Speed Range	400 - 8000 rpm
AC Voltage Supply	400 V (3 phase)
Frequency	50 Hz
Machinable Area	1168 mm X 457 mm
Tool Changer Capacity	16
Table Load Capacity	550 kg
Machine Weight	4080 kg

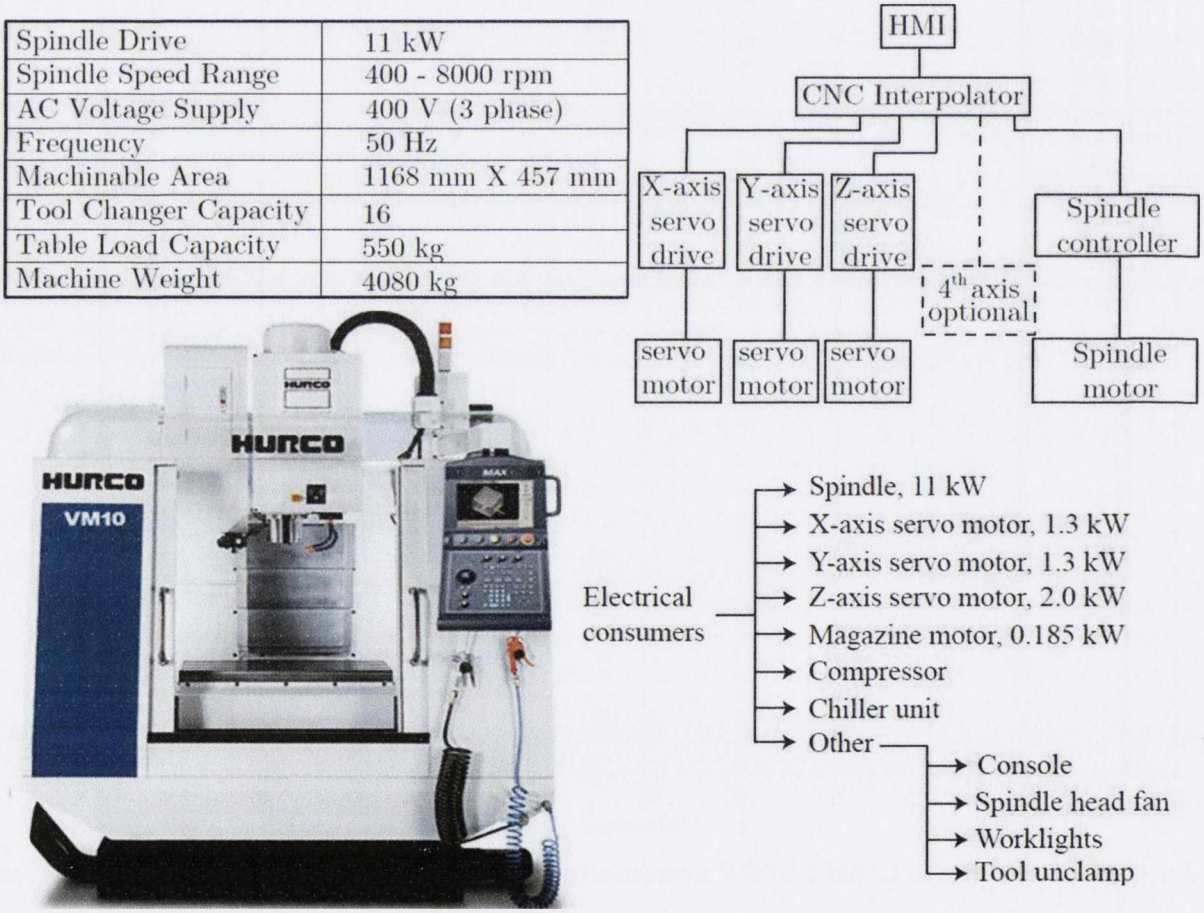

Figure 4.5: HURCO VM10 used to perform milling investigations on CFRP composites. [198]

The main specifications of this machine are described in Table 4.1.

Table 4.1: HURCO VM10 Specifications [198]

Specification	*VM10*
X, Y, Z Axis Travel, (mm)	660 x 356 x 457
Table Size (mm)	762 x 356
Max Weight On Table (Kg)	340
Peak Spindle Motor (Kw)	11
Max Spindle Motor Torque (Nm @ rpm)	73 @ 1,450
Rapid Traverse X,Y / Z Axis (M / min)	24/19
Tools	20 Cat 40
Positioning (mm)	±0.005
Repeatability (mm)	±0.0025
Machine Weight (Kg)	2,812

4.3.2 Vacuum chuck

In order to better replicate the machining practices used in industry, a polyurethane vacuum chuck, as illustrated in Figure 4.6, was manufactured. This adds additional dynamics to the system due to the mechanical stiffness of the polyurethane, which will have an impact on both the stiffness and force damping associated within the system. In a typical moulded component, due to the three dimensional shapes developed, the degrees of freedom of the component are constrained by the downward pulling force of the vacuum (Z-direction constraint) and the non-uniform conformance to the chuck in the horizontal planes (X and Y constraints). However, with flat specimens, the X and Y constraints were enforced using pins connecting the workpiece to the vacuum chuck. Therefore, holes were drilled into the workpiece at specific positions in order to allow for precise workpiece positions to be enforced during cutting experiments.

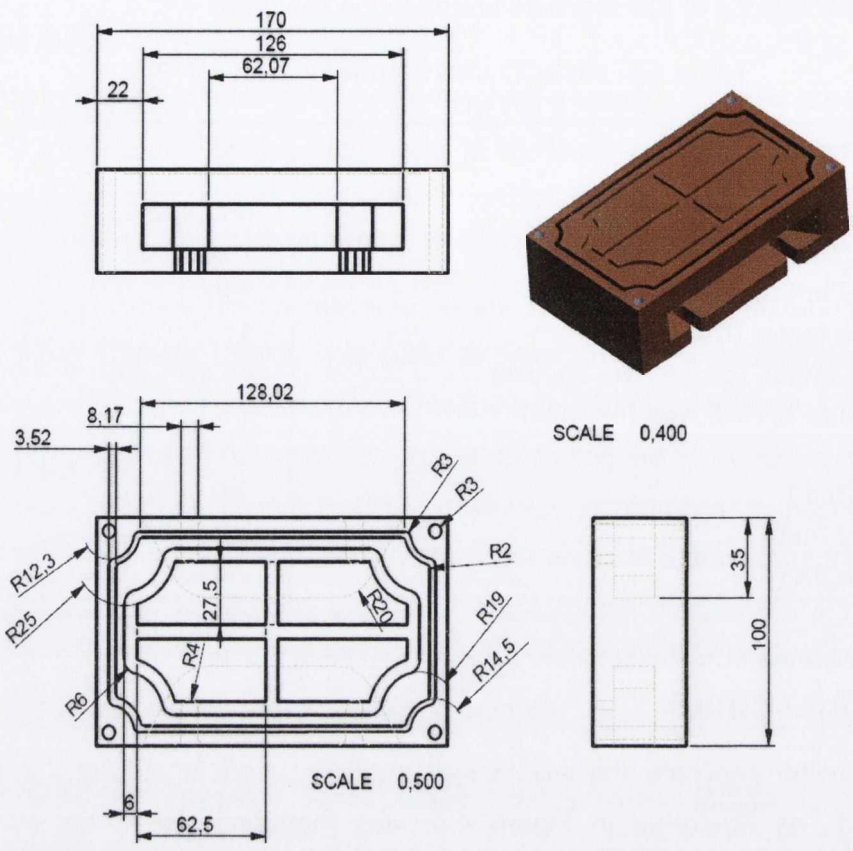

Figure 4.6: Vacuum chuck for realistic machining representation.

The fully installed system is shown in figure 3.3, in which the CFRP workpiece is held atop the vacuum chuck, which in turn is bolted to the force dynamometer, described in section 3.2.2.

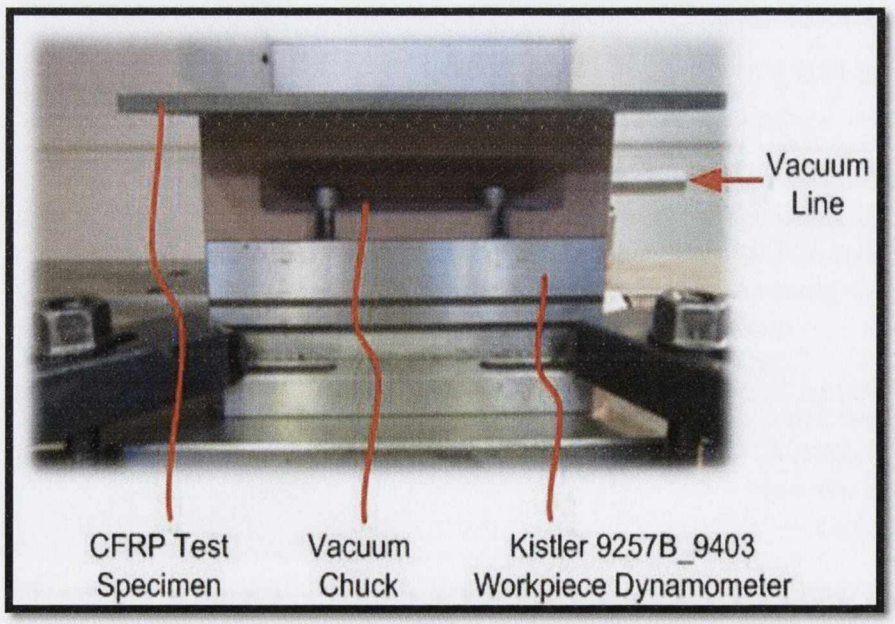

Figure 4.7: Campaign 2 experimental setup with prepared workpiece.

4.3.3 Force measurement

A piezoelectric dynamometer was used in order to obtain the X, Y and Z components of force during the milling process. This sensor is also classified as an indirect measurement device, measuring charge generated by deflections caused by a force. These measurements are then resolved into a resultant force component to allow comparisons to be made for various process arrangements. During the current research, force was measured by a Kistler three-component Type 9257B workpiece dynamometer, shown in Figure 4.8.

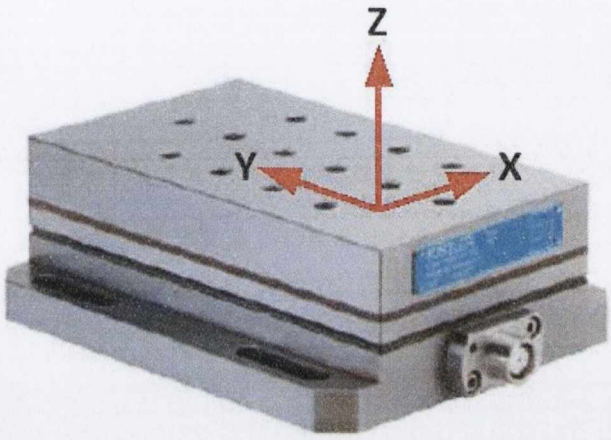

- Range: F_x, F_y, F_z → -5 – 5 kN
- Threshold: < 0.01 N
- Overload: F_x, F_y, F_z → -7.5 – 7.5 kN
- Linearity: < ± 1 % FSO
- Hysteresis: < ± 0.5 % FSO
- Cross talk: < ± 2 %
- Natural Freq: f_n (x, y, z) → 3.5 kHz
- Capacitance: F_x, F_y, F_z → 220 pF
- Weight: 7.3 kg

Figure 4.8: Kistler Type 9257B workpiece dynamometer with orientation of the three force components.

This dynamometer consists of four three-component force transducers fitted under high preload between a base plate and a top plate. Each force transducer contains three pairs of quartz plate. One pair is sensitive to pressure in the z-direction, while the other two pairs react to shear in the x and y directions respectively.

The electrical charge generated as a result of changes in pressure in the crystals is converted to a proportional voltage via a Kistler Type 5038A 3-channel charge amplifier, shown in Figure 4.9. From this device, the three channels are sent to the PXI chassis, where they are acquired simultaneously. Due to the relatively long time constant associated with the 5038A charge amplifier, minimal drift was seen to occur over the time periods associated with the cutting experiments in this research. Drift is the build-up of charge leading to a transient shifting of the signal sent from the charge amplifiers without any actual force causing such a shift. To further ensure that force signals did not acquire drift, the charge amplifier unit was reset before each test run, to remove any charge that may have accumulated over time.

- Measuring range: 100 – 1,000 pC
- Setting tolerance: < 0.1 %
- Drift: < 0.3% at 25 °C
- Reset/operate transition: < ± 1 pC
- Output voltage: 0 – 5 V
- Supply voltage: 15 – 30 VDC
- Current consumption: < 32 mA for 3 channels
- Dimensions:

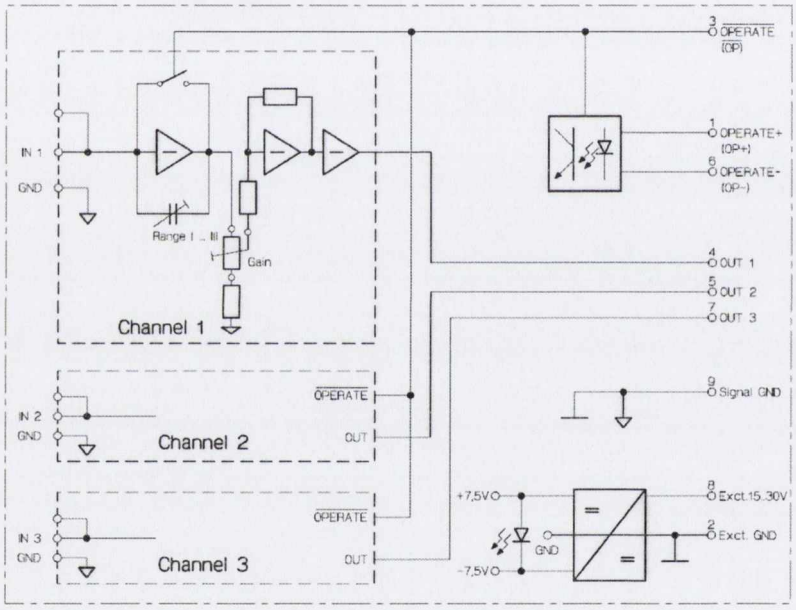

Figure 4.9: Kistler Type 5038A Charge Amplifier

The sensitivity (F_X & F_Y = -7.5 pC/N; F_Z = -3.7 pC/N) and long time constant of the charge amplifier were preset and validated during dynamic load calibration experiments on an Instron 8874 axial-torsion fatigue testing system located in the Department of Mechanical Engineering in Trinity College Dublin. Drift was confirmed as approximately 2%/min while cross talk for this dynamometer was confirmed as less than ±2% of the acceptable reading. The calibration curve and coefficients obtained during calibration of this sensor are shown in Figure 4.10. Figure 4.10 also illustrates an example of the accuracy during dynamic loading of the sensor, which indicates excellent conformance with the high precision Instron built-in load cell result for the same load cycle.

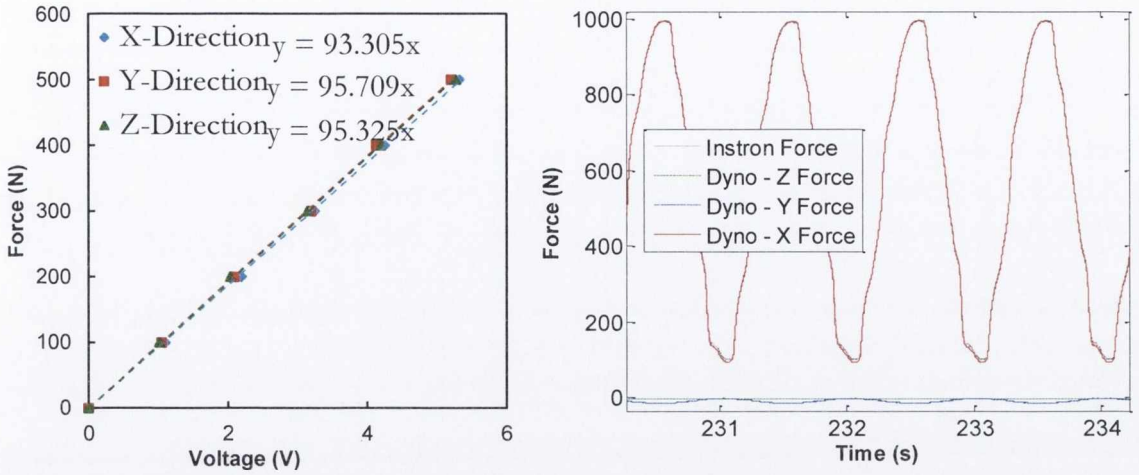

Figure 4.10: (left) Dynamometer calibration curve with correction coefficients and (right) example of calibrated X-component and Instron load cell comparison under a sinusoidal load.

4.3.4 Temperature measurement

As well as the ITT sensor measurements performed, tool surface temperature was also monitored using a FLIR A40M Researcher infrared thermal imaging camera with a spectral range of 7 to 13 μm and a temperature range of 0 to 500 °C with an accuracy of ±2%. The camera emissivity was calibrated for the K10 tungsten carbide (WC) cutting tool material using a combination of the 'black paint method' and a T-type thermocouple, in a similar experiment to that shown in Figure 4.11.

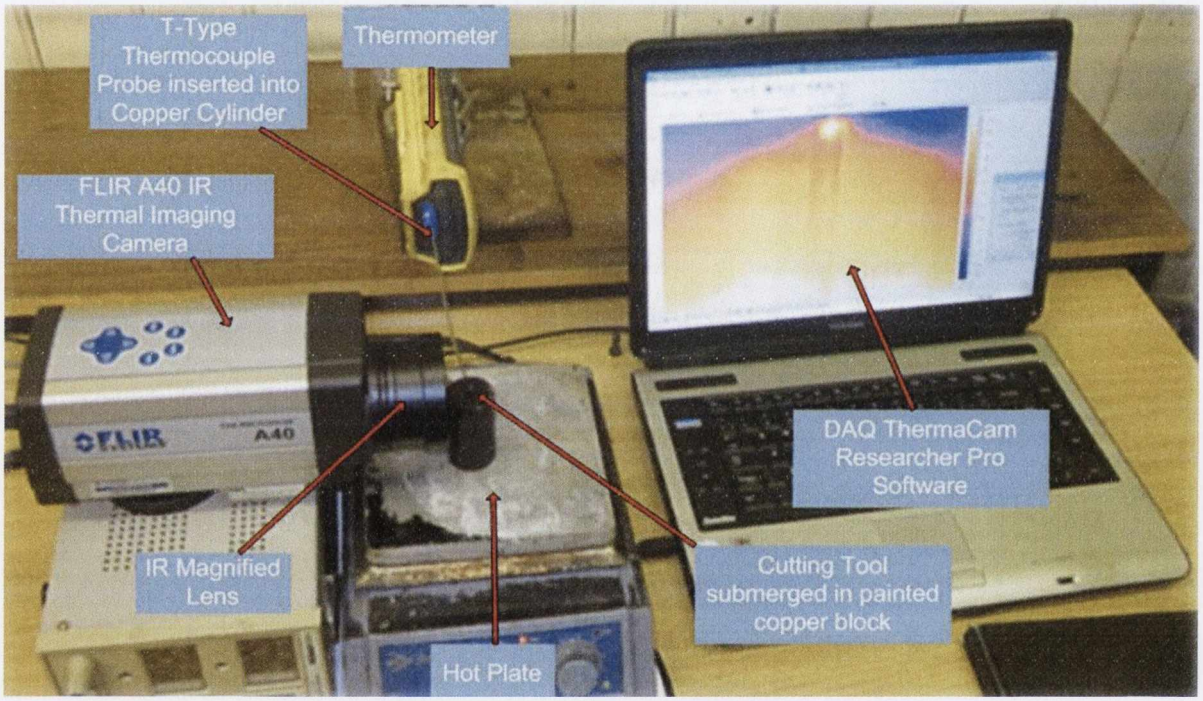

Figure 4.11: Setup for calibration of emissivity.

To ensure even distribution of heat throughout the tool during calibration, the tool was submerged into a copper block, as shown in Figure 4.12, also painted black to allow a known emissivity of 0.95 to be used (after validation with a thermocouple) during infrared measurement.

An emissivity calibration curve was generated over the temperature range of 0 to 200 °C, as appropriate for the current investigations. The emissivity was seen to stabilise at approximately 0.81 ± 0.5 during the examinations using the FLIR A40 focused at a distance of 1 meter and with an ambient temperature of 20 – 22 °C.

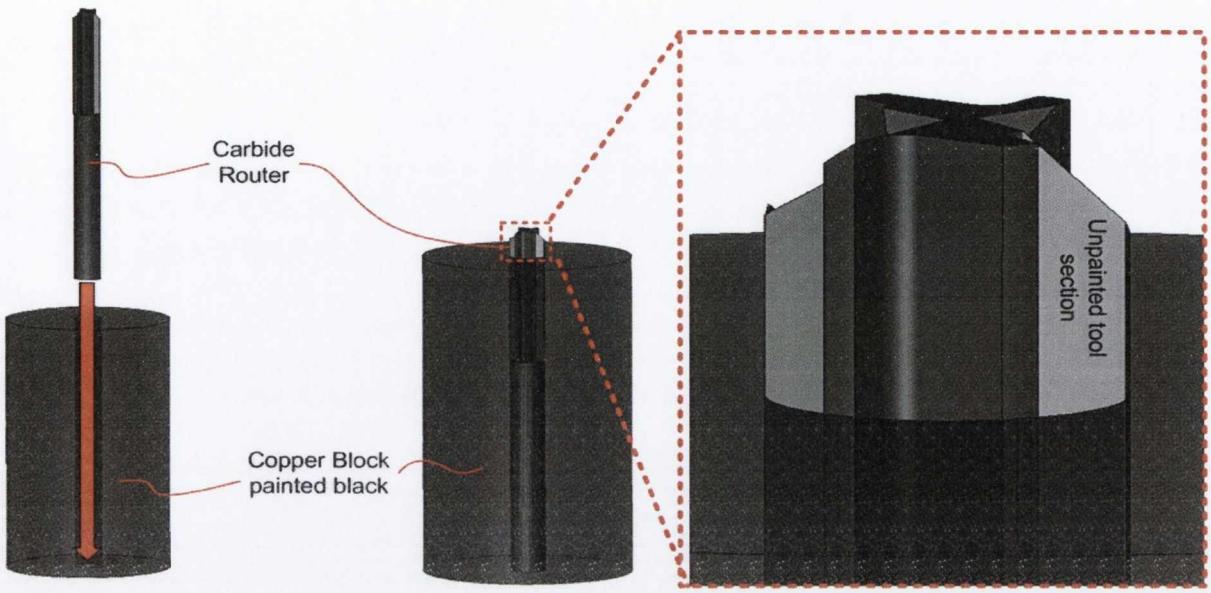

Figure 4.12: Methodology of tool submerged into a painted copper cylinder of known emissivity

For machining investigations, the camera was oriented horizontally in line with the trimming process at a distance of 1 meter. The camera was focused on the back of the cutting tool, as this provided the least obstructed view. Chip removal was aided by the use of a carefully positioned extraction tube, which ensured that little if any chip obscured the camera's view.

Once the thermal imaging recordings had been acquired, individual frames were converted into .MAT files and processed using Matlab. Processing involved assessing each sequence of images and selecting the appropriate section from which to extract the temperature information. An example of such image assessment is shown in Figure 4.13. An appropriate pixel range, shown in image 2 of Figure 4.13, was identified, ensuring that the maximum temperature on the tool throughout the cutting process was detected. The maximum temperature within the refined pixel matrix was then detected for each image in the sequence via the built-in Matlab *max* function.

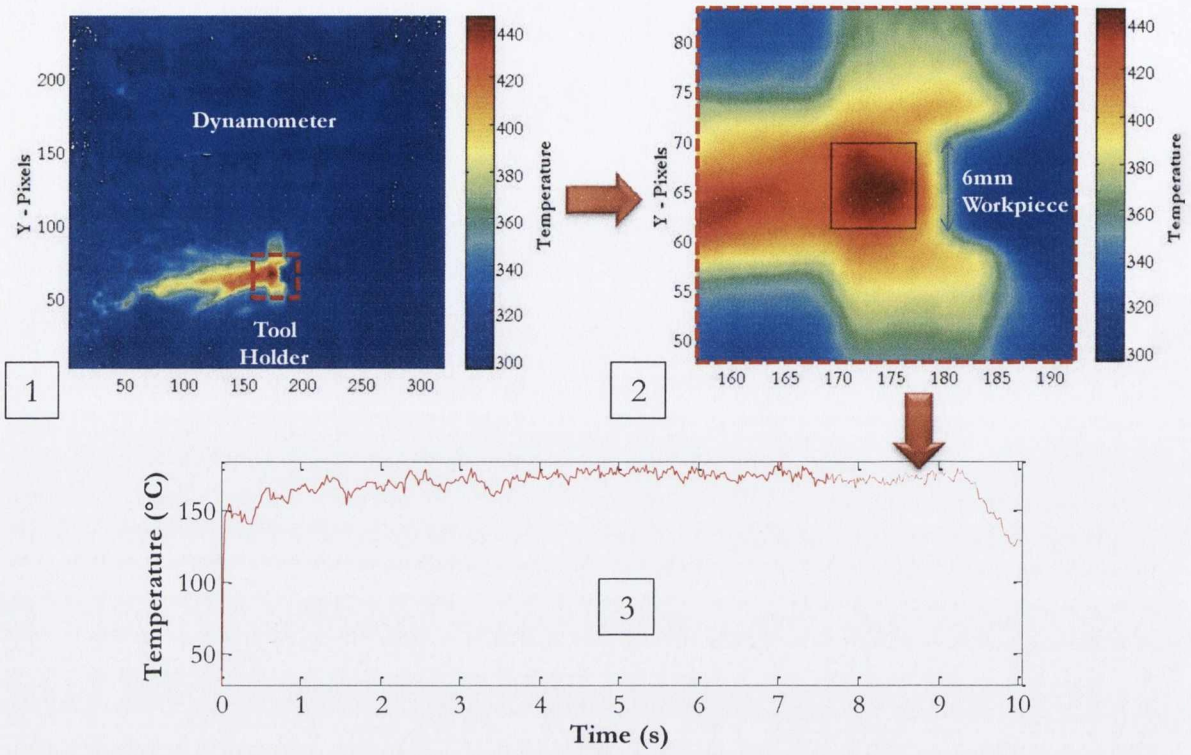

Figure 4.13: Post-processing steps required to extract the maximum temperature acquired by the thermal imaging camera. (1) Matlab inverted temperature pixel plot from a single image in recorded sequence, (2) A zoomed in view of the temperatures on the cutting tool with the area of interest shown in the black box and (3) the resulting plot of maximum tool surface temperature.

4.3.5 Surface roughness measurement and tool wear analysis

Preliminary analysis of both the tool and the machined surfaces was performed using the Mitutoyo Toolmaker's Microscope. Following this, sections of the workpiece were identified, as shown in Figure 4.16.

Stylus profilometer

The Mitutoyo Surftest SJ-402 stylus profilometer as illustrated in Figure 4.14 was used for an initial roughness assessment.

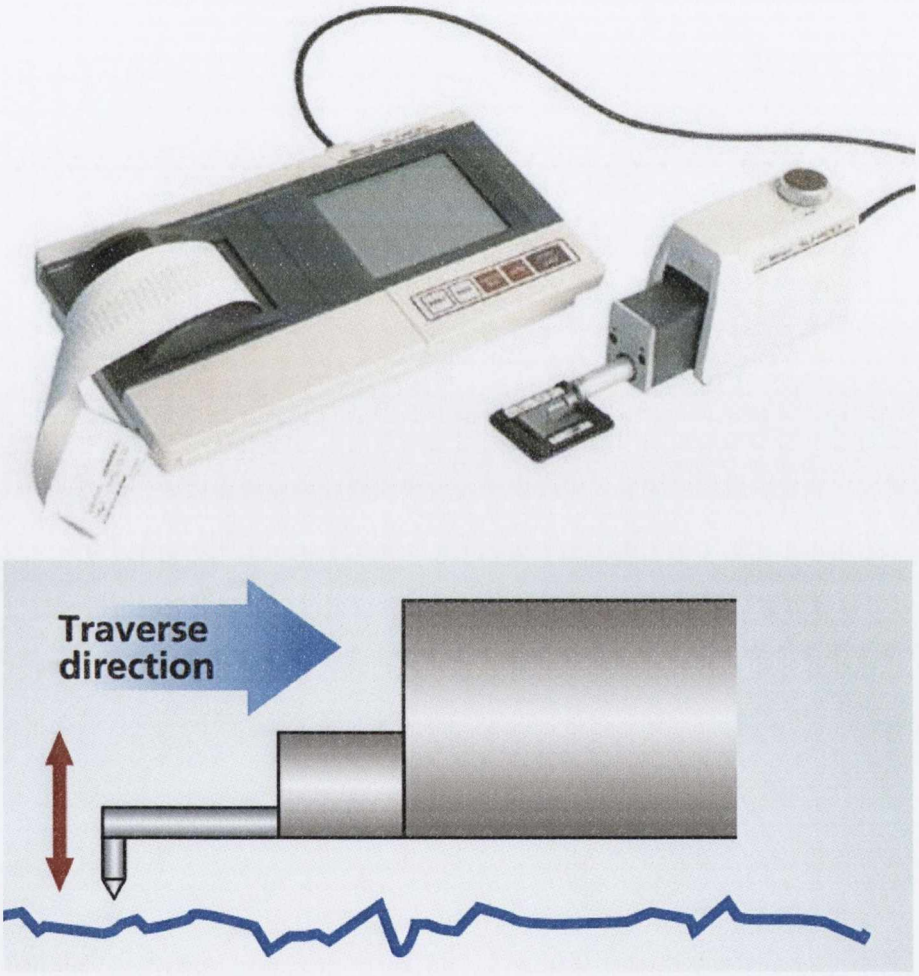

Figure 4.14: Mitutoyo Surftest SJ-402 Stylus Profilometer.

For surface roughness analysis of the CFRP machined surface, a primary profile was studied to capture the larger defects potentially associated with thermal degradation. A cut-off length of 0.8mm was used. Measurements were made in both the feed and transverse directions. The profilometer contains a diamond probe stylus tip of 2μm, which has a measuring force of 0.75 mN and an angle of 90° to the measurement surface. The profilometer was connected via an RS-232 cable to a notebook to enable 2D digital profiles

to be analysed. Both R_A and R_Y values were obtained during analysis. Measurements were performed at each location as depicted in Figure 4.15. However, to prevent scratching of the workpiece measurements were repeated three times approximately 0.5mm apart for each location. This allowed for an overall value of the surface roughness to be obtained, consisting of all of the measurements taken. The complete view of the various roughness measurements taken and during analysis to form the overall roughness characterisation is illustrated in Figure 4.16. This image also provides more detail of the locations at which measurements were taken along the CFRP trimmed sample. A custom-built specimen holder was used in order to ensure that the trimmed coupons were as flat as possible during analysis.

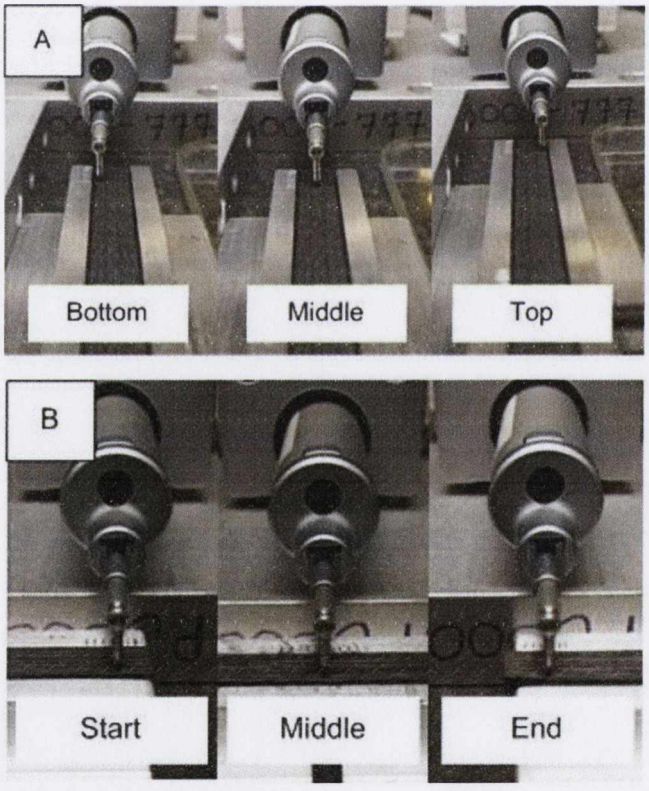

Figure 4.15: Roughness measurement set locations in the (A) feed and (B) transverse direction.

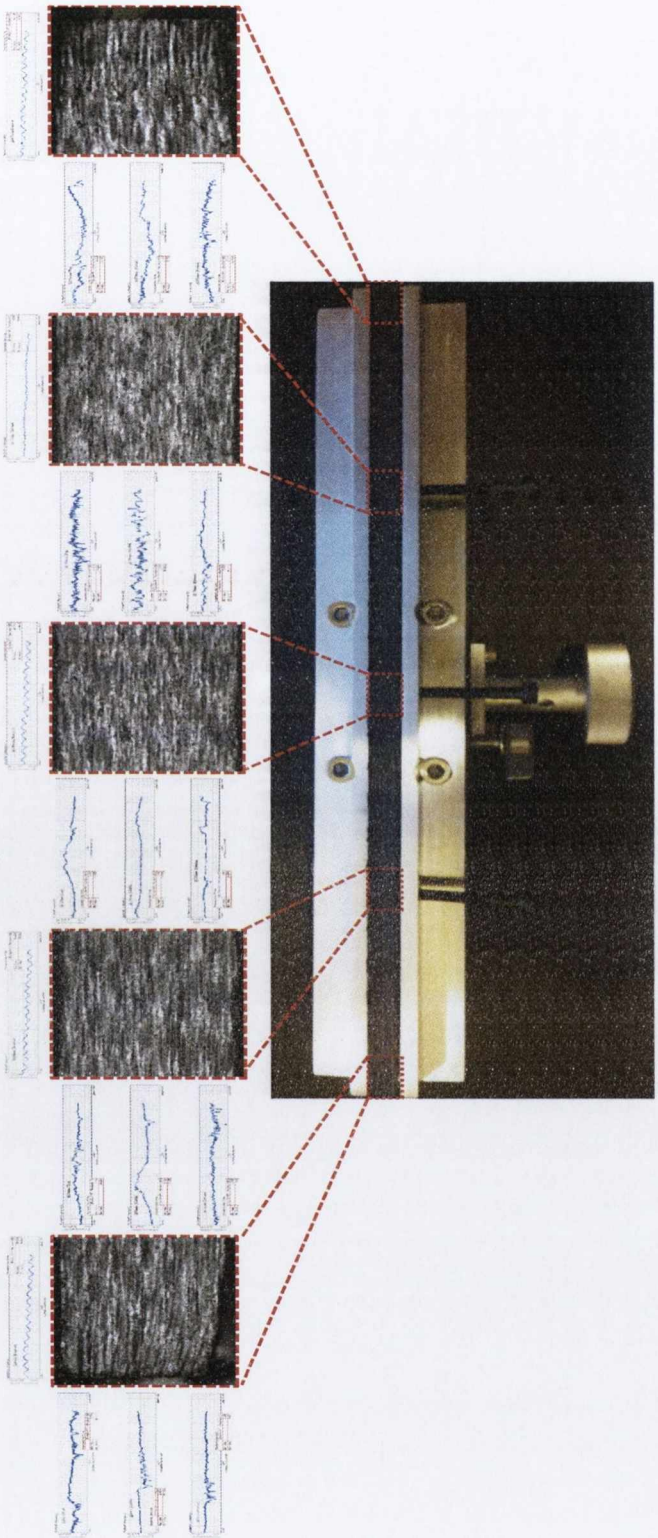

Figure 4.16: Sections used for microscope and styles roughness investigations.

White light interferometry

An alternative method used to measure the roughness and profile of the surface was via white light interferometry (WLI) using the OmniScan MicroXAM surface mapping microscope in the centre for microscopy and analysis (CMA) in Trinity College Dublin. The interferometry technique uses the wave theory concept of interference and coherence to analyse interference fringe patterns obtained from laser light that has been separated and then re-combined. This is achieved through the use of a beam splitter, which allows half of the light to pass through it and reflect off the object being studied, while the other half is reflected from the splitter to a reference of known distance from the splitter. The resulting interference pattern is then used to determine the height of the object being studied and allows for highly accurate 3D surface maps to be generated. In the current research, 3D mapping was performed at a distance of 100mm into the workpiece, when the force data indicated that the process had reached a steady state. CFRP samples were first sputtered in order to improve their ability to reflect the light back to the microscope as illustrated in Figure 4.17. The x50 microscope lens was used, shown in Figure 4.17, as lower magnification lenses proved to produce poor scans due to low light capture even with sputtered specimens.

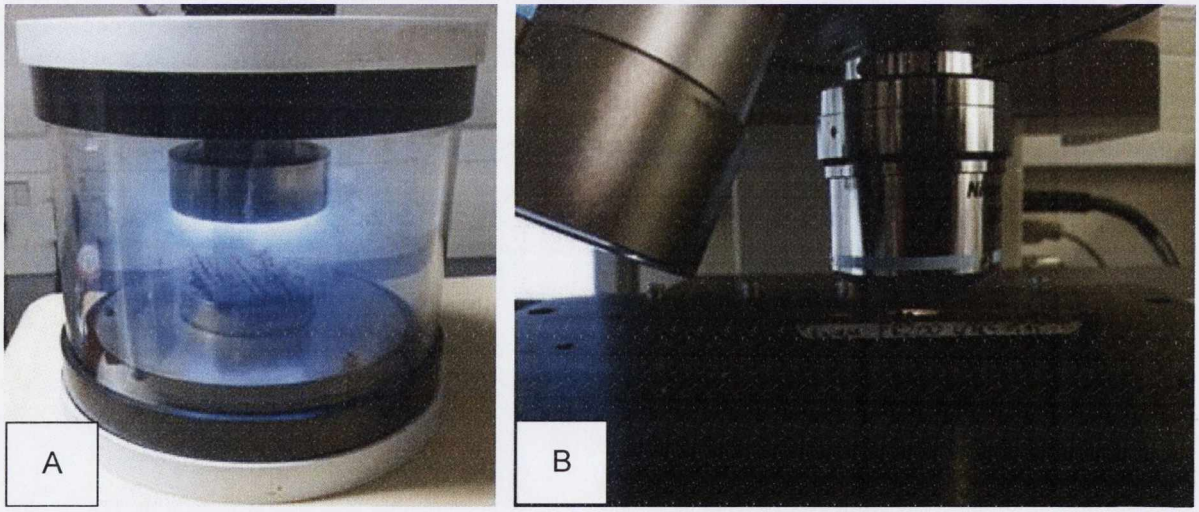

Figure 4.17:(A) Gold sputtering with a layer of approximately 0.2µm thickness. (B) CFRP specimen under the WLI x50 microscope lens.

Therefore, due to the reduced size of the scanned area, a stitching routine was performed, whereby 9 x 4 scans were stitched together using the commercial software package SPIP 2.0. The resulting images allow for 2D or 3D roughness analyses to be performed.

Scanning electron microscope

More detailed surface analyses were performed using a Tescan Mira Variable Pressure Field Emission Scanning Electron Microscope (SEM), also found in the CMA. This device functions by transmitting a focused beam of high-energy electrons over the surface of the sample in a high vacuum environment. After interaction with the specimen, a number of signals are produced including secondary electrons, X-rays and back-scattered electrons. The low energy secondary electrons were used in this investigation to form magnified high resolution images.

As shown in Figure 4.18, the setup for both the tool and CFRP workpiece required specialized clamping fixtures, which allowed a known, repeatable position to be used for comparisons either for a returning tool or between a variety of CFRP specimens.

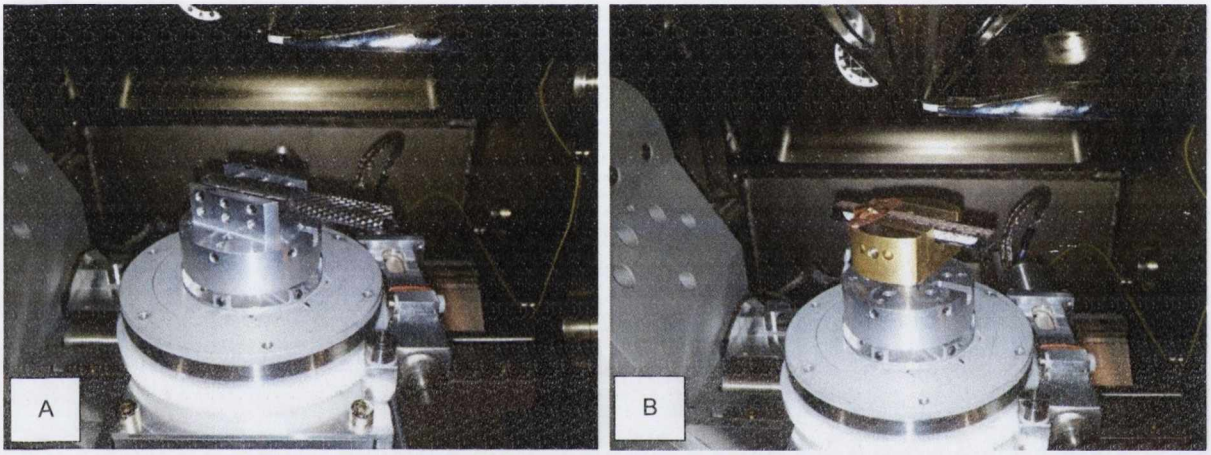

Figure 4.18: SEM setup for (A) cutting tool and (B) CFRP machined workpiece.

4.4 Experimental goals, designs and setups

4.4.1 Test 4.1: FE model validation

Goal

To assess the validity of the FE model in predicting the temperature at the tool surface.

Design

The factors and levels used in this investigation are displayed in

. In order to ensure that the heat ring hypothesis was achieved in this experiment, the cutting speed was raised slightly above the recommended level, while the feed rate was reduced substantially. Due to the double helix design of the tool it is not possible to provide an exact feed per tooth value, however, the feed used was approximately 20 μ/rev.

Table 4.2: Factors and levels used for cutting experiment – 3 repeats used for each test.

Factor	*Low Level*	*High Level*
Cutting Speed – v_c – (m/min)	250	
Feed – v_f – (mm/rev)	0.02	
Radial Depth of Cut – a_e – (mm)	8	
Axial Depth of Cut – a_p – (mm)	6	
Axial Location – L_a - (mm)	16	5

Setup

As illustrated in Figure 4.19, the setup for the experiment required a number of sensors to be utilised to monitor both thermal and load behaviour of the *roughing* edge trimming process. The sensors used were:

- ITT sensor
- Infrared thermal imaging camera
- Force dynamometer
- Thermocouples embedded into the workpiece

While the goal of the various temperature sensors was to measure the variation between temperatures for differing factor levels in the experimental design, the force sensor was utilised to monitor the stability of the process forces, thus ensuring that a stable trimming

process was achieved with each run. This allowed for greater certainty in, and understanding of, the results achieved. To ensure that both sensor requirements were met, a straight section of 200mm was machined at various feed speeds. Another aim of this experiment was to achieve an approximately steady state ITT temperature during machining. From previous experiments it was found that this required an extended length of cut.

In addition to the sensors used, vacuum clamping, mechanical clamping and a vacuum extraction chip removal system were also employed in order to ensure repeatable, realistic-to-industry, comparable run-to-run results.

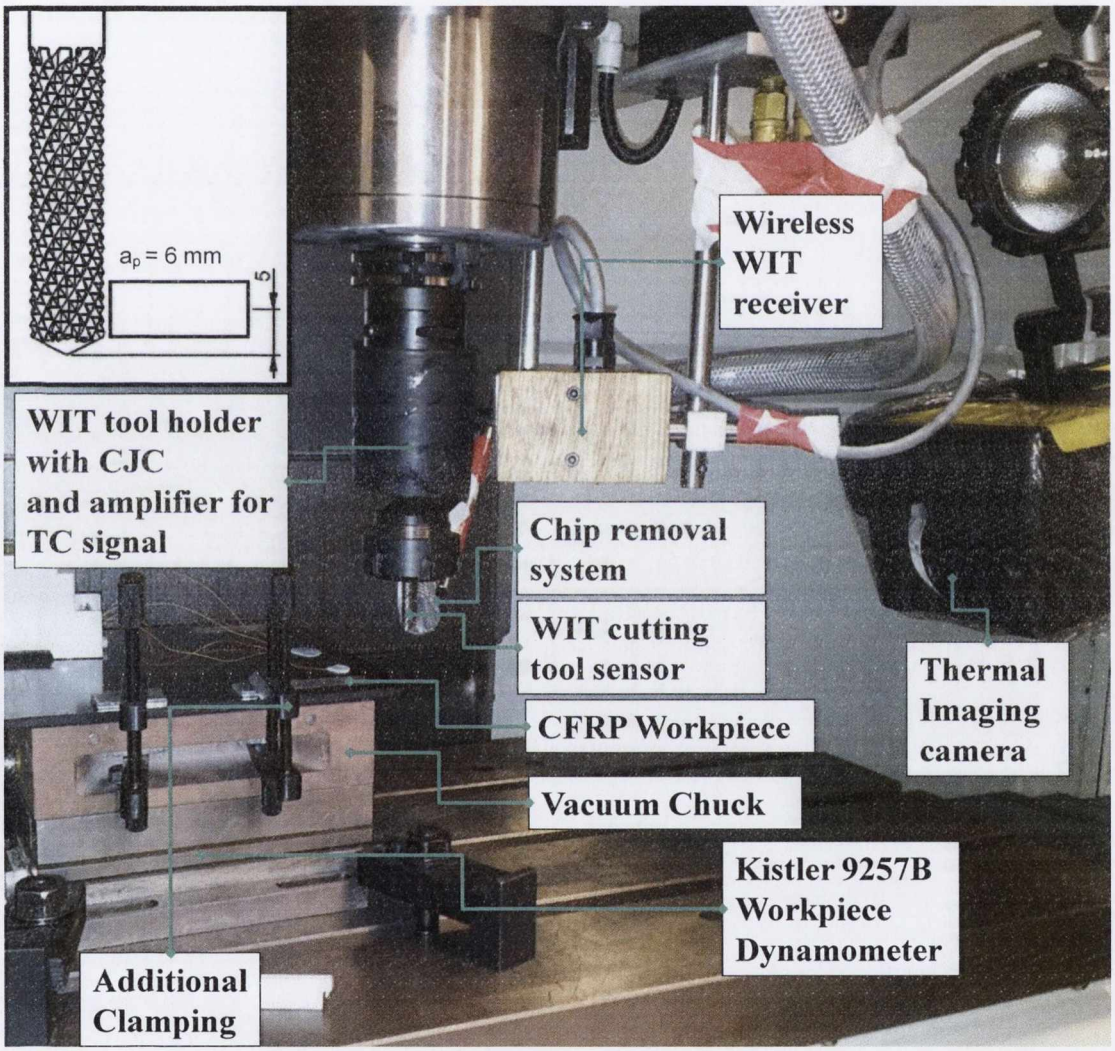

Figure 4.19: Experimental setup for CFRP roughing edge trimming process monitoring

Another aspect of the experiment that was critical for run-to-run comparisons was the level of tool wear. The specific cutting tool used in this investigation was an OSG uncoated tungsten carbide deburring router which was recommended by a number of

industrIn this experiment, the number of runs was minimised in order to ensure that tool damage and wear did not contribute significantly to the results. To confirm that minimal tool wear occurred during experimentation, SEM images were taken before and after the test campaigns were used to measure the sharpness of a specific set of points on the tool pre-selected due to their association with the cutting process.

Sensor response data, apart from thermography, was extracted from all sensors using the National Instruments PXI-1033 chassis, which housed two PXI-4472B acquisition cards. Each card is capable of acquiring 16 channels of 24bit and incorporates simultaneous sigma-delta analogue to digital conversion at up to 100 kHz per channel. The PXI chassis was interfaced to a PCIe Notebook. A sample rate of 6 kHz was used for this experiment. The data was oversampled in order to ensure that the Nyquist criterion was met for the force data and due to the ease of post-process down-sampling for the temperature data. The measurement chain used is shown in Figure 4.20.

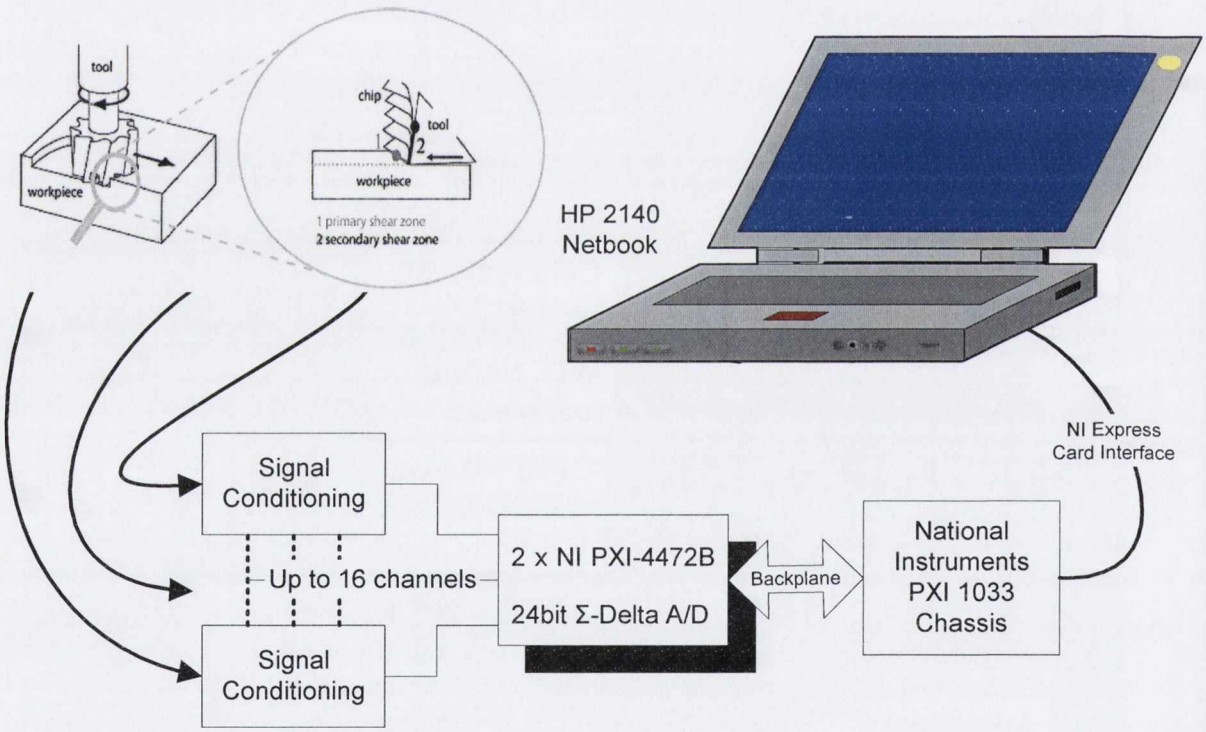

Figure 4.20: Data acquisition setup for edge trimming experiments.

Post-processing and feature extraction was performed using Matlab, in conjunction with the calibration data obtained for each of the sensors using the full *system calibration* technique. This included the use of the FE model for the predicted surface temperature data obtained and the resulting heat flux calculated.

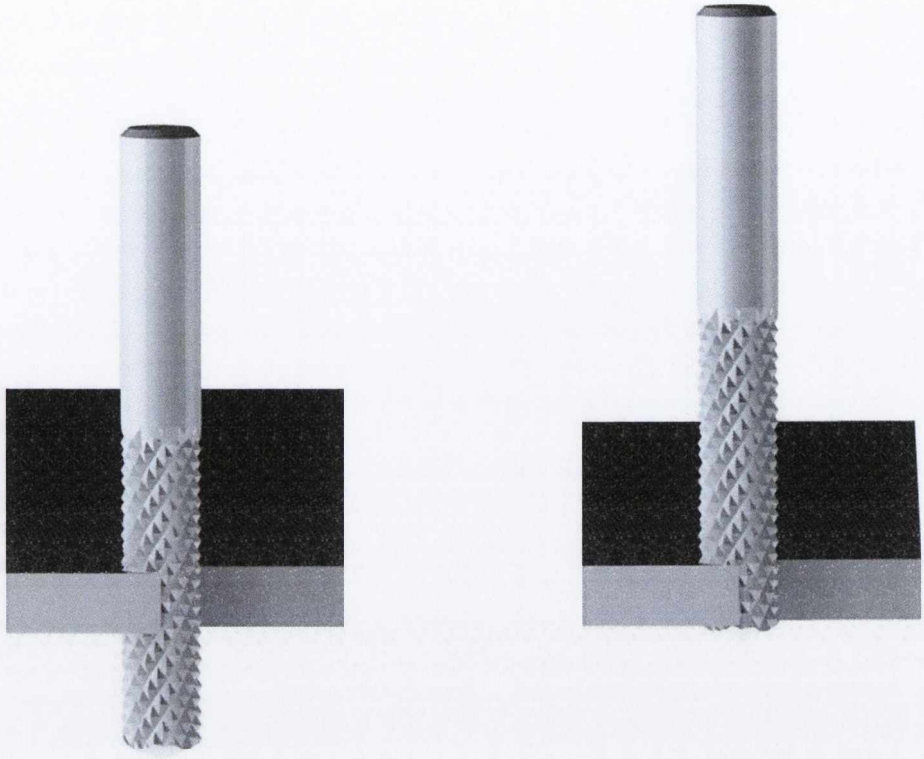

Figure 4.21: Axial engagement strategies (left) at the ITT sensor and (right) at the tool tip.

4.4.2 Test 4.2: Parameter investigations

Goal

To explore the validity of hypotheses developed regarding the behaviour of the cutting tool as a thermal system during cutting and determine the effect of 1) in-cut heat flux boundary condition, 2) Axial depth of cut (DOC), a_p, 3) axial cutting location, and 4) Feed rate on the workpiece surface integrity

Design

To satisfy the goal of this experiment, factors were selected based on their potential to cause thermal damage if ill-selected. Factor selection criteria included:

- Exposure time in cut
- Potential for accumulation of heat in the tool - geometric
- Influence on heat flux generation rate
- Known potential to increase the forces in cut

From these selection criteria, the factors outlined in Table 4.3 were selected and two levels were selected using a heuristic approach based on industrial recommendations. The first level aimed to produce a healthy workpiece, and the second to produce a thermally damaged workpiece.

Table 4.3: Variable factors set for experiment 4.2 – 3 repeats used for each design point.

Variable Factor	Low Level	High Level
Feed Rate	200 mm/min	1275 mm/min
Workpiece Thickness	3 mm	6 mm
Axial position of WP/Tool interaction	At ITT sensor (L_a = 16 mm)	At tool tip

Setup

The same setup, as described in section 4.4.1 was used for this experiment.

4.5 Results and discussion

4.5.1 Test 4.1: FE model and validation

Experimental versus FE model temperature results: At the tool tip

The initial estimation of results from the edge trimming process was based on a constant heat flux boundary condition, in which the location of the heat ring was determined by the axial position of the cutting interface, L_a, and the thickness of the workpiece, A_p. In order to determine the accuracy of the FE model in representing the behaviour of the cutting process, the results obtained from the IR camera and ITT sensor in a CFRP edge trimming test were plotted at both the cutting interface, i.e. at the tool surface, and at the ITT sensor embedded location, described previously in section 3.1.2. Figure 4.22 illustrates the cutting conditions and time-series responses of both sensors during the CFRP edge trimming process.

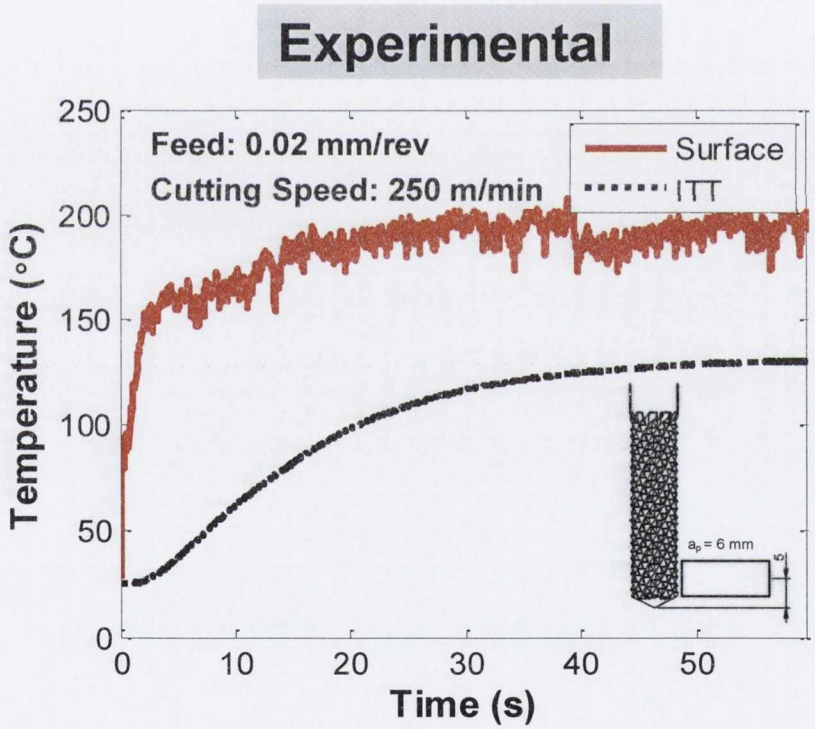

Figure 4.22: Plot of the experimental time-history temperature response of the IR camera at the surface and ITT sensor from an embedded position for feed: 0.02 mm/rev, cutting speed: 250 m/min and axial location of 5 mm.

The results of Figure 4.22 were then used as a baseline for validation of the FE model specifically applied to the edge trimming process. In order to initiate the comparison, an FE model, based on a constant heat flux, was used.

The constant heat flux (CHF) model is defined as the FE model which uses only a linear step input heat flux as the boundary condition. This step input is applied to the heat ring in order to represent the cutting process.

An iterative process, described in flow chart form in Figure 4.23, was developed in order to obtain a value for the CHF to be applied to the FE model. The assessment factor used to optimise this value was the ratio of experimental to FE simulated temperatures at time t = t_{end}, where . t_{end}, is the time at the end of the cutting process which was 60 s in the current validation test. The temperatures compared were the ITT sensor response and the temperature in the FE model at the position of the ITT thermocouple head. An initial guess was used in order to start the iterative process using the FE model, based on heuristic knowledge of previous FE simulation temperature results. The criterion used to determine when an acceptable CHF value had been determined using the FE model was:

$$0.95 < \frac{T_{EXPERIMENTAL}}{T_{FE}} < 1.05$$

Thus once the CHF value from the FE simulation produced a final simulated temperature to within 5 % of the experimental result, it was considered optimised. In this validation experiment, using an initial guess of 350 kW/m^2, the criterion was achieved at a value of 280 kW/m^2.

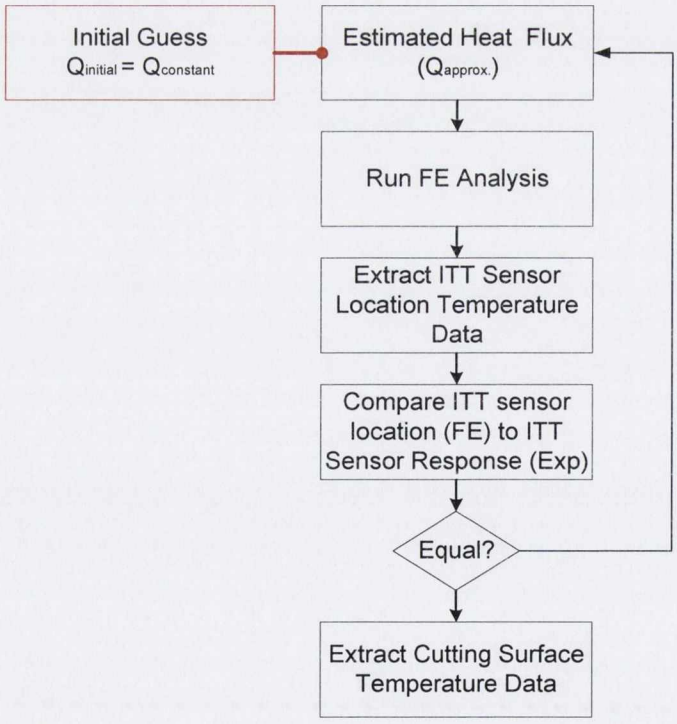

Figure 4.23: Iterative process used to determine heat flux boundary condition.

As is illustrated in Figure 4.24, this FE model with CHF of 280 kW/m^2 shows little ability to reproduce the surface temperatures seen from the experimental results of Figure 4.22.

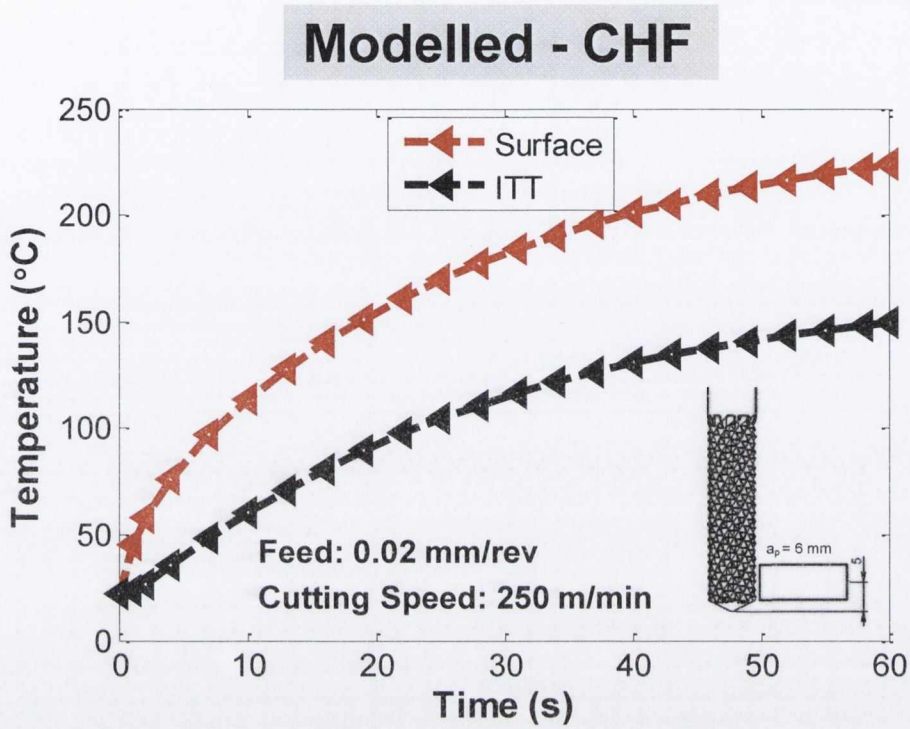

Figure 4.24: Plot of the FE simulated time-history temperature response of the surface and ITT sensor position for feed: 0.02 mm/rev and cutting speed: 250 m/min assuming a constant heat flux of 280 kW/m^2.

In comparison to experimental cutting temperatures acquired, the transient temperature profile of the optimised CHF shape function results in:

1. A large under-prediction of the surface temperature until approximately 45 s into the cut.
2. A variation of over- and under-prediction throughout the time-series data of ITT sensor.

The implications of the poor match between experimental and CHF simulated temperature transient profiles indicate that further criteria should be introduced to the iterative process to generate the heat flux shape function. In order to more accurately represent the heat flux shape function associated with the CFRP edge trimming process, the experimental surface temperatures (ESTs), recorded during the trimming test, were incorporated into the FE model. The EST data replaced the CHF data as the input boundary condition to the FE model, allowing the FE software to generate both the heat flux at the cutting interface boundary and the temperatures at the ITT thermocouple head

location in the model. The time-series temperature profiles generated using the experimental surface temperature (EST) are shown in Figure 4.25.

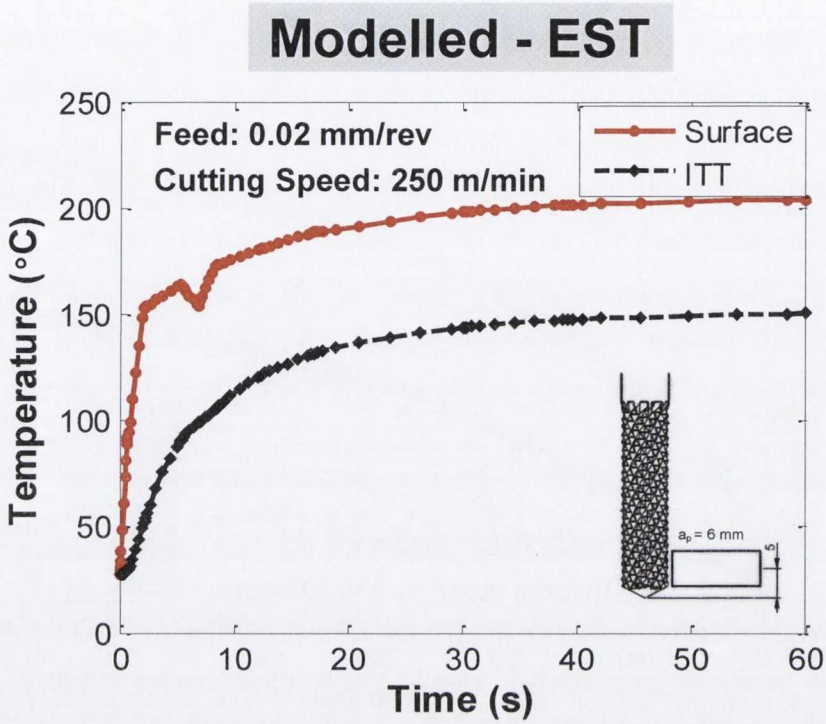

Figure 4.25: Plot of the FE simulated time-history temperature response of the surface and ITT sensor position for feed: 0.02 mm/rev and cutting speed: 250 m/min using the experimental surface temperatures recorded during trimming.

As shown in Figure 4.25, the EST model over-predicts the ITT sensor temperature in the initial 30 s of cutting in comparison to the TT sensor response of Figure 4.22. The EST model differences could potentially be due to a number of reasons:

1. Inaccurate position of the ITT sensor within the tool: This was ruled out by removing the ITT sensor, measuring hole depth into the tool and calculating the axial distance based on the angle of orientation of the hole.
2. Thermal resistances associated with the material of the sensor itself: From previous research [187] it is known that the thermal diffusivity of the thermocouple is required to be at least one order of magnitude better than that of the measured domain, i.e. solid surrounding material, in order to obtain meaningful results in transient measurements. In the current investigation, the thermal diffusivity of the Chromel – Alumel k-type thermocouple material, based on Chromel properties, is approximately 4.9×10^{-6} m^2/s, while that of the tungsten carbide tool material is approximately 2.1 x

10^{-5} m^2/s, indicating that the order of magnitude criterion is achieved. As the thermocouple meets this criterion, the thermal resistances associated with the sensor can be removed as a cause for the discrepancy.

3. Imperfect thermal contact between the sensor and tool due to motion or adhesive material introducing further thermal resistance to the sensor system: It is extremely difficult to determine whether or not imperfect contact occurs with an embedded thermocouple, particularly when embedded within a metal, therefore extreme caution was taken to ensure that the thermocouple head remained in pressurised contact with the tool material while the high temperature adhesive cured.
4. Misleading surface temperature results from the thermal imaging camera: The infrared thermal imaging result was processed as described in section 4.2.4, whereby the maximum temperature of the tool surface during machining is recorded by selecting the maximum of multiple pixels, which are calibrated to a pre-determined emissivity value. The response frequency of the IR camera is 50Hz, which is relatively high in comparison to most thermocouple response rates.
5. ITT sensor lag: This is a fundamental component associated with the contact resistance in the zone between the tool wall and the thermocouple head.

The physics associated with the lag of the sensor may be over-come by adding additional complexity into the FE model in the form of an ultra-fine mesh. However, the computation time would be significantly increased, with only a minor improvement to the reasonable approximation of the real situation.

Heat Flux Estimations

The corresponding time-series heat flux values at the tool surface input boundary were extracted from the FE simulation results. An average value, taken from all surfaces to which the input boundary was applied, is presented in Figure 4.26. This plot indicates that the heat flux associated with this EST boundary condition is not constant, with a large degree of energy expended during the plunge phase of cutting, i.e. the first ~1 s at feed rate of 200 m/min, as the tool submerges into the workpiece. This is intuitive as the area of the tool in contact rises from 0 mm^2 prior to contact up to a very small value ~ 1 x 10^{-12} as the first cutting edge engages and on to a larger area value of the same magnitude as the constant heat ring discussed previously. As the spindle is supplying the same amount of power to the process, and the chip formation mechanism remains approximately the same throughout the process, a sharp spike in the heat flux at this early stage of the cutting process is intuitive.

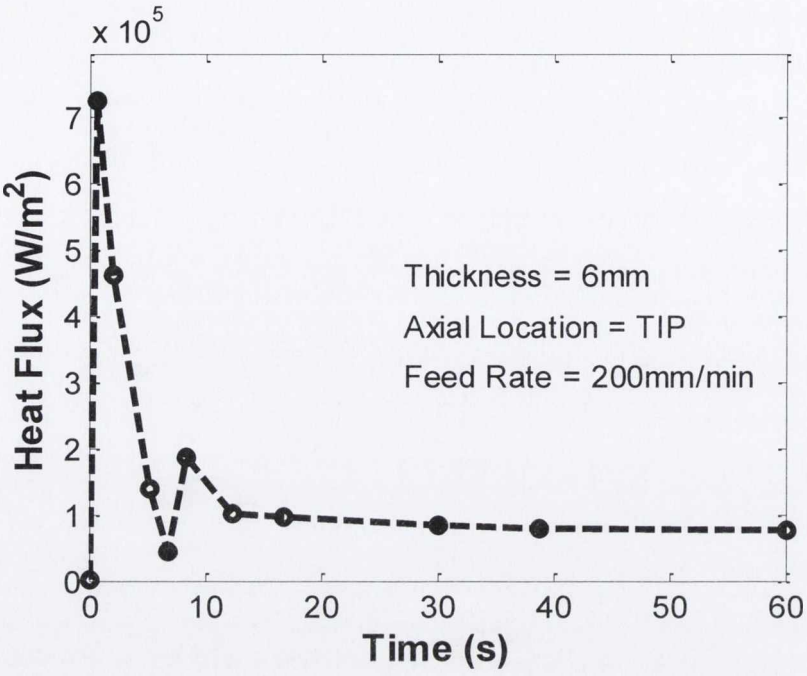

Figure 4.26: Calculated heat flux for EST model for feed: 0.02 mm/rev, cutting speed: 250 m/min and axial location: 5 mm.

The shape function in Figure 4.26 can be approximated by identifying the following components:

- An initial burst of q = 4,900kW/m^2 at t ~ 0.01 s.
- Approximately exponential decay in magnitude of q to 1,000kW/m^2 at 5 < t < 20 s
- Approximately constant magnitude of q = 1,000k W/m^2 at 20 s < t < 60 s.

Experimental versus FE model temperature results: At the ITT sensor

The temperature responses obtained from the temperature sensors is illustrated in Figure 4.27. It is noted that there is a lower maximum surface temperature reached during this investigation, which is in-line with the expectation from the parametric investigations of the previous chapter.

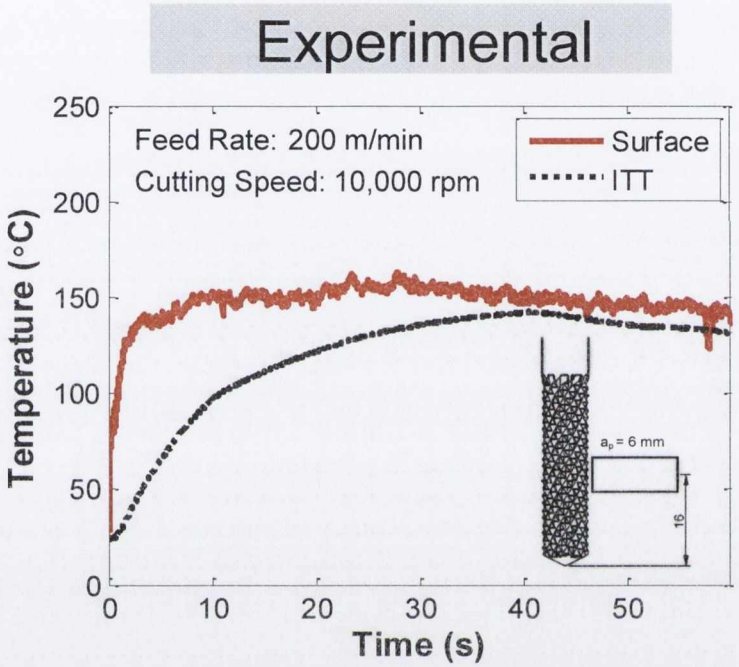

Figure 4.27: Plot of the experimental time-history temperature response of the IR camera at the surface and ITT sensor from an embedded position for feed: 0.02 mm/rev, cutting speed: 250 m/min and axial location of 16 mm.

The same iterative process, as described previously, was used to assess the cutting process applied at an axial location in-line with the ITT cutting tool, L_a = 16 mm. With the knowledge obtained from the heat flux shape function associated with the EST model result of the previous machining test, the iterative process was revised to allow for additional adjustments to be made, particularly during the initial ~0.1 s of the simulation in the form of an order of magnitude rise in heat flux from the steady state value initially calculated, as described in the previous section. This was followed by a sudden drop to a steady state value of the same order as the original steady state heat flux value, once the tool reaches full engagement. The simulation results of this advanced iterative approach are shown in Figure 4.28. In this plot, although there is a high degree of agreement between the experimental and simulated surface temperature responses, the ITT sensor is again over-predicted. This indicates that the heat is transferring too quickly to the embedded location of the ITT sensor. Therefore, it may be necessary to adjust the thermal properties of the model in order to introduce an intentional lag. This can be done

by altering the thermal properties of the FE model in order to slow the transfer of heat and therefore effectively lag the ITT sensor response in the model.

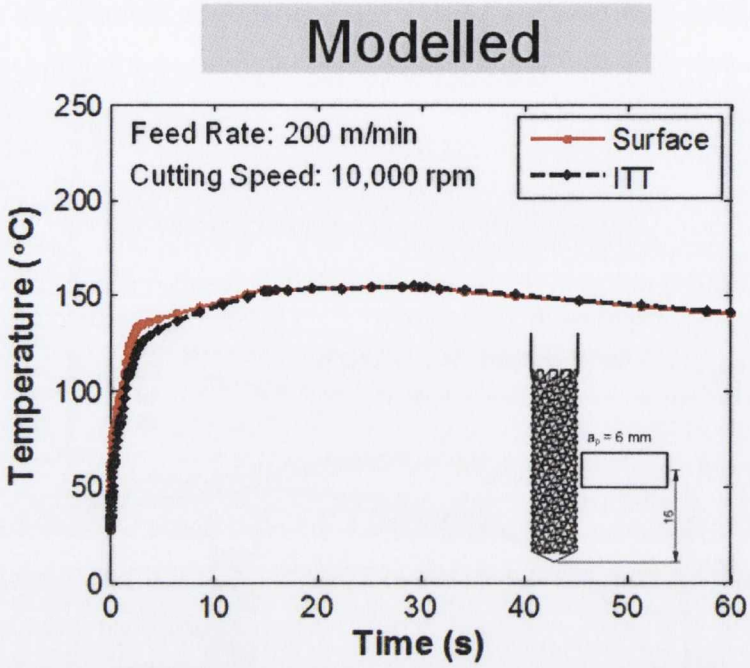

Figure 4.28: Plot of the FE simulated time-history temperature response of the surface and ITT sensor position for feed: 0.02 mm/rev, cutting speed: 250 m/min and axial location: 16 mm.

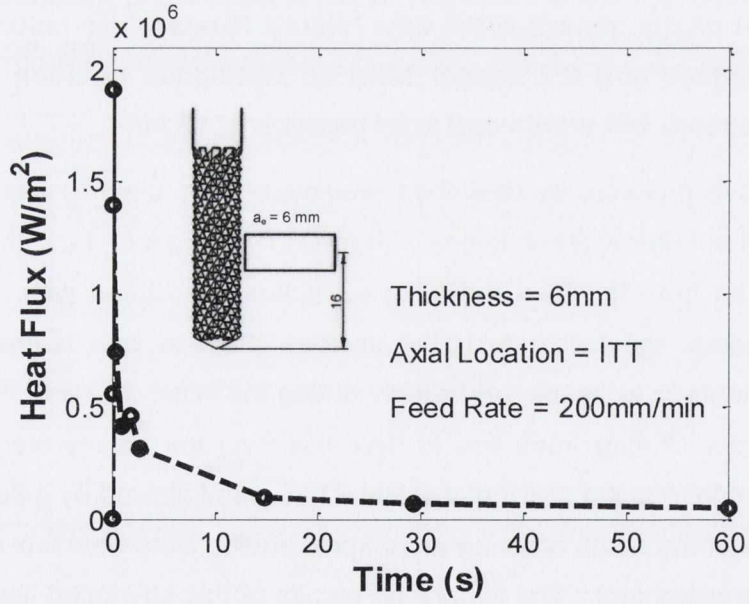

Figure 4.29: Input heat flux boundary condition applied to the FE model for feed: 0.02 mm/rev, cutting speed: 250 m/min and axial location: 16 mm.

The corresponding heat flux shape function for this simulation temperature response plot is shown in Figure 4.29. The shape function in Figure 4.29 can be approximated by identifying the following components:

- An initial burst of q = 18,000kW/m^2 at t ~ 0.01 s.
- Approximately exponential decay in magnitude of q to 1,000kW/m^2 at 1 < t < 14 s
- Approximately constant magnitude of q = 1,000k W/m^2 at 20 s < t < 60 s.

4.5.2 Test 4.2: Parameter Investigations

The results of this investigation are presented in a two-phase comparative manner. In the first phase, the indirect responses, i.e. temperature and force are studied. The relationship between the variables used, i.e. axial cutting strategy, feed rate and axial depth of cut, and responses is determined. Regression analysis is then used to quantify such relationships. In the second phase, the relationship between the direct responses, i.e. workpiece surface integrity, is investigated with respect to the variables of the study. Finally, conclusions are drawn regarding the potential of the indirect response to identify and monitor direct responses of the cutting process. In this way, the usefulness of the ITT sensor as a process monitoring tool is identified.

The results of each of the three repetition sets, relating to each of the experimental design points, were processed in Matlab and collected and compiled using Minitab. The main effects plots were studied and findings presented herein.

Cutting Force Response

The null hypothesis being tested for this response was that a variation of specific process parameters does not change the forces associated with the process.

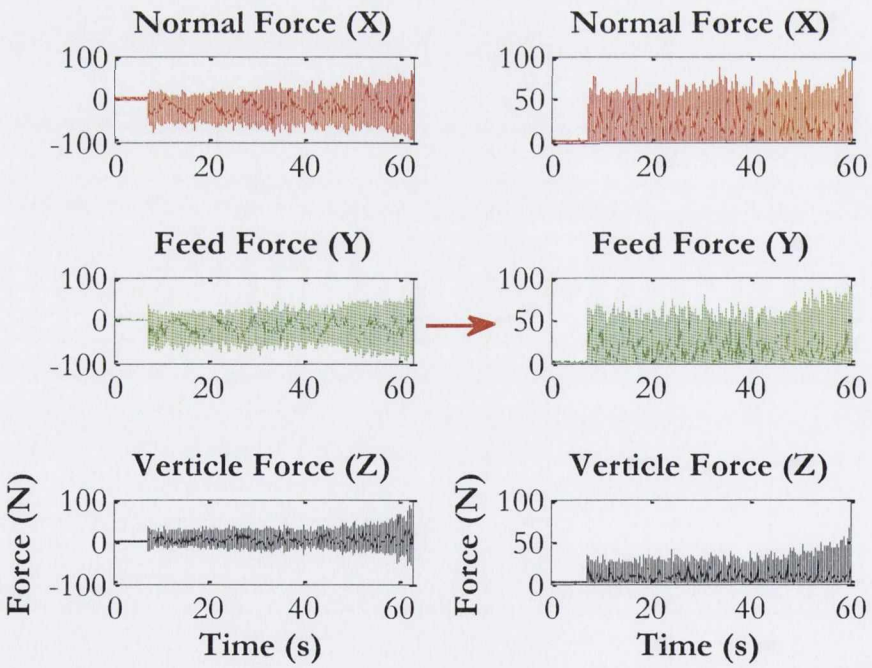

Figure 4.30: Example of the (left) raw and (right) absolute X, Y and Z force data components recorded during edge trimming tests.

The raw and absolute X, Y and Z force results recorded during edge trimming are shown in Figure 4.30. It is noted that there is some fluctuation, particularly in the vertical force, at

the very end of the cut. This is consistent with the findings of Zaghbani *et al.* [199] in which the authors state that "...the decreasing thickness of the machined section leads to a high vibration level, which causes an increase in the cutting force level." Therefore, only forces within the steady state cutting zone were used to assess the average forces used in the process. These results were used to calculate the resultant horizontal response, using X and Y forces in the cutting plane, and quantify the vertical response, using the absolute Z force. The formula used to calculate the resultant horizontal forces is shown in Equation 4.6.

$$F_R = \sqrt{{F_X}^2 + {F_Y}^2} \qquad \textbf{4.6}$$

Overall it was noted that the vertical forces were significantly lower than those recorded in the horizontal direction for all design points tested. This indicates that the clamping system, in conjunction with the workpiece stiffness, provided a controlled, low vibration cutting process in which the majority of energy expended went into the material removal process itself.

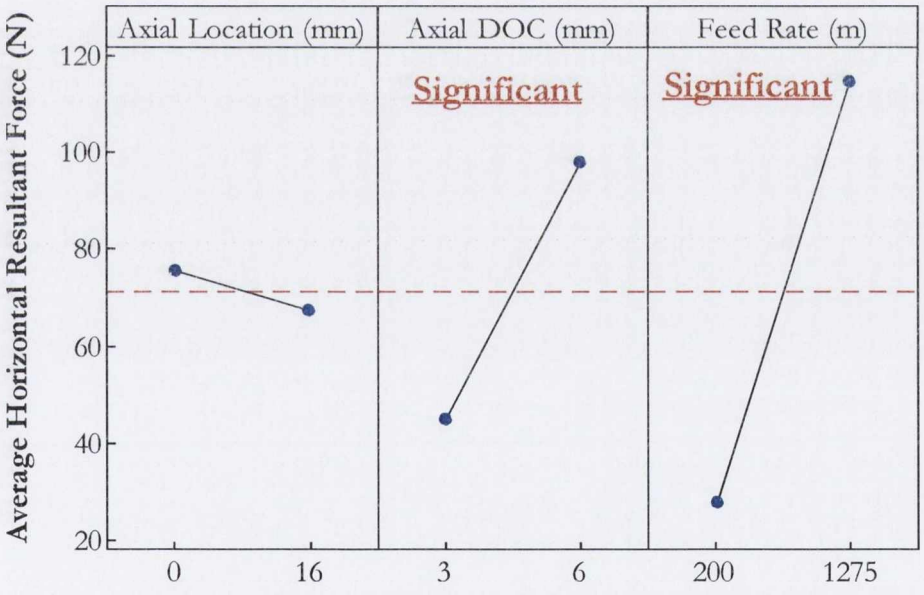

Figure 4.31: Main effects plot for average horizontal resultant force.

Table 4.4: ANOVA results for average horizontal resultant forces in edge trimming.

Source	*DF*	*SS*	*MS*	*F*	*P*	*PCR*
Axial Location (mm)	1	277	277	0.45	0.513	0.00
Axial DOC (mm)	1	11350	11350	18.62	0.001	21.61
Feed Rate (mm/min)	1	30139	30139	49.44	0.000	59.42
Error	12	7316	610			18.96
Total	15	49083				

From the results of Figure 4.31 and Table 4.4, there is strong evidence to show that feed rate and axial depth of cut produce significant force effects, indicated particularly by the low p-values of Table 4.4, with feed rate contributing approximately 60% of the force effect noted. Therefore, for these parameters the null hypothesis is rejected and it can be stated that the change from lower to higher level of these factors produces a significant effect. The same results were noted for the vertical force response results, shown in Figure 4.32 and Table 4.5. This is in line with findings by Colligan and Ramulu [200] that cutting force increases with material removal rate. In contrast, the axial location parameter did not produce any significant force effect during testing and variations seen in the data are consistent with run-to-run chance variation. It is therefore not possible to reject the null hypothesis for axial location. Although this effect is not stated as being significant, there is a reduction shown as the engagement location moves upward from the tool tip. This would concur with the heat flux values obtained for the tool, which indicated a slightly higher initial spike in energy at the tool tip location. This energy on the thermal side could have been generated due to a small amount of mechanical energy due to the lower stiffness associated with using the tool tip.

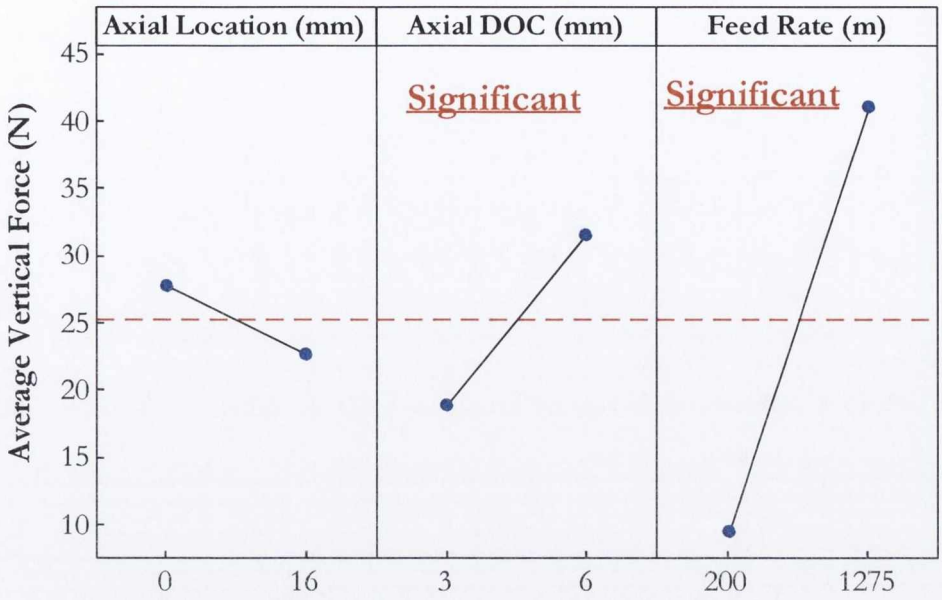

Figure 4.32: Main effects plot for average vertical force.

Table 4.5: ANOVA results for average vertical forces during edge trimming tests.

Source	*DF*	*SS*	*MS*	*F*	*P*	*PCR*
Axial Location (mm)	1	104.3	104.3	1.55	0.237	0.65
Axial DOC (mm)	1	652	652	9.67	0.009	10.37
Feed Rate (mm/min)	1	4004.1	4004.1	59.39	0	69.84
Error	12	809	67.4			19.14
Total	15	5569.5				

Temperature Results

The statistical tests for temperature responses follow a similar hypothesis as was used for the previous response. In this case, the null hypothesis is that variation of specific process parameters do not change the maximum temperature associated with the process.

The individual response plots are as previously illustrated in section 4.5.1 of this chapter. While the ITT sensor response has an exponential-type shape, the surface data, both modelled and measured using thermography, appears to follow a different function. This function initiates with a sudden initial temperature rise, followed by a relatively steady state level for the duration of cutting. This is supported by research into wood composite machining by Kusiak *et al.* [201] in which the authors show a similar, although less pronounced, temperature increase in the initial stages of the process using the embedded thermocouple technique. Such a surface tool temperature profile has also been noted by Armendia *et al.* [8] in interrupted cutting experiments via the micro-thermal imaging technique.

In order to perform the statistical analysis of this response function the maximum surface temperature was used to assess the null hypothesis. The ITT sensor response, in conjunction with the FE model provided the maximum surface temperatures. The ITT corrected results were validated as previously described using thermography.

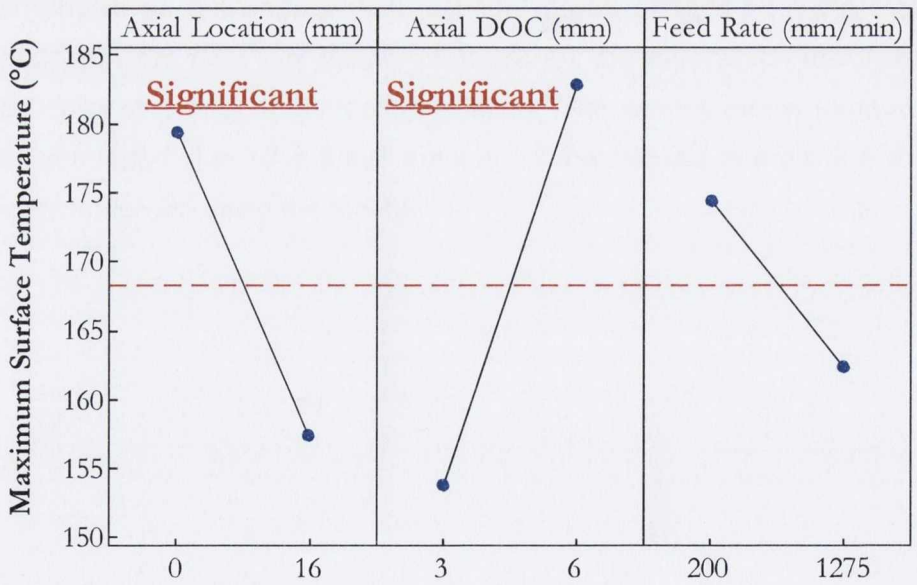

Figure 4.33: Main effects plot for maximum surface temperature.

Table 4.6: ANOVA results for max. surface temperature during edge trimming tests.

Source	*DF*	*SS*	*MS*	*F*	*P*	*PCR*
Axial Location (mm)	1	1943.2	1943.2	11.47	0.005	21.91
Axial DOC (mm)	1	3370.9	3370.9	19.9	0.001	39.55
Feed Rate (mm/min)	1	578.2	578.2	3.41	0.089	5.05
Error	12	2033	169.4			33.49
Total	15	7925.3				

The main effects plot, Figure 4.33, and ANOVA table, Table 4.6, indicate that both axial location, contributing 22% and depth of cut, contributing 40%, produce a strongly significant effect on the maximum process temperature reached during cutting, generating p-values much lower than 0.05. For these two parameters, the null hypothesis is therefore rejected. The statistics indicate that the effect of feed rate is significantly smaller than the other parameters. This is likely due to the use of comparisons performed over distance of cut, as governed by the experimental setup, rather than by time. From analysis of the individual curves, it is noted that while the lower feed rate produces approximately steady state temperatures towards the latter part of the cutting process, the higher feed rate level shows rapid temperature increase with no signs of steady state temperatures. Therefore, the feed rate effect is not identified clearly by considering only the maximum temperature.

If a basic approximation of the time derivative of temperature is used to represent the system response, described by Equation 4.7, the effect of feed rate becomes highly statistically significant as shown in Figure 4.34.

It is important to state that both responses are valid for the set of factors under scrutiny in this investigation, due to the time-independent nature of axial depth and location versus the time-dependent nature of feed rate.

$$T'(t) = \frac{T_{MAX}}{t_{TOTAL}} \qquad \textbf{4.7}$$

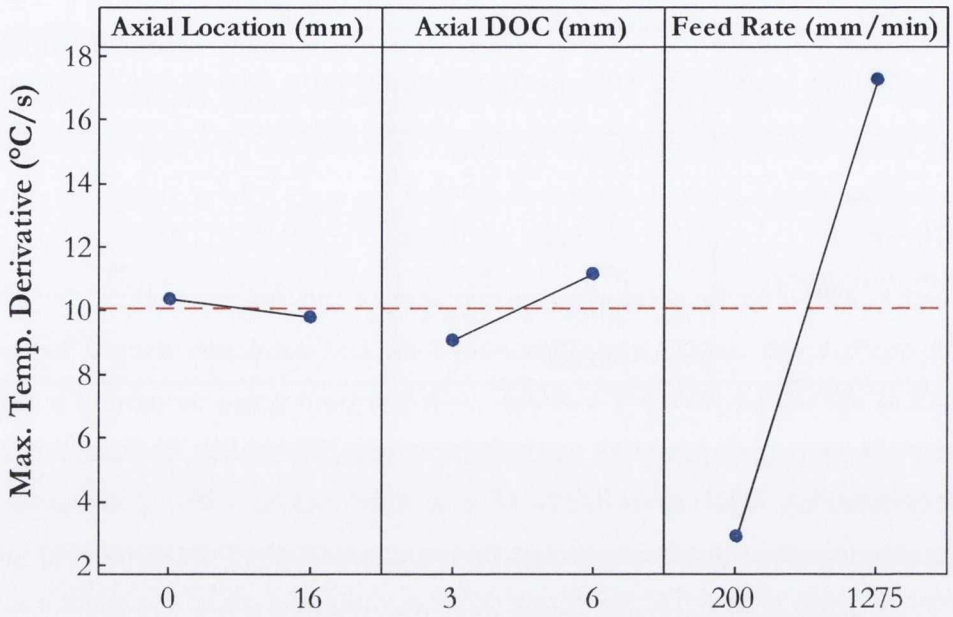

Figure 4.34: Main effects plot of temperature derivative.

Table 4.7: ANOVA results for temperature derivative during edge trimming tests.

Source	*DF*	*SS*	*MS*	*F*	*P*	*PCR*
Axial Location (mm)	1	1.45	1.45	0.92	0.357	0
Axial DOC (mm)	1	17.17	17.17	10.85	0.006	1.81
Feed Rate (mm/min)	1	822.69	822.69	519.99	0	95.27
Error	12	18.99	1.58			2.92
Total	15	860.3				

Heat flux effect

A sample of the heat flux calculated by the FE simulations for each design point in the design of experiment are presented in Figure 4.35 to Figure 4.42.

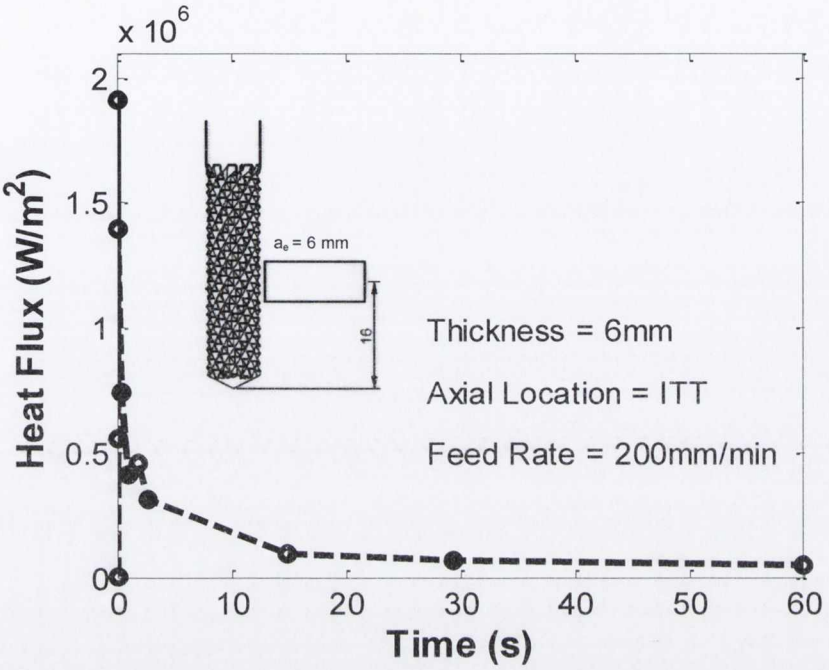

Figure 4.35: Plot of the time-series heat flux associated with the tool surface for thickness = 6mm, L_a = 16 mm, v_f = 200 m/min, v_c = 250 m/min.

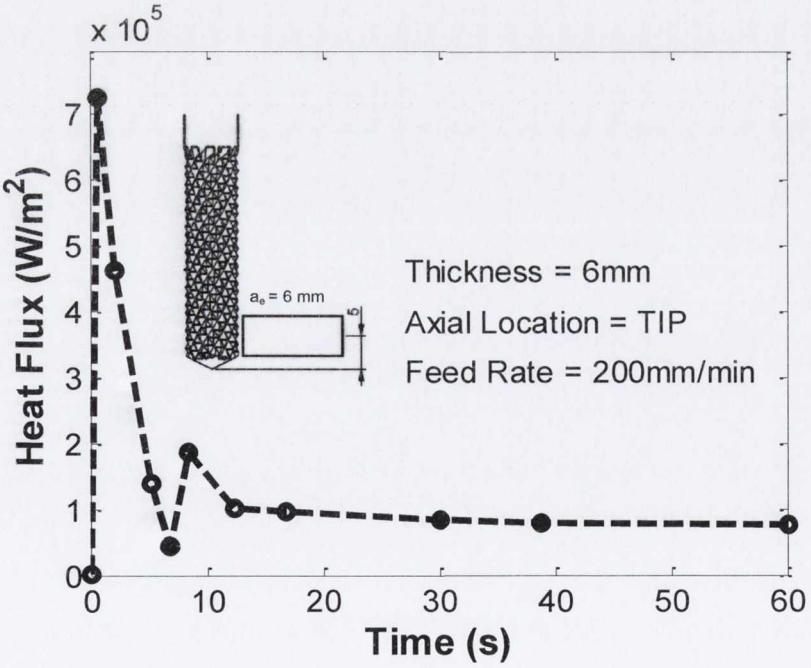

Figure 4.36: Plot of the time-series heat flux associated with the tool surface for thickness = 6mm, L_a = 5 mm, v_f = 200 m/min, v_c = 250 m/min.

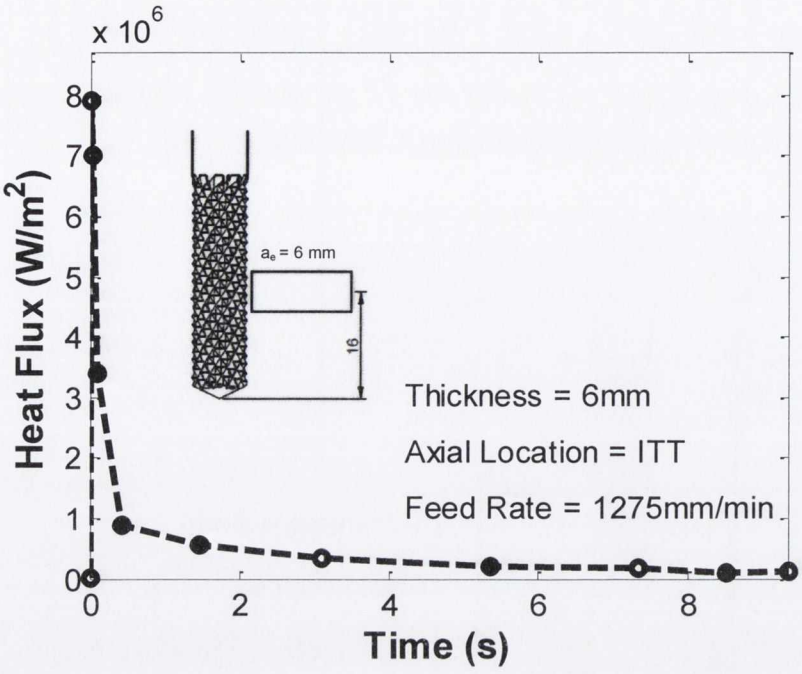

Figure 4.37: Plot of the time-series heat flux associated with the tool surface for thickness = 6mm, L_a = 16 mm, v_f = 1275 m/min, v_c = 250 m/min.

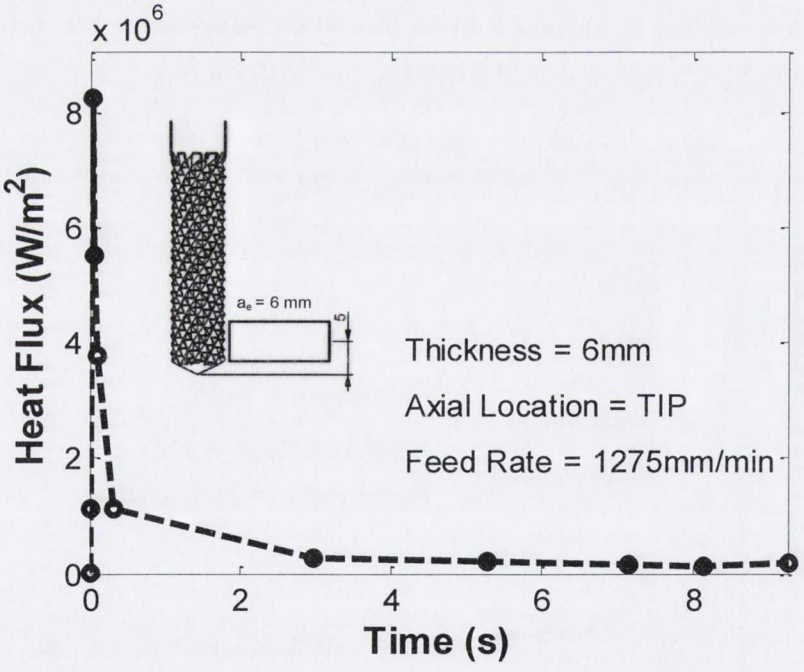

Figure 4.38: Plot of the time-series heat flux associated with the tool surface for thickness = 6mm, L_a = 5 mm, v_f = 1275 m/min, v_c = 250 m/min.

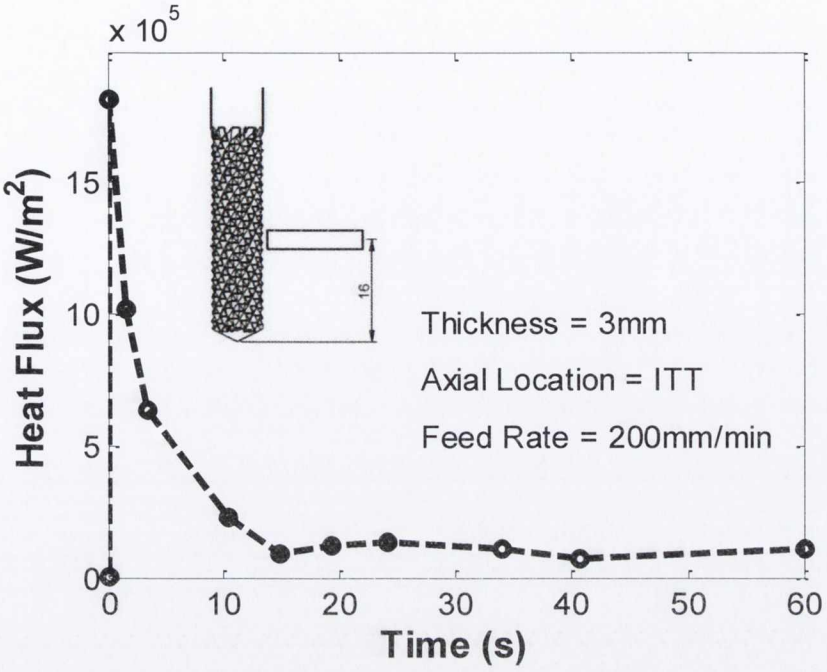

Figure 4.39: Plot of the time-series heat flux associated with the tool surface for thickness = 3mm, L_a = 16 mm, v_f = 200 m/min, v_c = 250 m/min.

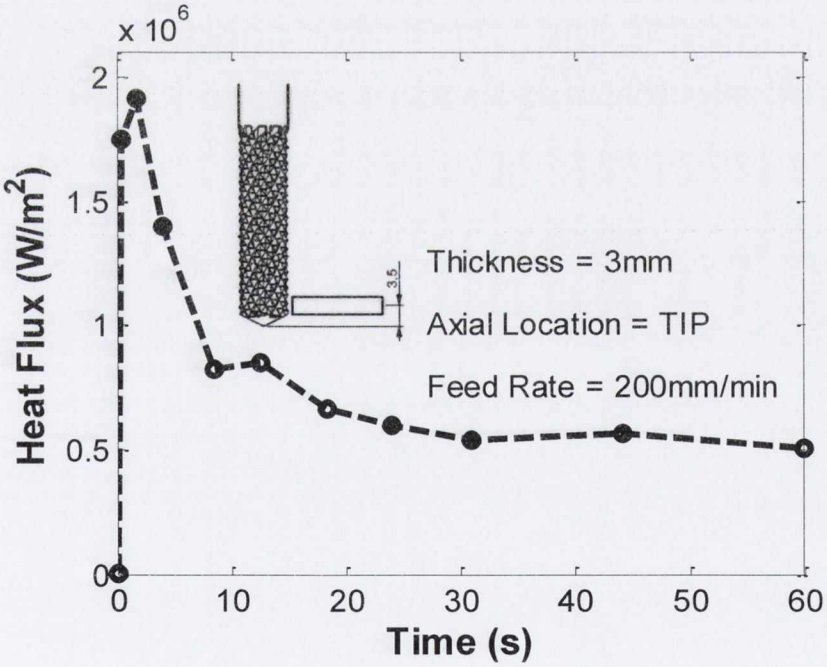

Figure 4.40: Plot of the time-series heat flux associated with the tool surface for thickness = 3mm, L_a = 3.5 mm, v_f = 200 m/min, v_c = 250 m/min.

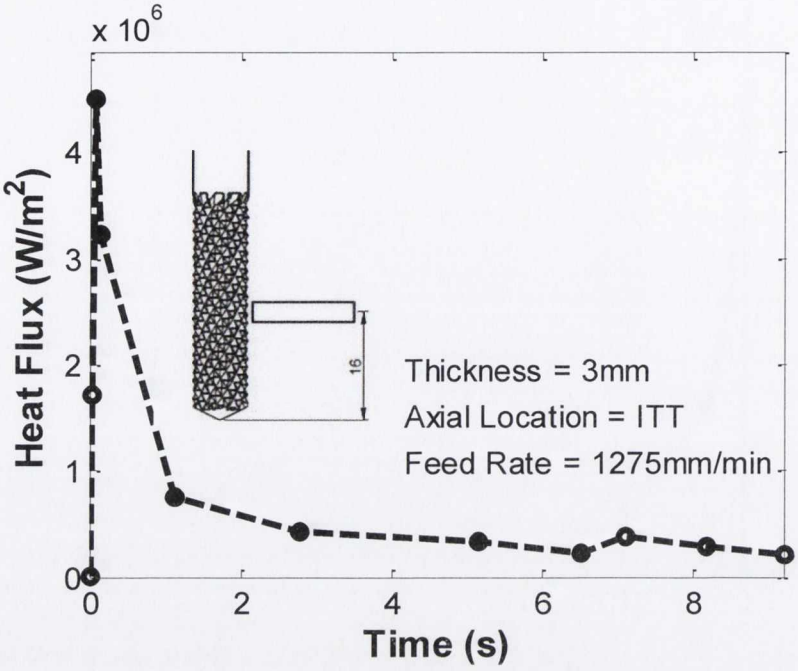

Figure 4.41: Plot of the time-series heat flux associated with the tool surface for thickness = 3mm, L_a = 16 mm, v_f = 1275 m/min, v_c = 250 m/min.

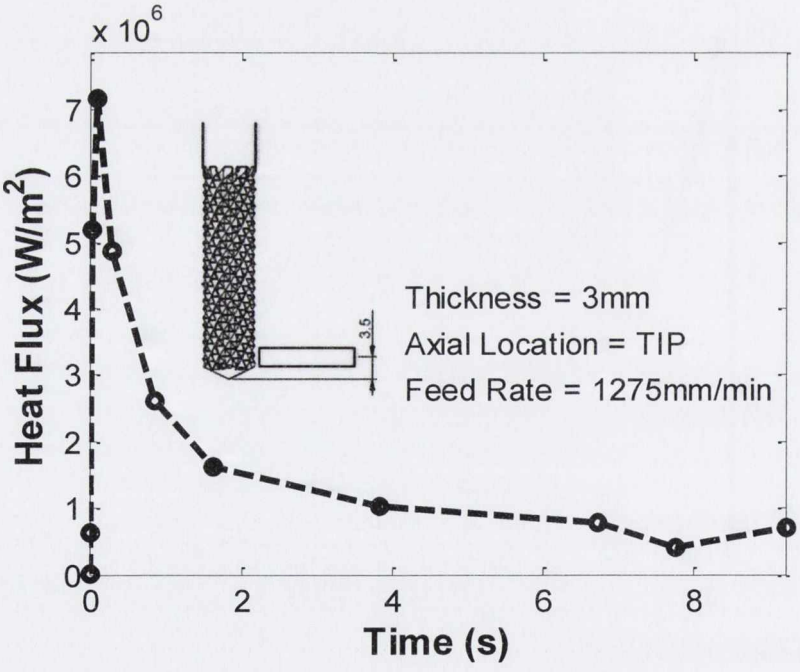

Figure 4.42: Plot of the time-series heat flux associated with the tool surface for thickness = 3mm, L_a = 3.5 mm, v_f = 1275 m/min, v_c = 250 m/min.

The important shape function components were identified in test 4.1. These parameters were extracted for each of the design points. The averages of the heat flux shape function components are summarised in Table 4.8.

Table 4.8: Heat flux component summary for test 4.2.

	Heat flux component		
Design Point	Peak value (kW/m2)	Time to decay (s)	Steady state magnitude (W/m2)
1	18,000	14	1,000
2	7,300	12	1,000
3	80,300	5	1,000
4	81,000	4	1,000
5	17,500	14	1,000
6	19,400	18	5,000
7	46,000	2.8	3,000
8	72,000	3.9	9,000

Surface Analysis

Preliminary microscope observations of the surfaces revealed a discrepancy between surfaces machined at the tool tip and those machined at the ITT sensor. These discrepancies, initially observed as shown Figure 4.44, were noted to be present for both workpiece thickness levels used, i.e. both radial depths of cut, although only the lower feed rate produced such results. The discrepancy is found in the lower section of the workpiece, in which there appears to exist a scattering of excess chip particles from the cutting process, causing the surface to appear fuzzy and matted in this section. Further analysis under the SEM indicates that there is in fact a cavity beneath this lower section of the workpiece, in which the matrix material has been degraded away to expose the underlying carbon fibres. This type of degradation is seen intermittently throughout the length of cut. An alternative surface is found between such voided sections in which fine chip particles appear bonded to the surface as a powdery covering over all fibre orientations apart from the 0° orientation, as illustrated in Figure 4.43(A). This is in stark contrast to the typical surface seen when machining with the same feed rate, cutting speed and depths of cut, but using a higher axial point on the tool teeth, as shown in Figure 4.43(B). In this image, there are clear fracture lines where the epoxy has been removed from the surface, and there is no evidence of chip particles or powder.

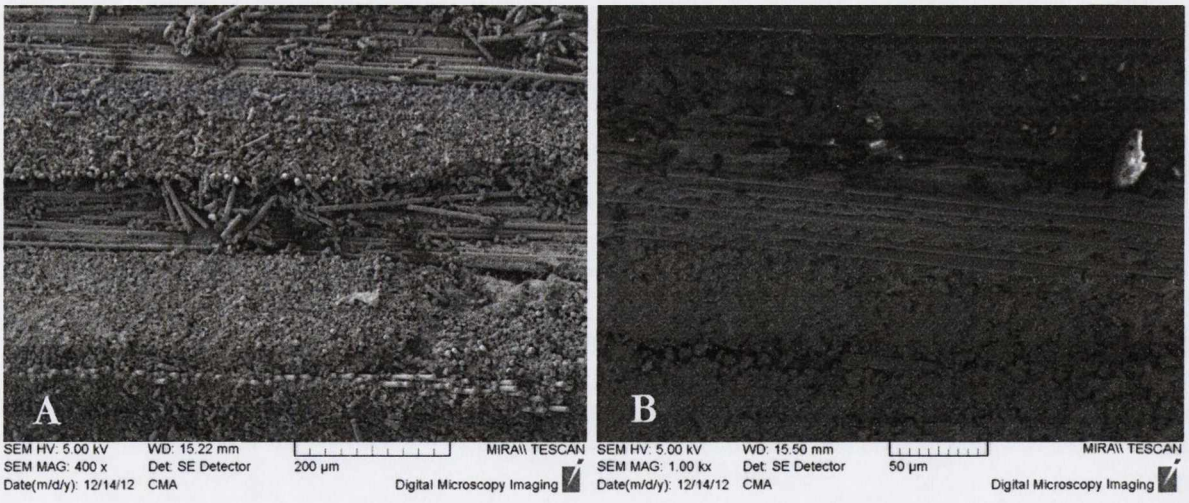

Figure 4.43: SEM images contrasting the surface quality associated with CFRP machined using V_c = 250 m/min; V_f = 200 mm/min; a_e = 6mm for (A) lower section machined at tool tip and (B) upper section of workpiece machined 16mm above the tool tip.

Figure 4.44: Edge trimmed surfaces with indications of difference in quality due to axial variation for (A) 6mm & (B) 3mm thick samples.

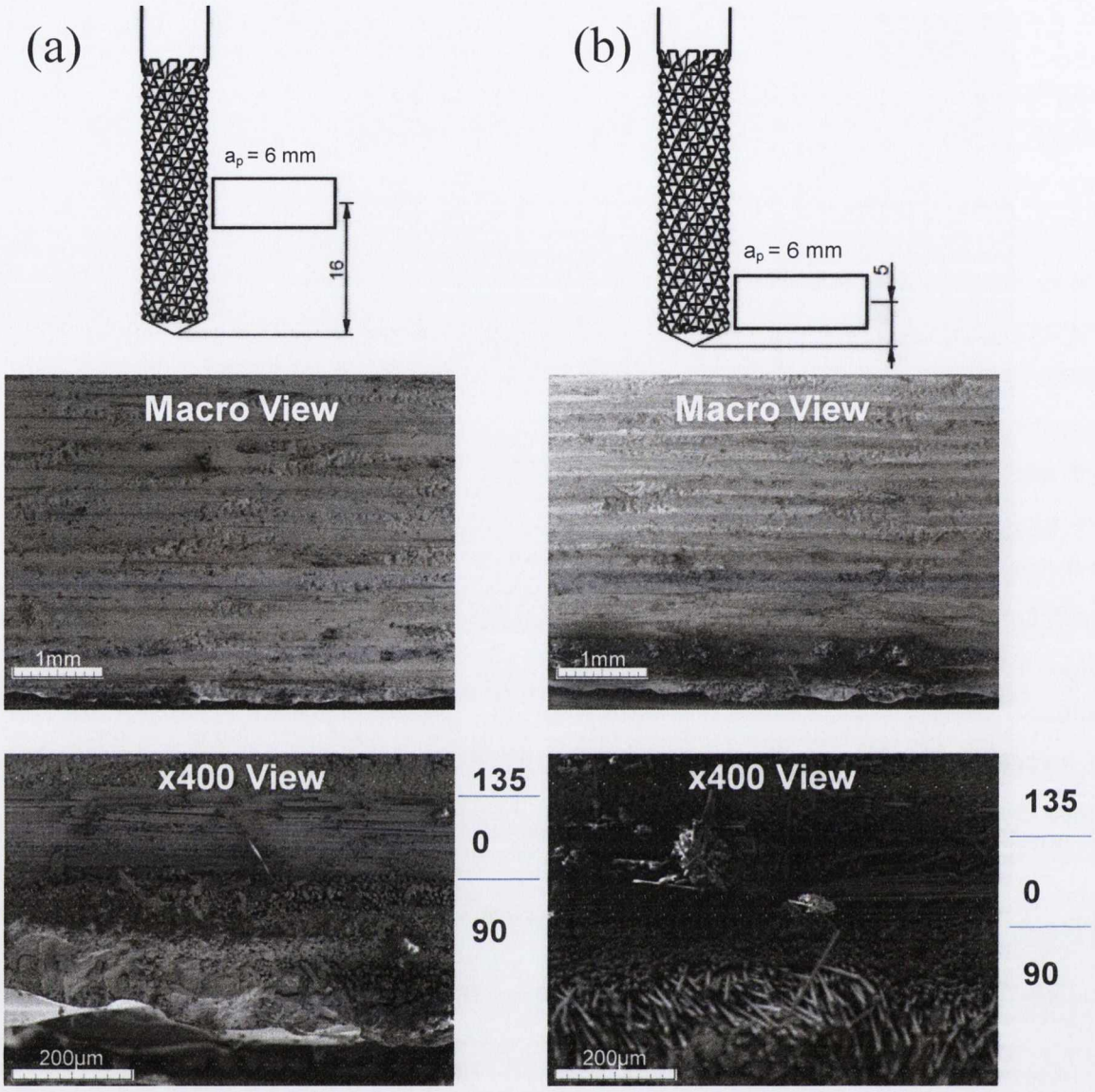

Figure 4.45: SEM images of the difference in machined CFRP surface quality due to variation in axial tool engagement location for 6mm axial depth of cut.

The onset of such a discrepancy is present after approximately 20 mm into the 200 mm long trimmed section. This can be connected with the temperature profile seen in the cutting tool, which has a rapid increase in temperature during the initial plunge phase of cutting. If this formation is caused by exceeding the stable temperature region, it is an indication that such a temperature was exceeded early on. In conjunction with the temperature data profiles acquired via thermography and the fully characterised ITT sensor, which indicates a steady state value is also achieved relatively quickly in the tool domain, there is strong evidence to support such a temperature profile.

Surface Roughness Results

In order to undertake this analysis, a surface roughness value was determined for each of the specimens. From the literature, [99] it has been established that R_Y, the maximum peak-to-valley profile height, provides a more comprehensive account of the surface roughness than R_A, the arithmetic mean, for CFRP surfaces. Therefore, R_Y was assessed in both the feed and traverse directions, as described in section 4.3.5. The results of the transverse investigation are presented in Figure 4.46 and Table 4.9. An example of the transverse profile is plotted in Figure 4.47, illustrating the amplified roughness levels due to grooves generated by the interaction of the helical cutting edges with the CFRP workpiece.

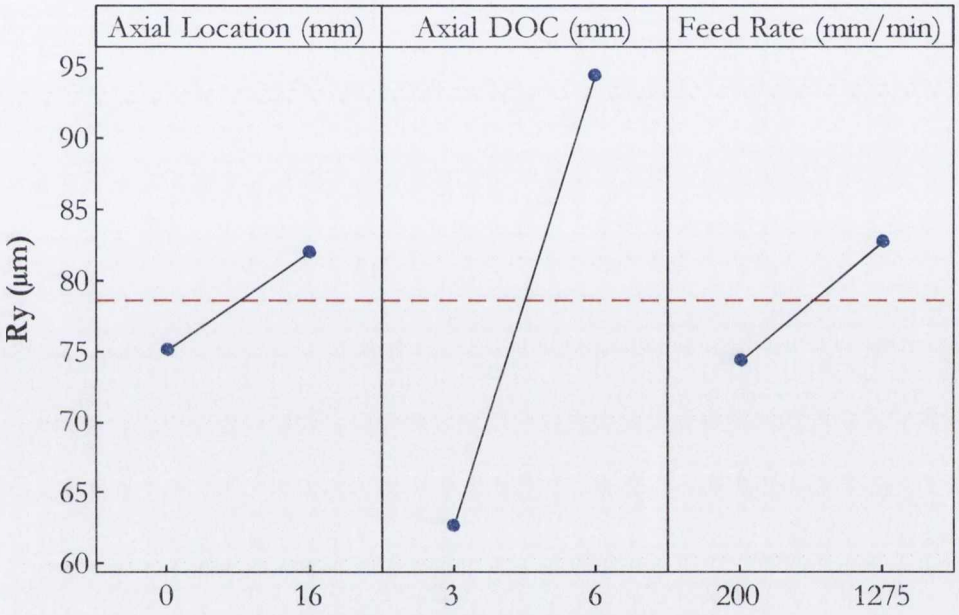

Figure 4.46: Main effects plot of R_Y.

Table 4.9: ANOVA results for R_Y from edge trimming tests.

Source	*DF*	*SS*	*MS*	*F*	*P*	*PCR*
Axial Location (mm)	1	192.2	192.2	0.45	0.516	0
Axial DOC (mm)	1	4065.3	4065.3	9.48	0.01	35.96
Feed Rate (mm/min)	1	281.6	281.6	0.66	0.434	0
Error	12	5146.8	428.9			64.04
Total	15	9686				

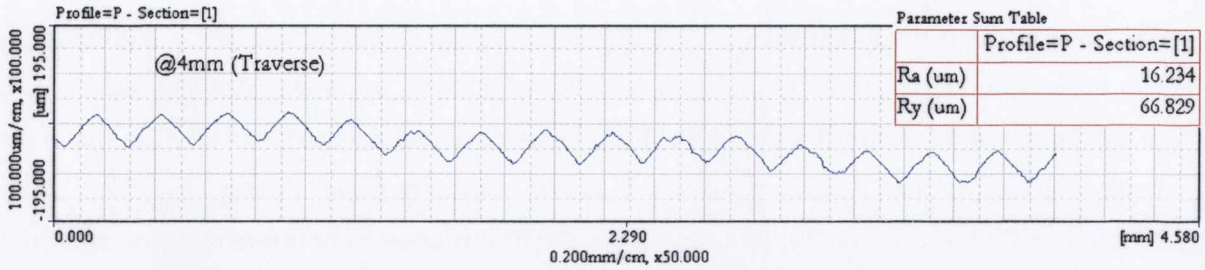

Figure 4.47: Example of the 2D profile generated by the stylus profilometer for surface roughness analyses.

These results indicate that only the axial depth of cut had any significant effect on the roughness response. However, there appears to be a large degree of uncertainty associated with this statistical result, due to the poor R-sq value of 47 % and large standard deviation of 20.7 µm. Similar results were reported by Sheikh-Ahmad *et al.* [202] who state that surface roughness in the traverse direction exhibited no clear trends with spindle speed and feed rate. This reinforces the unreliable nature of 2D stylus analyses for CFRP materials. No trends were obtained for the feed or longitudinal direction, although as was found by [202] in general longitudinal R_Z values were lower than transverse values, and as a result these were excluded from this research. To further attempt to obtain information regarding the roughness of the surface, a 3D surface analysis tool in the form of WLI was used in order to obtain surface quality descriptive values.

The images presented in Figure 4.49 show the typical outputs of the 3D surfaces generated using WLI. As the lower section of the workpiece indicated significant visible damage during previous inspection, scans were focused on this lower axial section of each workpiece specimen. The area covered by the scan was 1.42mm by 0.646mm. Scans were made at the 100mm and 200mm points along the workpiece length. The resulting S_Y values were calculated using SPIP software and analysed using Minitab.

The statistical results are presented in Figure 4.48 and Table 4.10. These results indicate a much higher level of statistical significance due to the increased R-sq value of 70%. The main effects plot shows axial location as having the largest effect on the S_Y response, with a PCR of 44.5%, causing a mean reduction of 118µm when the cutting tool moves from the tool tip to the location of the ITT sensor 16mm above this. Axial depth of cut is also shown to produce a lesser, though still significant effect, increasing the mean roughness value by approximately 75µm. Interestingly, the feed rate is not shown to have any significant effect when only this section of the workpiece is assessed. This is due to the overriding level of damage caused due to the change in location of the tool, which makes any comparison with regular surface anomalies, such as ridges due to the rate at which material is removed, impossible.

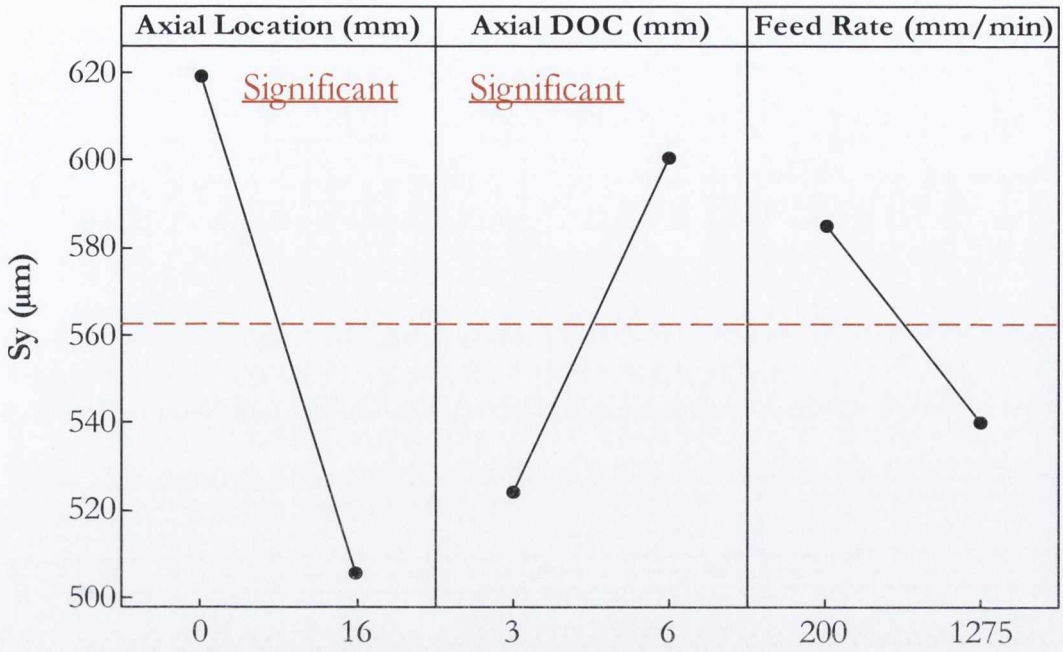

Figure 4.48: Main effects of the Sy surface roughness response.

Table 4.10: ANOVA results for S_Y from edge trimming tests.

Source	*DF*	*SS*	*MS*	*F*	*P*	*PCR*
Axial Location (mm)	1	59378	59378	18.92	0.001	44.54
Axial DOC (mm)	1	19092	19092	6.08	0.03	12.63
Feed Rate (mm/min)	1	7010	7010	2.23	0.161	3.07
Error	12	37658	3138			39.76
Total	15	123138				

Relating the surface roughness response of this investigation to the temperature responses, there is a clear pattern. Maximum tool temperature is shown to experience a significant effect due to both axial location and axial depth of cut.

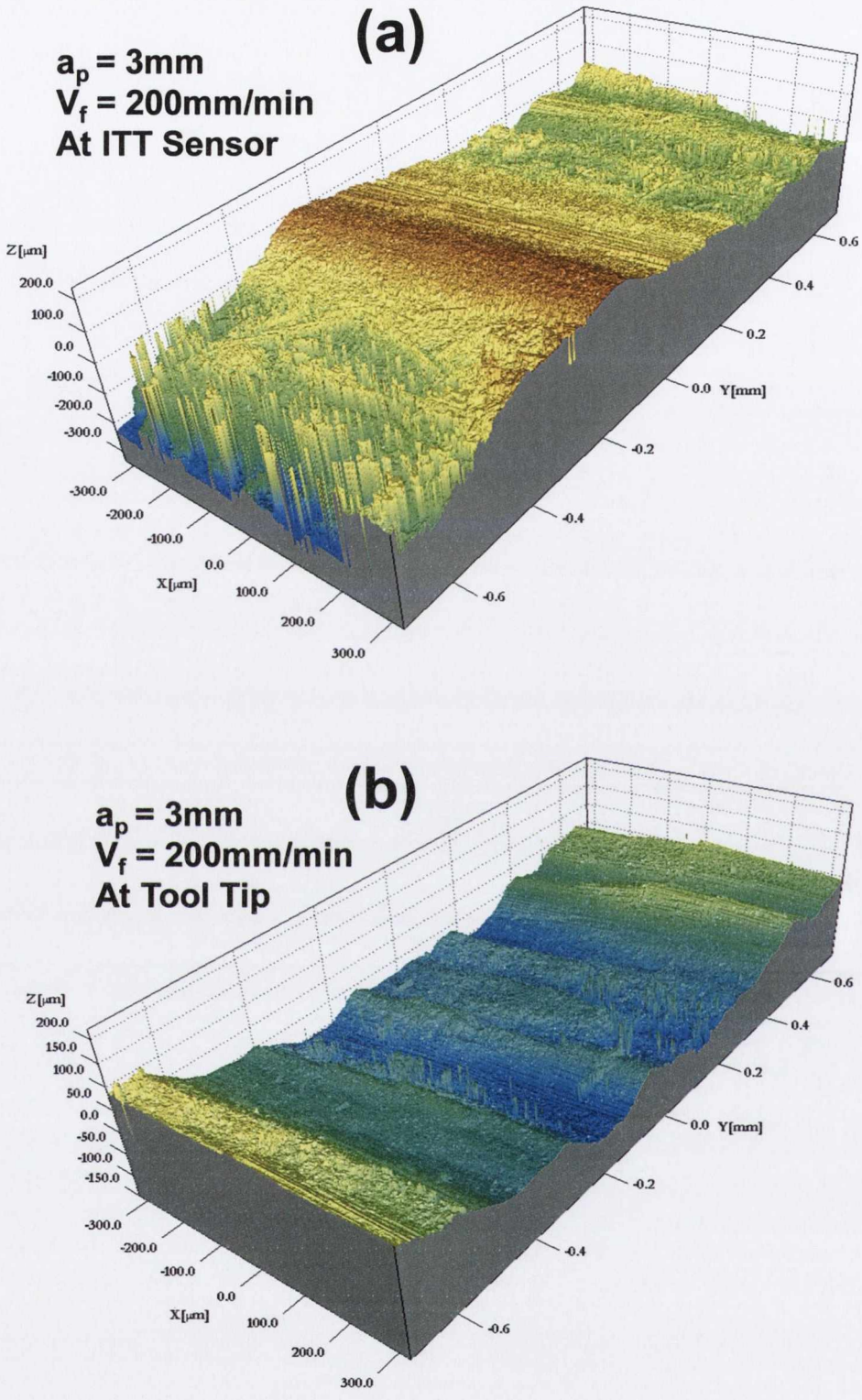

Figure 4.49: WLI scanned images used to generate the maximum peak-to-valley parameter (S_Y) for surface roughness analysis showing the difference between axial engagement location at (a) the ITT sensor location and (b) the tool tip.

Tool Wear Assessment

Due to the low cutting distance used in this investigation, minimal tool wear was anticipated. SEM images of the tool before and after the edge trimming campaign were captured to ensure no such wear took place. Figure 4.50 shows the images used in this assessment. This image also indicates a large build-up of epoxy on the lower slopes of both the rake and clearance faces of the pyramidal teeth. A primary tool wear mechanism during initial stage of machining for this particular type of tool is tooth fracture, with flank wear and tip recession becoming more prevalent beyond the scope of the machining distances used in this experiment. Thus, this was the main focus for this assessment and it was found that no such wear occurred.

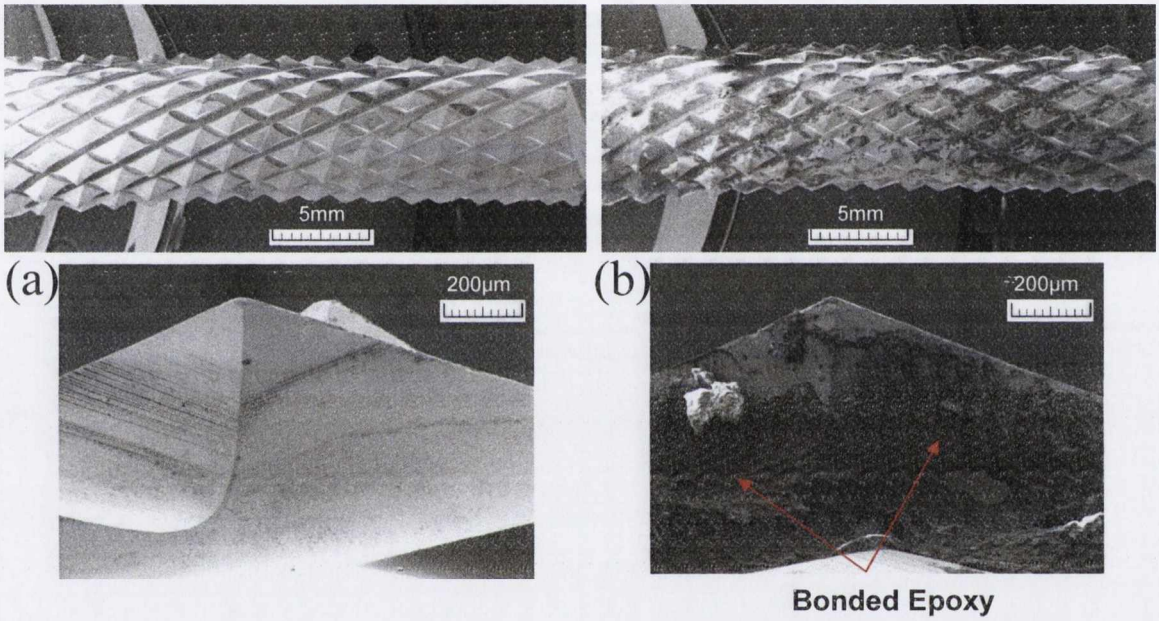

Figure 4.50: SEM images of the cutting tool taken (a) pre- and (b) post-machining.

5 CONCLUSIONS

From the finite element investigations, a number of findings were achieved regarding the representation of the cutting tool as a thermal system for sensorial perception purposes.

- Initially, the cutting tool was assumed to behave similarly to a cylinder in rotation. However, the cutting tool geometry is seen to result in notably higher maximum tool temperatures for a specific heat flux when compared to a basic cylinder – this is due to a higher area to volume ratio.
- The complexity and realism of the finite element model was further increased with the introduction of a 'Tool Holder' to the system by preventing heat choking at the top of the tool and allowing 'quasi-steady state' temperatures in the theoretical cutting zone to be achieved.
- A sensitivity analysis performed on thermal contact resistance (TCR) indicated that approximating the contact as *perfect* provided an appropriate level of accuracy for the system response.
- A similar sensitivity analysis of the influence of convection indicated that this did not change the system temperature response significantly. This evidence, in addition to the evidence in literature, which states that radiation does not contribute in any significant way to the heat transfer process, lead to the conclusion that conduction is the dominant form of heat transfer in this cutting process.
- Due to the asymmetric nature of the 'double helical tool' design, intended to ensure cutting edge overlap and prevent delamination and fraying, it was noted that the radial sensor location has a minor influence on the magnitude of the ITT sensor response, with contour plots of the radial cross section showing irregular isotherm patterns, rather than the concentric circular isotherms associated with the cylindrical geometry. This was enhanced further when localised rake face-specific input boundary conditions were incorporated into the model.
- A parametric analysis performed on axial depth of cut and axial cutting location indicated that both produced largely different results for the same heat flux value, introducing the hypothesis that for optimal temperature control in the cutting process, while one cannot change the axial depth of cut in many instances, it is prudent to work with the upper section of the tool – closest to the acting heat sink, i.e. the tool holder – to reduce the temperatures during machining and thus ensure that potential critical temperature limits are not exceeded.
- The heat flux input boundary condition specific to milling of CFRP has not been well explored in the literature and as such, an initial approximation of a constant heat flux,

or an equivalent heat flux, was employed. This lead to the hypothesis that multiple input heat flux functions can produce the same response from the sensor yet show markedly different surface temperature results more directly linked to the heat flux input type. This is possible due to the damping and lag associated with the ITT sensor.

- The FEM tool developed acts as an add-on calibration tool to the ITT sensor to improve sensorial perception of the edge trimming temperature. The parametric nature of the code developed enables for alternative tool geometries and materials to be implemented and investigated provided such tools can be 3D modelled and meshed appropriately.

The sensor behavior was assessed using specific metrics to close the gap between the unknown behavior of the ITT sensor and a known, well established technology – thermography. While there is a small degree of error associated with the microbolometer of the single colour thermometer in recording temperatures from a rotating complex geometry surface, these are relatively small in comparison to those associated with the ITT sensor. Therefore, comparing the ITT sensor temperature, an embedded, lagging, damped response, to a highly calibrated, surface-based sensor response is a reasonable method by which to develop sensorial perception of the ITT sensor. Additionally, availing of a known heat flux allows for validation of the finite element model using the surface temperature result captured by thermography. Due to the complexity and relatively unexplored nature of the heat flux associated with the CFRP milling process, an analogous constant heat flux, supplied by a diode laser, was used.

A number of findings from the analogous experiments were achieved regarding the ability of the ITT sensor to perceive transient temperature changes occurring at a cutting interface on the tool surface for a range of key parameters:

- Rotation has no significant effect on the gradient or magnitude of the maximum surface temperature response over a period of 7 to 24 s.
- Increasing the heat flux input proved to be the most significant variable in dictating the maximum temperature achieved at the surface of the tool.
- The axial location of the heat source was found to validate the FEM hypothesis that heat choking occurs at the tool tip, although a lower ITT maximum temperature is reported at the lower axial location for the same boundary conditions.
- A regression equation using linear coefficients for maximum temperature response was generated to display the relationship for heating period and heat flux.

- The constant heat flux experiments validated FE model parameters, allowing for the conclusion that the model represents a reasonable approximation of the heat transfer occurring in the tool system for a specified input boundary condition.

A number of findings from the CFRP edge trimming applied investigations were achieved regarding the appropriateness of the ITT sensor to perceive non-uniform heat flux input types similar to those associated with the temperature during edge trimming.

- Surface temperature data acquired during trimming experiments was applied to the model to determine an approximation of the *real* heat flux for this process. The FE model, in conjunction with experimental ITT sensor data produced a good approximation of the behavior of heat transfer from the cutting zone to the tool for specific cutting parameters, as validated using thermography.
- During validation of the FE model using cutting data, a partial over-estimation of the ITT sensor response was noted when the experimental surface data was applied as the input boundary condition to the FE model. A closer look at the ITT sensor indicates that a reason for this effect is due to the ITT sensor's inability to account for such highly transient heat flux changes due to:
    1. The thermal resistances associated with the tool and sensor fixation materials between the sensor and cutting process.
    2. The response time of the ITT sensor.
- The use of the ITT sensor is therefore found to be most appropriate in determining the long-term steady state cutting temperature over an extended period of cutting greater than 100mm. Due to the large time constant associated with the ITT sensor, it appears that this device is more appropriate for use as a process characterisation tool to develop machinability look-up tables.

- Investigations into the heat flux associated with the CFRP edge trimming process indicated a general trend throughout all combinations of cutting parameters investigated in which an initial short spike in thermal energy of 5 to 50 times the remaining constant heat flux was noted, with values for the constant heat flux ranging from 100 kW/m^2 to 1000 kW/m^2. This was validated using experimentally obtained surface temperature data via thermography.

This work provides a methodology developed to use ITT sensor technology to acquire quantitative tool temperatures and study heat fluxes associated with the cutting interface during rough edge trimming of CFRP. From the CFRP edge trimming investigations on parameter effects it is concluded that:

- The hypothesis developed during the modelling phase of investigations regarding the relationship between axial cutting location and tool temperature significantly influenced the resulting workpiece quality. The appearance of intense cratering and agglomerated matrix occurred for an axial location at the tool tip, where heat choking became most prevalent. For identical cutting parameters and environmental conditions, at an axial location 16mm above the tool tip, no evidence was found to indicate the presence of thermally related damage on the workpiece.
- With tool wear minimised due to the low volume of material removed with the tool, the evidence indicates that CFRP as a workpiece material is extremely sensitive to temperatures during edge trimming. This is due to the relationship noted between the temperature of the process and the surface roughness, with an increase in axial position away from the tool tip producing both a reduced maximum process temperature and an improved surface finish. Conversely, an increase in workpiece thickness was found to increase the maximum process temperature by an average of 16% whilst surface roughness was seen to increase by an average of 33%. This indicates that the impact on surface roughness is approximately twice that of temperature effect when the workpiece thickness is doubled from 3mm to 6mm.

6 FUTURE WORKS

This research highlighted a number of areas where further investigation is warranted:

- Further FEM research should be undertaken to develop an advanced add-on software tool for ITT sensor-type applications, which investigates the input boundary conditions in greater detail. Due to the level of importance associated with the boundary conditions on the effectiveness of the FEM in representing reality, the dynamic location of boundary conditions within such a model should be investigated. This has applications in monitoring variable engagement strategies for tool-preservation and in 5-axis milling applications. To validate such research, a tool with multiple thermocouple sensors embedded at a variety of axial locations should be developed.
- Investigations into the effect of cutting speed on the CFRP milling tool temperature should be investigated, as this is a primary factor in the generation of heat during a cutting process.
- A key conclusion related to the application of this type of sensor in the monitoring of rotary machine tool operations. A strategy for potential future works is the use of the ITT sensor and FEM tool in building a look-up table type database of steady-state process temperatures for the appropriate range of machining parameters associated with the particular tool being investigated.
- The use of the ITT sensor and FEM, in conjunction with a similarly designed workpiece sensor and FEM could be developed in order to confirm or deny the currently unknown heat partition ratio associated with CFRP edge trimming.
- The relationship between tool temperature and surface roughness and quality should be further developed to determine the thermal limits of the CFRP edge trimming process from a workpiece quality perspective. In addition, simultaneous tool wear investigations should be performed in order to make inferences regarding the long term effects of temperature on the dry cutting process.
- An effective, appropriate means by which to cool the CFRP edge trimming process should also be investigated in detail. With a larger proportion of heat dispersed into the workpiece than is typically seen in metals, CFRP-specific tool design should be focused on cooling mechanisms. The cooling of the CFRP edge trimming process could then be investigated using the advanced status ITT sensor.

- The use of multiple thermocouples along the length of the cutting tool should be investigated in order to generate a more detailed perception of the thermal behaviour of a cutting tool during machining.

REFERENCES

[1] Byrne, G., D. Dornfeld and B. Denkena, *Advancing Cutting Technology.* CIRP Annals - Manufacturing Technology, 2003. **52**(2): p. 483-507.

[2] Fraden, J., *Temperature Sensors*, in *Handbook of Modern Sensors*. 2010, Springer: London. p. 519 - 566.

[3] Teti, R., K. Jemielniak, G. O'Donnell and D. Dornfeld, *Advanced monitoring of machining operations.* CIRP Annals - Manufacturing Technology, 2010. **59**(2): p. 717-739.

[4] Gregory, R.L., *Knowledge in Perception and Illusion.* Philosophical Transactions: Biological Sciences, 1997. **352**(1358): p. 1121 - 1127.

[5] Davies, M.A., T. Ueda, R. M'Saoubi, B. Mullany and A.L. Cooke, *On The Measurement of Temperature in Material Removal Processes.* CIRP Annals - Manufacturing Technology, 2007. **56**(2): p. 581-604.

[6] Klocke, F., S. Kratz, T. Auerbach, Sascha Gierlings, GuidoWirtz and D. Veselovac, *Process monitoring and controll of machining operations.* International Journal of Automation Technology, 2011. **5**(3): p. 403 - 411.

[7] Klocke, F., S. Gierlings, M. Brockmann and D. Veselovac, *Influence of Temperature on Surface Integrity for Typical Machining Processes in Aero Engine Manufacture.* Procedia Engineering, 2011. **19**(0): p. 203-208.

[8] Armendia, M., A. Garay, A. Villar, M.A. Davies and P.J. Arrazola, *High bandwidth temperature measurement in interrupted cutting of difficult to machine materials.* CIRP Annals - Manufacturing Technology, 2010. **59**(1): p. 97-100.

[9] Byrne, G., D. Dornfeld, I. Inasaki, G. Ketteler, W. König and R. Teti, *Tool Condition Monitoring (TCM) — The Status of Research and Industrial Application.* CIRP Annals - Manufacturing Technology, 1995. **44**(2): p. 541-567.

[10] Roberts, T., *The Carbon Fibre Industry Worldwide 2011-2020: An Evaluation of Current Markets and Future Supply and Demand*, 2012.

[11] Kozarsky, R., A. Vicari and M. Holman, *Stronger, Lighter, Faster...Cheaper? How Innovation Will Affect Carbon Fiber's Cost and Market Impact*, in *State of the Market Report*2012.

[12] Ashby, M.F. and D.R.H. Jones, *Engineering Materials 2: An Introduction to Microstructures, Processing and Design*. 1998, Oxford: Butterworth-Heinemann.

[13] Peters, S.T., *Introduction, Composite Basics and Road Map*, in *Handbook of Composites*, S.T. Peters, Editor. 1998, Chapman & Hall: London.

[14] Nelson, T., *787 Systems and Performance*, Boeing, Editor 2005, Boeing Management Company.

[15] König, W., C. Wulf, P. Graß and H. Willerscheid, *Machining of Fibre Reinforced Plastics.* CIRP Annals - Manufacturing Technology, 1985. **34**(2): p. 537-548.

[16] Schulze, V., C. Becke and R. Pabst, *Specific machining forces and resultant force vectors for machining of reinforced plastics.* CIRP Annals - Manufacturing Technology, 2011. **60**(1): p. 69-72.

[17] Walker, J.M., *Handbook of Manufacturing Engineering*. 1996, Basel: Marcel Dekker Inc.

[18] Barlier, C., *Procede pour la detection et la mesure direct et en continu de l'unsure des outils de coupe par sonde incorporee*, INPI, Editor Patent Number FR 216218A1 - 1990, C. Barlier: France.

[19] Barlier, C., *Process on detection and direct continuous measurement of tool wear by embedded sensor*, EPO, Editor Patent Number EP 0369087 B1 - 1994. p. 1 - 6.

[20] Barlier, C., D. Benoit and L. Velnom, *Cutting tool with measuring means*, EPO, Editor Patent Number EP 1599303 - 2005: France.

[21] Mallick, P.K., *Fiber-Reinforced Composites*. 2008, New York: Taylor and Francis Group.

[22] Taylor, J.G., *Phenolic Resins: A Century of Progress*, ed. L. Pilato. 2010, Heidelberg: Springer.

[23] Åström, B.T., *Manufacturing of Polymer Composites*. 2002, London: Chapman & Hall.

[24] Fitzer, E., D.D. Edie and D.J. Johnson, *Carbon fibers-present state and future expectation; Pitch and mesophase fibers; Structure and properties of carbon fibers.*, in *Carbon Fibers Filaments and Composites*, J.L. Figueiredo, et al., Editors. 1989, Springer: New York, NY, USA. p. 3–41, 43–72, 119–146.

[25] Mallick, P.K., *Fiber-Reinforced Composites: Materials, Manufacturing and Design*. 3rd ed. 2008, London: CRC Press.

[26] Huang, X., *Fabrication and Properties of Carbon Fibers.* Materials, 2009. **2**: p. 2369-2403.

[27] AdvancedCompositesGroup, *Introduction to Advanced Composites and Prepreg Technology*, Umeco Composites.

[28] Penn, L.S. and H. Wang, *Epoxy Resins*, in *Handbook of Composites*, S.T. Peters, Editor. 1998, Chapman & Hall: London.

[29] Harper, C.A., *Handbook of Plastics, Elastomers, & Composites*. 4th ed. 2002, New York: McGraw-Hill.

[30] Costantino, S. and U. Waldvogel, *Epoxy Polymers: New Materials and Innovations*, ed. J.-P. Pascault and R.J.J. Williams. 2010, Weinheim: WILEY-VCH Verlag GmbH & Co.

[31] Sheikh-Ahmad, J.Y., *Machining of Polymer Composites*. 2009, New York: Springer.

[32] Chung, D.D.L., *Thermal analysis of carbon fiber polymer-matrix composites by electrical resistance measurement.* Thermochimica Acta, 2000. **364**(1-2): p. 121-132.

[33] Kalpakjian, S. and S.R. Schmidt, *Manufacturing Engineering and Technology*. 4th Ed. ed. 2001, London: Prentice Hall International.

[34] Smith, G.T., *Cutting Tool Technology*. 2008, London: Springer-Verlag.

[35] Jahromi, A.S. and B. Bahr, *An Analytical Method for Predicting Cutting Forces in Orthogonal Machining of Unidirectional Composites.* Composites Science and Technology, 2010. **In Press, Accepted Manuscript**.

[36] Wang, D.H., M. Ramulu and D. Arola, *Orthogonal cutting mechanisms of graphite/epoxy composite. Part I: unidirectional laminate.* International Journal of Machine Tools and Manufacture, 1995. **35**(12): p. 1623-1638.

[37] Davim, J.P., *Machining Composite Materials*. 2010, London: ISTE Ltd.

[38] Wang, D.H., M. Ramulu and D. Arola, *Orthogonal cutting mechanisms of graphite/epoxy composite. Part II: multi-directional laminate.* International Journal of Machine Tools and Manufacture, 1995. **35**(12): p. 1639-1648.

[39] Kim, K.S., D.G. Lee, Y.K. Kwak and S. Namgung, *Machinability of carbon fiber-epoxy composite materials in turning.* Journal of Materials Processing Technology, 1992. **32**(3): p. 553-570.

[40] Ferreira, J.R., N.L. Coppini and G.W.A. Miranda, *Machining optimisation in carbon fibre reinforced composite materials.* Journal of Materials Processing Technology, 1999. **92-93**: p. 135-140.

[41] Sreejith, P.S., R. Krishnamurthy, K. Narayanasamy and S.K. Malhotra, *Studies on the machining of carbon/phenolic ablative composites.* Journal of Materials Processing Technology, 1999. **88**(1-3): p. 43-50.

[42] Mata, F., V.N. Gaitonde, S.R. Karnik and J.P. Davim, *Influence of cutting conditions on machinability aspects of PEEK, PEEK CF 30 and PEEK GF 30 composites using PCD tools.* Journal of Materials Processing Technology, 2009. **209**(4): p. 1980-1987.

[43] Hocheng, H., H.Y. Puw and Y. Huang, *Preliminary study on milling of unidirectional carbon fibre-reinforced plastics.* Composites Manufacturing, 1993. **4**(2): p. 103-108.

[44] Davim, J.P., P. Reis and C.C. António, *A study on milling of glass fiber reinforced plastics manufactured by hand-lay up using statistical analysis (ANOVA).* Composite Structures, 2004. **64**(3-4): p. 493-500.

[45] Teti, R., *Machining of Composite Materials.* CIRP Annals - Manufacturing Technology, 2002. **51**(2): p. 611-634.

[46] Gaitonde, V.N., S.R. Karnik, J.C. Rubio, A.E. Correia, A.M. Abrão and J.P. Davim, *Analysis of parametric influence on delamination in high-speed drilling of carbon fiber reinforced plastic composites.* Journal of Materials Processing Technology, 2008. **203**(1-3): p. 431-438.

[47] Kobayashi, A., *Machining of Plastics.* 1967, New York: McGraw-Hill Book Company.

[48] Ramakrishna, S., Z.-M. Huang, G.V. Kumar, A.W. Batchelor and J. Mayer, *An Introduction to Biocomposites.* Vol. Vol. 1. 2004, London: Imperial College Press.

[49] Malkusch, W., B. Rehn and J. Bruch, *In vitro method for medical risk assessment of laser fumes.* Optics & Laser Technology, 1995. **27**(1): p. 39-43.

[50] *TLVs and BEIs*, A.C.o.G.I. Hygienists, Editor 2008: Cincinnati, OH.

[51] NIOSH, *Recommendations for Occupational Safety and Health*, in *Compendium of policy documents and statements,*1992: http://www.cdc.gov/niosh/92–100.html.

[52] Konig, W. and S. Rummenholler, *Technological and industrial safety aspects in milling FRPS.* Machining of Advanced Composites, ASME, 1993. **Vol. 66**.

[53] Busch, H., W. Holländer, K. Levsen, J. Schilhabel, F.J. Trasser and L. Neder, *Aerosol formation during laser cutting of fibre reinforced plastics.* Journal of Aerosol Science, 1989. **20**(8): p. 1473-1476.

[54] *Composite Materials Handbook: Polymer Matrix Composites Guidelines for Characterization of Structural Materials*, D.o. Defense, Editor 2002.

[55] Adam Khan, M. and A. Senthil Kumar, *Machinability of glass fibre reinforced plastic (GFRP) composite using alumina-based ceramic cutting tools.* Journal of Manufacturing Processes, 2010. **In Press, Corrected Proof**.

[56] Arola, D. and M. Ramulu, *Orthogonal cutting of fiber-reinforced composites: A finite element analysis.* International Journal of Mechanical Sciences, 1997. **39**(5): p. 597-613.

[57] Arola, D., M. Ramulu and D.H. Wang, *Chip formation in orthogonal trimming of graphite/epoxy composite.* Composites Part A: Applied Science and Manufacturing, 1996. **27**(2): p. 121-133.

[58] Beckwith, S.W., *Drilling, Cutting, Machining Composite Materials and Structures.* SAMPE Journal, 2009. **45**(2): p. 1-2.

[59] Iliescu, D., D. Gehin, I. Iordanoff, F. Girot and M.E. Gutiérrez, *A discrete element method for the simulation of CFRP cutting.* Composites Science and Technology, 2010. **70**(1): p. 73-80.

[60] Lasri, L., M. Nouari and M. El Mansori, *Modelling of chip separation in machining unidirectional FRP composites by stiffness degradation concept.* Composites Science and Technology, 2009. **69**(5): p. 684-692.

[61] Mkaddem, A., I. Demirci and M.E. Mansori, *A micro-macro combined approach using FEM for modelling of machining of FRP composites: Cutting forces analysis.* Composites Science and Technology, 2008. **68**(15-16): p. 3123-3127.

[62] Palanikumar, K. and J.P. Davim, *Assessment of some factors influencing tool wear on the machining of glass fibre-reinforced plastics by coated cemented carbide tools.* Journal of Materials Processing Technology, 2009. **209**(1): p. 511-519.

[63] Rao, G.V.G., P. Mahajan and N. Bhatnagar, *Three-dimensional macro-mechanical finite element model for machining of unidirectional-fiber reinforced polymer composites.* Materials Science and Engineering: A, 2008. **498**(1-2): p. 142-149.

[64] Santhanakrishnan, G., R. Krishnamurthy and S.K. Malhotra, *Machinability characteristics of fibre reinforced plastics composites.* Journal of Mechanical Working Technology, 1988. **17**: p. 195-204.

[65] Santhanakrishnan, G., R. Krishnamurthy and S.K. Malhotra, *High speed steel tool wear studies in machining of glass-fibre-reinforced plastics.* Wear, 1989. **132**(2): p. 327-336.

[66] Santiuste, C., H. Miguélez and X. Soldani, *Out-of-plane failure mechanisms in LFRP composite cutting.* Composite Structures, 2011. **93**(11): p. 2706-2713.

[67] Venu Gopala Rao, G., P. Mahajan and N. Bhatnagar, *Machining of UD-GFRP composites chip formation mechanism.* Composites Science and Technology, 2007. **67**(11-12): p. 2271-2281.

[68] Bhatnagar, N., N. Ramakrishnan, N.K. Naik and R. Komanduri, *On the machining of fiber reinforced plastic (FRP) composite laminates.* International Journal of Machine Tools and Manufacture, 1995. **35**(5): p. 701-716.

[69] Lasri, L., M. Nouari and M.E. Mansori, *Wear resistance and induced cutting damage of aeronautical FRP components obtained by machining.* Wear, 2011. **271**(9-10): p. 2542-2548.

[70] Rahman, M., S. Ramakrishna, J.R.S. Prakash and D.C.G. Tan, *Machinability study of carbon fiber reinforced composite.* Journal of Materials Processing Technology, 1999. **89-90**: p. 292-297.

[71] Santhanakrishnan, G., R. Krishnamurthy and S.K. Malhotra, *Investigation into the machining of carbon-fibre-reinforced plastics with cemented carbides.* Journal of Materials Processing Technology, 1992. **30**(3): p. 263-275.

[72] Palanikumar, K., L. Karunamoorthy and R. Karthikeyan, *Assessment of factors influencing surface roughness on the machining of glass fiber-reinforced polymer composites.* Materials & Design, 2006. **27**(10): p. 862-871.

[73] Sreejith, P.S., R. Krishnamurthy and S.K. Malhotra, *Effect of specific cutting pressure and temperature during machining of carbon/phenolic ablative composite using PCBN tools.* Journal of Materials Processing Technology, 2007. **183**(1): p. 88-95.

[74] Sreejith, P.S., R. Krishnamurthy, S.K. Malhotra and K. Narayanasamy, *Evaluation of PCD tool performance during machining of carbon/phenolic ablative composites.* Journal of Materials Processing Technology, 2000. **104**(1-2): p. 53-58.

[75] Palanikumar, K. and R. Karthikeyan, *Assessment of factors influencing surface roughness on the machining of Al/SiC particulate composites.* Materials & Design, 2007. **28**(5): p. 1584-1591.

[76] Soldani, X., C. Santiuste, A. Muñoz-Sánchez and M.H. Miguélez, *Influence of tool geometry and numerical parameters when modeling orthogonal cutting of LFRP composites.* Composites Part A: Applied Science and Manufacturing, 2011. **42**(9): p. 1205-1216.

[77] Shyha, I., S.L. Soo, D. Aspinwall and S. Bradley, *Effect of laminate configuration and feed rate on cutting performance when drilling holes in carbon fibre reinforced plastic composites.* Journal of Materials Processing Technology, 2010. **In Press, Accepted Manuscript**.

[78] Abrate, S. and D.A. Walton, *Machining of composite materials. Part I: Traditional methods.* Composites Manufacturing, 1992. **3**(2): p. 75-83.

[79] Chen, W.-C., *Some experimental investigations in the drilling of carbon fiber-reinforced plastic (CFRP) composite laminates.* International Journal of Machine Tools and Manufacture, 1997. **37**(8): p. 1097-1108.

[80] Davim, J.P. and P. Reis, *Study of delamination in drilling carbon fiber reinforced plastics (CFRP) using design experiments.* Composite Structures, 2003. **59**(4): p. 481-487.

[81] El-Sonbaty, I., U.A. Khashaba and T. Machaly, *Factors affecting the machinability of GFR/epoxy composites.* Composite Structures, 2004. **63**(3-4): p. 329-338.

[82] Franke, V., *Drilling of long fiber reinforced thermoplastics--Influence of the cutting edge on the machining results.* CIRP Annals - Manufacturing Technology, 2011. **60**(1): p. 65-68.

[83] Karnik, S.R., V.N. Gaitonde, J.C. Rubio, A.E. Correia, A.M. Abrão and J.P. Davim, *Delamination analysis in high speed drilling of carbon fiber reinforced plastics (CFRP) using artificial neural network model.* Materials & Design, 2008. **29**(9): p. 1768-1776.

[84] Khashaba, U.A., *Delamination in drilling GFR-thermoset composites.* Composite Structures, 2004. **63**(3-4): p. 313-327.

[85] Quan, Y. and W. Zhong, *Investigation on drilling-grinding of CFRP.* Frontiers of Mechanical Engineering in China, 2009. **4**(1): p. 60-63.

[86] Rahme, P., Y. Landon and P. Lagarrigue, *Study into causes of damage to carbon epoxy composite material during the drilling process.* International Journal of Machining and Machinability of Materials, 2008. **3**(3/4): p. 309 -325.

[87] Rawat, S. and H. Attia, *Characterization of the dry high speed drilling process of woven composites using Machinability Maps approach.* CIRP Annals - Manufacturing Technology, 2009. **58**(1): p. 105-108.

[88] Schulze, V., C. Becke, K. Weidenmann and S. Dietrich, *Machining strategies for hole making in composites with minimal workpiece damage by directing the process forces inwards.* Journal of Materials Processing Technology, 2011. **211**(3): p. 329-338.

[89] Seif, M.A., U.A. Khashaba and R. Rojas-Oviedo, *Measuring delamination in carbon/epoxy composites using a shadow moiré laser based imaging technique.* Composite Structures, 2007. **79**(1): p. 113-118.

[90] Shyha, I.S., S.L. Soo, D.K. Aspinwall, S. Bradley, R. Perry, P. Harden, and S. Dawson, *Hole quality assessment following drilling of metallic-composite stacks.* International Journal of Machine Tools and Manufacture, 2011. **51**(7-8): p. 569-578.

[91] Stone, R. and K. Krishnamurthy, *A neural network thrust force controller to minimize delamination during drilling of graphite-epoxy laminates.* International Journal of Machine Tools and Manufacture, 1996. **36**(9): p. 985-1003.

[92] Tsao, C.C. and H. Hocheng, *Taguchi analysis of delamination associated with various drill bits in drilling of composite material.* International Journal of Machine Tools and Manufacture, 2004. **44**(10): p. 1085-1090.

[93] Tsao, C.C. and H. Hocheng, *Computerized tomography and C-Scan for measuring delamination in the drilling of composite materials using various drills.* International Journal of Machine Tools and Manufacture, 2005. **45**(11): p. 1282-1287.

[94] Brinksmeier, E., S. Fangmann and R. Rentsch, *Drilling of composites and resulting surface integrity.* CIRP Annals - Manufacturing Technology, 2011. **60**(1): p. 57-60.

[95] Quan, Y. and L. Sun, *Experimental investigation on drilling temperature of composites.* International Journal of Machining and Machinability of Materials, 2008. **3**(3-4): p. 356-363.

[96] Gilpin, A., *Tool solutions for machining composites.* Reinforced Plastics, 2009. **53**(6): p. 30-33.

[97] Arola, D. and M. Ramula, *Machining-induced surface texture effects on the flexural properties of a graphite/epoxy laminate.* Composites, 1994. **25**(8): p. 822 - 834.

[98] Davim, J.P. and P. Reis, *Damage and dimensional precision on milling carbon fiber-reinforced plastics using design experiments.* Journal of Materials Processing Technology, 2005. **160**(2): p. 160-167.

[99] Ramulu, M., C.W. Wern and J.L. Garbini, *Effect of fibre direction on surface roughness measurements of machined graphite/epoxy composite.* Composites Manufacturing, 1993. **4**(1): p. 39-51.

[100] Sasahara, H., T. Ogawa and T. Yashiro. *Cutting Temperature Measurement on Milling Process of CFRP.* in *Proceedings of the 4th CIRP International Conference on High Performance Cutting*. 2010. Nagaragawa Convention Centre, Gifu, Japan: CIRP.

[101] Abrate, S. and D. Walton, *Machining of composite materials. Part II: Non-traditional methods.* Composites Manufacturing, 1992. **3**(2): p. 85-94.

[102] Hocheng, H. and C.C. Tsao, *The path towards delamination-free drilling of composite materials.* Journal of Materials Processing Technology, 2005. **167**(2-3): p. 251-264.

[103] Herzog, D., P. Jaeschke, O. Meier and H. Haferkamp, *Investigations on the thermal effect caused by laser cutting with respect to static strength of CFRP.* International Journal of Machine Tools and Manufacture, 2008. **48**(12-13): p. 1464-1473.

[104] Kim, J.-D. and E.-S. Lee, *A study of the ultrasonic-vibration cutting of carbon-fiber reinforced plastics.* Journal of Materials Processing Technology, 1994. **43**(2-4): p. 259-277.

[105] Cenna, A.A. and P. Mathew, *Analysis and prediction of laser cutting parameters of fibre reinforced plastics (FRP) composite materials.* International Journal of Machine Tools and Manufacture, 2002. **42**(1): p. 105-113.

[106] Klotzbach, A., M. Hauser and E. Beyer, *Laser Cutting of Carbon Fiber Reinforced Polymers using Highly Brilliant Laser Beam Sources.* Physics Procedia, 2011. **12**(Part 1): p. 572-577.

[107] Pan, C.T. and H. Hocheng, *The anisotropic heat-affected zone in the laser grooving of fiber-reinforced composite material.* Journal of Materials Processing Technology, 1996. **62**(1-3): p. 54-60.

[108] Koplev, A., A. Lystrup and T. Vorm, *The cutting process, chips, and cutting forces in machining CFRP.* Composites, 1983. **14**(4): p. 371-376.

[109] Sheikh-Ahmad, J., N. Urban and H. Cheraghi, *Machining Damage in Edge Trimming of CFRP.* Materials and Manufacturing Processes, 2012. **27**(7): p. 802-808.

[110] Pecat, O., R. Rentsch and E. Brinksmeier, *Influence of Milling Process Parameters on the Surface Integrity of CFRP.* Procedia CIRP, 2012. **1**(0): p. 466-470.

[111] Davis, J.R., *Tool Materials (ASM Speciality Handbook).* 1996: ASM International.

[112] Lee, L.-H., *Mechanisms of thermal degradation of phenolic condensation polymers. II. Thermal stability and degradation schemes of epoxy resins.* Journal of Polymer Science Part A: General Papers, 1965. **3**(3): p. 859-882.

[113] Chatterjee, A., *Thermal Degradation Analysis of Thermoset Resins.* Journal ofApplied Polymer Science, 2009. **114**: p. 1417–1425.

[114] Shyha, I.S.E.M., *Drilling of Carbon Fibre Reinforced Plastic Composites*, in *School of Manufacturing and Mechanical Engineering*2010, University of Birmingham: Birmingham.

[115] Ramulu, M. and D. Arola, *Water jet and abrasive water jet cutting of unidirectional graphite/epoxy composite.* Composites, 1993. **24**(4): p. 299-308.

[116] Goeke, A. and C. Emmelmann, *Influence of Laser Cutting Parameters on CFRP Part Quality.* Physics Procedia, 2010. **5**: p. 253-258.

[117] Chatelain, J.-F. and I. Zaghbani, *A comparison of special helical cutter geometries based on cutting forces for the trimming of CFRP laminates.* International Journal of Mechanics, 2012. **6**(1): p. 52-59.

[118] Soo, S.L., I.S. Shyha, T. Barnett, D.K. Aspinwall and W.-M. Sim, *Grinding performance and workpiece integrity when superabrasive edge routing carbon fibre reinforced plastic (CFRP) composites.* CIRP Annals - Manufacturing Technology, 2012(0).

[119] Cajori, F., *The History of the Conservation of Energy: The Age of the Earth and Sun*, in *The Popular Science Monthly*1908. p. 97-111.

[120] Haven, K.F., *Marvels of Science: 50 fascinating 5-minute reads.* 1994, Westport, CT: Libraries Unlimited.

[121] Bever, M.B., E.R. Marshall and L.B. Ticknor, *The Energy Stored in Metal Chips during Orthogonal Cutting.* Journal of Applied Physics, 1953. **24**(9): p. 1176 - 1179.

[122] Da Silva, M.B. and J. Wallbank, *Cutting temperature: prediction and measurement methods - a review.* Journal of Materials Processing Technology, 1999. **88**(1): p. 195-202.

[123] Basti, A., T. Obikawa and J. Shinozuka, *Tools with built-in thin film thermocouple sensors for monitoring cutting temperature.* International Journal of Machine Tools and Manufacture, 2007. **47**(5): p. 793-798.

[124] Longbottom, F.M. and F.D. Lanham, *Cutting temperature measurement while machining - a review.* Aircraft Engineering and Aerospace Technology: An International Journal, 2005. **77**(2): p. 122-130.

[125] Trent, E.M.a.W., P.K. , *Metal Cutting.* 4th ed. ed. 2000, Boston, MA.: Butterworth-Heineman.

[126] Rosenthal, D., *The Theory of Moving Surfaces of Heat Transfer and its Application in Metal Treatment.* Transactions of the American Society of Mechanical Engineers, 1946. **68**(840): p. 849-866.

[127] Nag, P.K., *Heat and Mass Transfer.* 2nd Ed. ed. 2007, New Delhi: Tata McGraw Hill.

[128] Grzesik, W., *Advanced Machining Processes of Metallic Materials: Theory, Modelling and Applications.* 2008, Amsterdam: Elsevier.

[129] Kitagawa, T., A. Kubo and K. Maekawa, *Temperature and wear of cutting tools in high-speed machining of Inconel 718 and Ti-6Al-6V-2Sn.* Wear, 1997. **202**(2): p. 142-148.

[130] Fleischer, J., R. Pabst and S. Kelemen, *Heat Flow Simulation for Dry Machining of Power Train Castings.* CIRP Annals - Manufacturing Technology, 2007. **56**(1): p. 117-122.

[131] Courbon, C., T. Mabrouki, J. Rech, D. Mazuyer and E. D'Eramo, *On the existence of a thermal contact resistance at the tool-chip interface in dry cutting of AISI 1045: Formation mechanisms and influence on the cutting process.* Applied Thermal Engineering, 2013. **50**(1): p. 1311-1325.

[132] Pabst, R., J. Fleischer and J. Michna, *Modelling of the heat input for face-milling processes.* CIRP Annals - Manufacturing Technology, 2010. **59**(1): p. 121-124.

[133] Childs, P.R.N., *Practical Temperature Measurement*
2001, Oxford, Woburn: Butterworth-Heinemann.

[134] Michalski, L., K. Eckersdorf, J. Kucharski and J. McGhee, *Temperature Measurement.* Second Edition ed. 2001, Weinheim: John Wiley and Sons Ltd.

[135] Incropera, F., D.P. DeWitt, A.S. Lavine and T.L. Bergman, *Fundamentals of Heat and Mass Transfer.* 2005: John Wiley & Sons, Inc.

[136] Lienhard, J.H.I. and J.H.V. Lienhard, *A Heat Transfer Textbook*. 3rd ed. 2005, Cambridge, Massachusetts: Phlogiston Press.

[137] Elgar, P., *Sensors for Measurement and Control*. 1998, Essex: TecQuipment Limited.

[138] Kreith, F., R.F. Boehm, G.D. Raithby, K.G.T. Hollands and N.V. Suryanarayana, *Heat and Mass Transfer*, in *The CRC Handbook of Mechanical Engineering*, F. Kreith and D.Y. Goswami, Editors. 2005, CRC Press LLC: Florida.

[139] Garnier, B., J.C. Krapez, F. Lanzetta, P.H. Lemasson and J. Virgone. *Measurements with and without contact in heat transfer.* in *METTI 5: Thermal Measurements and Inverse Techniques*. 2011. Roscoff, France: Eurotherm.

[140] Komanduri, R. and Z.B. Hou, *A review of the experimental techniques for the measurement of heat and temperatures generated in some manufacturing processes and tribology.* Tribology International, 2001. **34**(10): p. 653-682.

[141] Richardson, D.J., M.A. Keavey and F. Dailami, *Modelling of cutting induced workpiece temperatures for dry milling.* International Journal of Machine Tools and Manufacture, 2006. **46**(10): p. 1139-1145.

[142] Arriola, I., E. Whitenton, J. Heigel and P.J. Arrazola, *Relationship between machinability index and in-process parameters during orthogonal cutting of steels.* CIRP Annals - Manufacturing Technology, 2011. **60**(1): p. 93-96.

[143] Hillery, M.T. and I. Shuaib, *Temperature effects in the drilling of human and bovine bone.* Journal of Materials Processing Technology, 1999. **92-93**: p. 302-308.

[144] Kusters, K.J., *The Temperatue Field in the Cutting Edge of a Cutting Tool*. 1954, Essen, Germany: Verlag Girardet.

[145] O'Sullivan, D. and M. Cotterell, *Temperature measurement in single point turning.* Journal of Materials Processing Technology, 2001. **118**(1-3): p. 301-308.

[146] Liu, Z.J., Y.M. Quan and L. Liang, *A wireless system for cutting temperature measurement*, in *Advanced Material Research*2011: Switzerland. p. 475-480.

[147] Ozisik, M.N. and H.R.B. Orlande, *Inverse Heat Transfer: Fundamentals and Applications*. 2000, London: Taylor & Francis.

[148] Battaglia, J.L., O. Cois, L. Puigsegur and A. Oustaloup, *Solving an inverse heat conduction problem using a non-integer identified model.* International Journal of Heat and Mass Transfer, 2001. **44**(14): p. 2671-2680.

[149] Rech, J., J.L. Battaglia and A. Moisan, *Thermal influence of cutting tool coatings.* Journal of Materials Processing Technology, 2005. **159**(1): p. 119-124.

[150] Samadi, F., F. Kowsary and A. Sarchami, *Estimation of heat flux imposed on the rake face of a cutting tool: A nonlinear, complex geometry inverse heat conduction case study.* International Communications in Heat and Mass Transfer, 2012. **39**(2): p. 298-303.

[151] Stephenson, D.A. *Tool-work thermocouple temperature measurements: theory and implementation issues.* 1992. Anaheim, CA, USA: Publ by ASME.

[152] Narutaki, N., A. Murakoshi, S. Motonishi and H. Takeyama, *Study on Machining of Titanium Alloys.* CIRP Annals - Manufacturing Technology, 1983. **32**(1): p. 65-69.

[153] Dewes, R.C., E. Ng, K.S. Chua, P.G. Newton and D.K. Aspinwall, *Temperature measurement when high speed machining hardened mould/die steel.* Journal of Materials Processing Technology, 1999. **92-93**: p. 293-301.

[154] Jaeschke, J.R., R.D. Zimmerly and S.M. Wu, *Automatic cutting tool temperature control.* International Journal of Machine Tool Design and Research, 1967. **7**(4): p. 465-475.

[155] Babic, D., D.B. Murray and A.A. Torrance, *Mist jet cooling of grinding processes.* International Journal of Machine Tools and Manufacture, 2005. **45**(10): p. 1171-1177.

[156] Choi, H. and X. Li, *Fabrication and application of micro thin film thermocouples for transient temperature measurement in nanosecond pulsed laser micromachining of nickel.* Sensors and Actuators A: Physical, 2007. **136**(1): p. 118-124.

[157] Brinksmeier, E., C. Heinzel and L. Meyer, *Development and Application of a Wheel Based Process Monitoring System in Grinding.* CIRP Annals - Manufacturing Technology, 2005. **54**(1): p. 301-304.

[158] Le Coz, G., M. Marinescu, A. Devillez, D. Dudzinski and L. Velnom, *Measuring temperature of rotating cutting tools: Application to MQL drilling and dry milling of aerospace alloys.* Applied Thermal Engineering, 2012. **36**(0): p. 434-441.

[159] Vollmer, M. and K.-P. Mollmann, *Infrared Thermal Imaging*. 2010, Weinheim: WILEY-VCH Verlag GmbH & Co.

[160] Minkina, W. and S. Dudzik, *Infrared Thermography: Errors and Uncertainties*. 2009, Chichester: Wiley.

[161] Pujana, J., L.d. Campo, R.B. Pérez-Sáez, M.J. Tello, I. Gallego and P.J. Arrazola, *Radiation thermometry applied to temperature measurement in the cutting process.* Measurement Science and Technology, 2007. **18**(11): p. 3409.

[162] Müller-Hummel, P. and M. Lahres, *Quantitative measurement of temperatures on diamond-coated tools during machining.* Diamond and Related Materials, 1995. **4**(10): p. 1216-1221.

[163] FLIR *Technical Note: Uncooled detectors for thermal imaging camera*. 2008.

[164] Sugita, N., T. Osa and M. Mitsuishi, *Analysis and estimation of cutting-temperature distribution during end milling in relation to orthopedic surgery.* Medical Engineering & Physics, 2009. **31**(1): p. 101-107.

[165] Del Campo, L., R.B. Ṕrez-Sáez, X. Esquisabel, I. Fernández and M.J. Tello, *New experimental device for infrared spectral directional emissivity measurements in a controlled environment.* Review of Scientific Instruments, 2006. **77**(11).

[166] Ueda, T., R. Nozaki and A. Hosokawa, *Temperature Measurement of Cutting Edge in Drilling -Effect of Oil Mist.* CIRP Annals - Manufacturing Technology, 2007. **56**(1): p. 93-96.

[167] Ueda, T., M. Sato, A. Hosokawa and M. Ozawa, *Development of infrared radiation pyrometer with optical fibers—Two-color pyrometer with non-contact fiber coupler.* CIRP Annals - Manufacturing Technology, 2008. **57**(1): p. 69-72.

[168] Ramsden, J.J., D.M. Allen, D.J. Stephenson, J.R. Alcock, G.N. Peggs, G. Fuller, and G. Goch, *The Design and Manufacture of Biomedical Surfaces.* CIRP Annals - Manufacturing Technology, 2007. **56**(2): p. 687-711.

[169] Çolak, O., C. Kurbanoglu and M.C. Kayacan, *Milling surface roughness prediction using evolutionary programming methods.* Materials & Design, 2007. **28**(2): p. 657-666.

[170] Peters, J., J.B. Bryan, W.T. Estler, C. Evans, H. Kunzmann, D.A. Lucca, . . . T.V. Vorburger, *Contribution of CIRP to the Development of Metrology and Surface Quality Evaluation during the last fifty years.* CIRP Annals - Manufacturing Technology, 2001. **50**(2): p. 471-488.

[171] Yang, J.L. and J.C. Chen, *A systematic approach for identifying optimum surface roughness performance in end-milling operations.* Journal of Industrial Technology, 2001. **17**(2).

[172] Benardos, P.G. and G.C. Vosniakos, *Predicting surface roughness in machining: a review.* International Journal of Machine Tools and Manufacture, 2003. **43**(8): p. 833-844.

[173] Killçkap, E., O. Çaklr, M. Aksoy and A. Inan, *Study of tool wear and surface roughness in machining of homogenised SiC-p reinforced aluminium metal matrix composite.* Journal of Materials Processing Technology, 2005. **164-165**: p. 862-867.

[174] Pramanik, A., L.C. Zhang and J.A. Arsecularatne, *An FEM investigation into the behavior of metal matrix composites: Tool-particle interaction during orthogonal cutting.* International Journal of Machine Tools and Manufacture, 2007. **47**(10): p. 1497-1506.

[175] Basheer, A.C., U.A. Dabade, S.S. Joshi, V.V. Bhanuprasad and V.M. Gadre, *Modeling of surface roughness in precision machining of metal matrix composites using ANN.* Journal of Materials Processing Technology, 2008. **197**(1-3): p. 439-444.

[176] Pramanik, A., L.C. Zhang and J.A. Arsecularatne, *Machining of metal matrix composites: Effect of ceramic particles on residual stress, surface roughness and chip formation.* International Journal of Machine Tools and Manufacture, 2008. **48**(15): p. 1613-1625.

[177] Kohles, S.S., M.B. Clark, C.A. Brown and J.N. Kenealy, *Direct assessment of profilometric roughness variability from typical implant surface types.* International Journal of Oral and Maxillofacial Implants, 2004. **19**(4): p. 510-516.

[178] Azmir, M.A. and A.K. Ahsan, *Investigation on glass/epoxy composite surfaces machined by abrasive water jet machining.* Journal of Materials Processing Technology, 2008. **198**(1-3): p. 122-128.

[179] Davim, J.P. and R. Cardoso, *Effect of the reinforcement (carbon or glass fibres) on friction and wear behaviour of the PEEK against steel surface at long dry sliding.* Wear, 2009. **266**(7-8): p. 795-799.

[180] Abraìfo, A.M., P.E. Faria, J.C.C. Rubio, P. Reis and J.P. Davim, *Drilling of fiber reinforced plastics: A review.* Journal of Materials Processing Technology, 2007. **186**(1-3): p. 1-7.

[181] Box, G.E.P., J.S. Hunter and W.G. Hunter, *Statistics for Experimenters: Design, Innovation, and Discovery*. 2005, New Jersey: John Wiley & Sons.

[182] Montgomery, D.C., *Design and Analysis of Experiments*. 6th ed. 2005, New York: McGraw-Hill.

[183] Trochim, W.M.K. and J.P. Donnelly, *The Research Methods Knowledge Base*. 2006, Florence, KY: Cengage Learning.

[184] Mullins, E., *Statistics for the quality control chemistry laboratory*. 2003, Cambridge: The Royal Society of Chemistry.

[185] Lazic, Z.R., *Design of Experiments in Chemical Engineering*. 2004, Weinheim: Wiley-VCH.

[186] Rittel, D., *Transient temperature measurement using embedded thermocouples.* Experimental Mechanics, 1998. **38**(2): p. 73-78.

[187] Rabin, Y. and D. Rittel, *A model for the time response of solid-embedded thermocouples.* Experimental Mechanics, 1999. **39**(2): p. 132-136.

[188] Mackerle, J., *Finite-element analysis and simulation of machining: a bibliography (1976–1996).* Journal of Materials Processing Technology, 1998. **86**(1–3): p. 17-44.

[189] Mackerle, J., *Finite element analysis and simulation of machining: an addendum: A bibliography (1996–2002).* International Journal of Machine Tools and Manufacture, 2003. **43**(1): p. 103-114.

[190] Atkins, T., *Toughness and processes of material removal.* Wear, 2009. **267**(11): p. 1764-1771.

[191] Yilbas, B.S., A.F.M. Arif, C. Karatas and M. Ahsan, *Cemented carbide cutting tool: Laser processing and thermal stress analysis.* Applied Surface Science, 2007. **253**(12): p. 5544-5552.

[192] Davies, J.R., *ASM Specialty Handbook - Carbon and Alloy Steels.* 1996, ASM International, Metals Park, OH: Davis & Associates.

[193] Badr, H.M. and S.C.R. Dennis, *Laminar forced convection from a rotating cylinder.* International Journal of Heat and Mass Transfer, 1985. **28**(1): p. 253-264.

[194] Byrne, A., G. Byrne, A. Davies and A.J. Robinson, *Transient and quasi-steady thermal behaviour of a building envelope due to retrofitted cavity wall and ceiling insulation.* Energy and Buildings, 2013. **61**(0): p. 356-365.

[195] Yvonnet, J., D. Umbrello, F. Chinesta and F. Micari, *A simple inverse procedure to determine heat flux on the tool in orthogonal cutting.* International Journal of Machine Tools and Manufacture, 2006. **46**(7–8): p. 820-827.

[196] Sepe, M.P., *Thermal Analysis of Polymers*, in *Rapra Review Reports: Expert overviews covering the science and technology of rubber and plastics*1997, Rapra Technoloy Ltd. p. 13-18, 22-33.

[197] Menczel, J.D. and R.B. Prime, *Thermal Analysis of Polymers: Fundamentals and Applications*. 2009, New Jersey: John Wiley & Sons.

[198] Available from: www.hurco.com.

[199] Zaghbani, I., J.-F. Chatelain, V. Songmene, S. Berube and A. Atarsia, *A comprehensive analysis of cutting forces during routing of multilayer carbon fiber-reinforced polymer laminates.* Journal of Composite Materials, 2012. **46**(16): p. 1955-1971.

[200] Colligan, K. and M. Ramulu, *Edge Trimming of Graphite/Epoxy with Diamond Abrasive Cutters.* Journal of Manufacturing Science and Engineering, 1999. **121**(4): p. 467-475.

[201] Kusiak, A., J.-L. Battaglia and R. Marchal, *Influence of CrN coating in wood machining from heat flux estimation in the tool.* International Journal of Thermal Sciences, 2005. **44**(3): p. 289-301.

[202] Kops, L. and M.C. Shaw, *Thermal Radiation in Surface Grinding.* CIRP Annals - Manufacturing Technology, 1982. **31**(1): p. 211-214.

[203] Shaw, M.C., *Energy Conversion in Cutting and Grinding.* CIRP Annals - Manufacturing Technology, 1996. **45**(1): p. 101-104.

APPENDICES

Appendix 1: Composite material categorisation chart

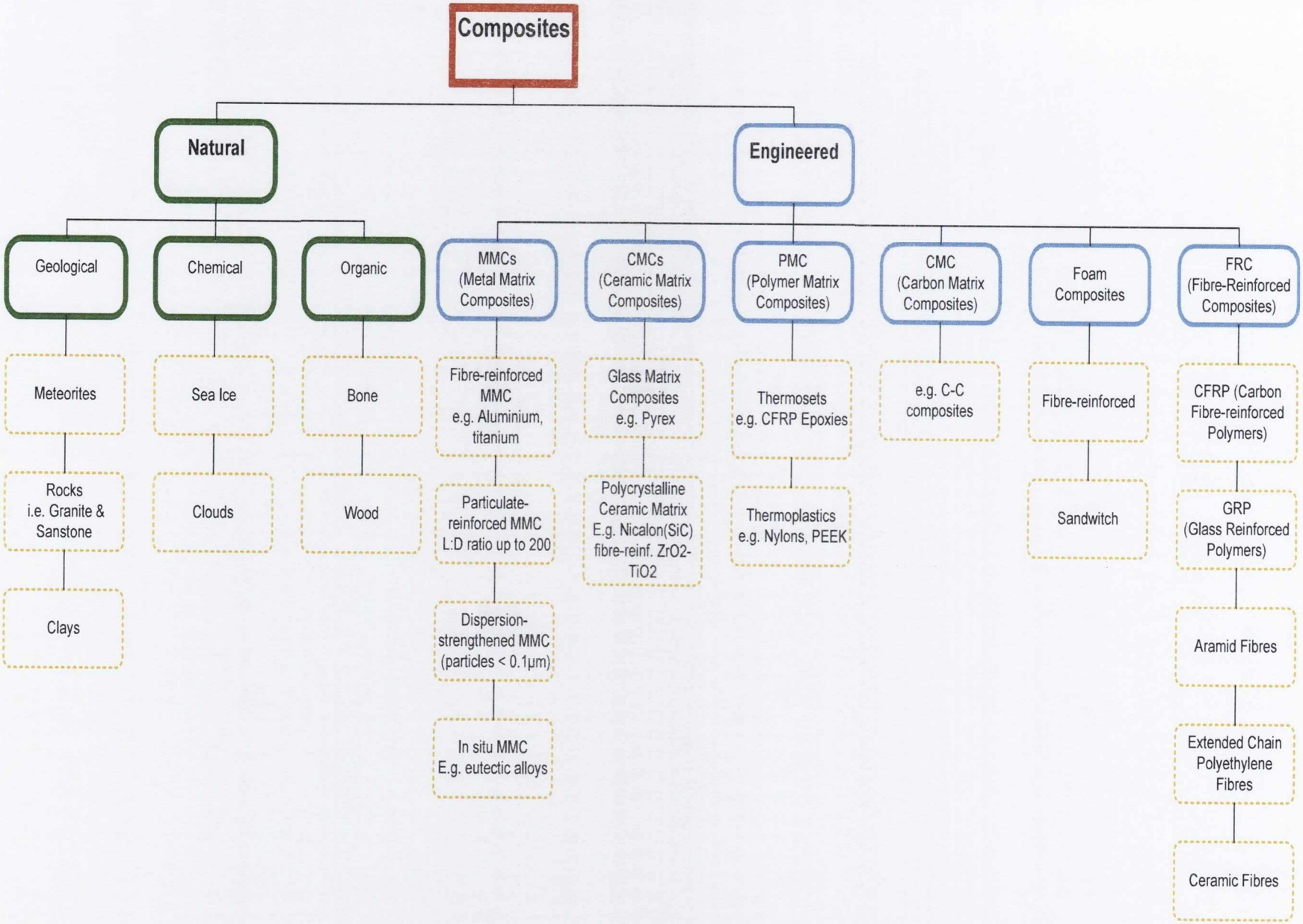

Appendix 2: Energy in the milling process.

Shaw states that there are 4 sources of energy consumption in the cutting process [203]:

- Plastic deformation
- Friction
- Surface energy
- Momentum transfer

However, Shaw also states that of these 4 sources only plastic deformation and friction are significant. This theory is advanced by Atkins [190], who states that rather than consider pure plastic deformation, all cutting of all materials forms a branch of fracture mechanics. As a result, the fracture toughness of the workpiece should be considered as much as the hardness in determining the chip formation. The fracture toughness of a material is defined as a property which describes the ability of a material containing a crack to resist fracture. Nevertheless, Shaw's concept of the specific cutting energy is still an important quantity by which to represent the cutting process.

Once the shear angle is known, it is possible to calculate a number of useful quantities including the cutting force, F_c, shear strain, shear force, F_s, acting on the shear plane, A_s, force acting on the plane normal to the shear plane, F_{ns}, frictional force, F_f, and force normal to the frictional plane, F_n, as detailed in [31]. Following knowledge of these forces, it is possible to calculate the power in the cutting process.

The machining power in the cutting process can be directly inferred by measuring the cutting force, F_c, in the direction of motion between tool and workpiece:

$$u = F_c v_c \qquad 6.1$$

Where u is the machining power (W)

As the vast majority of the energy in the cutting process is converted into heat energy, relating the energy to the geometric cutting parameters, whilst removing relationships with machining parameters such as cutting speed, can give an indication of the heat partition ratio for that process.

The specific cutting energy in milling is the machining power per unit volume per unit time and is represented by:

$$u = \frac{F_c v_c}{v_c\, b\, h} = \frac{F_c}{b\, h} = \frac{F_c}{A_c} \qquad 6.2$$

Where u is the specific cutting energy (J/mm^3)

F_c is the cutting force (N)

v_c is the cutting speed (m/min)

b is the width of cut or workpiece thickness (m)

h is the uncut chip thickness (m)

A_c is the area of the uncut chip (b x h) - (m^2)

As can be seen from 6.2, the specific cutting energy is independent of cutting speed and inversely proportional to the uncut chip dimensions. The specific cutting energy also varies with feed rate and workpiece mechanical properties such as hardness and fracture toughness.

The shear energy per unit volume during cutting can be determined using:

$$u_s = \frac{F_s v_s}{v\, A_c} = \frac{F_s v_s}{v\, A_s\, sin(\phi)} = \tau_s \cdot \gamma \qquad 6.3$$

Where u_s is the shear energy (J/m^3)

v_s is the shear velocity (m/s)

While the friction energy per unit volume is calculated as:

$$u_f = \frac{F_f v_c}{v\, A_c} = \frac{F_f\, r}{A_c} \qquad 6.4$$

Where u_f is the friction energy (J/m^3)

The shear and friction energy partitions are traditionally summed in metal cutting to produce the total cutting energy. However, in FRP composite machining, as the chip formation is

typically brittle fracture rather than shearing along the shear plane Sheikh-Ahmad [31] recommends the following expression for determining the total cutting energy:

$$\mathbf{p_s \approx [(1 - V_f)u_m + V_f u_{fibre}] + u_d + u_f} \qquad \textbf{6.5}$$

In milling operations, literature has shown that the specific cutting energy continually changes throughout the revolution of the tool as the relative orientation between the tool and workpiece change. Thus the specific cutting energy can be determined from the cutting and thrust forces using:

$$\mathbf{K_c(a_c, \theta) = \frac{F_c}{a_c\, a_w}} \qquad \textbf{6.6}$$

And

$$\mathbf{K_t(a_c, \theta) = \frac{F_t}{a_c\, a_w}} \qquad \textbf{6.7}$$

Where K_c is the specific principle cutting energy (N/m^2)
K_t is the specific thrust cutting energy (N/m^2)
a_c is the uncut chip thickness (m)
a_w is the uncut chip width (m)

In order to make comparisons between the specific cutting energy and the energy content calculated from the temperature change during the trimming process, an additional calculation is required. The calculation required can be determined from an examination of the units associated with the specific cutting energy and heat flux:

$$N = \frac{kg\, m}{s^2} = \frac{J}{m} \therefore J = \frac{kg\, m^2}{s^2} \therefore \frac{N}{m^2} \rightarrow \frac{W}{m^2} \times \frac{s}{m} \qquad \textbf{6.8}$$

Thus in order to convert the heat flux energy rate associated with the cutting process into specific cutting energy, divide the heat flux by the feed rate. This will allow for direct assessment of the energy ratio converted from the mechanical process of material removal into heat energy.

Elementary calculation of power in CFRP milling process

The machining power in the cutting process can be directly inferred by measuring the cutting force, F_c, in the direction of motion between tool and workpiece:

$$u = F_c v_c = (100N)\left(\frac{300m/min}{60}\right) = 500W \qquad 6.9$$

Where u is the machining power (W)

As the vast majority of the energy in the cutting process is converted into heat energy, relating the energy to the geometric cutting parameters, whilst removing relationships with machining parameters such as cutting speed, can give an indication of the heat partition ratio for that process. The specific cutting energy in milling is the machining power per unit volume per unit time and is represented by:

$$u = \frac{F_c v_c}{v_c\, b\, h} = \frac{F_c}{b\, h} = \frac{F_c}{A_c} = \frac{100}{(6)(8)} = 2.1\, J/mm^3 \qquad 6.10$$

Where u is the specific cutting energy (J/mm^3)

F_c is the cutting force (N)

v_c is the cutting speed (m/min)

b is the width of cut or workpiece thickness (m)

h is the uncut chip thickness (m)

A_c is the area of the uncut chip (b x h) - (m^2)

As can be seen from 6.2, the specific cutting energy is independent of cutting speed and inversely proportional to the uncut chip dimensions. The specific cutting energy also varies with feed rate and workpiece mechanical properties such as hardness and fracture toughness.

Appendix 3: Analytical study of a radial conduction in a heat cylinder

- By Leo Revil

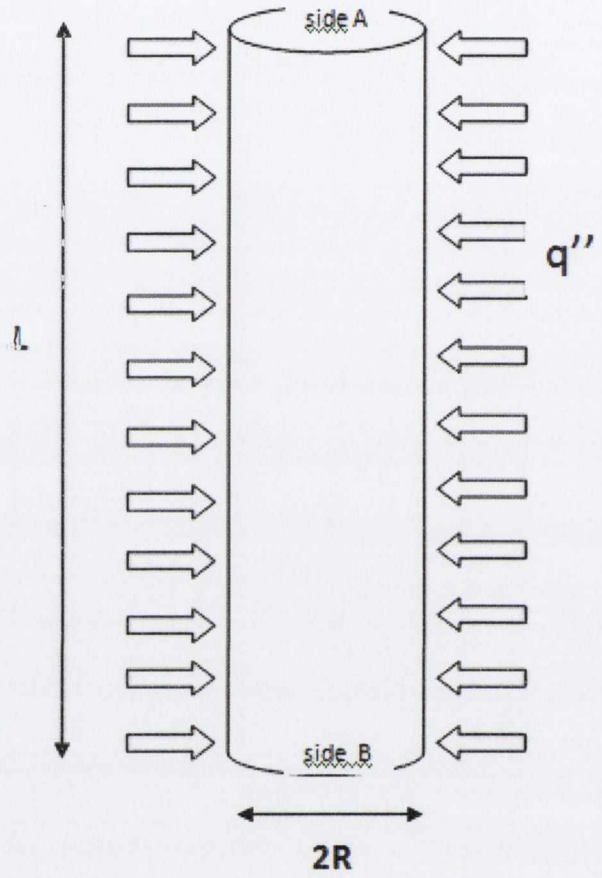

Mathematical Model (no heat sink)

Assumptions:

The 1D assumption, shown above, is used herein. Indeed, the axisymmetry of the problem permits to consider only the variables r (radial) and z (vertical). Then, three different scenarios permit to not take account of z:

- If sides A and B are isolated.
- If the cylinder is infinite (L>>R)
- If the characteristic time of the vertical heat sinks is higher than the characteristic time of this model, this assumption is fair for the beginning of the phenomenon.

So, for $0<r<R$ and $t>0$, $T(r,t)$ is solution of the system:

$$\begin{cases} \dfrac{\partial T}{\partial t} - a\left(\dfrac{1}{r}\dfrac{\partial T}{\partial r} + \dfrac{\partial^2 T}{\partial r^2}\right) = 0\ (1) \\ \left.\dfrac{\partial T}{\partial r}\right|_{r=0} = 0\ (2) \\ \left.\dfrac{\partial T}{\partial r}\right|_{r=R} = \dfrac{q''}{k}\ (3) \\ T(r,0) = Ti\ (4) \end{cases}$$

Where k is the conductivity, R the radius and a the diffusivity.

The following variable change is used:

$$v(r,t) = T(r,t) - w(r,t)$$

$$w(r,t) = \frac{q''}{2kR}r^2 - (\frac{2q''}{\rho c_p R})t$$

w(r,t) solves (1),(2) and (3). So v(r,t) is solution of this new system:

$$\begin{cases} \dfrac{\partial v}{\partial t} - a\left(\dfrac{1}{r}\dfrac{\partial v}{\partial r} + \dfrac{\partial^2 v}{\partial r^2}\right) = 0\ (1') \\ \left.\dfrac{\partial v}{\partial r}\right|_{r=0} = 0\ (2') \\ \left.\dfrac{\partial v}{\partial r}\right|_{r=R} = 0\ (3') \\ v(r,0) = Ti - \dfrac{q''}{2kR}r^2 (4') \end{cases}$$

According to the variable separation method, the shape of v(r,t) is:

$$v(r,t) = \sum_{n\epsilon N} G_n(t)F_n(r)$$

Equation (1') becomes:

$$\frac{G_n'(t)}{aG_n(t)} - \frac{F_n''(r) + \frac{1}{r}F_n'(r)}{F_n(r)} = -\lambda_n^2,\ \ \lambda_n \epsilon \mathbb{C}$$

F_n is solution of:

$$\begin{cases} F_n'' + \dfrac{1}{r}F_n' + \lambda_n^2 F_n = 0\ (a) \\ F_n'(0) = 0\ (b) \\ F_n'(R) = 0\ (c) \end{cases}$$

Equation (a) gives:

$$F_n(r) = B_n J_0(\lambda_n r) + C_n Y_0(\lambda_n r)$$

Where J_0 and Y_0 are respectively Bessel functions of the first and the second kind, order 0.

$$F_n(0)\ has\ to\ be\ real.\ Or\ \lim_{r\to 0} Y_0(\lambda_n r) = -\infty.\ So\ C_n = 0.$$

Equation (c) involves:

$$F_n'(R) = -B_n\lambda_n J_1(\lambda_n R) = 0$$

$$\rightarrow \lambda_n = \frac{Z_n}{R}\ ,where\ Z_n\ are\ the\ roots\ of\ J_1$$

F_n does solve (c).

G_n is solution of:

$$G_n'(t) + a\lambda_n^2 G_n(t) = 0$$

$$\rightarrow G_n(t) = D_n e^{-a(\frac{Z_n}{R})^2 t}$$

V(r,t) is now equal to:

$$v(r,t) = \sum_{n\epsilon N} A_n\, e^{-a(\frac{Z_n}{R})^2 t} J_0\left(\frac{Z_n}{R} r\right)$$

Or,

$$v(r,0) = Ti - \frac{q''}{2kR} r^2 = \sum_{n\epsilon N} A_n J_0\left(\frac{Z_n}{R} r\right)$$

The $J_0\left(\frac{Z_n}{R} r\right)$ are solution of the system [(a),(b),(c)]. So they are orthogonal two-by-two and form a base of the vectorial space associated to an adapted scalar product. The weight of this scalar product is equal to r. The A_n are the coefficients of the projection of v(r,o) on this base:

$$A_n = \frac{1}{\left\| J_0\left(\frac{Z_n}{R} r\right)\right\|^2} \left\langle Ti - \frac{q''}{2kR} r^2 \middle| J_0\left(\frac{Z_n}{R} r\right)\right\rangle$$

$$A_n = \frac{2}{R^2 {J_0}^2(Z_n)} \int_0^R r\, v(r,0) J_0\left(\frac{Z_n}{R} r\right) dr$$

T(r,t) is finally equal to:

$$T(r,t) = \sum_{n\epsilon N} A_n\, e^{-a(\frac{Z_n}{R})^2 t} J_0\left(\frac{Z_n}{R} r\right) + \frac{q''}{2kR} r^2 + (\frac{2q''}{\rho c_p R})t$$

For t high, T has an asymptotical behaviour:

$$T_{asym}(r,t) = A_0 + \frac{q''}{2kR}r^2 + (\frac{2q''}{\rho c_p R})t$$

So:

$$\lim_{t\to+\infty} \Delta T_{R/0} = \frac{q''R}{2k}$$

A characteristic time, τ, of the "transient" state (before reaching the asymptote) could be the characteristic time of the slowest exponential $e^{-a(\frac{Z_n}{R})^2 t}$:

$$\tau = \frac{1}{a}\left(\frac{R}{Z_1}\right)^2, where\ Z_1 = 3.8317$$

Results of the Model

For sample cylinder of radius R=4mm, thermal conductivity of k=84 W/mK, a density of ρ = 15630 kg/m^3, and a specific heat of Cp=258 J/kgK.

$$\rightarrow \tau = 0.0523\ s$$

$$\rightarrow 5\tau = 0.26\ s$$

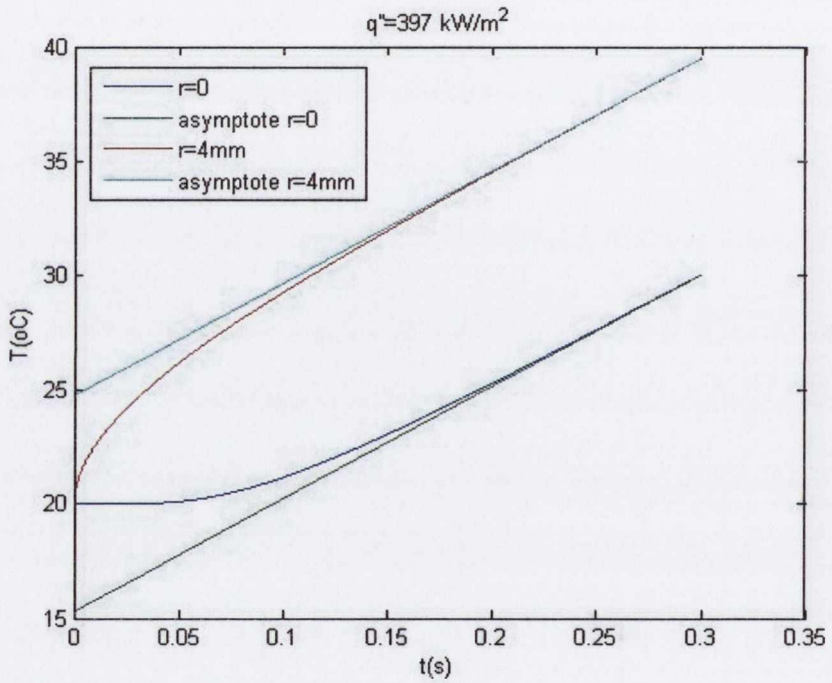

$$\lim_{t \to +\infty} \Delta T_{R/0} = 9{,}45\ ^oC$$

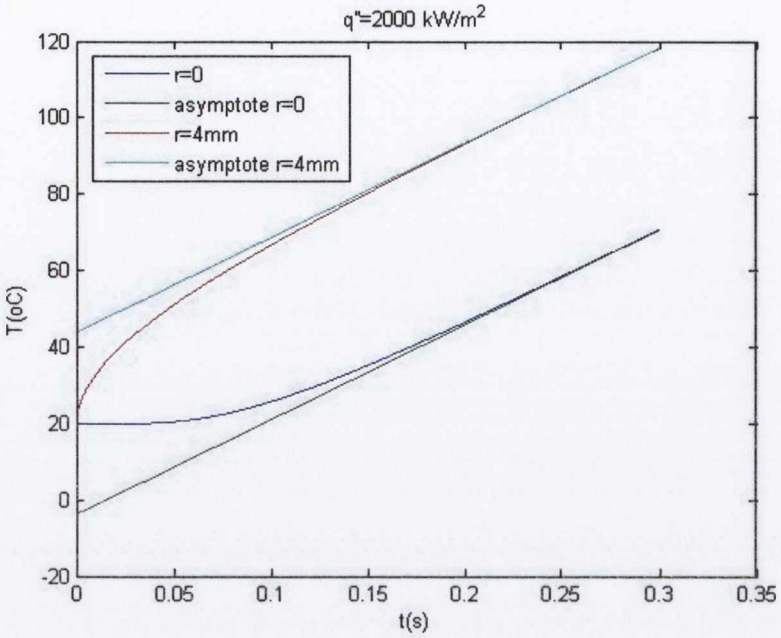

$$\lim_{t \to +\infty} \Delta T_{R/0} = 47{,}62\,^{o}C$$

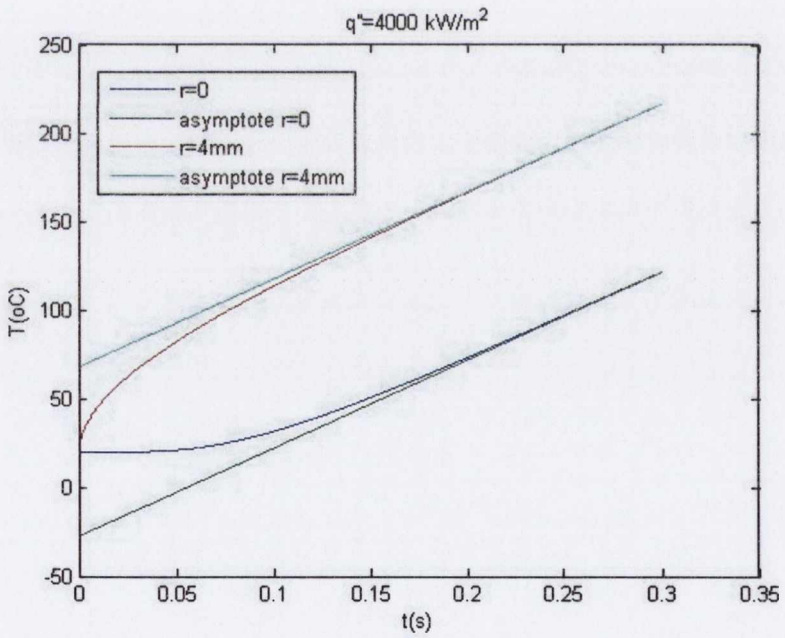

$$\lim_{t \to +\infty} \Delta T_{R/0} = 95{,}24\,^{o}C$$

Appendix 4: ANSYS APDL Code - Basic cylinder parametric

```
!Simulate a controlled heat flux at the boundary of a 3D cutting tool

FINISH
/CLEAR
C***
C***CALCULATION OF TEMPERATURE DISTRIBUTION IN THE CUTTING TOOL
C***

/view,1,2,3

/plotts,info,1

/filename,3D_CYLINDER

/PREP7
!ELEMENT
ET,1,PLANE55
ET,2,SOLID278

!Draw the circle and mesh
X_CENTRE=0
Y_CENTRE=0
*ask,DIAMETER,What is the Tool Diameter (m),0.008
*ask,DEPTH,What is the Tool Length (m),0.06

CYL4,X_CENTRE,y_CENTRE,(DIAMETER/2),,,,DEPTH

NUMMRG,ALL
NUMCMP,ALL

!Mesh the Tool Diameter
LSEL,S,,,1,8
```

```
LESIZE,ALL,DIAMETER/32
ALLS
LSEL,s,,,9,10
LESIZE,ALL,DIAMETER/16
TYPE,1
AMESH,1
ALLS

!Sweep the diametric mesh over the length of the tool
TYPE,2
VSWEEP,1,1,2,1

!Results in 115797 nodes

!Apply the Tungsten Carbide Material model to the volume
!Define thermal properties of Tungsten Carbide
MP,DENS,1,15630  !Unit - kg/m^3
MP,KXX,1,84                !Unit - W/mK
MP,C,1,258          !Unit - J/kgK
MAT,1
alls

!---------------------------------
! Defining the Analysis     --
!---------------------------------

!Set the type of Thermal Analysis
ANTYPE,TRANS,NEW

!Set the input Fluxes load and base temperature
*ask,HEAT_FLUX,What is the heat flux at the surface (W/m^2)?,397000
*ask,TEMP_INIT,What is the initial temperature (K)?,20

!Set the time step and time between steps
```

```
*ask,STEP_TIME,What is the time per step (s)?,0.3
*ask,SUB_TIME,What is the time between steps (s)?,0.001

!-----------------------------------
!Step 1 - Initialisation          --
!-----------------------------------

!Specify model starts at ambient temperature
TUNIF,TEMP_INIT

ALLS
!Specify initial conditions
!IC,ALL,TEMP,TEMP_INIT

!Time at end of load step
TIME,SUB_TIME
!Specify whether loads are ramped (0) or stepped (1)
KBC,1

!Specify the boundary conditions on ends of cylinder
ASEL,S,,,1,2
SFA,all,,HFLUX,0
ALLS

!Select the areas on which to apply the heat flux BC
ASEL,S,,,3,4
SFA,all,,HFLUX,0
ALLS

!Specify the number of substeps for the load step
AUTOTS,ON
NSUBST,5,80,5
LSWRITE
alls
```

```
!-----------------------------------
!Step 1A                    --
!-----------------------------------

!Specify model starts at ambient temperature
TUNIF,TEMP_INIT

!Time at end of load step
TIME,STEP_TIME
!Specify whether loads are ramped (0) or stepped (1)
KBC,1

!Specify the boundary conditions on bottom surface
ASEL,S,,,1,2
SFA,all,,HFLUX,0
ALLS

!Select the nodes on which to apply the heat flux BC
ASEL,S,,,3,4
SFA,all,,HFLUX,HEAT_FLUX
ALLS

!Specify the number of substeps for the load step
AUTOTS,ON
NSUBST,20,80,10
LSWRITE
alls


!-----------------------------------
!Enter the solution phase of analysis
!-----------------------------------
```

```
/SOLU
!Activate the optimized nonlinear solution defaults
!and some enhanced internal solution algorithms
SOLCONTROL,ON
!Tell the program to print out the
!nodal DOF solution for every time substep
OUTPR,NSOL,all
!Write the nodal solution to file for every substep
OUTRES,NSOL,all
!Turn on graphical solution tracking
/GST,ON
!Solve for load steps 1 to...
LSSOLVE,1,2
FINISH
```

Appendix 5: ANSYS APDL Code - Tool and Holder 3D model import, meshing, material properties and contact properties

```
!Simulate a controlled heat flux at the boundary of a 3D cutting tool

FINISH
/CLEAR
C***
C***MESH GENERATION FOR THE ITT CUTTING TOOL SENSOR
C***

/VIEW,all,1,1,1

/FILNAME,ToolandHolder

!---------------------------------
!Import the Geometries
!---------------------------------

/INPUT,tool_fake_holder.anf

/UNITS,SI

/PREP7
!ELEMENT
ET,1,SOLID87

!Apply the Tungsten Carbide Material model to the volume
!Define thermal properties of Tungsten Carbide

MP,DENS,1,15800          !Density :              Unit - kg/m^3
MP,C,1,210          !Specific Heat :        Unit - J/kgK
MP,KXX,1,92              !Thermal Conductivity : Unit - W/mK
MAT,1
```

```
alls

!---------------------------------
!Meshing Cutting Tool
!---------------------------------

SMRTSIZE,7
VMESH,2

!---------------------------------
!Generate the 2nd Volume
!---------------------------------

VSEL,S,,,1

!For Transient Thermal Contact Conduction - Check out:
!http://www.eng-tips.com/viewthread.cfm?qid=158397

!Apply the AISI 4140 Annealed Steel model to the volume

MP,DENS,2,7850          !Density :              Unit - kg/m^3
MP,KXX,2,42.2           !Thermal Conductivity : Unit - W/mK
MP,C,2,473          !Specific Heat :        Unit - J/kgK
MAT,2
alls

!---------------------------------
!Meshing Tool Holder
!---------------------------------

SMRTSIZE,4
VMESH,1

!-------------------------------------------------------------
```

```
!PERFORM MANUAL CONTACT PAIRING
!------------------------------------------------------------

CNCHECK,TRIM
CNCHECK,ADJUST
CNCHECK,AUTO,3
CNCHECK,SUMMARY

SAVE,Sample_Run,db
```

Appendix 6: ANSYS APDL Code – FE model boundary condition application and iteration setup of tool and holder

```
finish
/CLEAR

C***
C***CALCULATION OF TEMPERATURE DISTRIBUTION IN THE CUTTING TOOL
C***

/VIEW,all,1,1,1

/FILNAME,Sample_Run


RESUME,Sample_Run,db

/PREP7

!---------------------------------
!Defining the Analysis
!---------------------------------

!Set the type of Thermal Analysis
ANTYPE,TRANS,NEW
NROPT,AUTO              !Specifies the Newton-Raphson option for transient analysis
!THOPT,QUASI            !Nonlinear transient thermal solution option
EQSLV,JCG               !Specifies the type of equation solver

!Set the input Fluxes load and base temperature
HEAT_FLUX = 397*1000
TEMP_INIT = 20
CONVECTION = 0
```

```
!Set the time step and time at end of steps
STEP_TIME = 7
SUB_TIME = 0.001

!Set the distance of the heat load from the tool cutting tip
HEAT_POS = 0.016
HEAT_POS1 = 0.137 - HEAT_POS
HEAT_BAND = 0.005

!---------------------------------
!Step 1sub - Initialisation
!---------------------------------

!Specify model starts at ambient temperature
TUNIF,TEMP_INIT

!Time at end of load step
TIME,SUB_TIME
!Specify whether loads are ramped (0) or stepped (1)
KBC,1

!Specify the boundary conditions on end of cylinder
ASEL,S,,,1
DA,ALL,TEMP,TEMP_INIT
ALLS

LOCAL,20,1,0,0,0

!Select the areas on which to apply the heat flux BC
ASEL,S,LOC,Z,HEAT_POS1 - (HEAT_BAND/2),HEAT_POS1 + (HEAT_BAND/2)
ASEL,R,LOC,X,0.0035,0.004
SFA,ALL,,HFLUX,0
```

```
!Select the areas on which to apply adiabatic BC
ASEL,S,,,440,441
ASEL,A,,,463,464
!ASEL,A,,,2
ASEL,A,,,5,7
ASEL,A,,,9,10
SFA,all,,HFLUX,0
ALLS

!Specify the number of substeps for the load step
AUTOTS,ON
NSUBST,5,10,3
LSWRITE
alls

!---------------------------------
!Step 2
!---------------------------------

!Time at end of load step
TIME,1
!Specify whether loads are ramped (0) or stepped (1)
KBC,1

!Specify the boundary conditions on end of cylinder
ASEL,S,,,1
DADELE,ALL,TEMP
DA,ALL,TEMP,TEMP_INIT
ALLS

LOCAL,20,1,0,0,0

!Select the areas on which to apply the heat flux BC
ASEL,S,LOC,Z,HEAT_POS1 - (HEAT_BAND/2),HEAT_POS1 + (HEAT_BAND/2)
```

```
ASEL,R,LOC,X,0.0035,0.004
SFADELE,ALL,,HFLUX
SFA,ALL,,HFLUX,HEAT_FLUX

!Select the areas on which to apply adiabatic BC
ASEL,S,,,440,441
ASEL,A,,,463,464
!ASEL,A,,,2
ASEL,A,,,5,7
ASEL,A,,,9,10
SFADELE,ALL,,HFLUX
SFA,all,,HFLUX,0
ALLS

!Specify the number of substeps for the load step
AUTOTS,ON
NSUBST,5,50,5
LSWRITE
alls

!---------------------------------
!Step 3
!---------------------------------

!Time at end of load step
TIME,STEP_TIME
!Specify whether loads are ramped (0) or stepped (1)
KBC,1

!Specify the boundary conditions on end of cylinder
ASEL,S,,,1
DADELE,ALL,TEMP
DA,ALL,TEMP,TEMP_INIT
ALLS
```

```
LOCAL,20,1,0,0,0

!Select the areas on which to apply the heat flux BC
ASEL,S,LOC,Z,HEAT_POS1 - (HEAT_BAND/2),HEAT_POS1 + (HEAT_BAND/2)
ASEL,R,LOC,X,0.0035,0.004
SFADELE,ALL,,HFLUX
SFA,ALL,,HFLUX,HEAT_FLUX

!Select the areas on which to apply adiabatic BC
ASEL,S,,,440,441
ASEL,A,,,463,464
!ASEL,A,,,2
ASEL,A,,,5,7
ASEL,A,,,9,10
SFADELE,ALL,,HFLUX
SFA,all,,HFLUX,0
ALLS

!Specify the number of substeps for the load step
AUTOTS,ON
NSUBST,10,40,10
LSWRITE
alls

!-----------------------------------------------
!Enter the solution phase of analysis
!-----------------------------------------------

/SOLU
!Activate the optimized nonlinear solution defaults
!and some enhanced internal solution algorithms
SOLCONTROL,ON
!Set the convergence values for nonlinear analysis
```

```
CNVTOL,TEMP,1E-7
CNVTOL,HEAT,1E-7
!Tell the program to print out the
!nodal DOF solution for every time substep
OUTPR,NSOL,all
!Write the nodal solution to file for every substep
OUTRES,NSOL,all
!Turn on graphical solution tracking
/GST,ON
!Solve for load steps 1 to...
LSSOLVE,1,3
FINISH

SAVE,Sample_Run,db,,all
```

Appendix 7: ANSYS APDL Code – Post processing analysis

```
!-----------------------------------------------
!Enter the post-processing phase
!-----------------------------------------------
/RESET
/ANNOT,DELE

/POST1
/ERASE
/RGB,INDEX,100,100,100, 0
/RGB,INDEX, 80, 80, 80,13
/RGB,INDEX, 60, 60, 60,14
/RGB,INDEX, 0, 0, 0,15
ALLS

/VIEW,all,1,1,1

/WINDOW,1,ltop $/WINDOW,2,rtop
/WINDOW,3,bot
/WINDOW,2,off $/WINDOW,3,off

/VIEW,all,1,1,1
!/VUP,ALL,Y
!/angle,all,240
/DIST,ALL,AUTO
/ANNOT,ON
/TSPEC,0,0.700,1,0,0
/PLOPTS,INFO,3
/PLOPTS,LEG1,0
/PLOPTS,LEG2,0
/PLOPTS,LEG3,1
/PLOPTS,FRAME,0
```

```
/PLOPTS,TITLE,0
/PLOPTS,MINM,0
/PLOPTS,LOGO,0
/PLOPTS,WINS,ON
/PLOPTS,WP,OFF
/PLOPTS,DATE,0
/TYPE,,2
/TRIAD,OFF
/LIGHT,all,1,10,1,0,0,ON
/DEVICE,FONT,1,ARIAL,500,0,14,14,14,0
/UDOC,1,CNTR,OFF
/GFORMAT,,,4
PLNSOL,TEMP

/NOERASE

/AUTO,all
/WINDOW,1,OFF, $/WINDOW,3,ON
/VIEW,3,-1,1,0
CSYS,0
VSEL,S,,,2
ESLV,S
!NSLE,S
!NSEL,R,LOC,X,0,0.5
!ESLN,S
!/VUP,ALL,Y
!/ANGLE,all,30
!/FOCUS,3,0,0,0,0
/FOCUS,3,AUTO
/DIST,3,AUTO
/ANNOT,OFF
PLNSOL,TEMP
ALLS
```

```
/WINDOW,3,OFF, $/WINDOW,2,ON
/NOERASE
/VIEW,2,0,0,-1
NSEL,S,LOC,Z,HEAT_POS1 - (0.001/2),HEAT_POS1 + (0.001/2)
ESLN,S
PLNSOL,TEMP

/IMAGE,SAVE,Sample_Result,PNG

NSEL,S,LOC,Z,HEAT_POS1 - (HEAT_BAND/2),HEAT_POS1 + (HEAT_BAND/2)
ESLN,S
NSORT,TEMP
*GET,MAX_NODE,SORT,0,IMAX

!-----------------------------------------------------------------
!Obtain Time History Results at Nodes of Interest
!-----------------------------------------------------------------

/RESET
/POST26

DIAMETER = 0.008
DEPTH = 0.0315
ITT_DEPTH = 0.0005

/ERASE
TIMERANGE,0,STEP_TIME+SUB_TIME
ALLS

!MAX_NODE = 1363
ITT_0 = 149838
ITT_90 = 76794
ITT_180 = 111318
ITT_270 = 156104
```

```
CNR_NODE = 240275

!Get the Surface Temperature Node
!*DIM,SURFACE,,12,1,1
!*VGET,SURFACE,NODE,MAX_NODE,TEMP,,TF,SUM
NSOL,2,MAX_NODE,TEMP,,SURFACE,,

!Get the ITT Depth Temperature Node
NSOL,3,ITT_0,TEMP,,ITT_0,,

/VIEW,1,0,0,0
/NOERASE
/FOCUS,1,AUTO
/DIST,1,AUTO
/AXLAB,X,Time (s)
/AXLAB,Y,Temperature (deg C)
/GRID,1
/GROPT,CURL,OFF
PLVAR,2,3
/GROPTS,VIEW,1
PRVAR,2,3
```

Appendix 8: LTM12 Tooling Material Manufacturing Instructions and Specifications

Instructions for use

Initial cure guidelines:

LTM prepregs contain highly reactive resin systems which can undergo severe exothermic heating during initial cure. The recommended curing procedures should therefore be followed in all cases, with special attention being paid to heat up rates and maximum cure temperatures. For non-standard applications always refer to ACG Technical Dept, or Manufacturing Procedures Manual TDS1001.

The prepreg is supplied in a lightly 'B' staged condition aimed at providing high flow plus maximum room temperature worklife. In this initial condition, which is preferred by some customers, the prepreg may feel wet and prove difficult to handle especially in hot weather.

If desired, further 'B' staging may be carried out by the customer to improve tack and handling characteristics for particular applications. This may be achieved as follows:-

LTM12 and LTM16:

The prepreg roll may be left out (suspended horizontally) and at 20 ±2°C (60 ± 5°F) for sufficient time to achieve exactly the desired degree and type of tack appropriate to the application.

LTM10:

This resin is very reactive and 'B' staging of the complete roll is not advised due to the risk of exotherm. However, LTM10 prepreg may be unrolled and 'B' staged as precut sheets. The sheet material should be laid flat as a stack containing not more than 3 layers and held at 20 ±2°C (60 ± 5°F) until the desired level of tack is achieved.

In all cases the work life at room temperature will be reduced proportionally from the times quoted, according to the additional 'B' Staging time used.

Please contact ACG Technical Dept for advice on these procedures if required.

The recommended time/temperature conditions to be applied to LTM10, LTM12 and LTM16 are summarised overleaf:

Resin System	LTM10		LTM12		LTM16	
Reinforcement	Carbon	Glass	Carbon	Glass	Carbon	Glass
Work life (days) at 22°C (68°F)	2-3	2-3	3-4	3-4	6-7	6-7
Min. Initial Cure °C (°F) for	22 (72) 6 days	22 (72) 6 days	30 (86) 70 hours	30 (86) 70 hours	40 (104) 48 hours	40 (104) 48 hours
Overnight Cure °C (°F)	46 (115)	44 (111)	53 (127)	50 (122)	60 (140)	58 (136)
Max. Initial Cure °C (°F) for	60 (140) 3 hrs	55 (131) 5 hrs	70 (158) 3 hrs	60 (140) 6 hrs	60 (140) 12 hrs	60 (140) 12 hrs
Shelf life at -18°C (0°F)	>1 year	>1 year	6 months	6 months	>1 year	>1 year
Max. Operating temp. in air °C (°F)	200 (392)	200 (392)	200 (392)	200 (392)	200 (392)	200 (392)

N.B 1. Maximum Heating Rate 0.5°C (1.0°F) per minute.
2. In all cases temperatures refer to tool or component being cured.

Post-Cure Options:

A post-cure should be applied whenever optimum properties and high temperature service are required.

Option One (Recommended) Single ramp post-cure - Figure 1.
Option Two (Alternative) Stepped ramp post-cure - Figure 2.

These examples are for tools to be used up to 200°C (392°F). For lower operating temperatures alternative cycles may be applied. Please consult ACG for advice in such cases.

For tool lay-up recommendations refer to detailed Manufacturing Procedure (TDS1001), available on request.

Technical Data

Typical Physical Properties - Tooling Laminates:

Cured Laminate Physical Property - LTM10, LTM12 or LTM16		UNITS	VALUES
Fibre Volume Fraction	Carbon Lay-up (Twill weaves)	%v/v	55-60
	Glass Lay-up (Various weaves)	%v/v	50-60
Laminate Void Content	Autoclave Cure	%v/v	<1
	Vacuum Bag Cure	%v/v	<1
Shrinkage During Manufacture	Carbon Tool	%	0.05*
	Glass Tool	%	0.12*
C.T.E. (Autoclave Laminates) RT -> 180°C (356°F)	Carbon Tool	E.x10^{-6}/°C	2.0-3.0*
	Glass Tool	E.x10^{-6}/°C	10.5-12*
Glass Transition Temperature Tg	Fully Post-cured (200°C/392°F)	°C	205-210
	Initial Cure (30°C)		45
	Initial Cure (40°C)		55
	Initial Cure (50°C)		65
	Initial Cure (60°C)		75

NB: *Shrinkage is dependent on construction and processing. Figures quoted are based on ACG's standard LTM10 tooling laminates using fabric styles CF0300 and CF0700 for the carbon and GF0100 and GF0200 for the glass tool laminate.

Typical Mechanical Properties - Tooling Laminates:

Laminates prepared from 280 gsm, 4x4 Twill (3K H.S. Carbon Fibre).
Autoclave cured, post-cured to 200°C.

Interlaminar Shear Strength

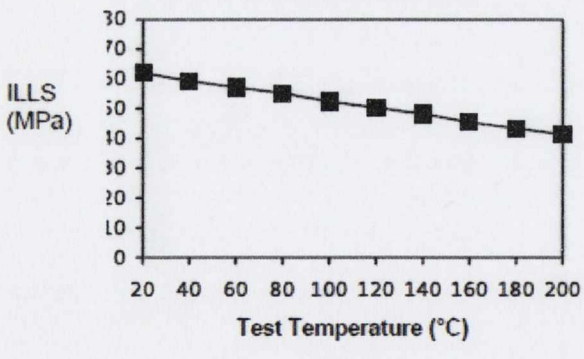

Flexural Strength

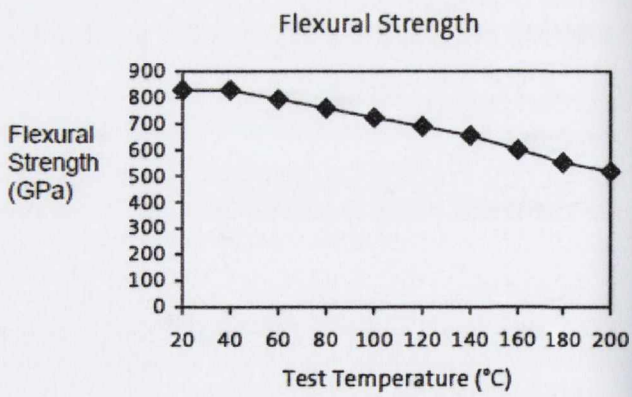

Appendix 9: Manufacturing Procedure for Prepreg CFRP Composite Parts Used in Test Campaign 2

The prepregs for this experiment were supplied by Advanced Composite Group (ACG) Ltd. The procedure for manufacturing these specimens from prepregs using the bag moulding method is shown below.